THE LOW-VELOCITY IMPACT RESPONSE OF THIN, STIFFENED CFRP PANELS

Alexander P Paran B.S.M.E, S.M.M.E

Thesis submitted to the University of Sheffield for the Degree of Doctor of Philosophy in the Faculty of Engineering and Materials.

Department of Mechanical Engineering,
University of Sheffield,
Mappin Street,
Sheffield,
S1 3JD

December 1998

ACKNOWLEDGEMENTS

I would like to thank the following organisations and individuals who have extended their invaluable assistance during the length of my studies at the University of Sheffield:

- The Department of Science and Technology of the Government of the Republic of the Philippines for the financial support they provided during the course of my work. I would like to especially thank Dr. E F Alabastro Ph.D., Undersecretary for R & D, for her support; and Ms. T Dayoan for her assistance in sorting out all the paperwork.
- The College of Engineering of the University of the Philippines in Diliman for granting me leave from my post so that I may pursue further studies.
- My supervisors Dr. M S Found and Dr. I C Howard for their able help, guidance and sound advice.
- Hurel-Dubois UK, Ltd and Mr. M W Jones for supplying the CFRP materials used in this work.
- Mr. D Hallford for allowing me the use of the photographic facilities.
- The highly skilful technicians at the Mechanical Engineering Workshop for their help in the fabrication of the vital components in the impact rig.
- My wife Julie and my sons Bertrand and Carl for being there for me.

SUMMARY

An extensive study of into the static loading response and low-velocity impact response of plain and stiffened CFRP panels was conducted. The study investigated the impact response of the CFRP panels over a range of impact energies that include incident kinetic energies sufficiently high to cause complete penetration of the panel by the impacting mass. Static tests were also conducted by driving a hemispherical-nosed indentor into the panel up to displacements that resulted in the complete penetration of the panel by the indentor. Results from these tests suggest that the static perforation energy could predict the impact perforation energy with reasonable accuracy.

A lumped-parameter mass-spring-damper model that attempted to incorporate the effects of material damage to the panel response was developed. The model was found to be sufficiently accurate in predicting the response of thin panels to static and impact loads up to the critical delamination force threshold.

Assessment of the damaged panels through Penetrant-Enhanced X-Ray methods led to the identification of damage transition energy thresholds that differentiate between changes in damage mechanism. The damage transition energy thresholds were found to be constant fractions of the impact perforation energy.

TABLE OF CONTENTS

1 INTRODUCTION

There has been a considerable amount of research into the impact response of Carbon Fibre Reinforced Plastics or CFRP (Abrate. 1991, 1994; Cantwell and Morton. 1991). This interest is primarily driven by the increasing use of CFRP as structural components in the aerospace industry. From an engineering point of view the use of CFRP in structural components is justified by several distinct advantages composite materials have over conventional materials such as steel or aluminium. These advantages are:

- High specific strength
- Better corrosion resistance
- Better fatigue resistance
- Ease of manufacture into complex shapes
- Design control of its multidirectional properties to suit specific requirements

These advantages, however, are diminished by one major disadvantage and this is the susceptibility of CFRP to damage under localised low-velocity impact loading. This susceptibility to impact damage is due to the limited capability of CFRP to absorb energy through plastic deformation and to the brittle nature of the matrix system used to bind the reinforcing fibres together. In its application in the aerospace industry CFRP components are put into a service environment where foreign object impacts are a common occurrence. The source of these impacts range from dropped tools during maintenance operations, runway debris thrown up against the aircraft during take off or landing and encounters with hailstorms during flight.

Impact damage in CFRP is created when the kinetic energy of the impacting foreign body is expended in a fracture process that creates matrix cracks, delaminations, fibre/matrix debonding and fibre fracture in the material. The severity of this damage is primarily dependent on the incident impact energy. At sufficiently high values of

incident impact energy the resulting impact damage can leave clearly visible marks on the impacted face of the CFRP component in the form of local indentation and crushing of the material. At yet higher impact energies complete penetration of the material can occur creating a hole that has been punched through the thickness of the laminate.

At relatively low incident impact energies it is possible to create damage in the CFRP component without leaving clearly visible evidence of such damage on the impacted face of the material. Such damage is confined within the body of the laminate and on the backface of the material and can be of sufficient size to cause significant reductions in the strength of the component. This phenomenon known as Barely Visible Impact Damage (BVID) and is of more concern than damage due to high-energy impacts. This concern stems from the difficulty of detecting such damage quickly and easily since access to the backface of the damaged component, where the damage can be visibly detected, is often restricted.

Investigations into the impact response and subsequent damage of CFRP have been going on for over twenty years and the work done in this field is already quite extensive. Research is being carried out in the following areas of interest:

- The dynamics of the impact event
- Modelling of the impact damage mechanisms
- The effect of impact damage on the residual properties
- The influence of the material properties and laminate lay-up on the impact damage resistance
- The use of hybrid lay-ups to improve impact damage resistance
- The development of toughened matrix materials to improve impact damage resistance

Most of the research into the impact behaviour of CFRP use plain panels as test samples and it is only recently that stiffened CFRP sections are being investigated. It seems that

significant improvements to the impact damage tolerance of CFRP structures can be achieved with the use of a thin plate or membrane to absorb the energy with the structural stiffness being provided by local stiffeners incorporated into the CFRP panel. The presence of local stiffeners could increase the available elastic energy that can be stored by the material before fracture begins (Davies and Zhang. 1995). This principle has been used in the development of the CFRP wing box for the ATR72 (Tropis et al. 1995) and in the development of the composite wing for the Deutsche Airbus Technology Program (Kolax. 1992).

Although the results of the work done in the impact response of CFRP is now voluminous there does not appear to have been an extensive effort to relate the results so far obtained. Clearly there needs to be more work done along this area. The purpose of the work reported in this thesis is to investigate the response of thin, stiffened CFRP panels subjected to low-velocity impact and to compare its impact behaviour to that of plain panels of similar thickness, material composition and lay-up.

This thesis is comprised of eight chapters. Chapter 1 introduces the background for the work undertaken followed by Chapter 2, which is the review of the available relevant literature on the subject matter. Chapter 3 describes the composite panels tested and details the static and impact tests carried out in the experiments. The results of the tests on the plain and stiffened panels are presented in Chapters 4 and 5 respectively and the modelling of the impact behaviour of the panels tested is discussed in Chapter 6. Chapter 7 discusses the results presented in Chapters 4 to 6. Chapter 8 presents the conclusions drawn from this investigation and suggests recommendations for further work.

2 LITERATURE REVIEW

2.1 INTRODUCTION

It is a well-known fact that impact damage can severely affect the residual mechanical properties of CFRPs (Cantwell et al. 1983, 1984; Davies et al. 1996; Lal. 1983b; Oxley. 1991). Because of this, investigations into the impact dynamics of CFRP have been given much attention. The rationale behind these studies is that the forces, stresses and strains generated during the impact event primarily govern the damage created in the laminate. This chapter reviews the available published work found relevant to the research program presented in this thesis.

2.2 THE STATIC LOAD-DEFLECTION RESPONSE OF THIN PLATES

For small deflections ($w<<h$), the differential equation of static equilibrium for a transversely loaded, thin isotropic plate in a state of plane stress (Timoshenko and Woinowsky-Krieger. 1959) is given by:

$$D\nabla^2\left(\nabla^2 w\right) = D\left(\frac{\partial^4 w}{\partial x^4}+2\frac{\partial^4 w}{\partial x^2 \partial y^2}+\frac{\partial^4 w}{\partial y^4}\right) = q \qquad \text{Eqn. 2.1}$$

where

D = flexural modulus of the plate

∇^2 = the scalar operator $\frac{\partial^2}{\partial x^2}+\frac{\partial^2}{\partial y^2}$

q = the load intensity or the intensity of a continuously distributed load on the plate

w = the deflection of the plate

The validity of the above Equation 2.1 is based on the following assumptions:

1. There are no external forces acting on the middle plane of the plate.
2. The effect of shear forces on the deflection of the plate can be disregarded.
3. The effect of normal stresses in the direction transverse to the plate can be disregarded.

When the deflection of the plate is of the same order of magnitude of (or even exceeds) the thickness of the plate, membrane action (due to supplementary tensile stresses in the middle plane of the plate) results in the introduction of non-linear terms into the differential equations of equilibrium. This naturally makes the solution of the problem more complicated and approximate solutions are often resorted to remove some of the difficulty in solving the equations of equilibrium. For thin circular plates with a single concentrated load P acting at the centre, Timoshenko and Woinowsky-Krieger (1959) expressed the approximate load-deflection characteristic by the non-dimensional relationship:

$$\frac{w_o}{h}+A\left(\frac{w_o}{h}\right)^3=B\frac{Pa^2}{Eh^4} \qquad \text{Eqn. 2.2}$$

where a is the radius of the plate, h is its thickness and w_o is the deflection of the plate at its centre. In the above equation A and B are functions of only the Poisson's ratio and whose mathematical form depend on the boundary conditions imposed on the plate. Thus for a given Poisson's ratio and a given set of boundary conditions A and B are constants.

For the case of a thin, specially orthotropic laminate in a state of plane stress, the differential equation of static equilibrium is (Calcote. 1969; Jones. 1975):

$$D_{11}\frac{\partial^4 w}{\partial x^4}+2(D_{12}+2D_{66})\frac{\partial^4 w}{\partial x^2\partial y^2}+D_{22}\frac{\partial^4 w}{\partial y^4}=q \qquad \text{Eqn. 2.3}$$

where the flexural and torsional moduli are given by

$$D_{11} = \frac{Q_{11} h^3}{12} \qquad D_{12} = \frac{Q_{12} h^3}{12} \qquad D_{22} = \frac{Q_{22} h^3}{12} \qquad D_{66} = \frac{Q_{66} h^3}{12},$$

and where Q_{ij}, the reduced stiffness coefficients, are

$$Q_{11} = \frac{E_1}{1-\nu_{12}\nu_{21}} \qquad Q_{12} = \frac{\nu_{12} E_1}{1-\nu_{12}\nu_{21}} = \frac{\nu_{21} E_2}{1-\nu_{12}\nu_{21}} \qquad Q_{22} = \frac{E_2}{1-\nu_{12}\nu_{21}}$$

$$Q_{66} = G_{12}$$

In the above equations $E_1, E_2, and\ G_{12}$ are the elastic constants and ν_{12}, ν_{21} are the Poisson's ratios in the plane of the laminate. These quantities are required in order to characterise the properties of the material.

For the particular case of an isotropic plate

$$E_1 = E_2 = E \qquad \nu_{12} = \nu_{21} = \nu \qquad G_{12} = G = \frac{E}{2(1+\nu)},$$

$$Q_{11} = Q_{22} = \frac{E}{1-\nu^2} \qquad Q_{12} = \frac{\nu E}{1-\nu^2} \qquad Q_{66} = G,$$

$$D_{11} = D_{22} = (D_{12} + 2D_{66}) = D = \frac{Eh^3}{12(1-\nu^2)}$$

With these additional conditions Equation. 2.3 reduces to Equation. 2.1

Timoshenko and Woinowsky-Krieger (1959) have shown that Equation.2.3 can be roughly applied to the case of an isotropic plate reinforced by a set of equidistant ribs (see Figure 2.1). Disregarding the effect of transverse contraction (i.e. $\nu = 0$), the flexural and torsional rigidities of the stiffened plate are given by

$$D_{11} = \frac{E a_1 h^3}{12\left(a_1 - t - \alpha_1^3 t\right)} \qquad D_{22} = \frac{EI}{a_1}$$

$$D'_{66} = D_{66} + \frac{C}{2a_1} \qquad D_{12} = 0$$

where

a_1 = spacing of the ribs

t = thickness of the ribs

$$\alpha_1 = \frac{h}{h+H}$$

h = thickness of the plate

H = height of the ribs

I = moment of inertia of a T-section of flange width and thickness a_1 and h, respectively; and web height and thickness H and t, respectively

D_{66} = torsional rigidity of the plate without the ribs

D'_{66} = torsional rigidity of the plate with the ribs

C = torsional rigidity of one rib

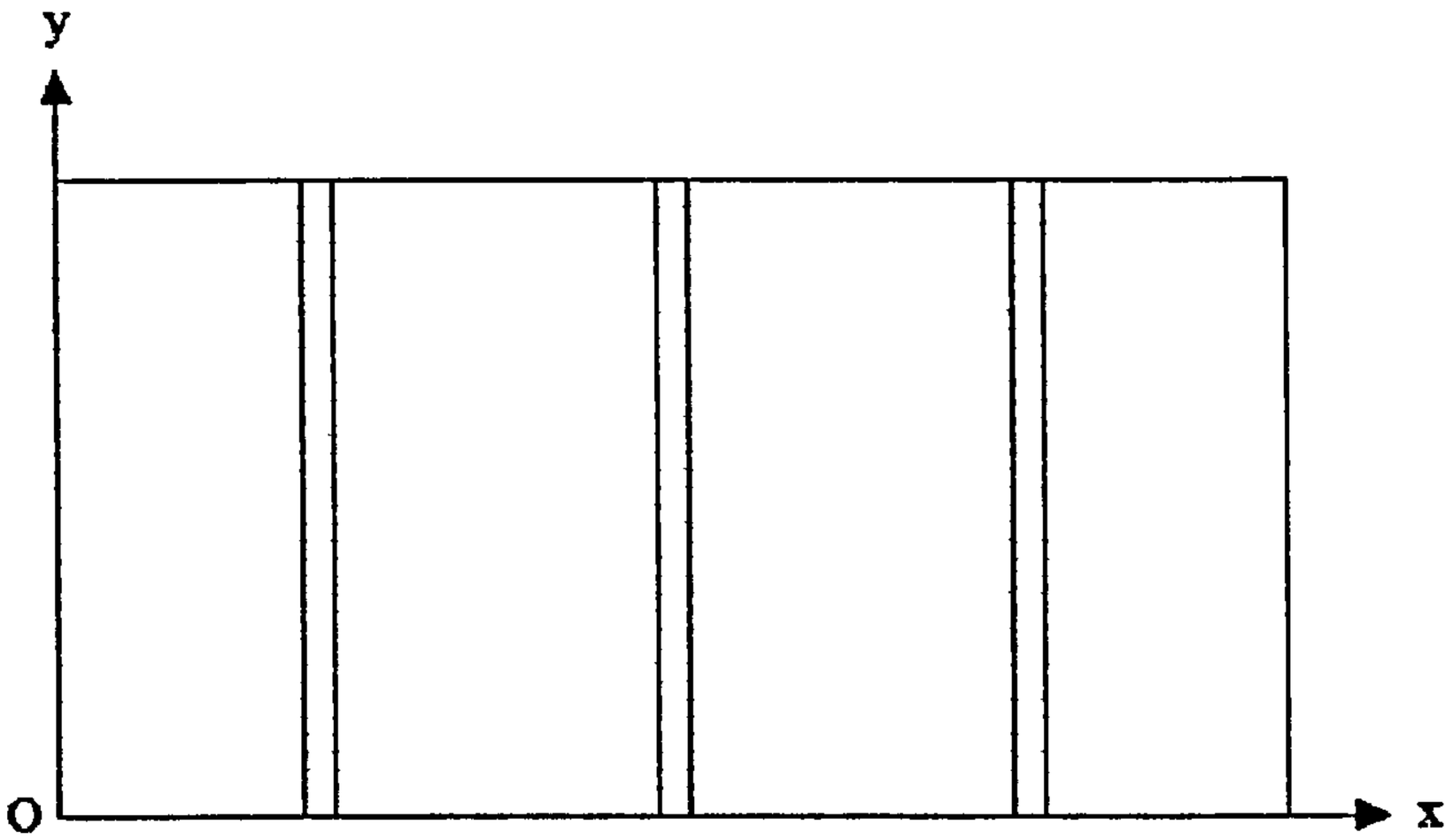

Figure 2.1. Thin plate reinforced by a set of equidistant ribs (Note: The x-y-z axes coincide with the principal 1-2-3 axes.)

2.3 THE LOW-VELOCITY IMPACT RESPONSE OF COMPOSITE PLATES

In the low-velocity impact between a mass or indentor and a thin plate, the contact force is modelled by using the Hertz contact law (Goldsmith. 1960) which is given by the equation

$$P(t) = n\alpha^{3/2} \qquad \text{Eqn. 2.4}$$

where

$P(t)$ = contact force history

n = contact stiffness parameter

α = relative approach (= $w_I - w$, if $w_I > w$, zero otherwise)

w_I = displacement of the mass

w = displacement of the plate at the point of application of the load

Although Equation 2.4 was developed for contact between two isotropic spheres or, if one of the spheres radius is made to approach infinity, that between an isotropic sphere and an isotropic half-space, it has been applied in modified form for contact between an isotropic sphere and a quasi-isotropic plate (Oxley. 1991 citing Willis, and Yang and Sun). The necessary modification involves finding a suitable expression for the contact stiffness parameter n appropriate to the contact problem being studied (Shivakumar et al. 1985 citing Conway and Agnew).

The displacement of the indentor with mass M_I and initial velocity V_0 can be calculated by integrating Newton's second law of motion (with the assumption that at time $t = 0$, when contact between the indentor and plate commences, $w_I = 0$ and $w = 0$):

$$w_I = V_0 t - \frac{1}{M_I} \int \left[\int P(t)\, dt \right] dt \qquad \text{Eqn. 2.5}$$

The displacement of the plate can be determined from the classical equation of dynamic equilibrium for an isotropic plate (Harris and Crede. 1961; Timoshenko et al. 1974):

$$D \nabla^2 \left(\nabla^2 w \right) + \rho h \frac{\partial^2 w}{\partial t^2} = q \qquad \text{Eqn. 2.6}$$

In the Equation 2.6

D = flexural modulus of the plate

∇^2 = the Laplace operator $\frac{\partial^2}{\partial x^2} + \frac{\partial^2}{\partial y^2}$

ρ = density of the plate

h = thickness of the plate

q = the load intensity (which reduces to $P(t)$ for a concentrated load)

Equation. 2.5 is similar to Equation. 2.1 except for the group of terms accounting for lateral inertia in the left-hand side of Equation. 2.5. Similarly the equation of dynamic equilibrium for a thin specially orthotropic plate (Calcote. 1969; Jones. 1975) is given by

$$D_{11} \frac{\partial^4 w}{\partial x^4} + 2(D_{12} + 2D_{66}) \frac{\partial^4 w}{\partial x^2 \partial y^2} + D_{22} \frac{\partial^4 w}{\partial y^4} + \rho h \frac{\partial^2 w}{\partial t^2} = q \qquad \text{Eqn. 2.7}$$

Equations 2.4 to 2.7 allow for a solution of the variables of interest from the dynamics of the impact between the indentor and the plate.

Mindlin (1951) has shown that in problems where sharp transients are involved or when vibration modes of higher order are present, the effect of rotary inertia and transverse shear on the flexural motions of an isotropic plate can be significant. This leads to large disagreements between classical plate theory and the exact three-dimensional equations of elasticity. To eliminate these errors, Mindlin (1951) introduced a correction factor into the set of equations he formulated for his plate theory. Furthermore Mindlin (1951) found that the transverse shear deformation accounts almost entirely for the discrepancy between classical plate theory and the three-dimensional theory when he evaluated his equations for the case of straight-crested flexural waves in an infinite plate.

Whitney and Pagano (1970) developed governing equations for heterogeneous anisotropic plates based on a bending theory for anisotropic laminated plates by Yang, Nomi and Stavsky. Like Mindlin's theory it includes the effects of rotary inertia and transverse shear on the flexural motions of the plate. Numerical solutions by Whitney et al (1970) for cross-ply laminates and square angle-ply laminates with $\theta = \pm 45°$ have shown results that deviate significantly from classical plate theory for span ratios (the ratio of the beam or plate width to its thickness) of up to 20. The deviations, however, reduce significantly at span ratios greater than 30. From these findings it is not surprising that many investigations into the impact of thin laminated plates using the classical plate theory (Lal. 1983a, 1983b; Shivakumar et al. 1985, Zhou and Davies. 1995) have found reasonable success in predicting the dynamic response.

An impact on a plate creates tensile, shear and flexural stress waves that propagate away from the impact point. If the magnitude of the impact velocity is much less than the speed of the slowest stress wave or, if the impact duration is longer than half the period of the stress wave with the longest wavelength in the plate, then the plate dynamics involves only the first mode of vibration. This implies that under these conditions the low-velocity impact response of a plate can be treated as a quasi-static problem. Robinson and Davies (1992), drawing on the work by Davies and Godwin, defined what

is meant by "low-velocity." They suggested an upper bound to the impact velocity defined in terms of the compressive failure strain and the velocity of the stress wave originating from the contact zone on the frontface and propagating to the backface of the laminate. This upper bound can be estimated from the equation

$$V_{0,u} = \varepsilon C \qquad \text{Eqn. 2.8}$$

where $V_{0,u}$ is the transition velocity below which the impact event may be considered as being "low-velocity", ε is the compressive failure strain and C is the speed of the stress wave (equal to the speed of sound) in the plate. For common epoxy composites Robinson and Davies (1992) calculated this transition velocity to be between 10 to 20 m/s. The implication that the quasi-static response can be applied in the low-velocity impact response has been used to advantage by many researchers (Lal. 1983a, 1983b; Shivakumar et al. 1985; Zhou and Davies. 1995) and the large deflection theory for thin isotropic plates (Eqn. 2.2) was often used in the formulation of the governing equations. The advantage of using the quasi-static relation is that the impact problem can be reduced to a set of one-dimensional, coupled differential equations to which solutions are more easily found.

2.4 IMPACT MODELS

Impact models of composite laminates reported in technical literature are varied. These models range from relatively simple lumped-parameter, mass-spring-damper systems (Caprino. 1984; Sjoblom. 1987; Lal. 1983a, 1983b; Shivakumar et al. 1985), to more complex multiple degree-of-freedom equations of motion as applied to anisotropic laminated plates or beams (Cairn and Lagace. 1989; Dobyns. 1980; Mindlin. 1951; Olsson. 1992; Whitney and Pagano. 1970) and to computationally intensive FEA models (Banerjee. 1992; Davies et al. 1994; Wu and Springer. 1988). Although the linear mass-spring-damper models may be sufficient in predicting the global dynamic

response of the composite panel to impact loading it may be too imposing for it to account for the development and growth of internal damage in the panel. To thoroughly account for the internal damage, FEA models are more appropriate and have been used with some success. Due to the non-linear behaviour of the dynamical systems modelled, numerical schemes based on time integration techniques are often resorted to in the solution of the equations.

The simplest analytical model is that due to Caprino (1984) which models the impactor-plate system by a single mass and a single linear spring. In this model the plate mass and membrane behaviour of the plate are completely ignored. Based on this model the peak impact force is given by:

$$P_{\max} = \sqrt{2\,U\,k_f} = V_0\sqrt{M_I\,k} \qquad \text{Eqn. 2.9}$$

where

U = incident kinetic energy

k_f = flexural stiffness of the laminate

This mass-spring model was improved upon by Sjoblom et al (1988) by incorporating the non-linear Hertzian contact stiffness between the plate and indentor and by including the plate mass in the equations of motion. This naturally led to a two-degree-of-freedom model that exhibited oscillations in the plate displacement throughout the duration of the impact event. Lal (1983a, 1983b) used a similar model but went further by implicitly including the effects of shear deformation and by using the large deformation theory of plates. Lal also accounted for the progressive reduction in the membrane stiffness of the plate due to possible internal damage by using his experimental data to relate the membrane parameter to the coefficient of restitution. The predictions by the model developed by Lal found close agreement with his experiments in spite of considering only the first mode of flexural vibrations in the plate.

Perhaps the most comprehensive lumped-parameter model reported in the literature was that developed by Shivakumar et al (1985). These authors used an energy balance model and a spring-mass model to predict the maximum impact force and impact duration respectively during the low-velocity impact of circular, quasi-isotropic graphite/epoxy composite plates. The models took into account the effects of Hertzian contact, plate mass, large plate deflection and transverse shear deformation. Shivakumar et al (1985) slightly modified Timoshenko and Woinowsky-Krieger's (1959) theory to describe the load-deflection characteristic of the plate by the relation:

$$P = k_{bs} w + k_m w^3 \qquad \text{Eqn. 2.10}$$

where

k_{bs} = plate stiffness due to bending and shear

k_m = membrane stiffness

From an energy balance of the resulting two degree-of-freedom system, Shivakumar et al (1985) have shown that the kinetic energy of the indentor is related to the maximum displacement of the plate (assuming negligible plate mass) by the equation:

$$M_I V_0^2 = \frac{4}{5}\left[\frac{\left(k_{bs} w_o + k_m w_o^3\right)^5}{n^2}\right] + k_{bs} w_o^2 + \frac{k_m w_o^4}{4} \qquad \text{Eqn. 2.11}$$

where w_o is the maximum deflection of the plate and n is the contact stiffness parameter as defined in Eqn. 2.4. The above equations were used to calculate for the maximum impact force. Comparing their results with predictions from other models, they found that models that neglect membrane stiffening and shear deformation underestimates the impact force for thin laminates and overestimates the force for thick laminates. To predict the force-time history of the impact event Shivakumar et al (1985) applied the equations of motion to a one-dimensional, two degree-of-freedom mass-spring system

and made use of the relations developed for the energy-balance model. The predictions of both models were found to agree very well with test results by other researchers.

In a more involved analytical approach, Dobyns (1980) investigated the static and dynamic responses of simply supported, rectangular orthotropic plates to different impulsive loading conditions. Dobyns' equations were based on the plate equations developed by Whitney and Pagano (1970) and its solution allowed for the calculation of the normal shear force distribution and bending strain distribution in the plate and their time histories as well. His results for constant energy (constant mass and constant velocity) impacts on solid laminate panels of different sizes and thicknesses revealed that the laminate thickness has only a small effect on the interlaminar shear stress but have significant influence on the maximum impact force and maximum bending strain. For a given panel size, the maximum impact force was observed to increase with panel thickness whilst the maximum bending strain tended to do the opposite. The effect of panel size was also investigated and Dobyns (1980) found that, across all panel thicknesses, interlaminar shear stress, maximum bending strain and maximum impact force decreased with increasing panel size.

In a similar approach, Olsson (1992) presented an approximate analytical solution that is valid for low-mass impacts. His analysis is based on the Hertzian contact law and on Kirchoff's plate theory for infinite, specially orthotropic plates. The most significant feature of Olsson's work is the inclusion of all the parameters describing the impact in a single non-dimensional parameter that was used to characterise the impact event. Olsson's results compared reasonably well with the results obtained by Cairns and Lagace (1989) in their analysis of relatively low impactor mass impacts on laminated plates. Olsson (1992) compared his results with the results from 2D and 3D FE Analysis by Aggour and Sun, and Sun and Liou, respectively. His results were in good agreement only during the initial stage of the impact event when the relative approach (the difference between the indentor displacement and the plate displacement) is essentially decreasing with time. The discrepancies were found to be greatest in the prediction for plate displacement in the later stage of the impact event when the relative approach is progressively increasing with time. These discrepancies are possibly due to

the fact that Olsson based his solution on an infinite plate rather than on a plate of finite size with prescribed boundary conditions.

Several investigators used models of the impact response of composite plates based on computationally intensive FEA techniques. Most of these models included the creation and subsequent effects of internal damage on the dynamics of the impact event. Chang and Chang (1987) presented a damage model that sets the appropriate lamina stiffness component to zero whenever maximum values of a tension criterion coupled with a shear criterion are attained. Davies et al (1994), in their attempt to numerially model impact damage, used 2-D plate elements based on a Mindlin-type eight-noded element that incorporated shear deformations. In addition to shear deformation, the effect of non-linear membrane stiffening was included as it was observed that the plates tested produced deformations in excess of the plate thickness. The results from the 2-D analysis found good agreement with test data from undamaged plates. At impact energies that created considerable damage in the test plates Davies et al (1994) resorted to a 3-D model to see if the internal delaminations seriously degraded the plate. The results from this analysis for thin laminates did not predict delamination areas accurately enough. They attributed this shortcoming to the fact that the failure criterion used was stress-based rather than fracture-based.

In his studies into the impact damage in graphite/epoxy laminates, Banerjee (1992) modelled the in-plane failure propagation in the laminate using a stress-based failure criterion. The prediction of the damage pattern distribution in the plies from his simulations suggests that matrix cracking was the initial mode of failure in the laminate. Banerjee (1992) also argued that since transverse stresses could not be modelled accurately by using shell elements, delamination failure could not be predicted accurately by his present model. In order to overcome this deficiency he suggested using solid elements or improved shell elements to obtain accurate predictions of the transverse stresses. Wu and Springer (1988) had more success in predicting the size of the delaminations in non-penetrating impacts on composites plates. Their results, which were based on 3D stress analysis using FEA techniques, show that the calculated and measured delamination lengths and widths agree within 20 percent.

2.5 SCALING RULES

In order to relate the impact response of laboratory test specimens to that of full size structures scaling rules were investigated by Morton (1998), Qian and Swanson (1990), and Qian et al (1990). Morton used Buckingham's π-theorem to determine the scaling rules and found 13 π-terms or dimensionless groups expressed in terms of the geometrical parameters, the material properties of the plate an indentor, and the input parameters (such as the initial velocity of the indentor). Morton found that in general complete similarity is not possible and that some relaxation of the similarity requirements has to be made. This is particularly true of strain rate-sensitive and/or notch-sensitive materials. His findings show that classical scaling laws apply to the elastic (undamaged) behaviour of transversely impacted carbon fibre/epoxy beams with impact duration and impact force scaling as s (the scale factor) and s^2 respectively. Nonetheless he warns that the scale modelling of laminated composite components be done with extreme caution and recommends that extensive testing be required to establish the validity of the pertinent scaling parameters.

Qian and Swanson (1990), and Qian et al (1990) used the dependence of the laminate properties on its thickness and the equations of motion governing the dynamic response of an orthotropic plate to determine the scaling factors for plates of the same material. In their analysis Qian et al found that if the geometry of the plates scale as λ the impact force scales as λ^2 and the time to maximum load and strain scale a λ. This is identical to Morton's findings for laminated beams discussed in the preceding paragraph. To verify the accuracy of the scaling rules impact tests were conducted in which the dimensions of the plates, impactors and strain gauges were varied by a factor ranging from one to five. Results from the tests show that the measured strain responses followed the scaling rules closely when there is no damage created in the plate. The scaling rules did not with meet much success when used to predict the size of the delaminations in the damaged plates. The application of the scaling rules predicts significantly smaller delaminations as the scale factor is increased.

Using finite element analysis, Kistler and Waas (1997) looked into the scaling of the impact response of cylindrically-curved laminates. They performed a parametric study into the effects of varying some input variables while holding others constant on the impact response of the laminates. Their results show that:

1. For constant impact energy, the small and large deformation response duration scale with the momentum whilst the peak force and displacement remain constant.
2. For constant indentor mass, momentum (or velocity) scales the small deformation force and displacement response. On the other hand, energy (or the square of the velocity) scales the large deformation response and there is no scaling quantity that can be applied to the time scale because of the apparent inverse relationship between velocity and contact duration.
3. For constant indentor velocity, momentum (or the mass of the indentor) scales the force response.

Based on these results Kistler and Waas (1997) deduced that the small deformation response may be momentum governed whilst the large deformation response may be energy dominated. In the discussion of their results Kistler and Waas (1997) described resulting impact displacements greater than the thickness of the shells modelled as large displacement response. Conversely shell displacements in the same order as the thickness of the shell were described as small displacement response.

Robinson and Davies (1992) conducted an experimental study into the effects of scaling on the low-velocity impact of laminated composites. They found that changes in the indentor mass which result in changes to the dynamics of the indentor-plate system do not significantly affect the stress distribution near the impact point implying that the plate is responding in a quasi-static manner. They also found that:

1. For the range of impact energies tested, the strain rate does not significantly affect the material behaviour.
2. Impact damage appears to be a function of incident kinetic energy and not of indentor mass or velocity taken separately.

3. There is a significant difference between the calculated values of absorbed energy and damage energy that needs to be resolved with further studies.

2.6 IMPACT DAMAGE IN CFRP PLATES

Low-velocity impact-induced damage in CFRP consist of matrix cracks, fibre fracture and delaminations. Of these damage types it is the delaminations that are particularly worrisome in that they can adversely affect the compression after impact properties of the material (Prichard and Hogg. 1990). Delaminations are always accompanied by matrix cracks and, in laminates made from unidirectional plies, have the characteristic double-lobe shape at the interface between two plies (Cantwell and Morton (1985),Liu. 1988; Hong & Liu (1989)]. These double-lobe patterns were always found to be oriented in the fibre direction of the ply furthest from the impacted face (see Figure 2.2). The delaminations were explained by Liu (1988), and Hong and Liu (1989) to be due to the mismatch of bending stiffness between two adjacent ply layers. They discovered that the larger the difference in the fibre orientation between two adjacent plies, the greater is this mismatch and the bigger is the delamination produced at the interface. Clark (1989) presented a model that could explain this observation. In his model the curvatures in each ply layer causes tension in the fibre directions that will either result in net forces that push the plies together or in peel forces that pull the plies apart and thus promote delamination.

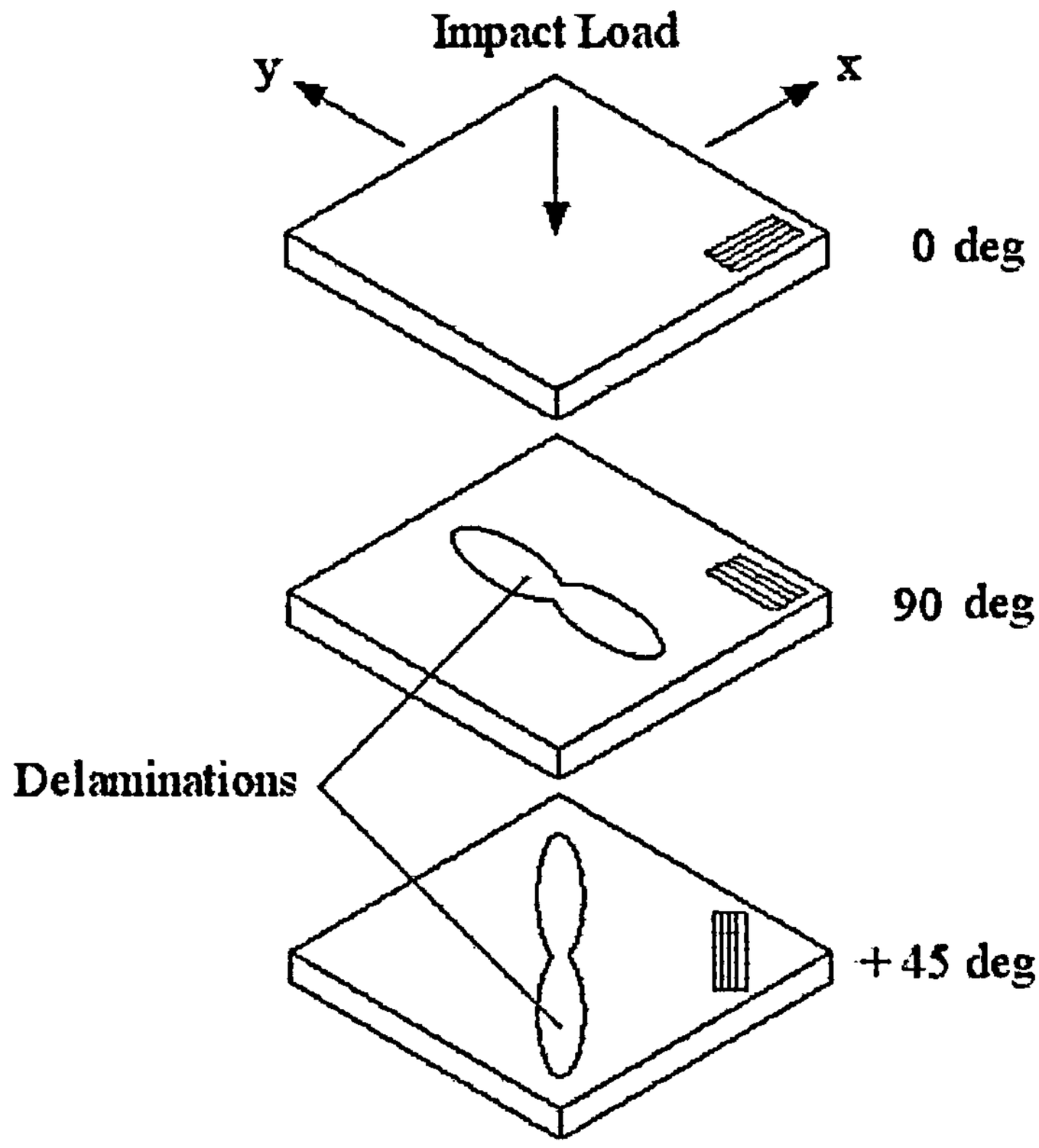

Figure 2.2. Exploded view of the first 3 plies of an impacted laminate illustrating the double-lobe delamination patterns and its orientation relative to fibre direction.

Matrix cracking also forms a pattern wherein the cracks propagate through the matrix between the fibres in a given ply. This propagation pattern together with the double-lobe shape of the delaminations gives rise to the top hat geometry (see Fig. 2.3) that is characteristic of the impact-damaged zone (Clark. 1989; Choi et al. 1991a, 199b). The pattern of matrix cracks and delaminations also depends on the rigidity of the laminate (Cantwell and Morton. 1985). In flexible laminates the high bending stresses generated by the impact event creates matrix cracks in the ply furthest from the impacted face. These cracks are then deflected at the nearest interface to form delaminations, which in turn are deflected to form more matrix cracks in the adjacent ply. This sequence of failures is repeated in the succeeding plies until enough energy has been expended to arrest further damage to the material. The progression of damage in rigid laminates occurs in a similar way except that it takes place in the opposite direction. The large

contact stress developed during the impact creates matrix cracks in the ply at the impacted face of the laminate. These are then deflected at the nearest interface to form delaminations. This sequence of matrix cracking and delamination is repeated in ply layers away from the impacted face until enough energy has been dissipated to prevent further damage growth. Fig. 2.4 illustrates the damage patterns described above. The use of woven fabrics in composite laminates adds further complication to the damage patterns. Bishop (1989) found that for laminates made with woven fabric, shear cracking and delamination are suppressed by the weave. This results in less extensive damage in the material than would occur had the laminate been made of unidirectional plies.

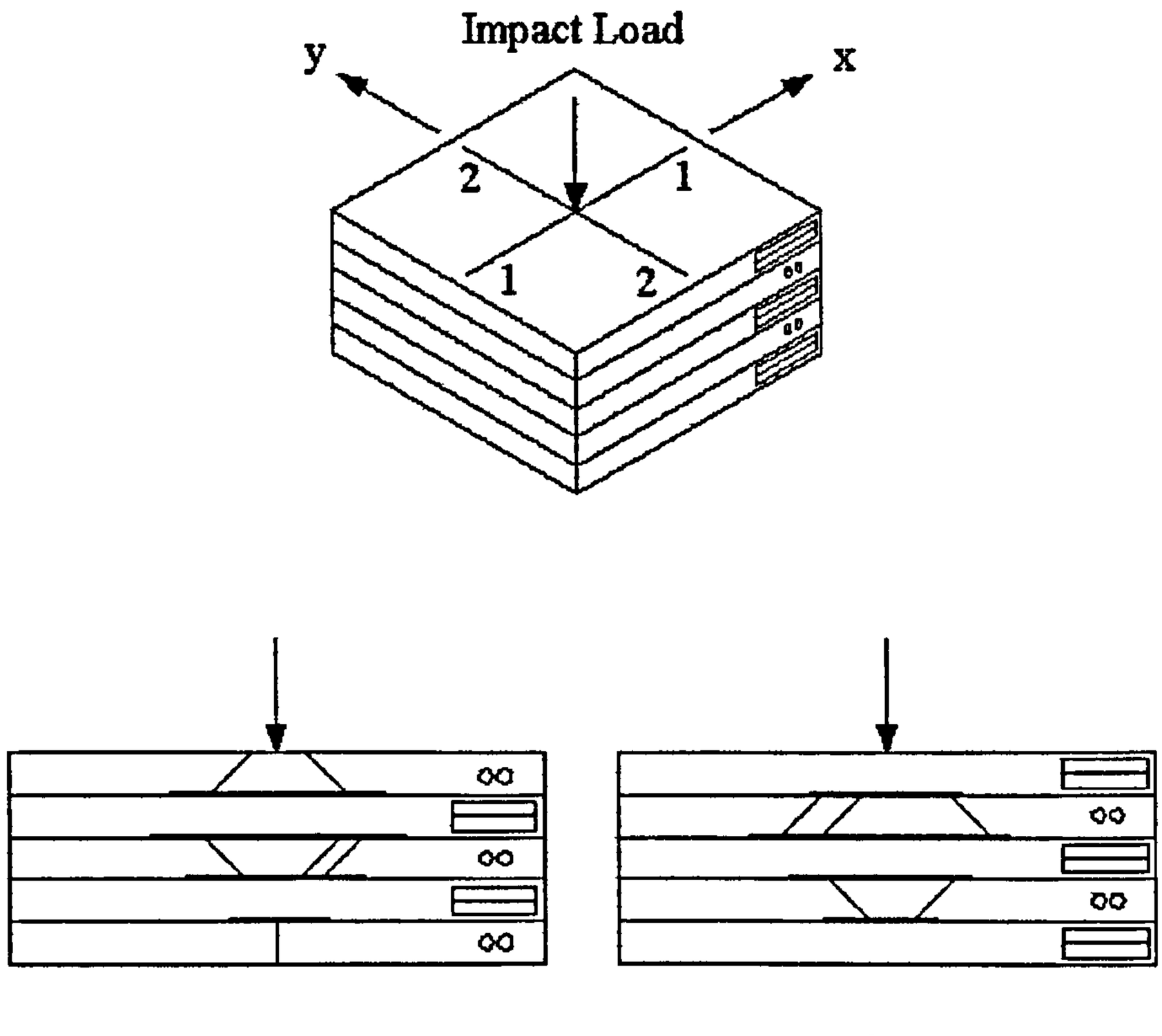

Figure 2.3. Top-hat pattern formed by intra-ply matrix cracks and inter-ply delaminations.

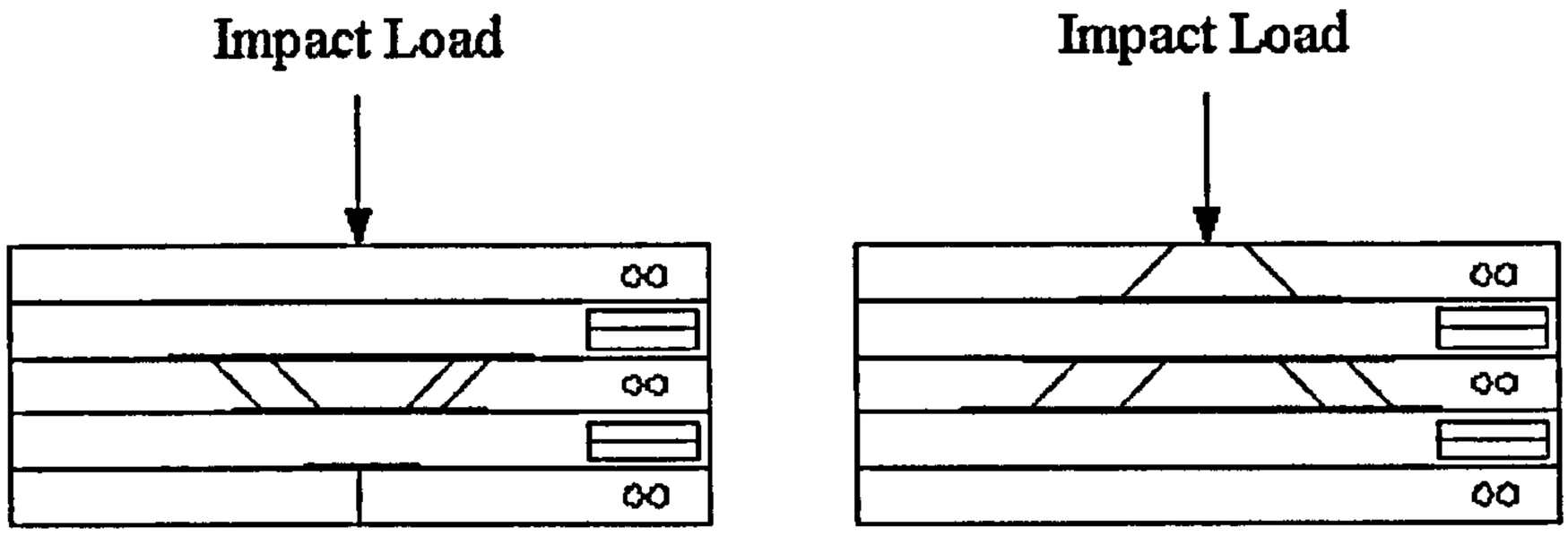

(a) Flexible Laminate (b) Rigid Laminate

Figure 2.4. Pattern of intra-ply matrix cracks and inter-ply delaminations for (a) flexible and (b) rigid laminates.

At sufficiently high impact energies, failure in the form of severe matrix cracking, fibre fracture and fibre pull-out appear at the backface of the laminate and, surprisingly, this can occur with almost no visible signs of damage on the front face, i.e., the impacted face of the laminate. At still higher energies ballistic penetration of the laminate can occur with the frontface plies failing by being sheared through and the backface plies failing by a combination of extensive matrix cracks, delaminations, fibre/matrix debonding and fibre fracture.

Previous works have shown that there is a threshold impact energy level below which no damage is created in the laminate. Above this threshold value delaminations and backface crack lengths grow with impact energy (Cantwell and Morton. 1985; Oxley. 1991). Recently Davies and Zhang (1995) and Davies et al (1994, 1996, 1997) proposed that it is the magnitude of the impact force, and not the impact energy, that determines the onset of delamination damage in carbon fibre composites. They developed a model based solely on a fracture criterion involving Mode II shear propagation. The model allows for the calculation of a critical force threshold that is a function of the quasi-isotropic flexural stiffness E, an experimentally determined Mode II energy release rate G_{IIc}, the Poisson's ratio ν and the thickness of the laminate h.

This critical force is:

$$P_c = \sqrt{\frac{8\pi^2 E h^3}{9(1-\nu^2)} G_{IIc}} \qquad \text{Eqn. 2.12}$$

The predicted values for the critical force threshold using the above equation were found to be very accurate in predicting the onset of damage in the CFRP plates tested. Equation 2.12 can be recast into the following from:

$$P_c = C h^{3/2} \qquad \text{Eqn. 2.13}$$

where $C = \frac{2\pi}{3}\sqrt{\frac{2E}{(1-\nu^2)} G_{IIc}}$ depends only on the properties of the material. Examination of Equation 2.12 and Equation 2.13 reveal that the critical force threshold is independent of the plate size and boundary conditions.

In an earlier work, Sjoblom (1987) arrived at a similar conclusion based on a shear plug model to predict the damage initiation force. He also found that the damage initiation force did not depend on the size of the plate and thus supported his assumption that failure in the plate is initiated by shear stresses.

The existence of a damage initiation force or critical force is helpful in determining the onset of damage but is not of much use when damage growth needs to be accounted for. Impact test results on CFRP panels have shown that impact force is limited by the critical force and any increase in impact energy only results in increasing the impact duration until complete penetration of the laminate is attained (Found et al. 1997). This suggests that it is the impact energy, not the impact force, that governs the growth of significant damage in the panel, a finding that is supported by the work of Delfosse and Poursartip (1997).

Cantwell and Morton (1990) tried to predict the impact penetration energy of CFRP beams and plates using fracture-based criteria. They proposed that the damaged zone is

in the shape of a frustrum of a cone and that the energies associated with shear-out and delamination can be estimated by multiplying the transverse fracture energy and the fracture energy for delamination by the corresponding damage area. The results from their work on beam and plate specimens led them to conclude that a simple quasi-static model for low-velocity impact can successfully predict penetration energy for thin laminates up to 4 mm thick. It is interesting to note that the span ratios of the samples tested by the authors were from 12.5 to 300 for the beam specimens and from 30 to 240 for the plate specimens. In the same paper Cantwell and Morton (1990) also measured the penetration energies of similar laminates at impact velocities approaching 700 m/s. Here they found the measured penetration energies to be slightly lower than that at low impact velocities. This difference was explained in the way the panels respond to impulsive loading. In the high-velocity tests, where the contact duration between the indentor and the panel is very short, the panels may not have enough time to elastically store a significant portion of the impact energy before they were completely penetrated. For 8 mm thick, 64-ply laminates subjected to high-velocity impact loading, Cantwell and Morton (1990) found a change in the penetration mode that resulted in large discrepancies between the predicted and measured values of the penetration energy. From this observation they concluded that a complex system of stress waves originating from the impact point and propagating through the volume of the material was now significantly influencing the damage creation mechanism in the material and thus the simple quasi-static model they developed no longer applied.

Ursenbach et al (1995) performed quasi-static displacement controlled punch tests on CFRP laminates with thicknesses from 3.35 to 8.30 mm. They found that the force required to penetrate a laminate did not change significantly with the planar dimensions. This observation is essentially what is being suggested by Equation 2.12 and may serve as experimental evidence of the equation's validity. Ursenbach et al also developed a semi-analytical method to model the deformation response of a damaged laminate. The model is an isotropic, circular panel of radius **b** embedded in a concentric, simply supported isotropic circular panel of radius **a>b** (see Figure 2.5). The bending rigidity of the embedded panel is **D** whilst that of the larger concentric panel is $\mathbf{D_0}$. Experimental data was combined with an approximate Rayleigh-Ritz method to estimate the size of the damage zone **2b.** Their results show that the delamination

radius, **b**, increases with panel thickness and appears to obey a relationship that is proportional to the thickness raised by an exponent. Extrapolation of their results to panel thicknesses less than 3.35 mm appear to suggest that the delamination radius for thin laminates tends to a minimum value at about 15 mm.

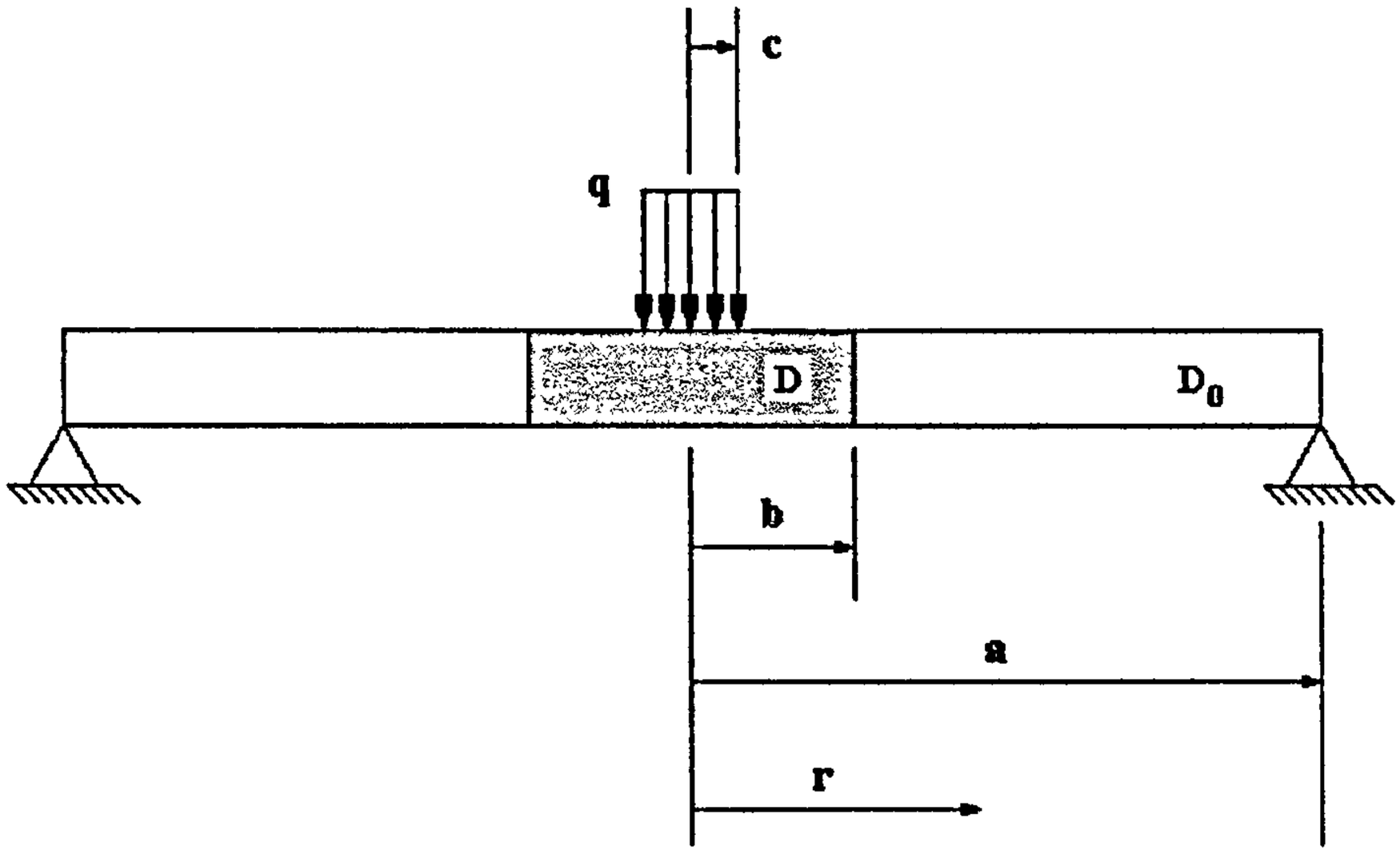

Figure 2.5. Embedded plate model proposed by Ursenbach et al (1995).

Wu and Springer (1988) also attempted to predict the delamination size in impact damaged composite plates by way of 3D FEA. Using a failure criterion based on tensile stresses normal to the plane of the plate and by applying the similarity laws on the parameters known to affect delamination size, they derived the following relations:

$$\frac{w_d}{l_o} = C_6 \left(\frac{\sigma_{\max} \sqrt{l_o}}{K_{IC}} \right)^{C_7} (Q^*)^{C_8} \left(\frac{t_f}{t_m} \right)^{C_9} \left(\frac{D^B_{\theta\theta}}{D^T_{\theta\theta}} \right)^{C_{10}} \qquad \text{Eqn. 2.15}$$

where

l_o = Inherent flaw size = $\frac{2 K_{Ic}^{\ 2}}{\pi S_{TT}}$

K_{IC} = Mode I critical stress intensity factor

S_{TT} = The transverse tensile strength

l_d = The length of the delamination

w_d = The width of the delamination

$D_{\theta\theta}^{B}$ = Flexural stiffness of the lower ply bounding the delamination

$D_{\theta\theta}^{T}$ = Flexural stiffness of the upper ply bounding the delamination

$$Q^{*} = \frac{Q_{xx}^{B} - Q_{\theta\theta}^{T}}{Q_{xx}^{B} - Q_{yy}^{T}}$$

$Q_{\theta\theta}^{T}$ = The transformed reduced stiffness of the upper ply corresponding to the angle α between the fibre orientations of the two plies bounding the delaminations

Q_{xx}^{B} = Reduced stiffness of the lower ply in the fibre direction

Q_{yy}^{T} = Reduced stiffness of the upper ply perpendicular to the fibre direction

σ_{max} = Maximum out-of-plane stress

t_f = Duration of out-of-plane stress

t_m = Time at which σ_{max} occurs

Application of the laws of similarity required that C_1 to C_{10} be constants independent of the impact velocity, material properties and ply lay-up. Wu and Springer (1988) achieved reasonable success in predicting delamination size between any two adjacent plies in a variety of rectangular laminates under different edge constraints.

Investigations into the effect of the indentor size, shape, mass and velocity as well as into the effect of test specimen dimensions and end or edge constraints have also been reported. Chaturvedi and Sierakowski (1985) found that the large indentor masses created smaller damage areas than smaller masses at the same impact energy. Their

tests were performed on glass fibre composites and it may be the rate sensitivity of these materials that influenced the results they observed. Verpoest et al (1987), in tests using similar materials, observed that larger specimens absorbed less energy than smaller ones and found a small effect of the clamping force on the impact response. They also found that loosely clamped specimens sustained less delamination damage than those that were firmly clamped. Tests by Lal (1983a, 1983b) on graphite epoxy, 8-ply laminates held in 50 mm and 100-mm diameter clamps showed similar trends although to a much lesser degree.

2.7 IMPACT ON STIFFENED CFRP PANELS

In the aerospace industry the quest to realise significant weight-savings in structural components has led to the use of thin composite skins reinforced by stiffeners or stringers. It is thought that improvements in resistance to impact damage may be best achieved with the use of a thin membrane to absorb the energy with the structural stiffness being provided by careful design and positioning of the stiffeners (Found et al. 1998a, 1998b). The presence of the stiffeners could increase the available elastic energy that can be absorbed by the panels before local failure starts (Davies and Zhang. 1995). This principle has been used in the development of CFRP wing boxes (Tropis et al. 1995).

Many of the recently published work on the impact on stiffened CFRP structures involve the use of FEA models owing to the availability of powerful computers running software that can analyse structures of complex geometry. Nonetheless experimental test results were required to test the veracity of the models. Murphy (1994) used DYNA3D to simulate selected impact tests on CFRP panels reinforced with hat-section stiffeners. One significant result of his analysis is the prediction of backface tensile failures due to the large strain associated with very localised bending. Cheung and Scott (1995) conducted static indentation and impact tests on plain and thin-skinned, blade-stiffened panels and simulated the low-velocity impact response by using an equivalent static indentation test. They found that the deformation characteristic of the

plain panels was dominated by membrane effects and was highly non-linear whilst that for the stiffened panels loaded directly above a stiffener was almost linear due to the increased bending stiffness. Cheung and Scott. (1995) also found that the stiffened panels exhibited extensive delaminations at the stiffener run-out regions even though no visible surface damage on the panel could be observed. This failure was attributed to the peel stress acting between the stiffener and skin interface near the run-out regions. Since the FEA model used employed plate elements, peel stresses were not considered and hence the onset of delamination failure in the run-out region cannot be predicted. Madan and Sutton (1988) also observed this type of delamination failure in their tests and analysis of 54-ply T-stringer stiffened panels. They attributed this failure to the flexural stiffness mismatch between the stiffener and panel skin and to a lack of through-the-thickness reinforcement between the stiffener and the skin. In subsequent tests they were able to prevent this failure by clamping the stiffener and skin together at the run-out regions with small C-clamps.

Experimental studies into the impact damage in stiffened CFRP panels were reported by Found et al (1998a, 1998b), Greenhalgh et al (1997), and Jackson and Scott (1996). Found et al (1998b) conducted preliminary low-velocity, low-energy mid-bay impact tests on 3-ply CFRP blade-stiffened panels with stiffener spacings of 63- and 53-mm. Tests were also conducted on plain panels of the same material. They reported that the increase in panel stiffness due to the presence of the stiffeners appeared to increase the size of the projected delamination area at the same impact energy but did not appear to significantly affect the growth of delamination damage with impact kinetic energy. Greenhalgh et al (1997) in their work to identify and understand the factors that affect impact damage in composite structures investigated the effects of geometry and substructure by impacting panels of different stiffener spacing and skin thickness, and by impacting the panels at different locations relative o the stiffeners. Their results from tests on 3- and 4-mm thick panels show that impact-induced delaminations were larger in those regions of the panel that were more compliant. They also found that the material properties significantly influenced the type and extent of impact damage produced wherein materials exhibiting a smaller degree of matrix cracking tended to have larger delaminated areas. In a study of hail impacts on stringer-stiffened carbon fibre/epoxy panels made from unidirectional plies Jackson and Scott (1996) found that

whilst flat panel specimens impacted with ice balls 52 mm in diameter showed no damage and ply delamination, stiffened panels exhibited delamination damage in the stiffener run-out region. As did Cheung and Scott (1995) and Madan and Sutton (1988) they attributed this damage to impact induced bending of the stiffener peeling the stiffener away from the skin. They also found that ice ball impacts failed to produce localised damage in neither the plain nor stiffened panels. Apparently the crushing of the ice ball during the impact event effectively distributes the impact load over a relatively large area and reduces the peak impact load.

2.8 SUMMARY

There has been an extensive amount of work done on the low-velocity impact response of plain CFRP panels. Much has been learned of the parameters governing the behaviour of the panels under both static and dynamic loading conditions. For low-velocity impacts where the impact velocity is under 10-20 m/s, the impact response can be treated as a quasi-static process and only the first mode of vibration need be considered when analysing the dynamic response. A majority of the research into the impact response of CFRP panels considers only non-damaging impacts and/or impacts that result in small damage to the material. There is clearly a need to investigate further those situations where material damage can have a significant effect on the impact response of the panel. Existing investigations into the response of impact damaged CFRP panels often resort to 3D FEA models which, although giving promising results, are currently expensive and time-consuming to implement for practical engineering purposes. However this situation may change in the near future as the accelerating advances in computer technology and the development of more efficient algorithms puts more and more computational power and resources into ordinary desktop personal computers. This is not to say, however, that FEA modelling is the only way forward as good results were also obtained by some researchers through the used of classical mathematical methods aided by clever and intuitive construction of the impactor-plate model.

In recent years there has been a growing interest into the use of thin, stiffened CFRP panels for aerospace applications. Because of this interest there have been a number of investigations into the impact properties of such CFRP structures. From what is reported in the literature it appears that much work still has to be done in this area and there seems to be no comparative studies made between the impact responses of plain and stiffened panels. The purpose of this research project is therefore to further investigate and characterise the impact response of both plain and stiffened CFRP panels to impact energies of sufficient magnitude to cause complete penetration of the panels. It is hoped that, by comparing the results to be obtained from the plain panels with those to be obtained from the stiffened panels, important insights would be gained into their impact behaviour.

3 EXPERIMENTAL WORK

3.1 INTRODUCTION

This chapter presents the tasks, important equipment, test specimens, procedures and precautions undertaken and/or used in the conduct of the experiments in this research project. It cannot be overemphasised that in order to obtain reliable data from the experiments, it is necessary to have a firm understanding of the physical variables and processes involved. Careful planning of the entire test process is of great importance as it allows one to determine and identify possible problem areas and thus enable their prompt resolution.

3.2 TEST SPECIMENS

Plain and stiffened panels were supplied by Hurel-Dubois UK Ltd. The material is a five-harness satin weave CFRP, supplied in prepreg sheets by Hexcel Composites, and designated Fibredux 914C-713-40 (See Appendices A and B for the ply and laminate properties respectively). The plain panels were supplied in sheets 500 mm wide by 1000 mm long and were laid up according to Table 3.1.

Table 3.1. Lay-up of Plain Panels

Numder of Plies	Lay-up	Panel Thickness (mm)
3	[0/90, ±45, 0/90]	0.9548
4	[0/90, ±45, ±45, 0/90]	1.2317
5	[0/90, ±45, 0/90, ±45, 0/90]	1.5380
6	$[0/90, \pm45, 0/90]_2$	1.7600
9	$[0/90, \pm45, 0/90]_3$	2.7125

The stiffened CFRP panels were supplied in the configuration shown in Figure 3.1. Like the 3-ply plain panel the stiffened panels were laid up as [0/90, ±45, 0/90] but were incorporated with stiffeners of 0/90 lay-up. Each stiffened panel was moulded in one shot by Hurel-Dubois UK Ltd to produce a nominal panel thickness of about 0.8 mm and a nominal fibre volume fraction of 58%. The stiffened panels supplied were 350-mm wide by 1000-mm long.

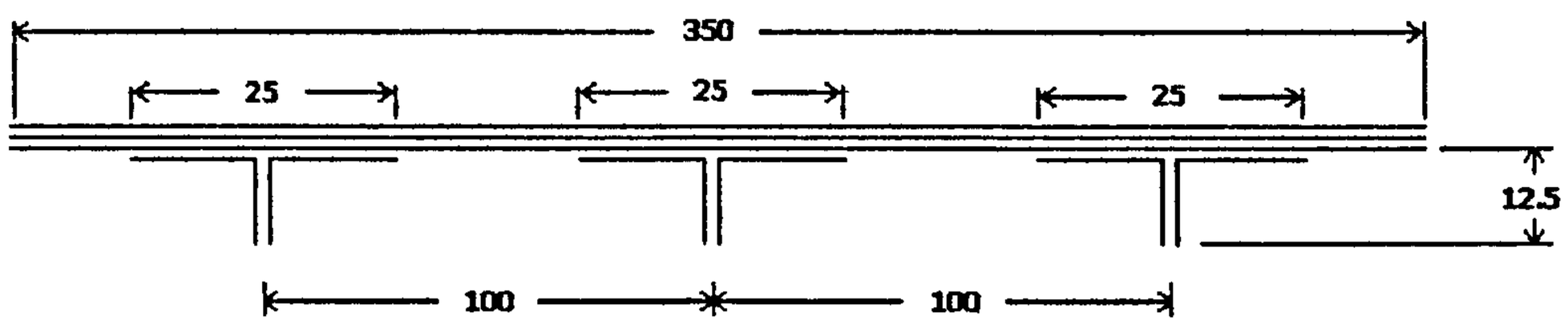

Figure 3.1. Lay-up and geometry of the stiffened panels.

In all the tests conducted in this thesis the panels were held between clamping rings of 100, 150, 200 or 300-mm diameter. The static or impact load was always applied at the geometric centre of the clamped panel. For the stiffened panels there were three variations of the load application points considered: (1) loading on the bay or between the stiffeners, (2) loading on the toe of the stiffener or at the ply drop-off line and (3) loading on the stiffener. These three loading conditions correspond to T1, T2 and T3 in Figure 3.2 respectively.

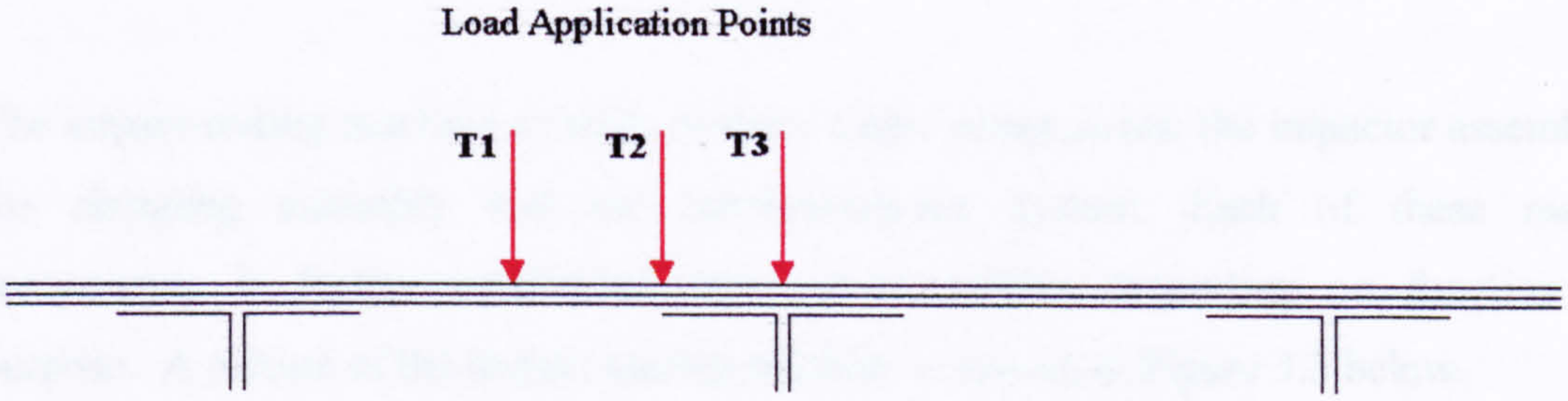

Figure 3.2. Load application points for the stiffened panels.

A data tagging or coding system was also devised to help distinguish between the many sets of data obtained from the experiments. This tagging system consists of a series four or five alphanumeric characters. The first three numeric characters in the code represent the thickness and diameter of the panel. The first digit indicates the number of plies making up the skin of the panel whilst the second and third digits give the panel diameter in centimetres. The fourth alphabetic character in the data code indicates whether the panel is plain or is stiffened with T sections. Thus a "P" indicates a plain panel and a "T" indicates a stiffened panel. The fifth numeric character is present only for the stiffened panels and it identifies the load application point relative to the stiffeners. For the fifth character in the code, "1" indicates impact on the bay or between two adjacent stiffeners, "2" indicates impact above the toe or ply drop-off line of the stiffener and "3" indicates impact above the stiffener blade (see Figure 3.2). For example, consider the data code 330T3: this code indicates a 3 ply, 300-mm diameter, stiffened panel loaded above the stiffener blade.

3.3 EQUIPMENT

3.3.1 THE IMPACT TESTING MACHINE

The impact-testing machine consists of three major components: the impactor assembly, the clamping assembly and the instrumentation system. Each of these major components is further subdivided into sub-assemblies depending on function or purpose. A picture of the impact-testing machine is shown in Figure 3.3 below.

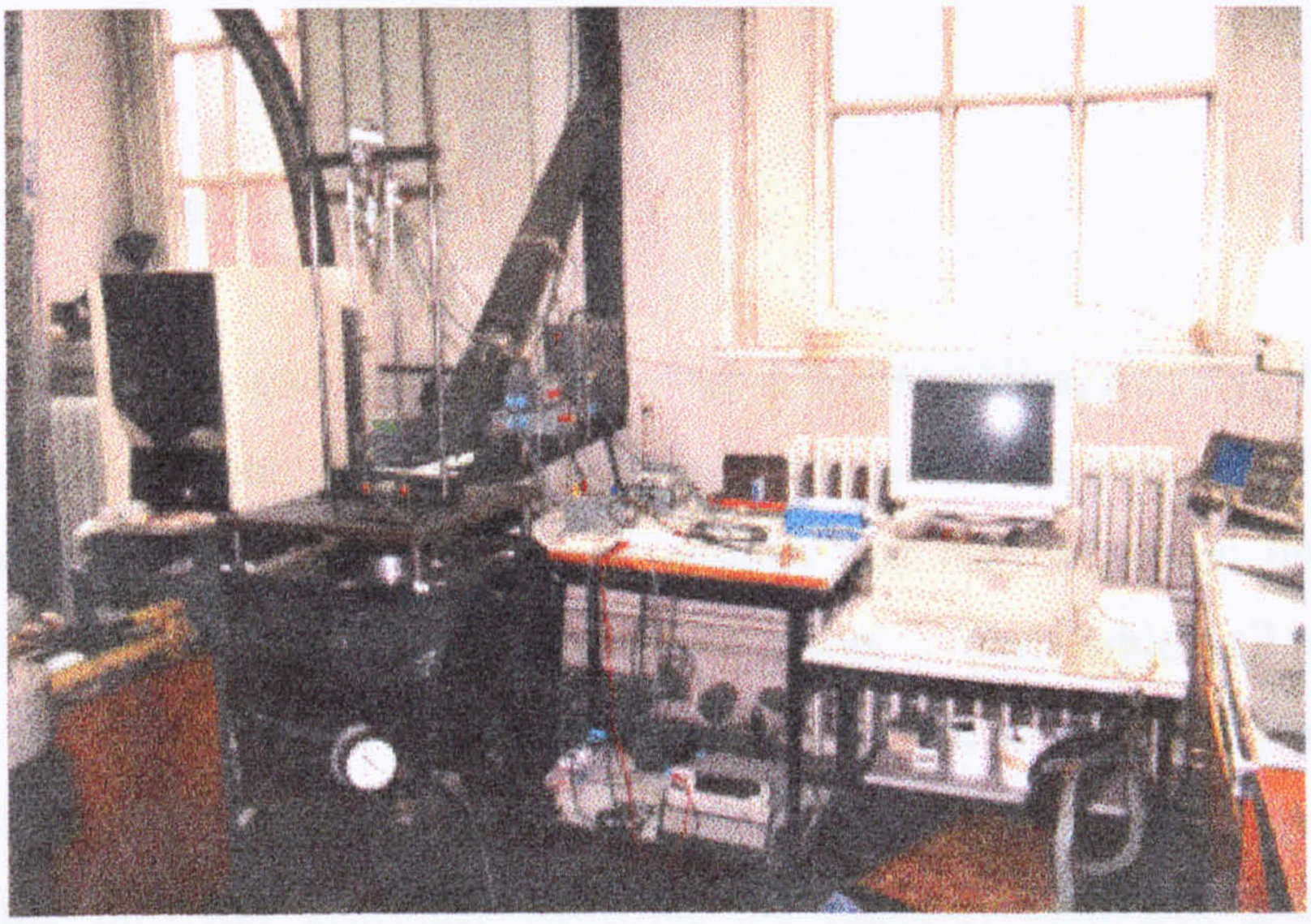

Figure 3.3. The impact-testing machine.

The different parts of the impact-testing machine can be identified in Figure 3.3. The impactor assembly and clamping system can be found in the upper-left and lower-left of the figure, whilst the instrumentation system and data acquisition system can be found in the centre and right of the figure.

The operation of the impact-testing machine can be briefly described as follows: A panel specimen is clamped between two rings of a given internal diameter in the clamping assembly. The clamping assembly is then moved relative to the impactor

assembly until the desired impact point is in line with the trajectory of the indentor. The indentor assembly, to which a fixed mass is attached, is released from a given height and dropped onto the target specimen. Measurements are made just before, during and after the impact event to obtain records of indentor velocity, indentor acceleration, impact force, panel lateral displacement and indentor rebound velocity. In addition static tests on panels can also be conducted on the same test rig by attaching a special block housing a bolt-driven indentor to the top plate of the clamping assembly.

Although the impact testing machine can accommodate clamping rings up to 300 mm in internal diameter, it conforms to the CRAG standards (Curtiss. 1988) for the impact testing of composite panels when using rings of 100 mm internal diameter.

3.3.1.1 THE IMPACTOR ASSEMBLY

The impactor assembly can be divided into two sub-assemblies, namely, the guide rail assembly and the indentor assembly. The guide rails serve the purpose of guiding the falling indentor onto the target panel and ensures that only a normal impact occurs between the indentor and the surface of the panel. The guide rail assembly is constructed from four vertically orientated steel rods that are held in tension in a C frame. The C frame is in turn firmly fixed to the wall of the Composites Laboratory. A picture of the impactor assembly showing the indentor assembly and guide rail assembly can be found in Figure 3.4.

The indentor assembly functions as the striking body during the impact event. It was designed to be light but strong to be able to withstand the impact forces generated in the tests. This assembly is made of five parts that can be described as follows: the hemispherical-nose indentor, the extension fitting, the carriage assembly, the detachable mass (or masses) and capture bracket. Figure 3.5 shows a picture of the indentor assembly and Figure 3.6 is a schematic diagram of it.

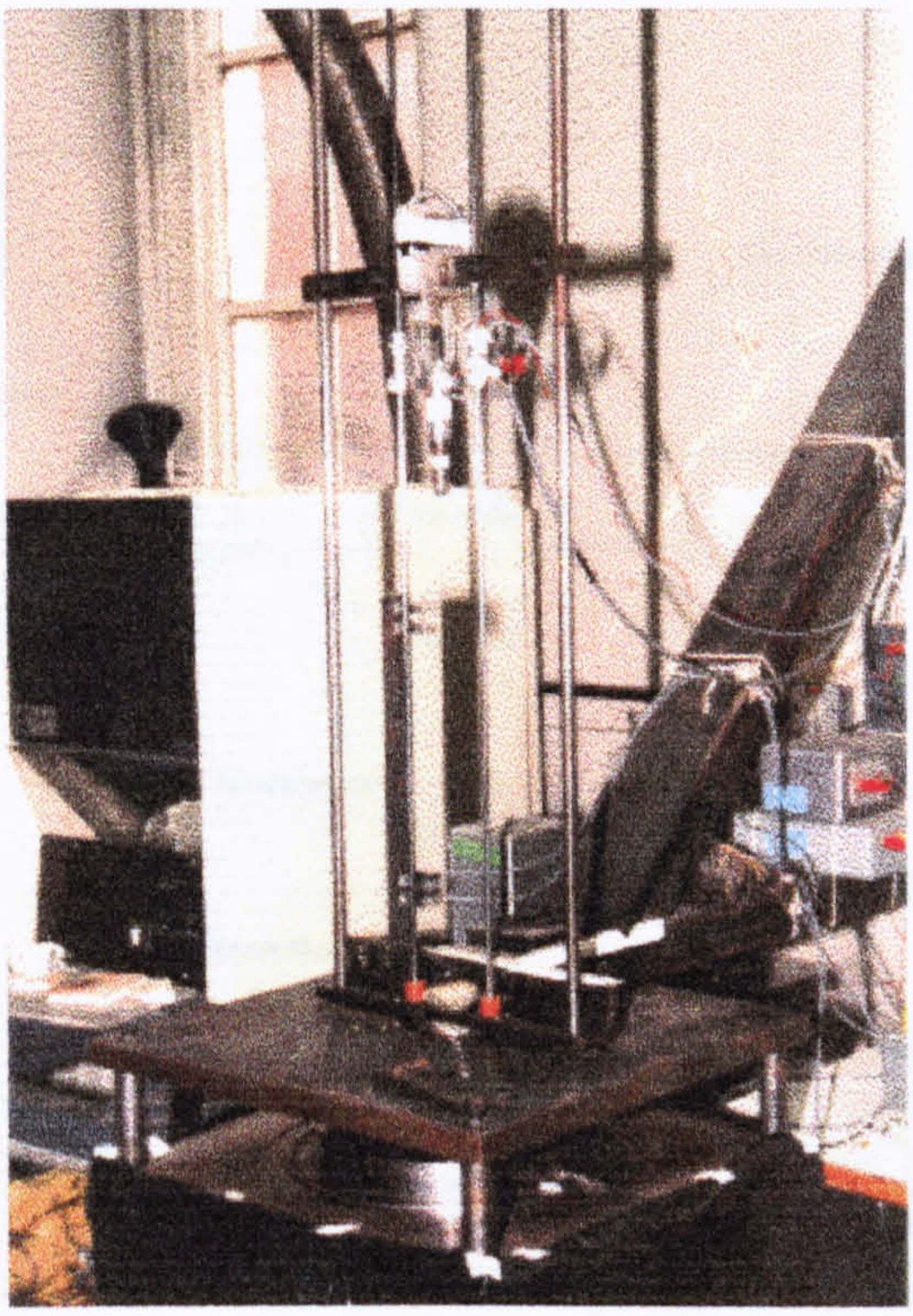

Figure 3.4. The impactor assembly.

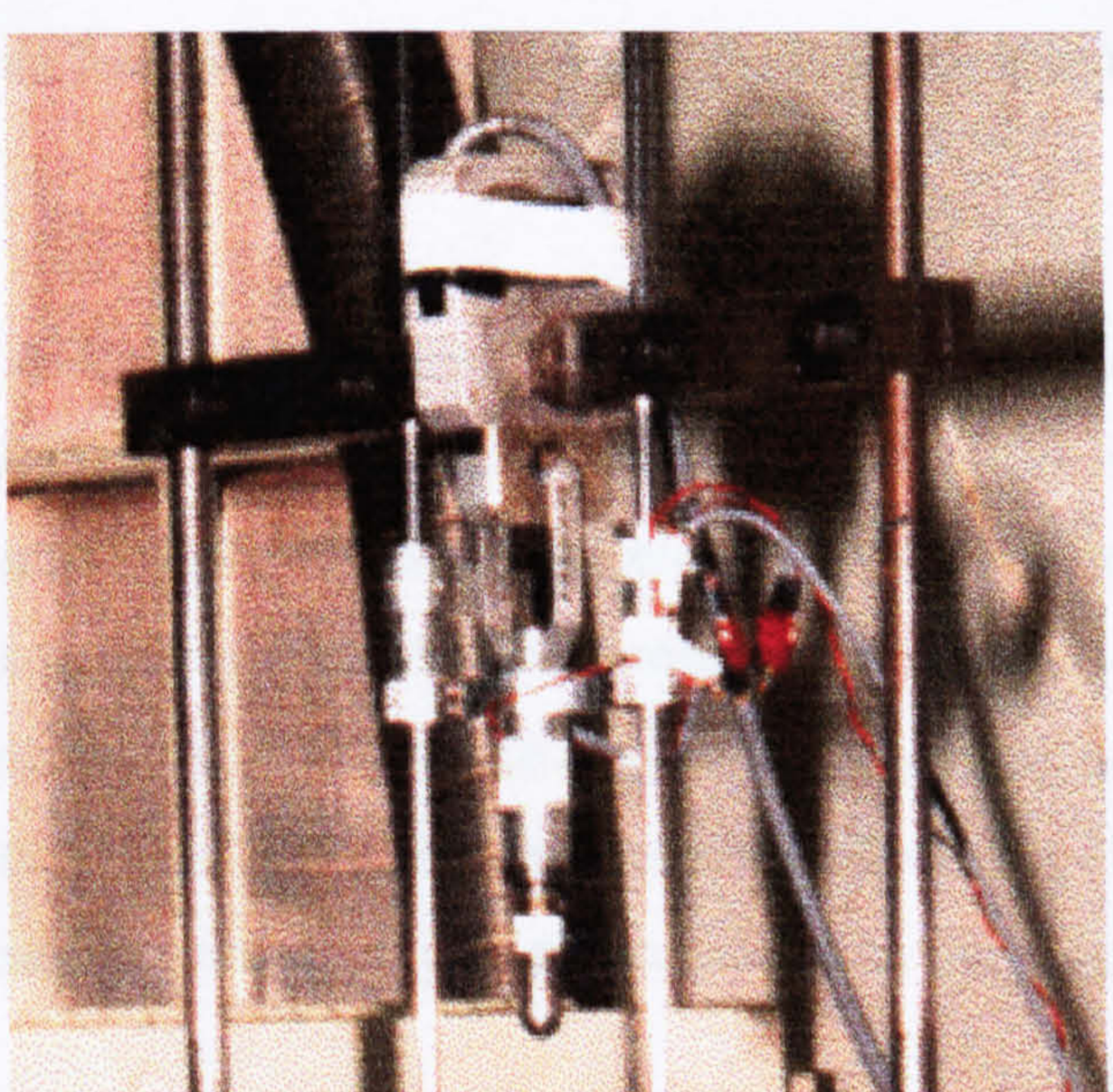

Figure 3.5. The indentor assembly and electromagnetic release claw.

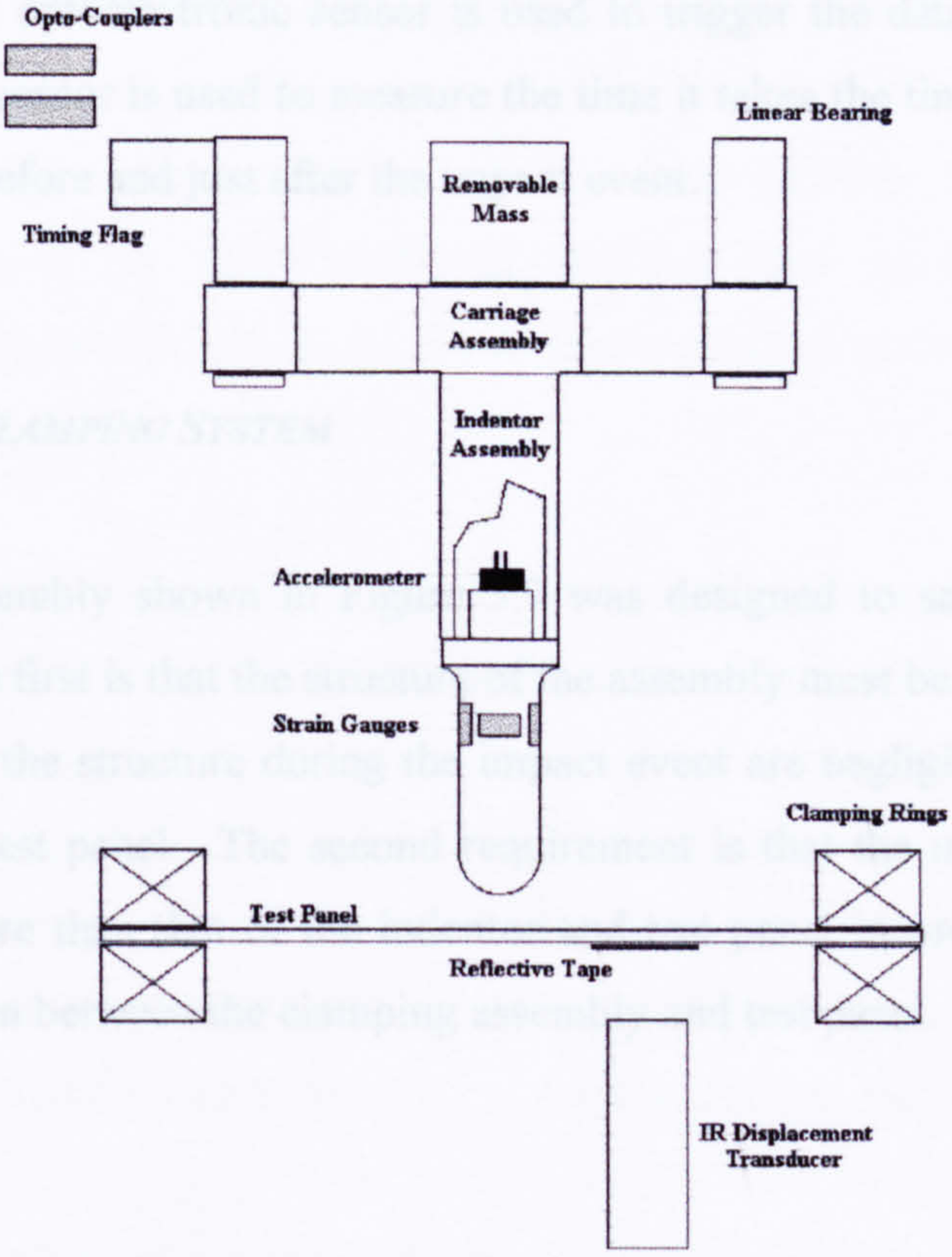

Figure 3.6. Schematic diagram of the indentor assembly.

Mounted on to one end of the hemispherical-nose indentor is a miniature piezoelectric accelerometer (see Figure 3.6). An aluminium extension piece fits between the indentor and the carriage assembly and protects the accelerometer. A drilled hole in the side of the fitting allows the signal wires of the accelerometer to pass through. Four 350-Ohm strain gauges arranged in a full bridge were also bonded on to the shank of the indentor. The transducers attached to the indentor assembly allow the measurement of the acceleration of the indentor and the forces generated during the impact event.

The small carriage assembly houses the linear bearings that ride the two inner steel rods in the guide rail assembly. The indentor and extension piece attach to the bottom of the centre piece of this assembly whilst the detachable masses and capture bracket are

attached to the top. The carriage assembly also carries an aluminium timing flag of 15.5-mm width. This flag is used to break the line-of-sight of two optoelectronic sensors. The first optoelectronic sensor is used to trigger the data acquisition system whilst the second sensor is used to measure the time it takes the timing flag to cross its line-of-sight just before and just after the impact event.

3.3.1.2 THE CLAMPING SYSTEM

The clamping assembly shown in Figure 3.7 was designed to satisfy two important requirements. The first is that the structure of the assembly must be rigid enough so that any deflections in the structure during the impact event are negligible compared to the deflection of the test panel. The second requirement is that the mass of the structure must be much more than that of the indentor and test panel in order to minimise any dynamic interaction between the clamping assembly and test panel.

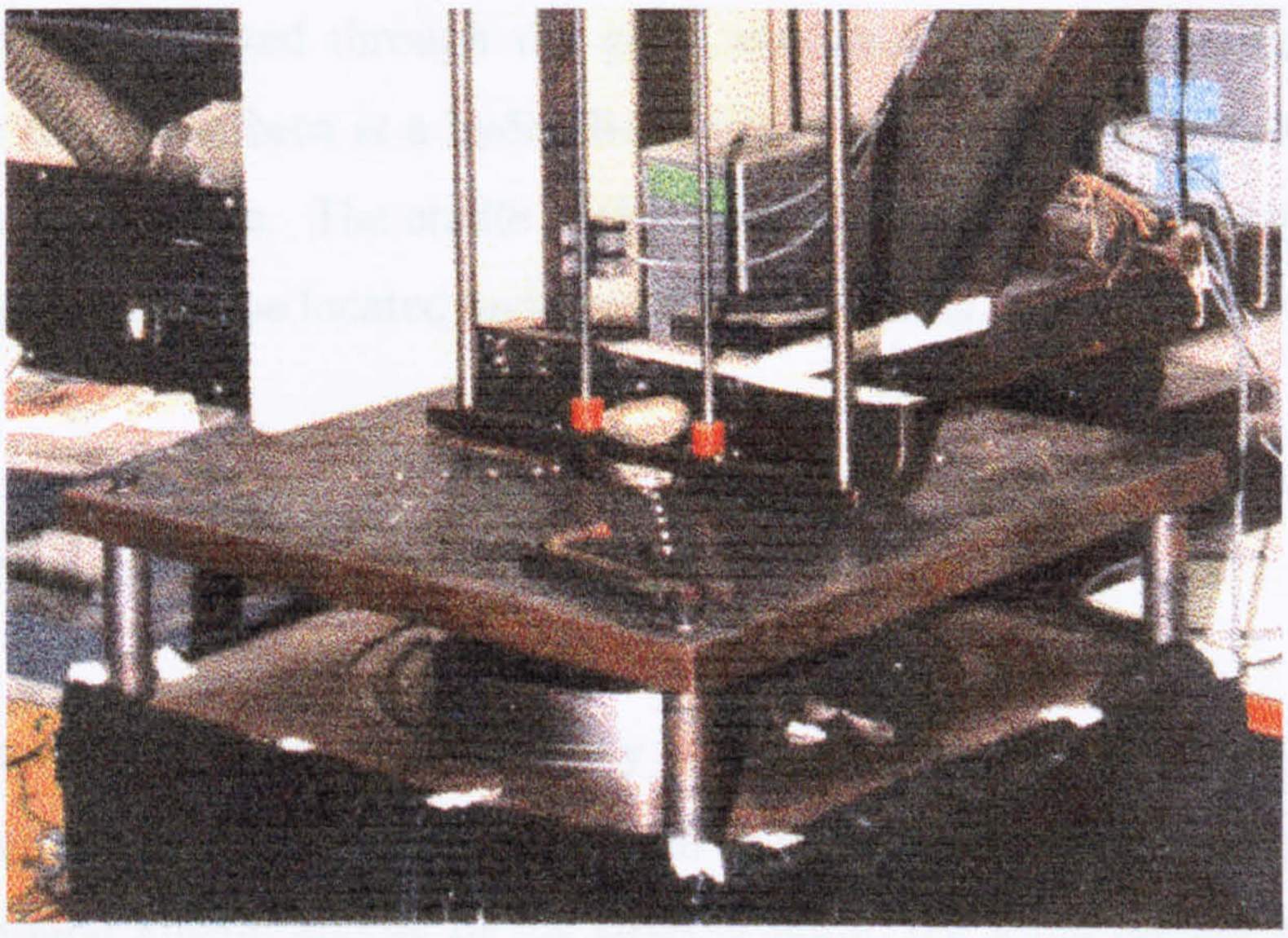

Figure 3.7. The clamping assembly.

The clamping assembly is constructed from three 19-mm thick steel plates and four 25.4-mm diameter steel rods. The steel rods function as support posts for the entire structure as well as guide rails for the moveable parts of the assembly. Two of the three steel plates are fixed to each of the ends of the four steel rods. The third plate is fitted between the other two plates and is capable of sliding between them using the steel posts as guide rails. The entire clamping assembly rests on two horizontal bars functioning as rails over which it can be slid into position underneath the impactor assembly.

Central holes were cut through the top plate and moveable plate to allow the indentor to strike the test panel and to be able to take displacement measurements at the backface of the panel. Concentric annular grooves 2 mm deep and 20 mm wide machined on the bottom face of the top plate and on the top face of the moveable plate to accommodate and align the clamping rings. At present the clamping system can accommodate rings with internal diameters of 80, 100, 150, 200, 250 and 300 mm. In addition, some of the rings had slots cut into them to accommodate the blades of the stiffened panel sections.

Attached to the bottom of the moveable plate is a cradle that evenly distributes the clamping force transmitted through the plate and through the clamping rings. The source of the clamping force is a hydraulic cylinder that is located between the cradle and the bottom base plate. The cradle is also used to support any measuring or sensing instrument that needs to be located underneath the test panel.

3.3.1.3 SENSORS AND TRANSDUCERS USED

Four parameters were essential to the study of the impact response of the panels tested in this research project. These are the inbound or incident kinetic energy of the striking body, the rebound kinetic energy of the striking body, the force history of the impact event and the lateral displacement history of the target panel. To acquire these parameters in the impact tests, two optoelectronic proximity transducers (supplied by RS Components, Type. 307-913), one piezoelectric miniature accelerometer

(ENDEVCO model 2255A-025), one strain gauge load cell (purpose-built) and one optoelectronic displacement transducer (purpose-built) were employed.

One of the optoelectronic proximity sensors was used to trigger the data acquisition system just before the indentor strikes the test panel. The other proximity sensor was used to measure the time it takes the 15.5-mm wide timing flag attached to the indentor assembly carriage to cross its line of sight immediately before and immediately after the impact event. This allows for the calculation of the incident and rebound velocities of the indentor.

The accelerometer is attached to one end of the indentor and is enclosed by the extension piece as described in Section 3.3.1.1. The accelerometer signal is sent to a signal conditioner for further processing prior to data acquisition. The strain gauge load cell is integrated to the design of the indentor. It is four electrical resistance 350-Ohm strain gauges mounted on the shank of the indentor, two longitudinally and two circumferentially, and wired in a Wheatstone bridge arrangement. A Keithley Instruments MB38-02 strain module processes the signal from the load cell.

The displacement transducer is a purpose-built LED/phototransistor reflective transducer constructed from a spectrally matched infrared LED and phototransistor. The LED is a GaAs infrared diode (type SE 3455) with a wide beam angle and the silicon phototransistor (type SD 5443) has a fixed-focus lens to allow a narrow acceptance angle (both devices were made by Honeywell Optoelectronics). The tranducer is located beneath the test panel at a position offset by 25 mm from the point of load application to prevent the signal from being affected by any damage on the backface of the panel. A gain amplifier processes the transducer signal prior to data acquisition.

The displacement transducer is calibrated from static load tests on similar panels under similar clamping conditions and transducer offsets using a dial gauge and/or LVDT to measure the defection at the centre of the panel.

3.3.2 THE DATA ACQUISITION SYSTEM AND SOFTWARE

Keithley Instruments Ltd of Reading supplied the data acquisition system and software. It consists of an IBM PC ISA bus compatible interface card and a software package incorporating the drivers and analysis programs. The DAS 1401 interface card is a high-speed analogue and digital interface card that is capable of taking up to 100,000 samples per second at 12 bit resolution (1 in 4096). It has 16 channels of single-ended inputs or 8 channels of differential inputs with software programmable input gain ranges of 1, 10, 100 and 500. Input and output signal connections to the card are easily made through an external terminal box.

The EASYESTLX software is an integrated program package that provides an icon-based graphical user interface to its comprehensive set of tools necessary to make effective use of the DAS 1401 data acquisition system. Its many functions include triggering the data acquisition sequence, capturing and storing the data, digital processing of the data (such as low-, high- or band-pass filtering; forward and inverse Fast Fourier Transforms) and plotting captured data.

3.3.3 THE HP FAXITRON X-RAY MACHINE

Delamination damage assessment was done through X-Ray radiography using a Model 43855A Hewlett-Packard Faxitron X-Ray cabinet. The Faxitron has an output power range of 10 to 110 kV_e at up to 3 mA. Both X-Ray energy and exposure time within the radiation-shielded cabinet can be carefully controlled to obtain the best results possible. Optimum exposure times for the different thickness of CFRP panels tested are shown in Table 3.2 below.

Table 3.2. X-Ray exposure times

Number of Plies	X-Ray Tube Voltage kV_e		Exposure Time min:sec
	Setting (X-Ray off)	Indicated (X-Ray on)	
3	22	20	1:20
4	22	20	1:45
5	27	25	1:00
6	27	25	1:15
8	27	25	1:30
9	27	25	1:45

3.3.4 THE P-3500 STRAIN INDICATOR

Strain gauge outputs were measured using a Micro-Measurement P-3500 Strain Indicator. Although the P-3500 Strain Indicator is very accurate and precise it was found to be too slow in following high change rate dynamic data. This limited its use to measuring load cell strain gauge output in the static indentation tests only.

3.3.5 OTHER EQUIPMENT USED

Other pieces of equipment used in the tests include two high-accuracy digital multimeters. Fabrication tools and equipment in the Sheffield University Machine Shop and the help extended by the technicians in the shop were indispensable throughout the duration of the project. The services of the Sheffield University Photography laboratory was also required in the development, printing and digitising of the x-ray film.

3.4 METHODOLOGY

The general procedures followed in the conduct of the static and impact tests in this project are outlined in the block diagram in Fig. 3.8. The description of the tasks outlined in this figure is as follows:

3.4.1 SAMPLE PREPARATION

Preparation of the samples for testing entails the laying-out of alignment lines on the test panels and the application of an adhesive reflective patch (a white, 9-mm diameter IVY sticky label) on the backface of the panel. The centre of the reflective patch was offset by 25 mm, along a longitudinal alignment line, from the load application point to prevent any backface damage on the panel from affecting the data acquired from the IR displacement transducer.

3.4.2 EQUIPMENT PREPARATION

All equipment and test instruments used in the experiments were calibrated according to manufacturers' specifications. Prior to the start of tests sufficient time (five minutes) must be allowed for some pieces of equipment to warm-up to their stable operating conditions. This is most especially true of high-power equipment and of instruments with signal amplifying devices built into them.

The test panels must carefully aligned in the clamping rings of the test rig to ensure that the indentor strikes the panel at the desired impact point. Careful alignment also ensures that the infrared beam from the IR displacement transducer illuminates the centre of the reflective patch on the backface of the test panel.

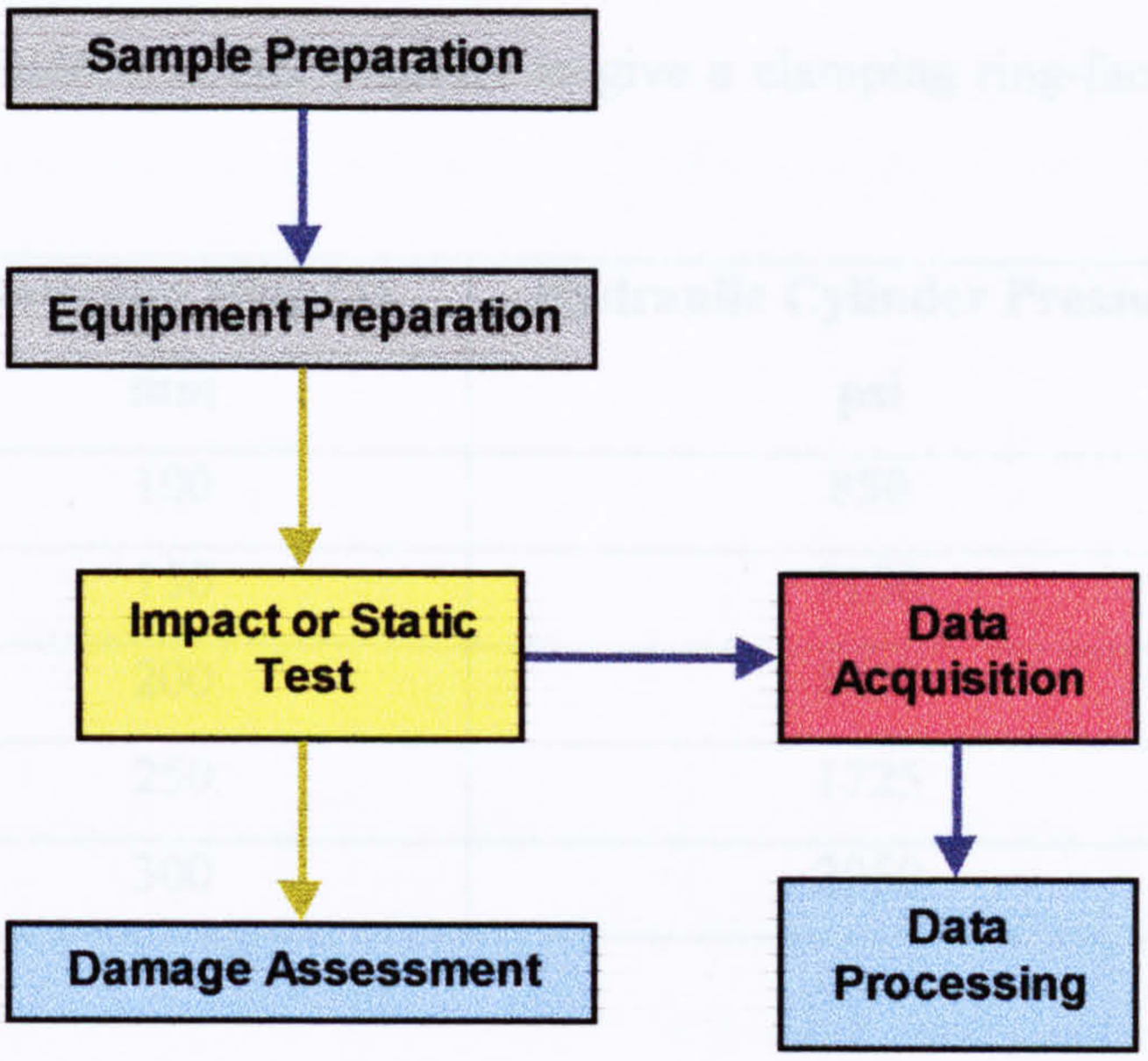

Figure 3.8. Task Flow Diagram for the Tests.

Because the CFRP panels are expensive to manufacture it is extremely important that each test is successfully concluded the first time around. Making sure that all power leads and signal wires are properly terminated and/or connected and that all the necessary power sources are switched on ensures this. It is recommended that a dummy test first be conducted on a piece of waste material (a steel or aluminium plate would suffice) to check if all the instruments working properly.

Prior to the start of each test, the panel in the test rig must be clamped to a ring-face pressure of about 105 psi. This pressure is the highest achievable ring face pressure on the largest clamping ring (which is 300-mm in diameter) within the operating limits of the pressure gauge attached to the hydraulic pump. The ring-face pressure is a variable that must be the same for all panels tested to ensure similarity of edge constraints. The correct hydraulic cylinder pressure to give a ring-face pressure of 105 psi for the different sizes of clamping rings is given in Table 3.3.

Table 3.3. Hydraulic cylinder pressure to give a clamping ring-face pressure of 105 psi.

Clamping Ring ID mm	**Hydraulic Cylinder Pressure psi**
100	850
150	1150
200	1450
250	1725
300	2050

3.4.3 DATA ACQUISITION

The capture and storage of the data from the static and impact tests were done through the operation of the Keithley Instruments data acquisition system and software. For the impact test this was a straightforward matter since the data acquisition sequence was automatically triggered by the action of the falling indentor as the timing flag attached to it breaks the beam of an optoelectronic sensor. The checks that need to be made prior to the start of each impact test are to make sure that the appropriate signal channels are activated and the correct sampling rate and number of data points are set. It is essential to ensure that the captured data from a test be committed to non-volatile storage (in the hard disk) before starting a new test sequence.

In the static tests the capture of each data vector (representing each test or data point) was done by manual triggering of the data acquisition system. This is so because of the manner in which the static test was conducted. The static test was conducted by driving an indentor/load cell assembly against the test panel up to and beyond panel penetration. The indentor was driven into the panel in fixed incremental displacements of 0.2 mm by turning a fine threaded bolt. At each increment, data corresponding to indentor displacement, panel displacement and transmitted force must be recorded. Manual

triggering of the data acquisition system reads in the data from the IR displacement transducer and load cell incorporated into the indentor. Except for the sampling rate, the precautions taken for the setting of the data channels and the number of data points and the requirement of storing the captured data at the conclusion of each test sequence in the impact tests are applicable.

3.4.4 DATA PROCESSING

The captured data are fundamentally voltage signals from all the sensors, transducers and instruments used in the tests. To transform them into physical parameters such as force, acceleration, velocity and displacement they must be mathematically processed, taking into account the relevant calibration curves and/or instrument characteristics peculiar to the sensor or transducer used. For this purpose a spreadsheet program such as Excel was of invaluable help. Processing of the data also makes it amenable to easy analysis and presentation.

3.4.5 DAMAGE ASSESSMENT

Damage assessment on the tested panels was done to correlate impact energy with damage type and damage size. The damage parameters measured and recorded were total backface crack length, permanent front-face indentation diameter, and projected interlaminar delamination area. The front-face indentation diameter and back-face crack lengths were measured by ocular means with the aid of a metallurgical microscope and a vernier caliper. From these measurements the total backface crack length was obtained by adding the measured lengths of the major cracks in the 0-degree and 90-degree directions on the backface of the panel. The indentation depth was calculated from the measured diameter of the bruise or dent on the front face of the panel at the load application point.

Delamination damage was made visible through the following process: A x-ray absorbing liquid penetrant solution (see Appendix C) is applied to the area around the

load application point on the panel. After allowing for a sufficient time (overnight) for the penetrant to seep into the damaged regions by capillary action, the panel was subjected to x-ray radiography and the resulting film negative was developed to reveal the internal delaminations in the material of the panel. A digital camera can then scan the developed negative and the resulting digital image of the projected delamination damage can be process through a software package such as AutoCAD to measure its area.

4 RESULTS FOR PLAIN PANELS

4.1 INTRODUCTION

This chapter describes the results from extensive tests conducted on plain CFRP panels according to the procedures and precautions discussed in Chapter 3. The tests were done on 3-, 4-, 5-, 6- and 9-ply plain panels held between different clamping rings of internal diameters from 100 to 300 mm.

4.2 STATIC LOADING RESPONSE

4.2.1 LOAD-DEFLECTION BEHAVIOUR

The static force-displacement responses of the plain panels are presented in Figures 4.1 to 4.5.

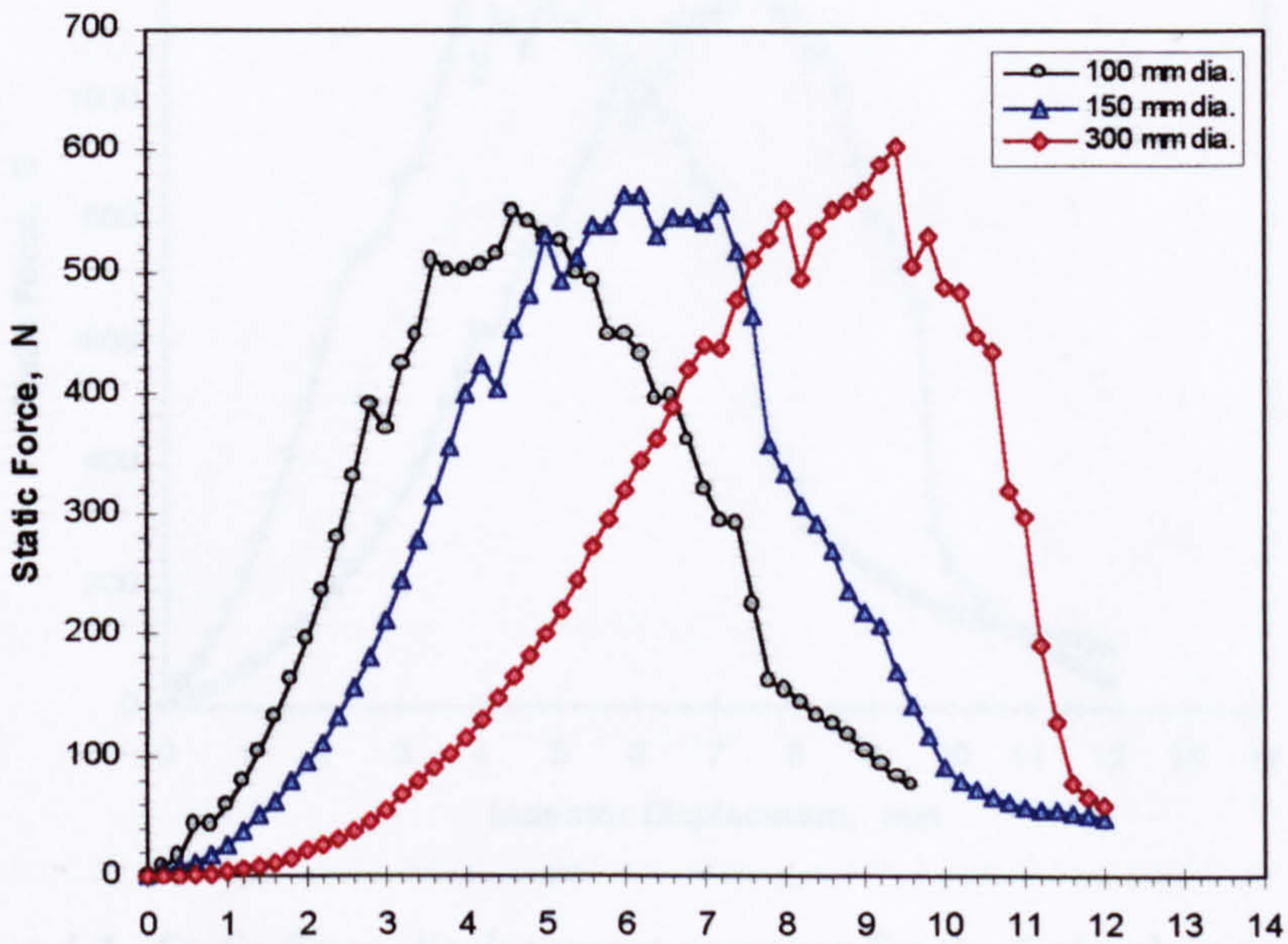

Figure 4.1. Static force-displacement response for the 3 ply plain panel.

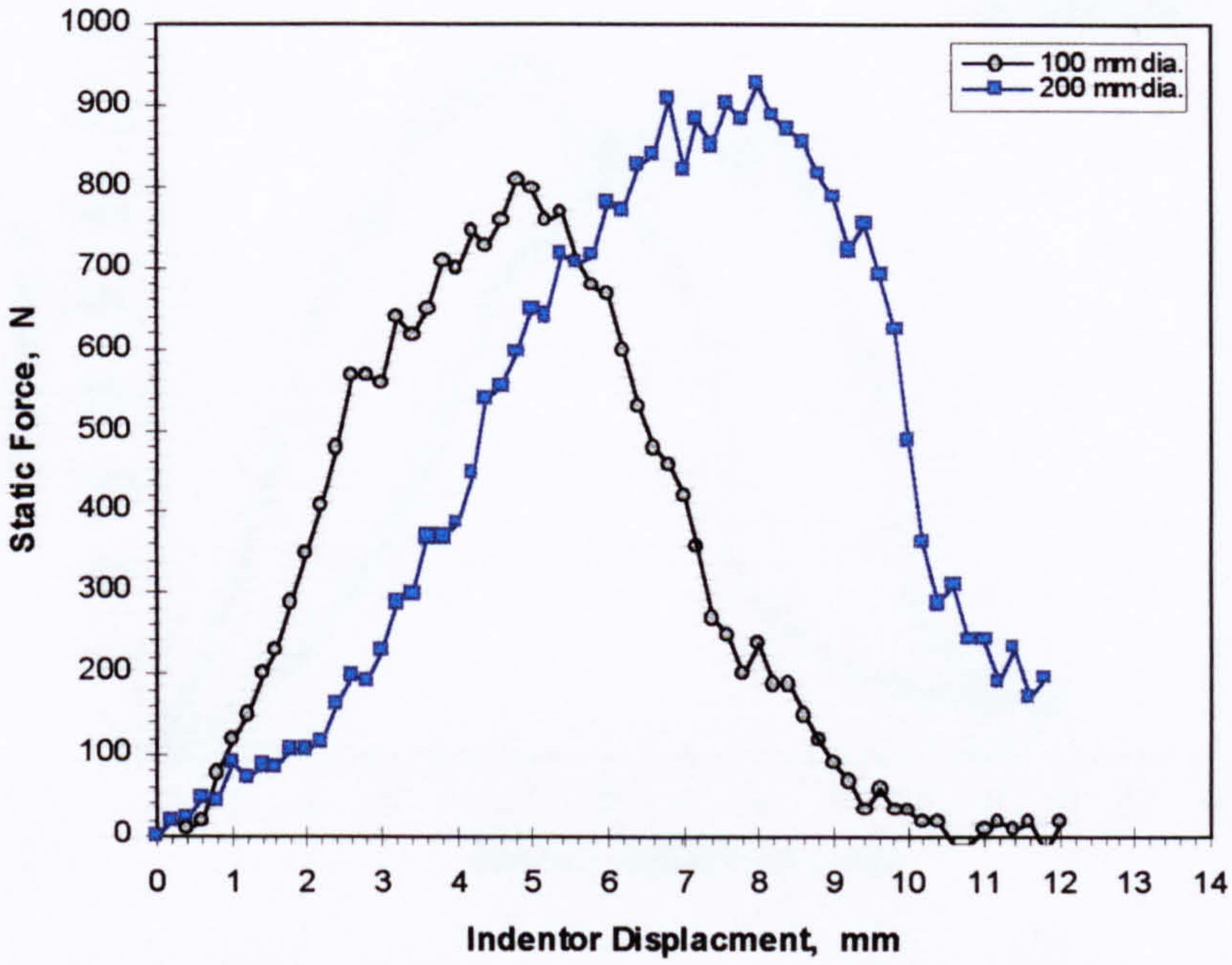

Figure 4.2. Static force-displacement response for the 4 ply plain panel.

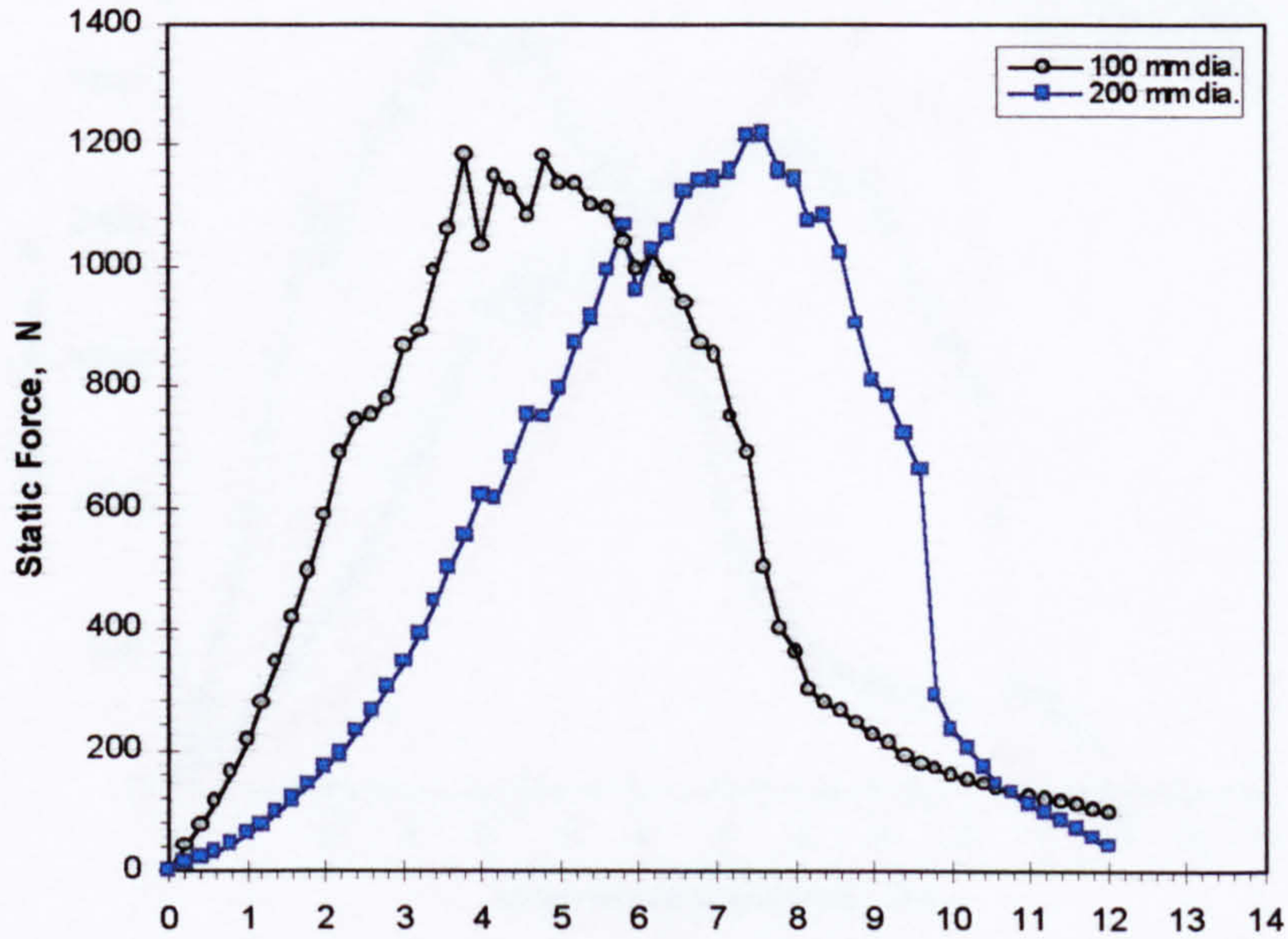

Figure 4.3. Static force-displacement response for the 5 ply plain panel.

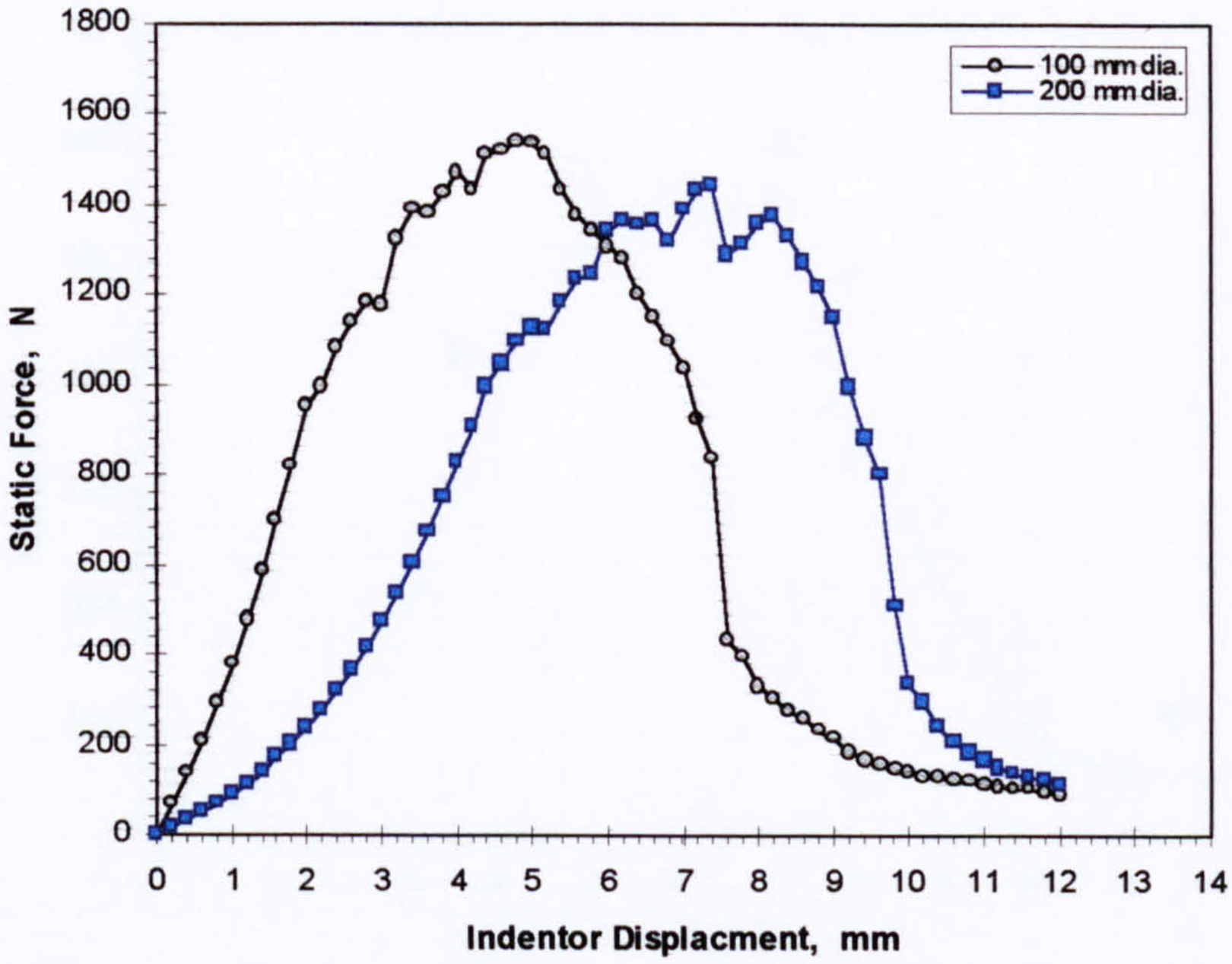

Figure 4.4. Static force-displacement response for the 6 ply plain panel.

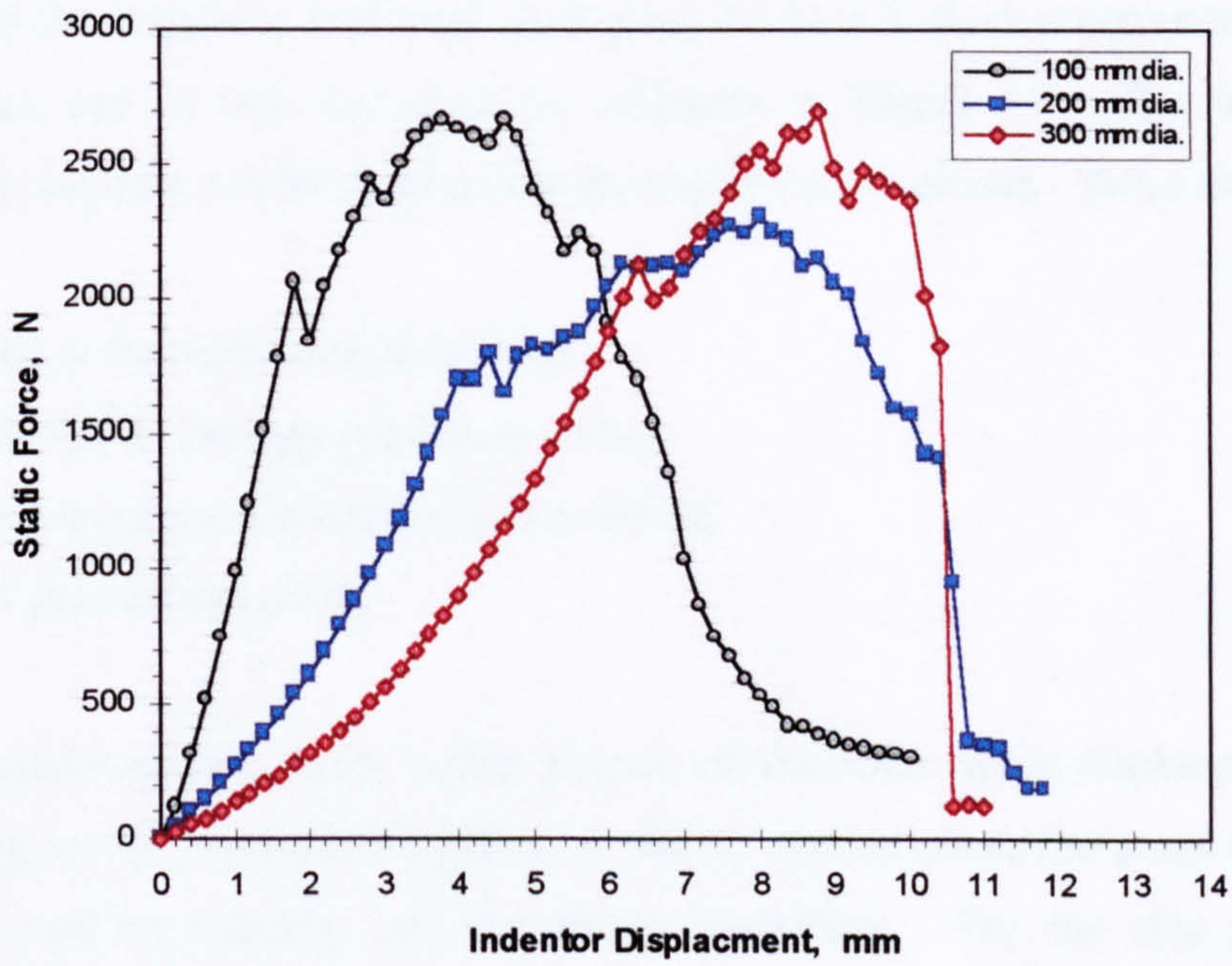

Figure 4.5. Static force-displacement response for the 9 ply plain panel.

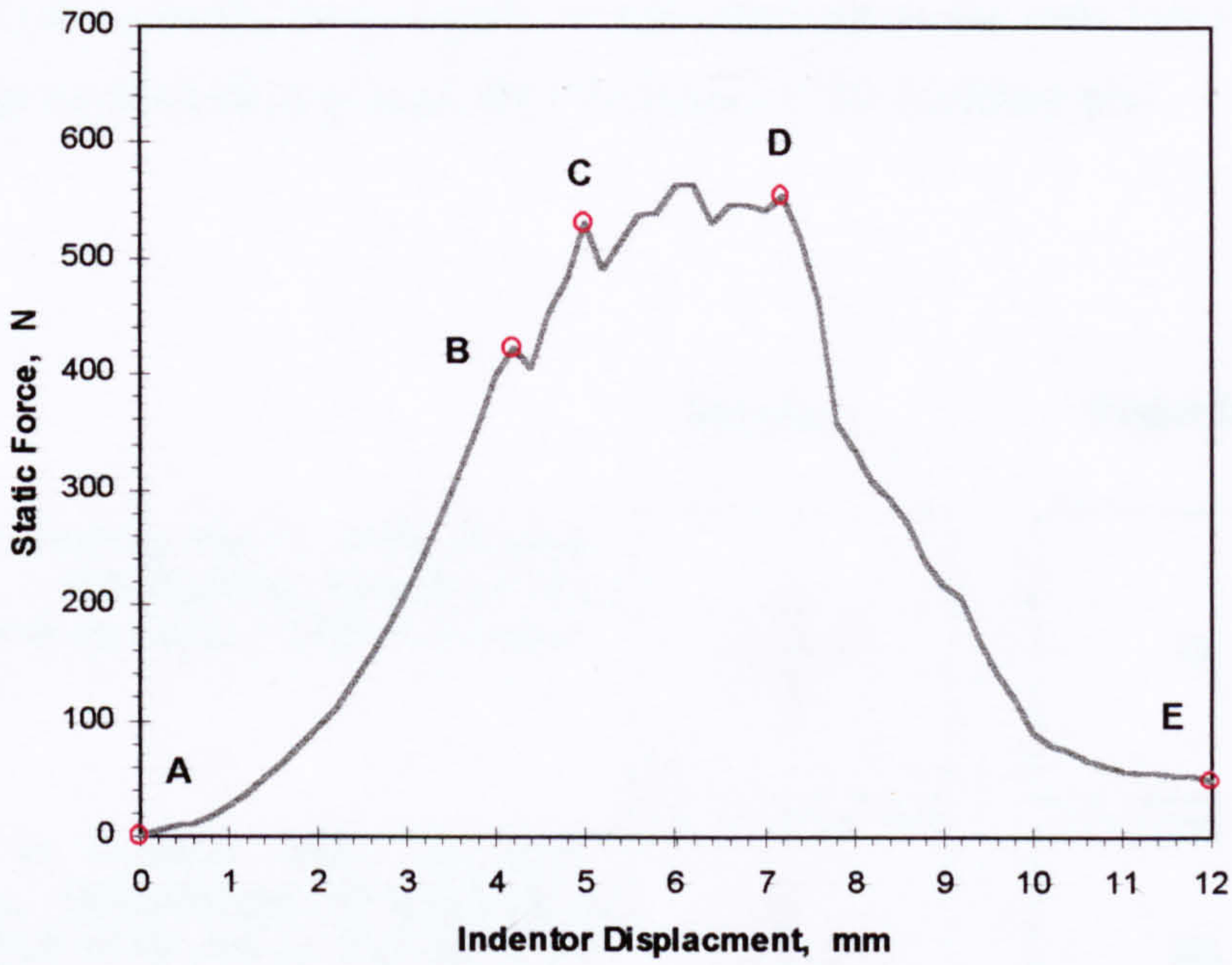

Figure 4.6. General features of the static force-displacement response.

The trends in the responses indicated in Figures 4.1 to 4.5 show a common pattern of behaviour that can be best described by reference to Figure 4.6. The static force-displacement response can be divided into four segments or phases. These are:

1. An undamaged-response phase.
2. An initial damaged-response phase.
3. A secondary damaged-response phase.
4. A penetration phase.

The undamaged-response phase is the portion of the static force-displacement curve (shown in Figure 4.6) between the points A and B. In this phase the panel responds to the applied load by bending and membrane stretching. For the thin panels, the membrane stretching is more pronounced and is manifested by the noticeably non-linear behaviour of the curve A-B. This membrane effect also manifests itself in the thicker panels when the panel diameter is increased. At point B the first cracks appear on the backface of the panel and this marks the start of the initial damaged-response phase. From the first appearance of backface cracks up to point C, any increase in the panel

load results in the growth of the cracks. It was observed in the tests that these cracks preferred to grow along the principal fibre directions of the backface ply.

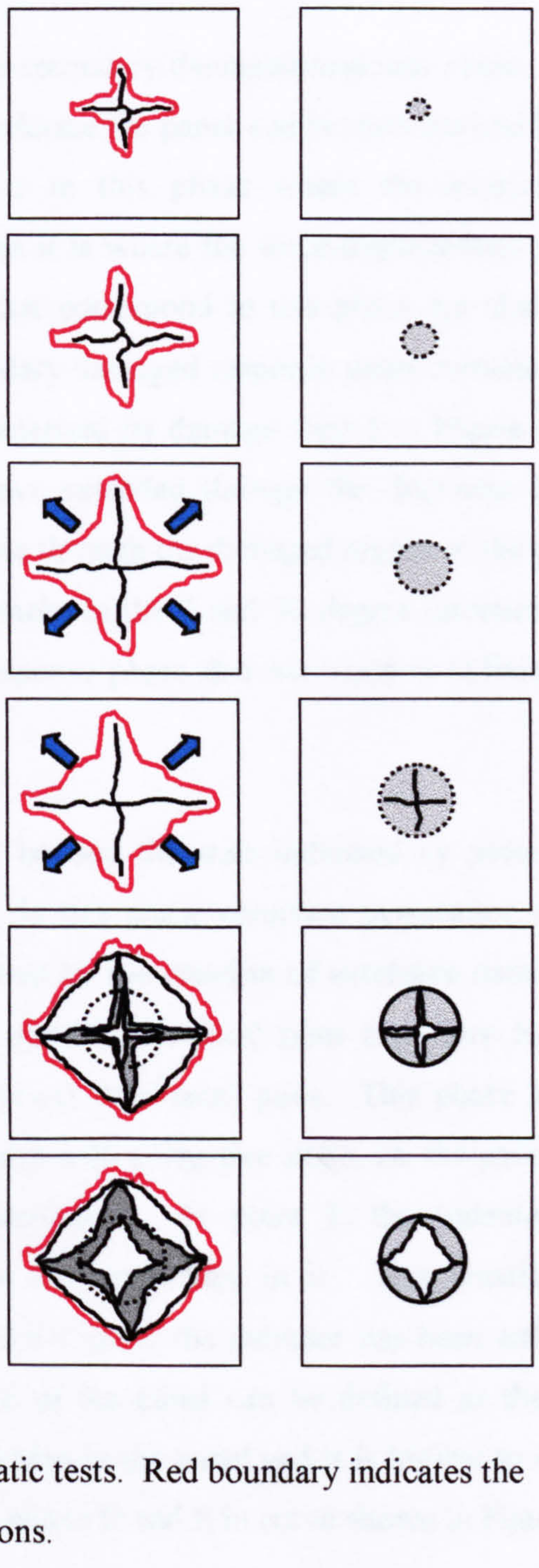

Figure 4.6-1. Damage morphology in the static tests. Red boundary indicates the extent of projected delaminations.

The development and progress of the damage in the static tests is illustrated in Figure 4.6-1. In this figure damage states 1 and 2 correspond to what could be happening to the panel in curve B-C of Figure 4.6. In these two states the delaminations are confined to the interface immediately adjacent to the backface and are possibly formed by the deflection of the first backface cracks at that interface. These delaminations are relatively small and extended up to a small region bounding the cracks.

From point C to point D in Figure 4.6 is the secondary damaged-response phase. This is the phase where the indentor begins to perforate the panel and is characterised by an erratic force displacement response. It is in this phase where the interlaminar delaminations were seen to grow rapidly and it is where the force-displacement curve tended to flatten out. The damage states that correspond to this phase are shown in Figure 4.6-1 as states 3,4 and 5. The secondary damaged response phase terminates at around point D of Figure 4.6 and this characterised by damage state 5 in Figure 4.6-1. At this stage the cracks in the laminate have extended through the thickness of the material allowing strong daylight to be visible through the damaged region of the panel, specifically at the intersection of the two cracks in the 0 and 90 degree directions. It was this state of the secondary damaged response phase that was used in defining the perforation limit of the panel.

Driving the indentor further into the panel beyond the state indicated by point D in Figure 4.6 initiates the penetration phase. In this phase complete penetration of the panel is achieved. This phase is characterised by the creation of extensive damage to the panel in the form of shearing of the upper (front-face) plies and fibre fracture brought about by the folding back of the lower (backface) plies. This phase is also characterised by a force-displacement response with a negative slope, i.e. the panel load decreases with increasing indentor displacement. At point E the indentor has completely penetrated the panel and is in fact embedded in it. This condition is characterised by damage state 6 in Figure 4.6-1 (after the indentor has been extracted from the panel). The penetration threshold of the panel can be defined as the state where the indentor is just about to be embedded in the panel and it is logical to expect that this threshold would occur between the points D and E in curve shown in Figure 4.6

In the large-diameter panels the penetration phase can occur rather abruptly because of the large elastic energy stored in the panel and the severe weakening of the panel around the vicinity of the load application point. This combination of conditions can lead to the abrupt failures indicated in Figures 4.1 and 4.5.

Figures 4.1 to 4.5 clearly show the effect of panel size on the static force-displacement response of the plain panels. For all the panels, the effect of increasing panel size is to extend the undamaged-response phase and to shift the start of each of the damaged-response phases towards larger values of indentor displacement. For the thin panels the membrane effect is seen to increase with panel size whilst for the thicker panels bending behaviour dominates membrane stretching except in the cases with the larger diameter panels. The panel size does not seem to affect the maximum value of the load significantly in the secondary damaged-response phase of each panel of the same thickness. The maximum forces appear to vary only within a narrow band of values in this phase.

The effect of laminate thickness on panels of the same diameter can be discerned by examining Figures 4.7 to 4.9. The effect of increasing laminate thickness is to increase the magnitude of the panel force in all the phases identified within the static force-displacement response curve. Increasing laminate thickness encourages thick plate behaviour, especially among the smaller diameter panels. In Figure 4.7 the contrast between thick plate behaviour and thin plate behaviour can be clearly seen: The undamaged response of the 3 ply panel is non-linear and concave upward owing to membrane stretching of the panel as it is loaded. On the other hand, the 9 ply panel's undamaged load response is essentially linear with indentor displacement, implying a behaviour dominated by plate bending.

The results for the panels with diameters of 200 mm and 300 mm are shown in Figures 4.8 and 4.9 respectively. In these figures the contribution of plate bending to the undamaged panel response loses its dominance as more membrane-like, thin plate behaviour manifests itself.

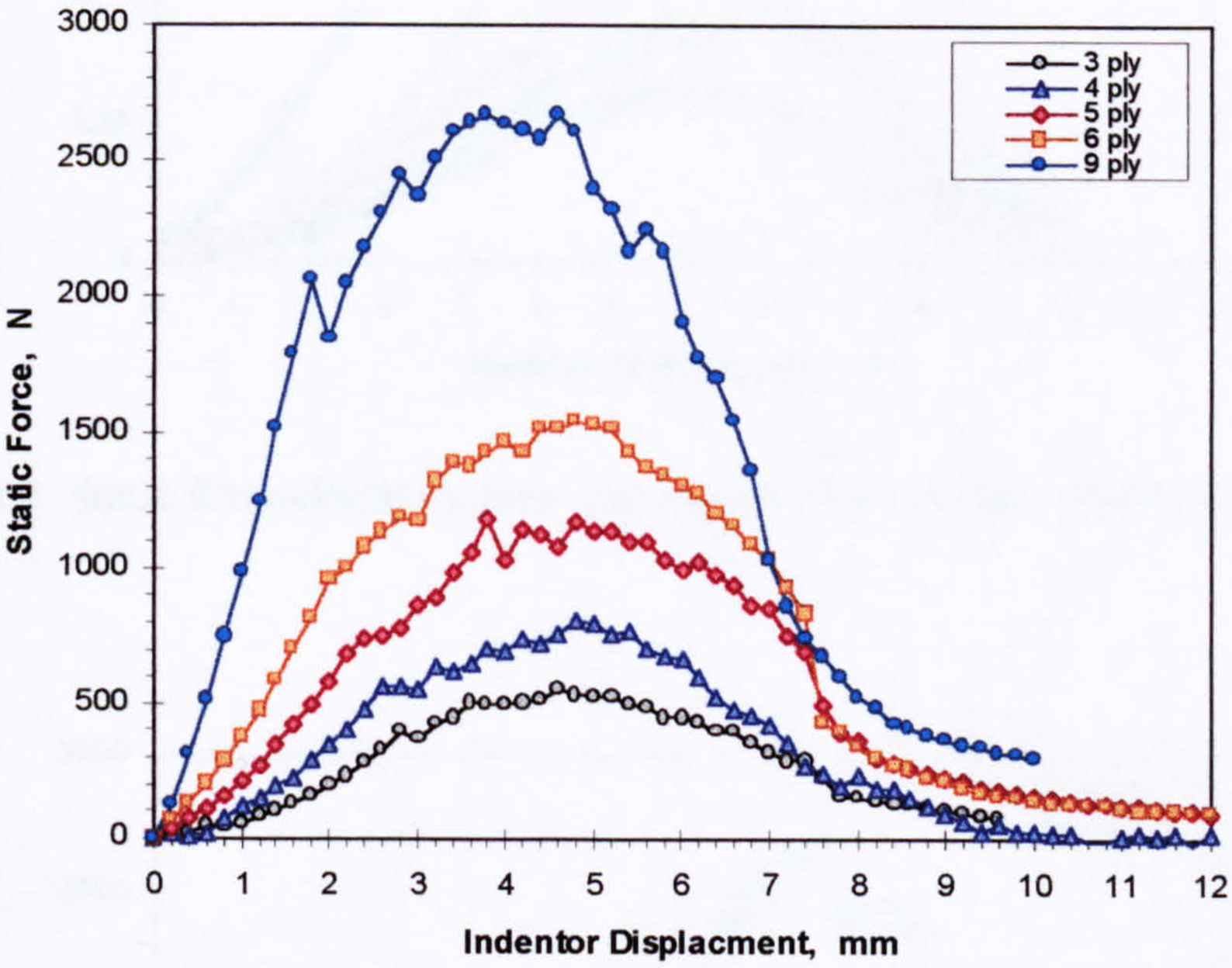

Figure 4.7. Static force-displacement response for the 100-mm diameter panels.

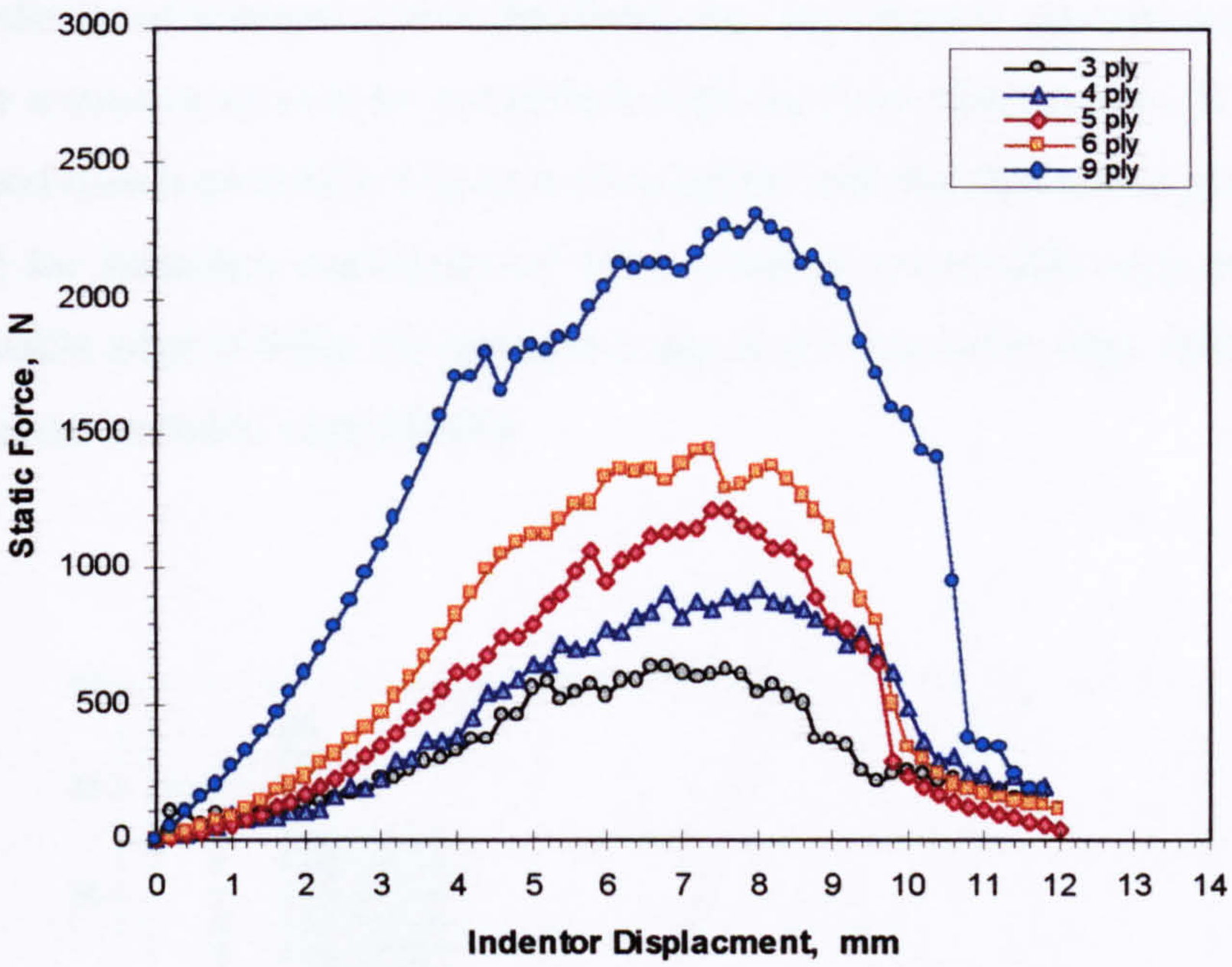

Figure 4.8. Static force-displacement response for the 200-mm diameter panels.

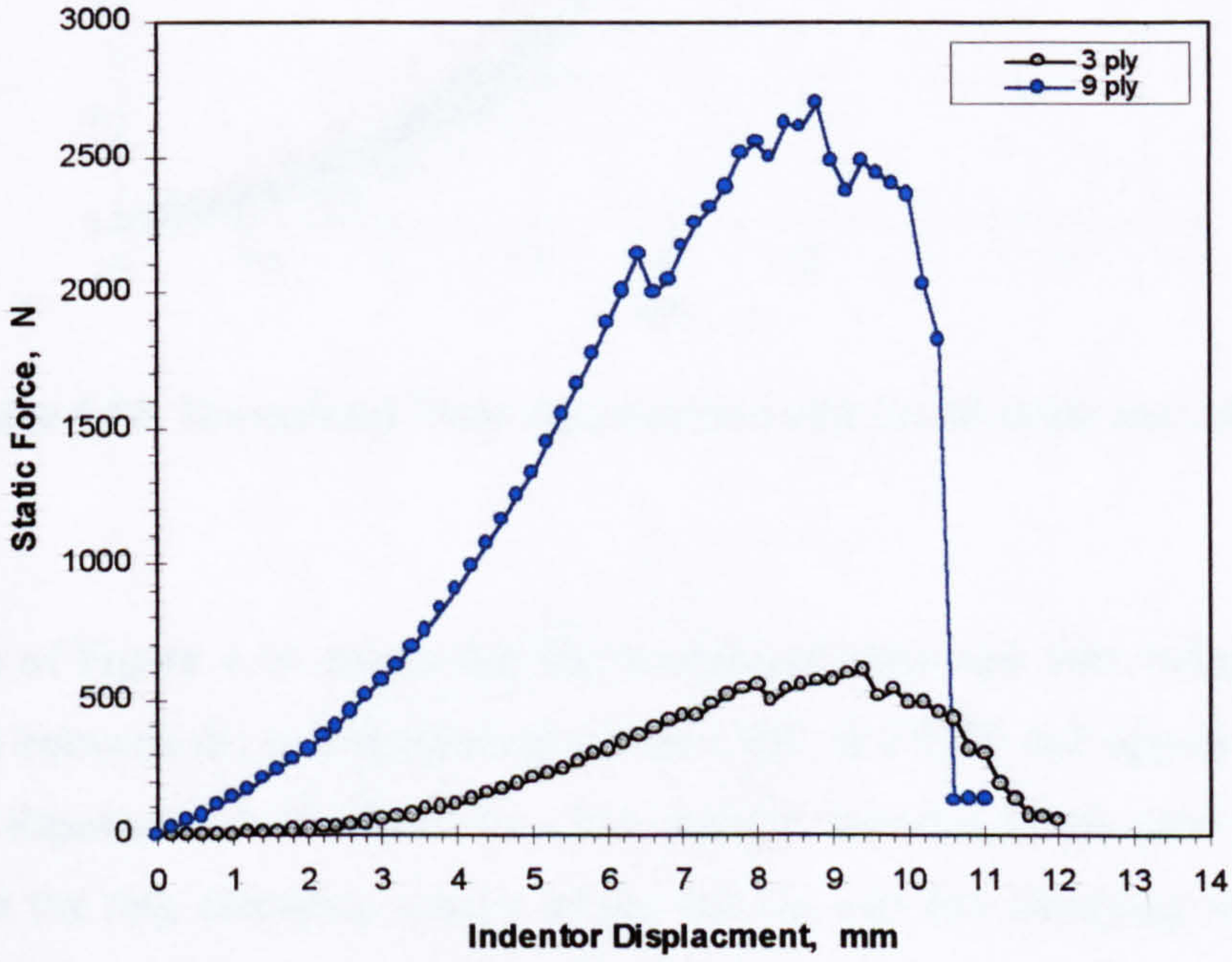

Figure 4.9. Static force-displacement response for the 300-mm diameter panels.

To compare the static force-deflection response of the panels tested with the large deformation theory of isotropic plates developed by Timoshenko, the data collected was normalised in a manner so as to be compatible with the form of Equation 2.2 in Sec. 2.2. The normalised data is plotted in Figure 4.10 together with the theoretical predictions of Equation 2.2 for boundary conditions of (1) a clamped immovable edge (CIE), (2) a clamped movable edge (CME), (3) a simply-supported immovable edge (SIE) and (4) a simply-supported movable edge (SME)

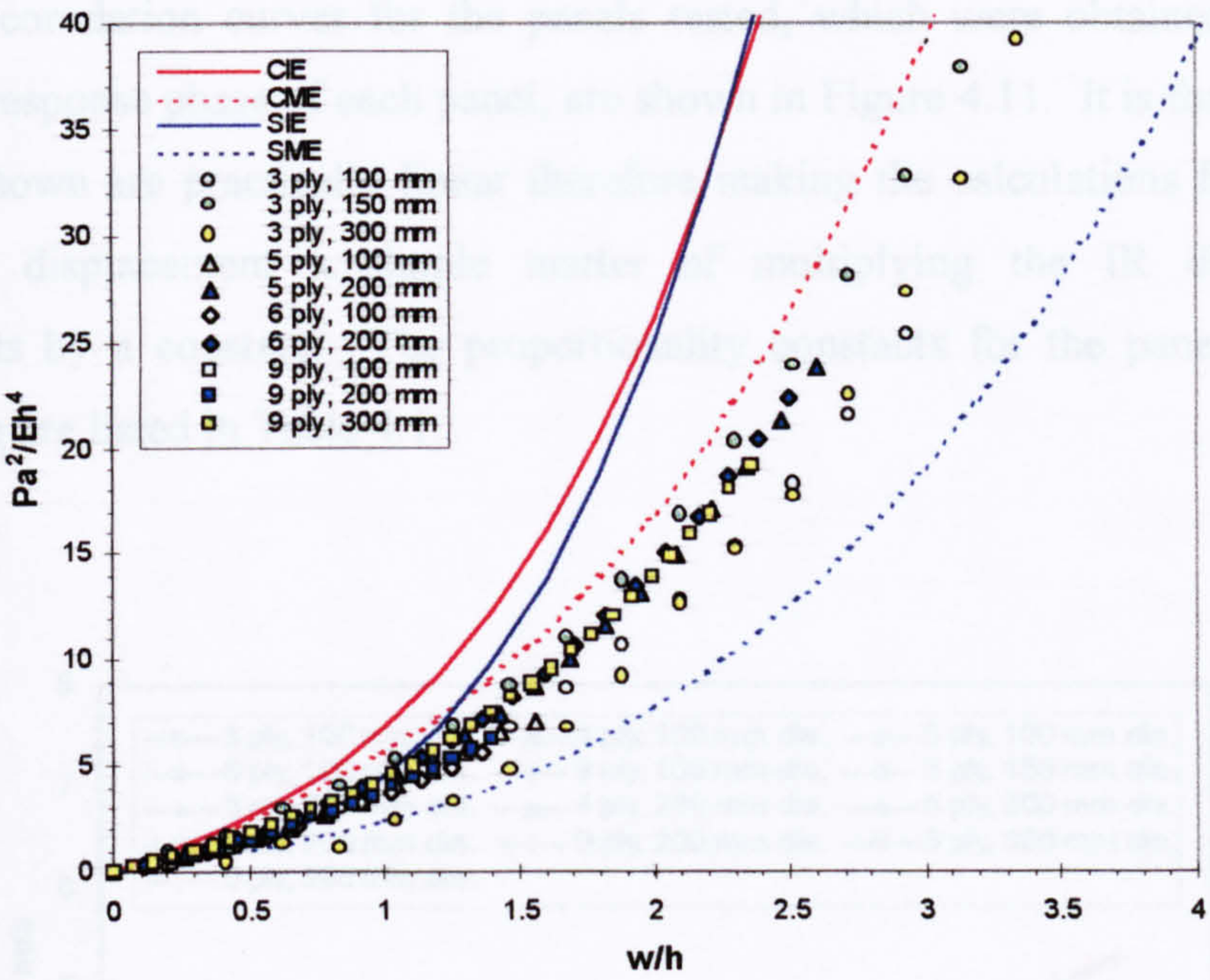

Figure 4.10. Normalised force-displacement plot for all static test data.

Examination of Figure 4.10 shows that the normalised static test data collapses into a narrow band between the two theoretical curves CME and SME and appears to satisfy the form of Equation 2.2 satisfactorily. The relative location of the data points also suggests that the ring clamping system of the test rig was not satisfying the intended boundary condition of a clamped immovable edge. This should not be a cause of too much concern, and perhaps the trend observed should even be expected, since the theoretical boundary conditions are difficult, if not impossible, to achieve in practice.

4.2.2 PANEL DISPLACEMENT UNDER STATIC LOADING

In the static indentation tests, the panels were loaded by mechanically driving the indentor against the frontface. As mentioned in Sec. 3.6, an IR displacement transducer measured the panel displacement at a location on the backface that was offset by a radial distance of 25mm from the load application point. A correlation between the indentor displacement and the IR transducer displacement measurements was then used to calculate for the displacement of the mid-plane of the panel at the load application point. The correlation curves for the panels tested, which were obtained using the undamaged-response phase of each panel, are shown in Figure 4.11. It is fortuitous that the curves shown are practically linear therefore making the calculations for the mid-plane panel displacement a simple matter of multiplying the IR displacement measurements by a constant. The proportionality constants for the panels tested in static loading are listed in Table 4.1.

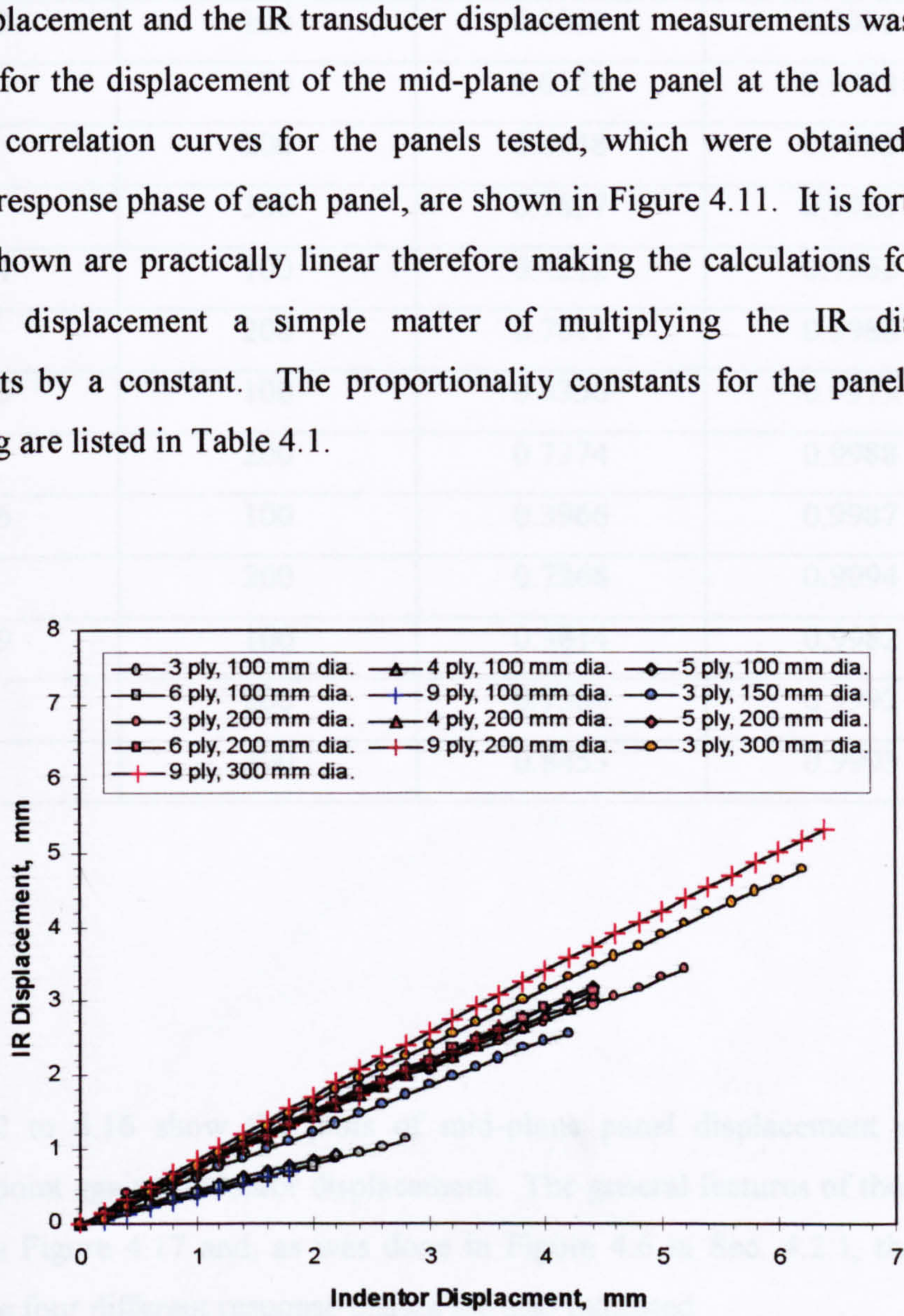

Figure 4.11. The relationship between indentor displacement and IR displacement.

Table 4.1. Proportionality constant between the IR displacement and the indentor displacement over the undamaged response phase of the static tests.

No. of Plies	Panel diameter, mm	Proportionality Constant	Coefficent of Correlation, R^2
3	100	0.3963	0.9996
	150	0.6172	0.9998
	200	0.6648	0.9992
	300	0.7827	0.9985
4	100	0.4212	0.9962
	200	0.7071	0.9988
5	100	0.4356	0.9979
	200	0.7374	0.9988
6	100	0.3966	0.9987
	200	0.7268	0.9994
9	100	0.3814	0.9982
	200	0.7301	0.9992
	300	0.8453	0.9993

Figures 4.12 to 4.16 show the plots of mid-plane panel displacement at the load application point against indentor displacement. The general features of these plots are illustrated in Figure 4.17 and, as was done in Figure 4.6 in Sec. 4.2.1, the transition points for the four different response phases are also indicated.

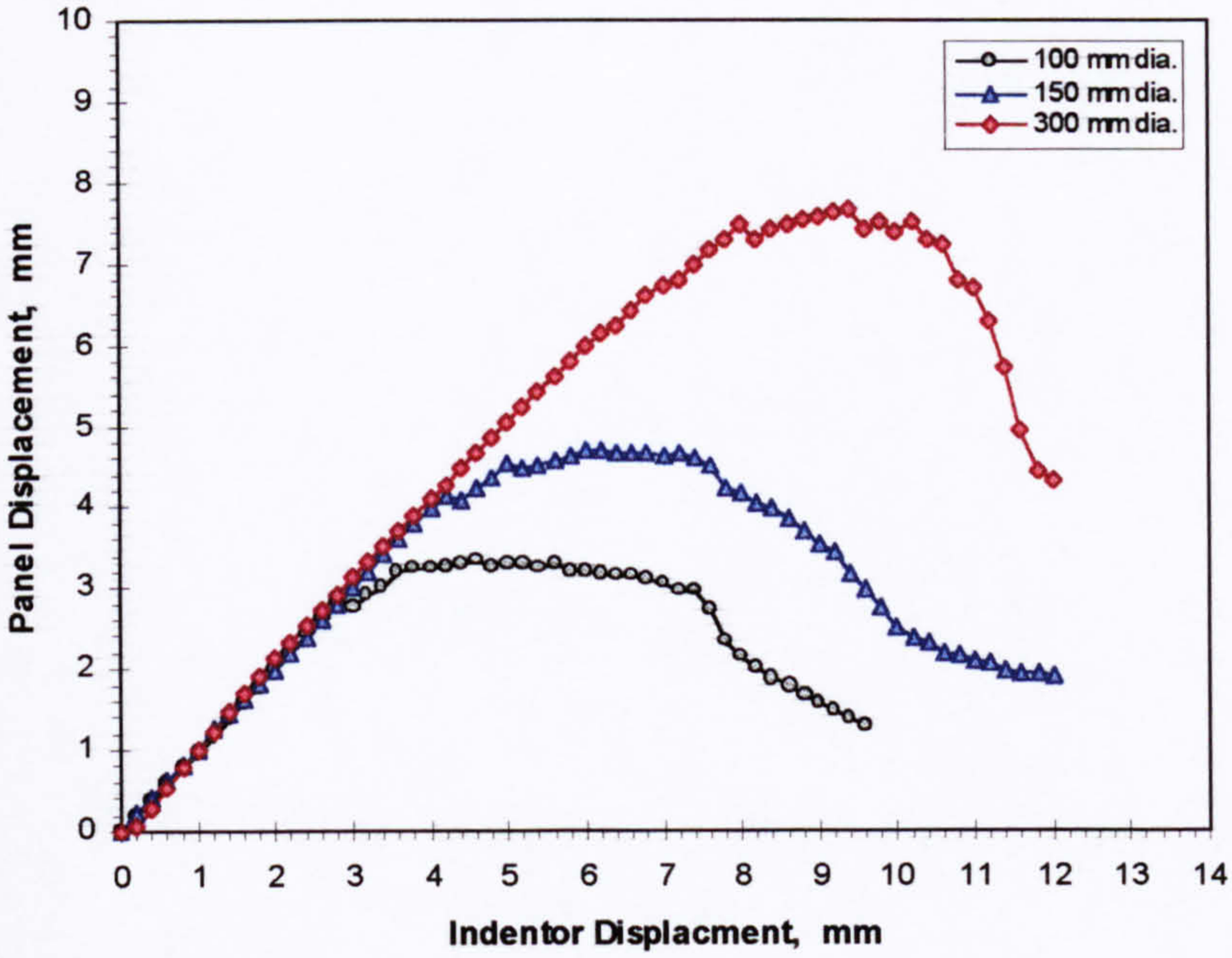

Figure 4.12. Mid-plane panel displacement for the 3 ply panels.

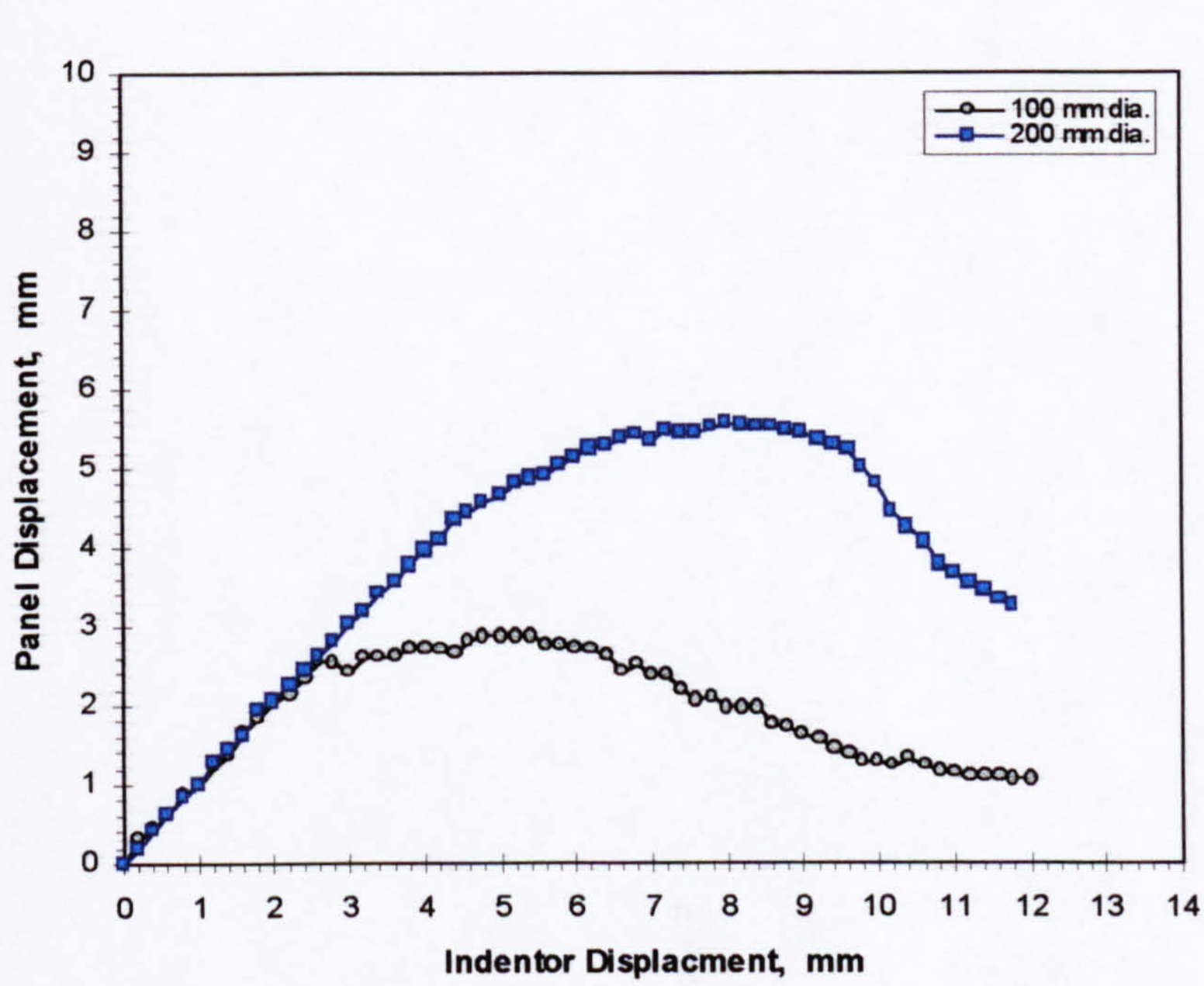

Figure 4.13. Mid-plane panel displacement for the 4 ply panels.

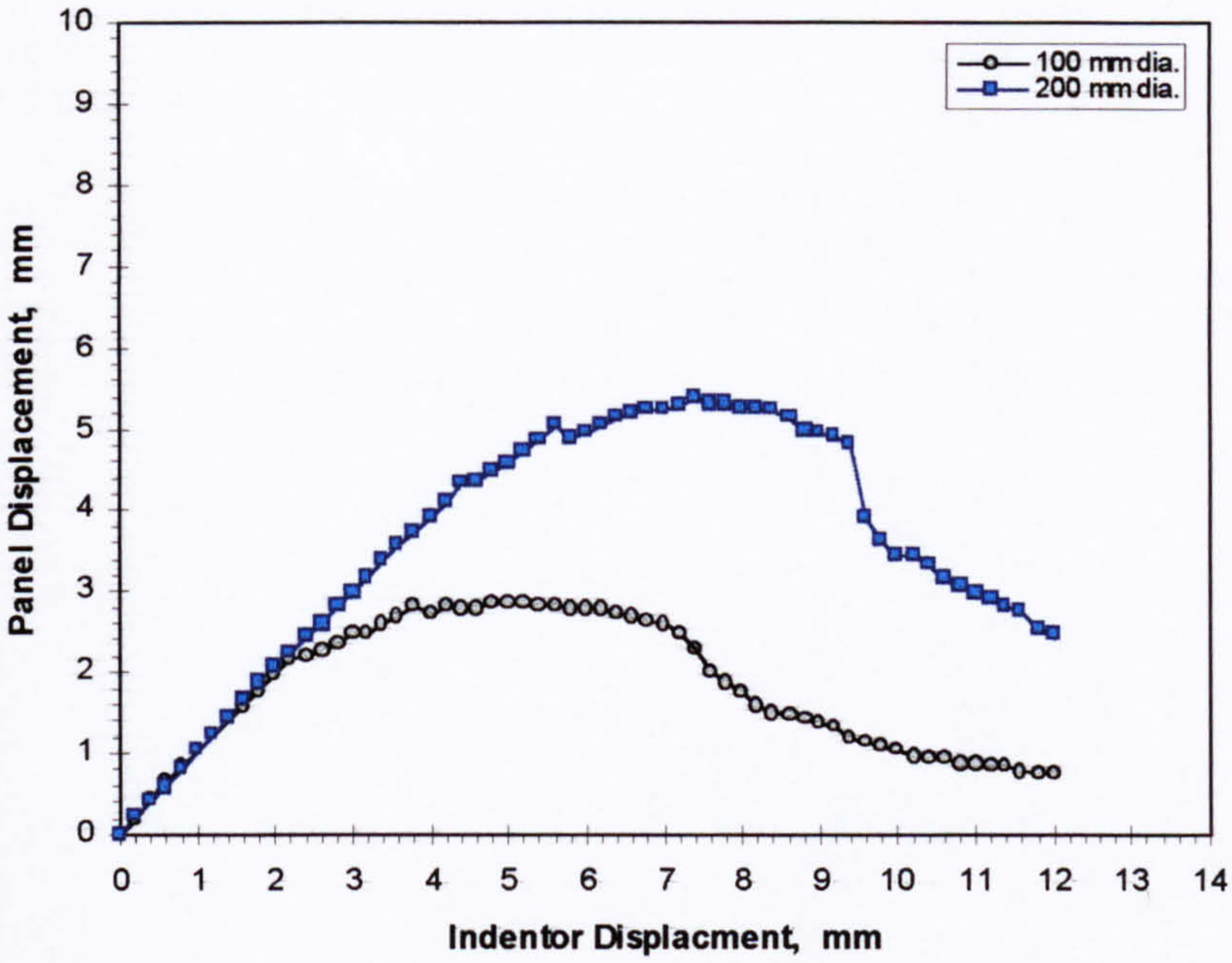

Figure 4.14. Mid-plane panel displacement for the 5 ply panels.

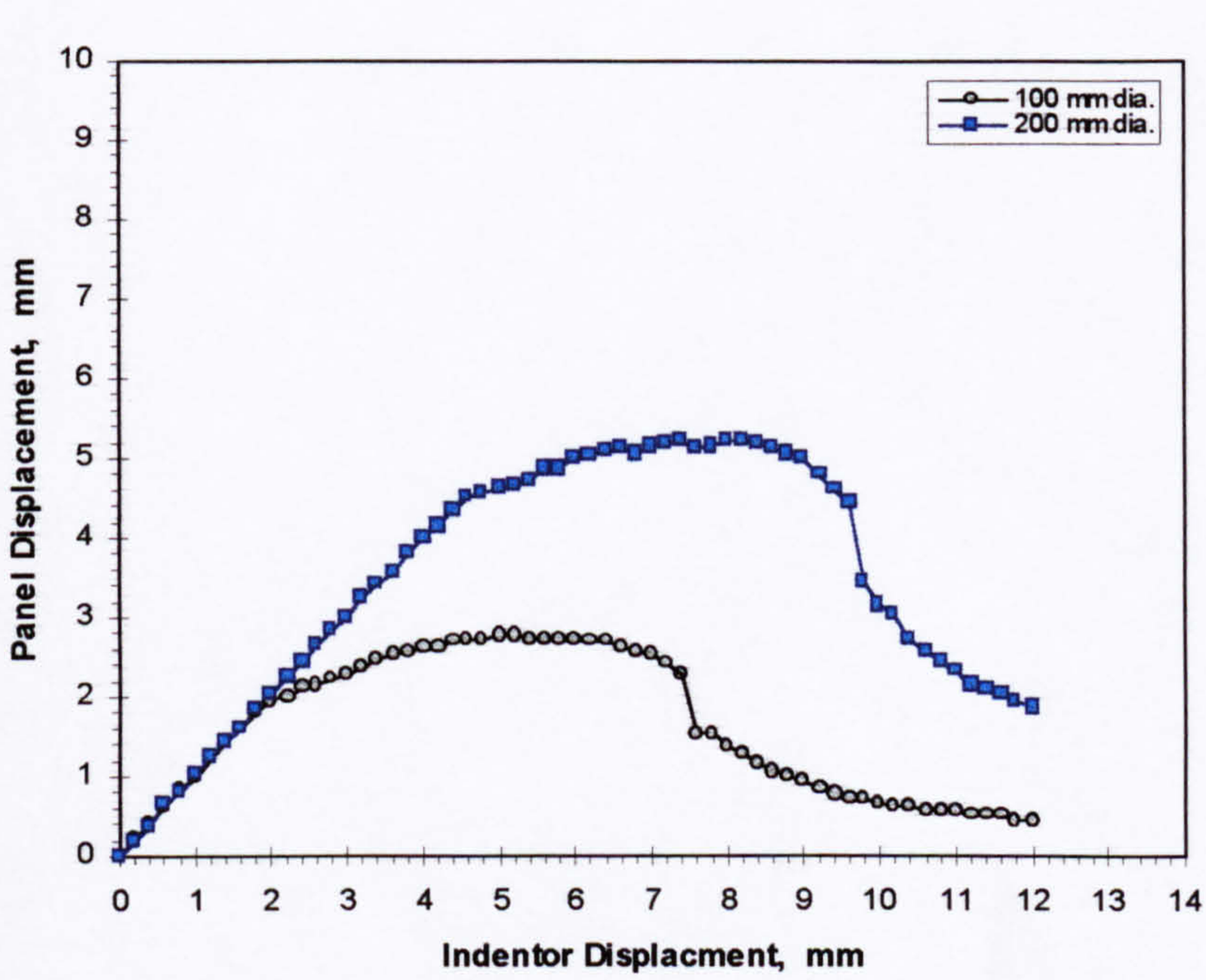

Figure 4.15. Mid-plane panel displacement for the 6 ply panels.

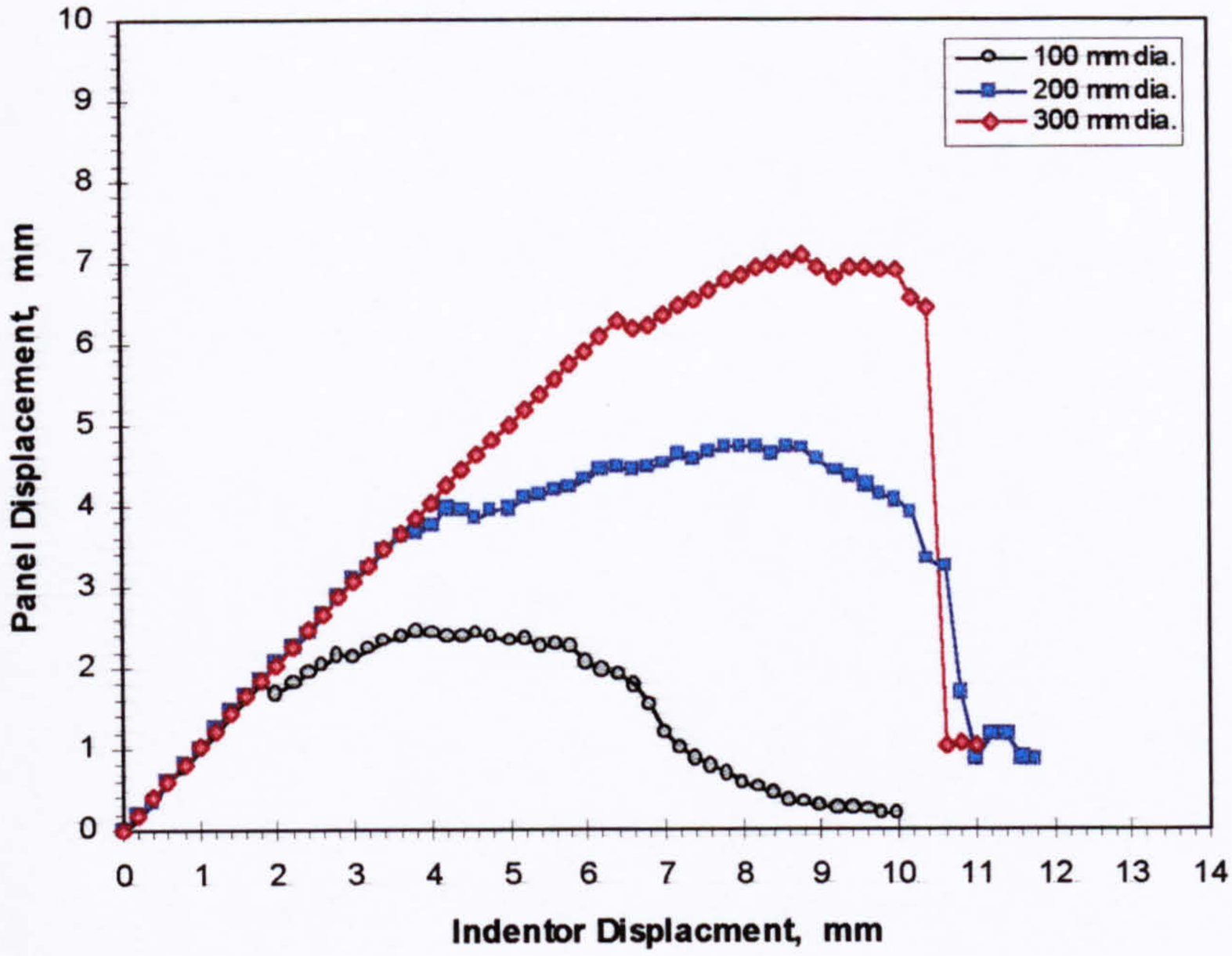

Figure 4.16. Mid-plane panel displacement for the 9 ply panels.

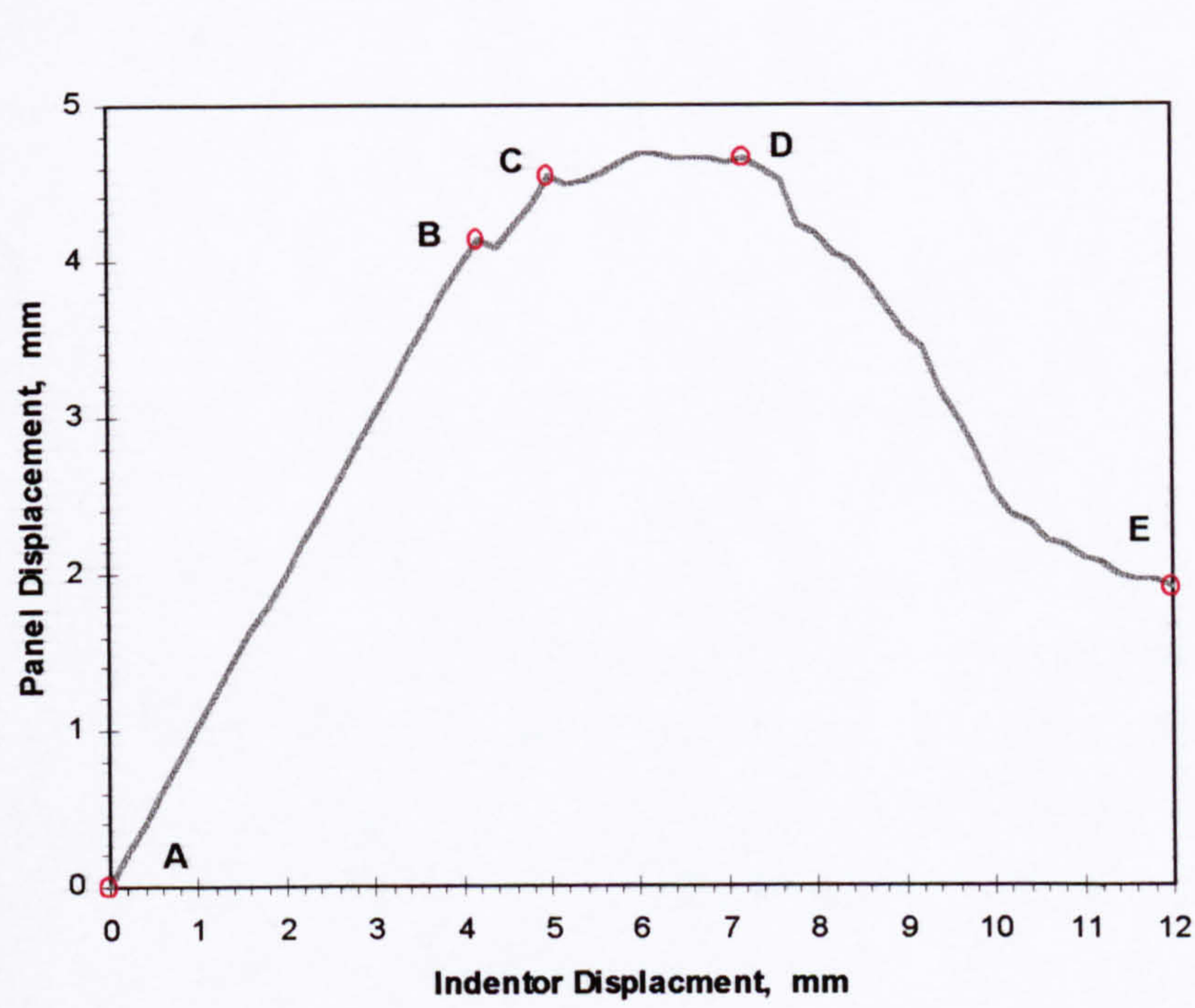

Figure 4.17. General features of the mid-plane displacement response.

In the undamaged-response phase (A-B in Figure 4.17) the panel displacement is practically equal to the indentor displacement. Although there is surface indentation of the panel during this phase it is relatively very small and its effect on the response is negligible. This implies that the work done by the indentor as it its driven into the panel is stored largely as elastic energy.

In the damaged-response phases (B-C-D-E) the panel displacement becomes affected by the growing damage in the panel and deviates significantly from the linear behaviour observed earlier. The effect of panel damage is significant and it appears that the amount of elastic energy stored in the plate accelerates the growth of damage. This observation is more apparent in the large diameter panels (which can store relatively large amounts of elastic energy) that often exhibit abrupt failure during the penetration phase.

In page 51b of Section 4.2.1 the perforation limit and the penetration threshold were defined and these parameters were associated with the states at point D and a point between D and E, respectively, in the static loading response curves (Figures 4.6 and 4.17).

4.2.3 PANEL PENETRATION UNDER STATIC LOADING

In the static indentation tests, the indentor was always driven into the panel as far as the equipment would allow. This procedure always resulted in the complete penetration of the panel by the indentor. The static penetration energy, or the indentor work required to attain incipient penetration of the panel, may be determined by integrating the static load-displacement response to obtain the work done by the indentor as a function of its displacement. The problem is to determine the value of the indentor work at which the indentor just begins to penetrate through the panels. Referring to the load-displacement curve shown in Figure 4.6, this condition of incipient penetration (the penetration threshold) can only occur in that portion of the response curve where the slope is negative (curve D-E). At point D (which is associated with the perforation limit), the panel would have accumulated severe local damage but may still have enough structural

integrity to support the load impressed on it by the indentor. When the indentor is driven beyond this point, rupture of the laminae of the panel occurs and the indentor pushes through the resulting opening. In this stage of the indentation process severe damage in the vicinity of the load application point results in the local failure of the panel and significantly reduces the capability of this local region to transmit the load to the undamaged portion of the panel. As a result the severely damaged panel rebounds some amount and releases some of the elastic energy it stored from the beginning of the indentation process. From this discussion it is reasonable to assume that the static penetration energy threshold must correspond to a state in the indentation process just beyond the point D in Figure 4.6.

The manner in which the static penetration energy threshold was estimated was to normalise the load-displacement curve and indentor work-displacement curve with respect to the maximum values of static force and indentor work, respectively. The resulting curves were cast into a single plot as typically shown in Figure 4.18. It was then taken that the static penetration threshold of the panel is where the two normalised curves intersect. Although this procedure is somewhat arbitrary, the resulting estimates of the static penetration energy thresholds were found to be reasonably close to the penetration energy determined from the impact tests. Figure 4.19 plots the estimates of the static penetration energy thresholds based on the scheme described above.

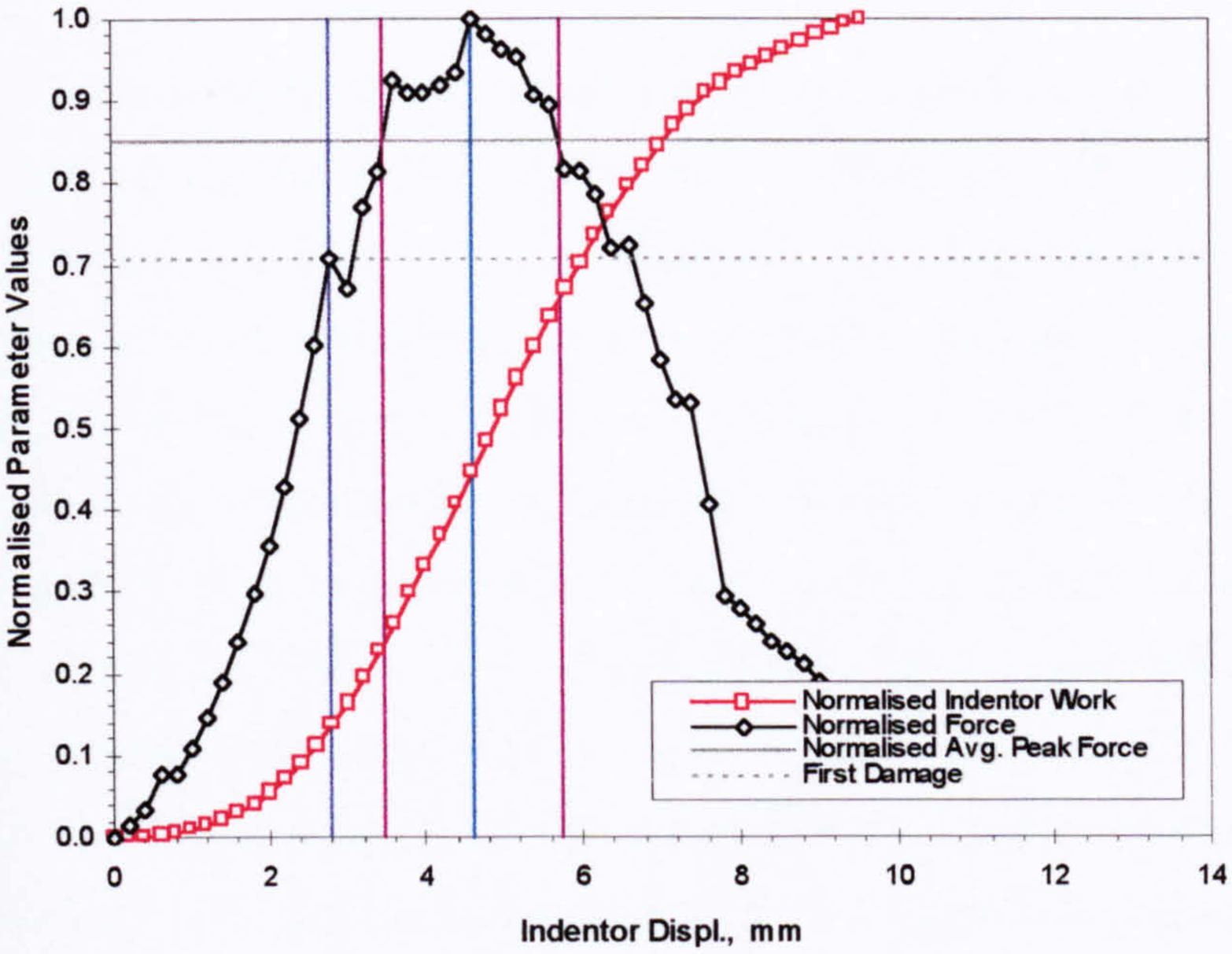

Figure 4.18 Normalised static force and indentor work for the 3 ply, 100-mm dia. plain panel.

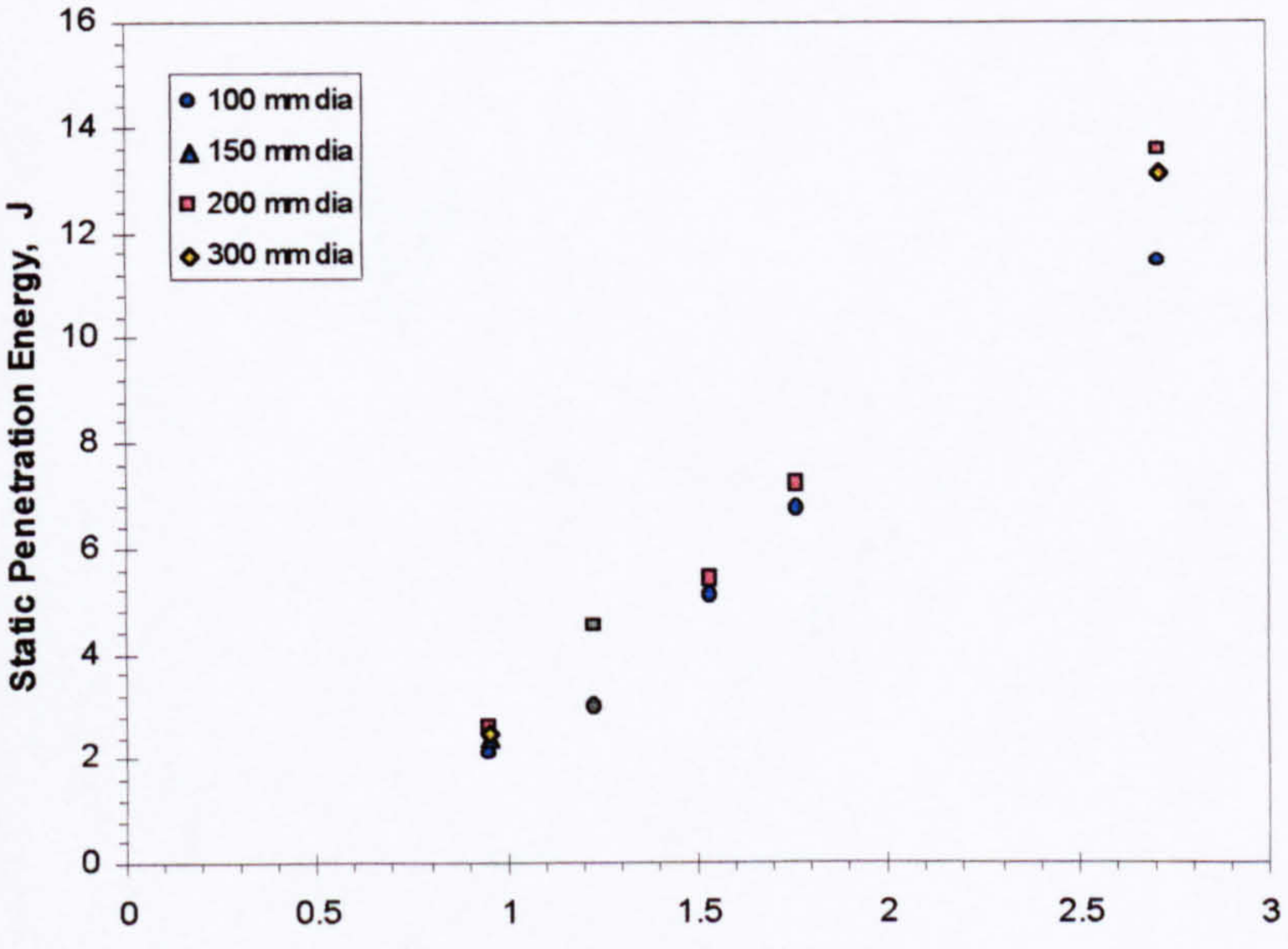

Figure 4.19. Estimates of the static penetration energy for the plain panels.

In the typical load-displacement plot shown in Figure 4.6, the force tends to level out (albeit erratically) in the region C-D. This region has been associated with the rapid growth of delaminations in the static tests (see pages 51a to 51b of Section 4.2.1). This suggests that the forces developed therein are close to the critical delamination force identified by Davies and Zhang (1995) and Davies et al (1994, 1996, 1997) and expressed in Eqn. 2.12. A comparison between the predicted values of the critical force and the values of the force corresponding to point C (in Figure 4.6) for all the plain panels tested is shown in Figure 4.20. The theoretical values were calculated using average panel properties determined from laminate theory (Jones. 1975; Tsai. 1985; Tsai and Hahn. 1980) and an assumed value of mode II energy release rate, G_{IIc}, equal to 0.7 N/mm (kJ/m^2). The assumption of a value for G_{IIc} was necessary because we had no data on this property for the materials tested. Nonetheless the assumed value falls within the range of values reported in published literature (Abrate. 1994; Charalambides et al. 1992; Davidson and Krafchak. 1993; Delfosse and Porsartip. 1997; Davis and Zhang. 1995).

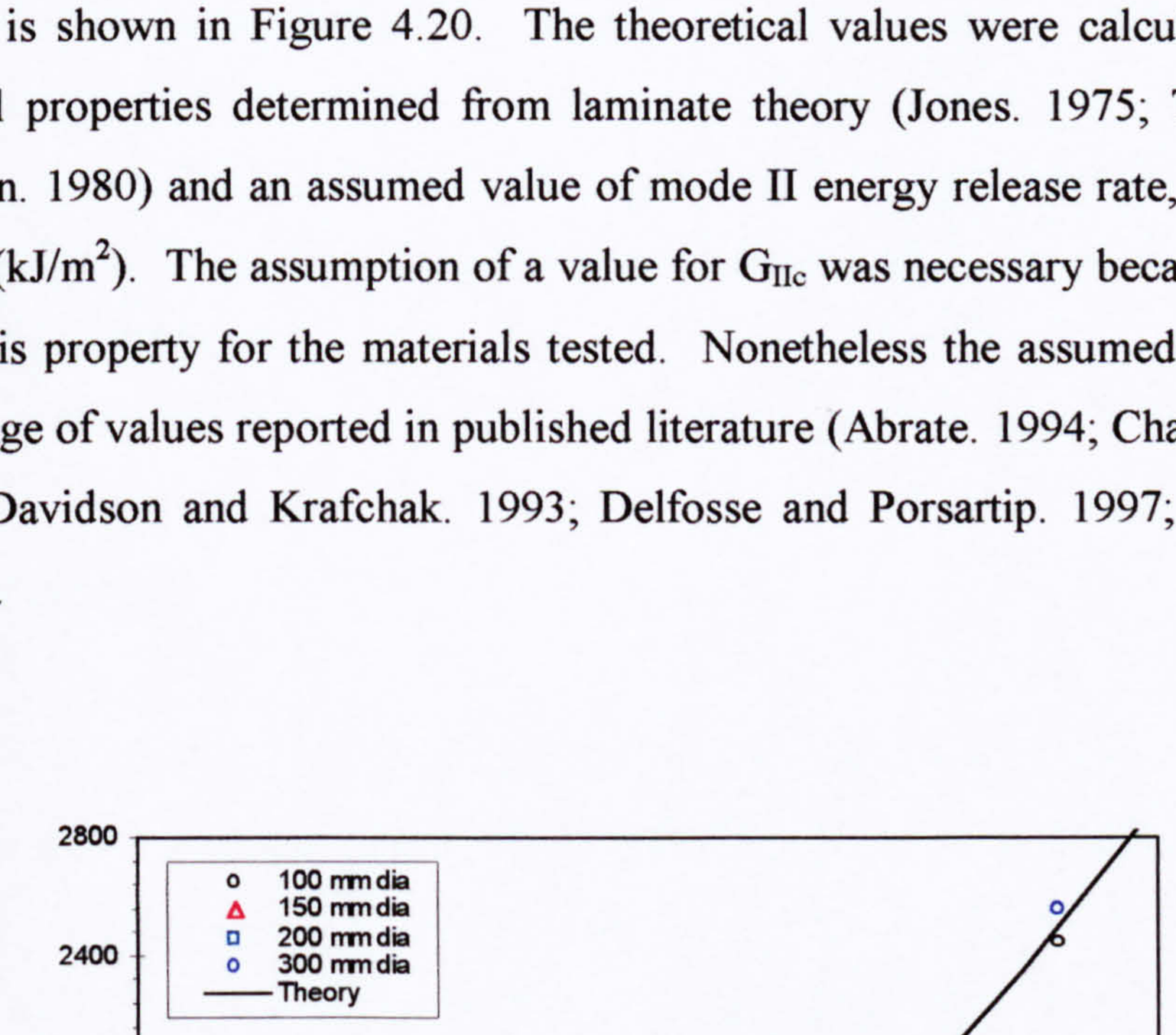

Figure 4.20. Delamination initiation force plotted against panel thickness.

The information presented in Figure 4.20 suggests that the delamination initiation force is dependent only on the panel thickness for the same material and, as was mentioned in Chapter 2, is independent of the panel size and boundary conditions. This has very important implications for stiffened panels that are loaded on the skin or between stiffeners.

It may be argued that point B in Figures 4.6 and 4.17 can be used to indicate the start of delamination failure. However this state is characterised by backface tensile failure due to high bending stresses and not by extensive delaminations. The static tests clearly show that the panels can still carry considerable load beyond the point of backface tensile failure and that the load essentially stops increasing with indentor displacement only from point C of Figure 4.6.

IMPACT RESPONSE

Figures 4.21 to 4.23 show typical impact force and panel displacement histories for some selected tests. In general the impact duration increases with increasing incident kinetic energy even when there is little or no damage to the panel. This is a consequence of the manner in which the impact energy is set during the tests. The adjustable-mass indentor is always dropped from a fixed height and strikes the panel at a fairly constant velocity. Therefore the only way to vary the incident energy is by adding or subtracting fixed masses to the indentor. This unavoidably alters the dynamics between the indentor and panel resulting in dynamical behaviour consistent with observation mentioned above.

The force histories captured by the accelerometer and the strain gauge load cell are shown in Figures 4.21 and 4.22 respectively. The signals correspond very well at low impact energy. At high energy levels the two signals deviate from each other with the accelerometer signal acquiring high-frequency and high-amplitude oscillations. This is thought to be due to the "ringing" of the indentor assembly and/or accelerometer brought about by impulsive loading as well as by the sudden change in panel stiffness in

impacts of sufficient energy to cause damage. Since the load cell indirectly measures the impact force through the axial compression of the indentor nose shank, it is not affected as much by this phenomenon. Figure 4.22 charts the change in the impact force response of the 5 ply plain panels clamped between 200-mm rings subjected to non-penetrating impacts. As the impact energy is increased form 0.690 J to 5.281 J, the peak forces first increases with energy and then seems to reach a plateau. Any further increase in impact energy only increases the impact duration and creates further damage in the panel. This behaviour is consistent with the findings from the static tests and confirms the validity of the existence of a damage initiation force. The displacement history for the same panel is shown in Figure 4.23. The displacement history exhibits the same trend as the force history including the saturation of the peak displacement at the higher impact energies. One interesting observation that can be made from the displacement history is the measurable free vibration of the plate after the indentor has rebounded. The free vibration was observed to eventually dampen out due to the action of internal friction in the material. This implies that even in a non-damaging impact some amount of energy will be retained in the panel as energy associated with wave motion and that the indentor cannot completely recover the elastic energy stored in the panel.

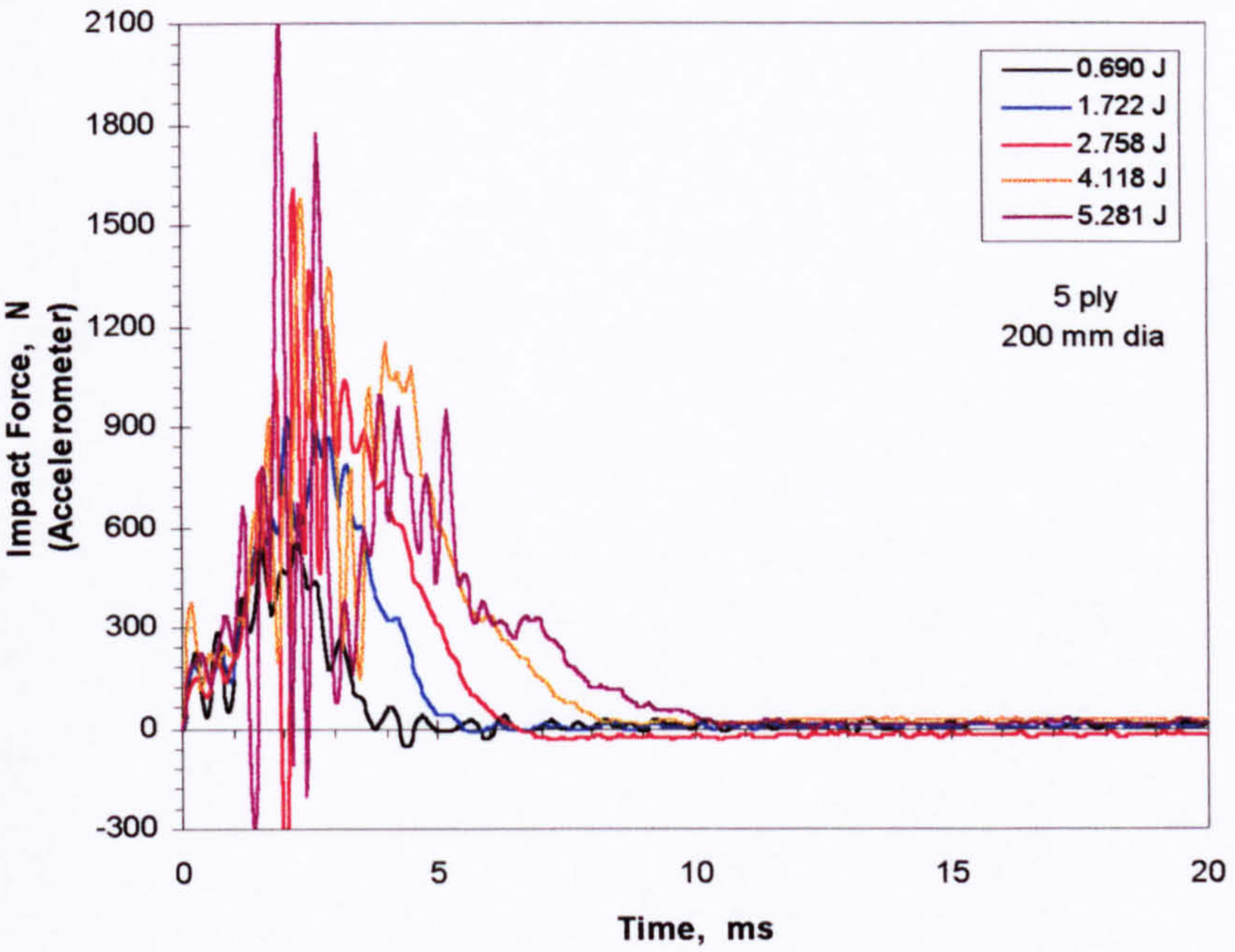

Figure. 4.21. Accelerometer force history for the 5 ply, 200-mm dia plain panels.

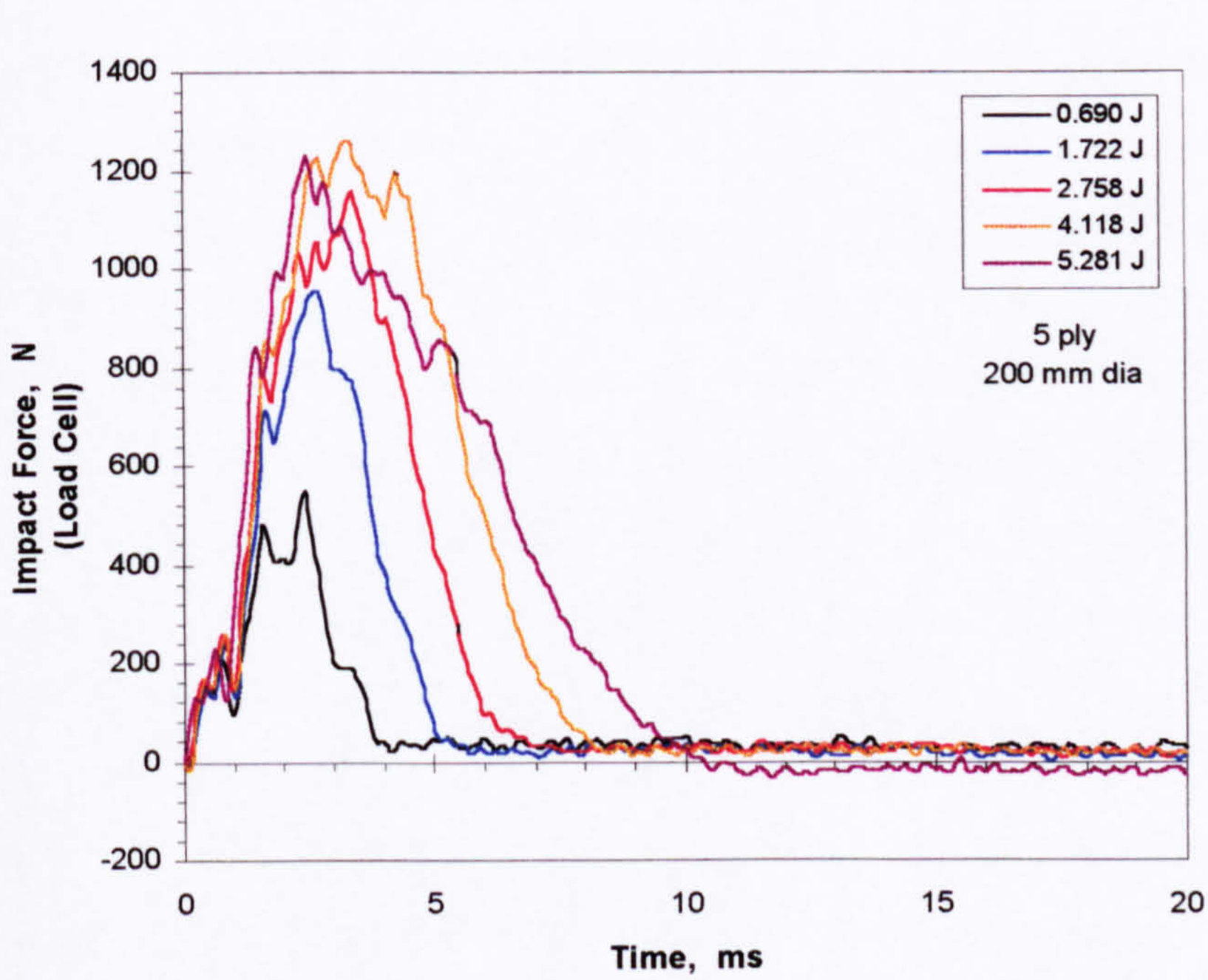

Figure. 4.22. Strain gauge/load cell force history for the 5 ply, 200-mm dia plain panels.

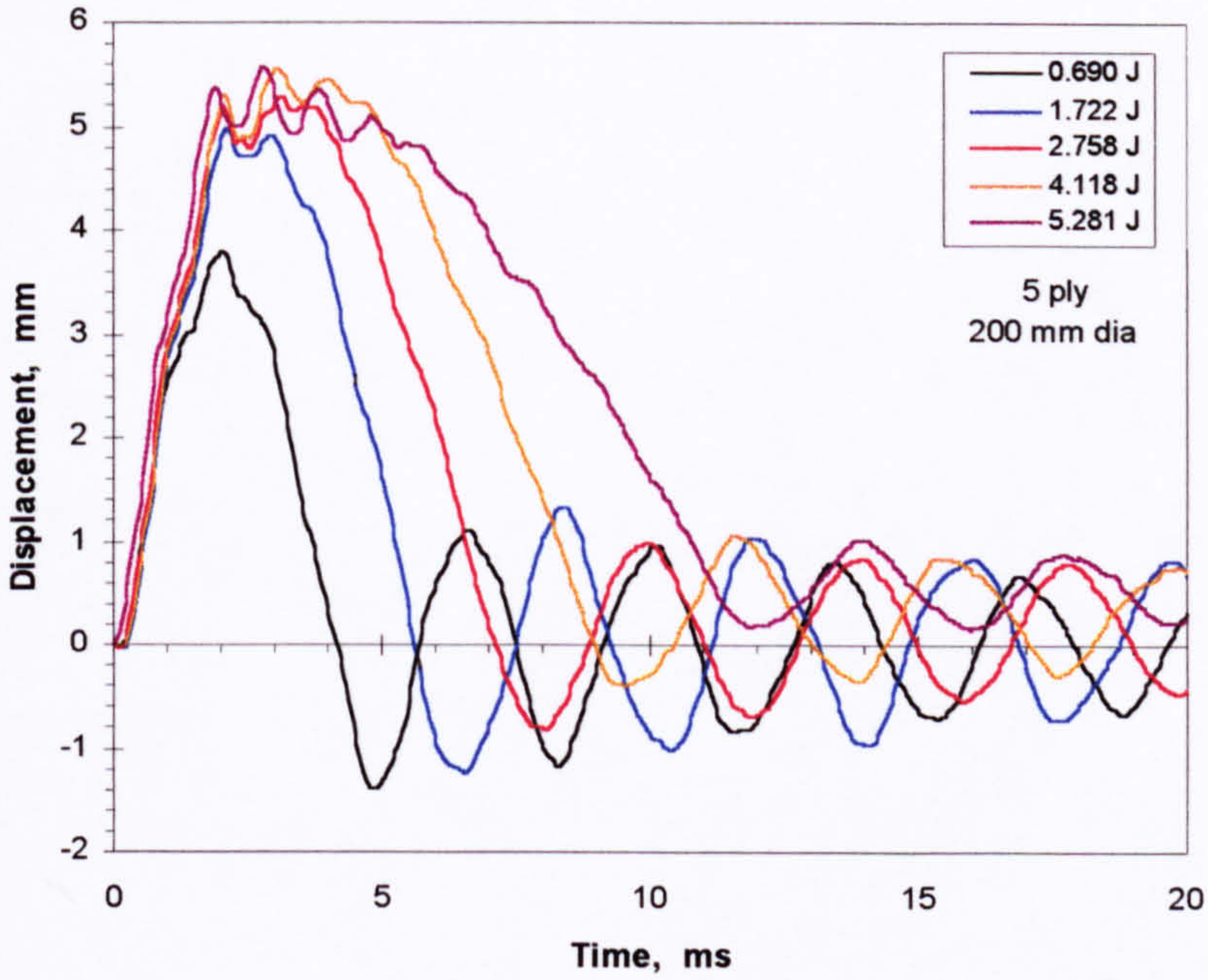

Figure. 4.23. Displacement history for the 5 ply, 200-mm dia. plain panels.

The force histories and displacement histories of the 3-ply, plain panels subjected to increasing impact energies, including a penetrating impact at 2.960 J, are shown in Figures 4.24 and 4.25, respectively. As was discussed with the 5-ply panel above, the impact duration, peak forces and peak displacements are seen to increase with incident kinetic energy. However, something interesting occurs at an impact energy of 2.960 J: the impact duration as observed from the force history appears to abruptly become shorter while that observed from the displacement history lengthens significantly. This apparent contradiction is resolved if one keeps in mind that this behaviour only occurs in penetrating impacts. When the incident kinetic energy is sufficiently high the indentor penetrates and goes through the panel and, depending on frictional forces, may get embedded in it. The abrupt drop in the impact force is due to the sudden loss of the structural integrity of the panel at the load point. If one looks closely at Figure 4.25, this abrupt loss of load carrying capability is manifested as a "kink" or discontinuity in the displacement history. The apparent extension of the displacement response is due to the embedding of the indentor in the panel.

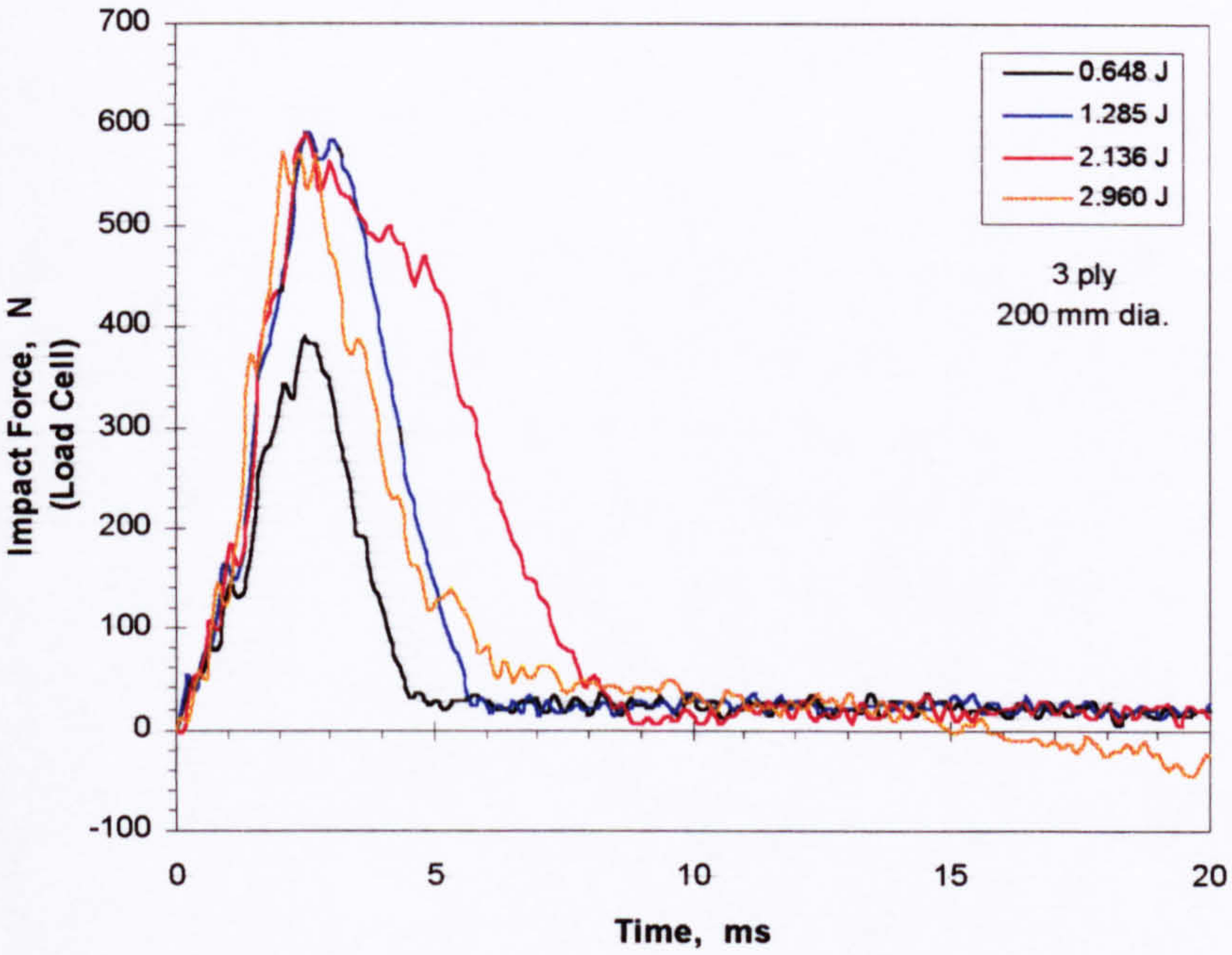

Figure. 4.24. Force history for the 3 ply, 200-mm dia. plain panels.

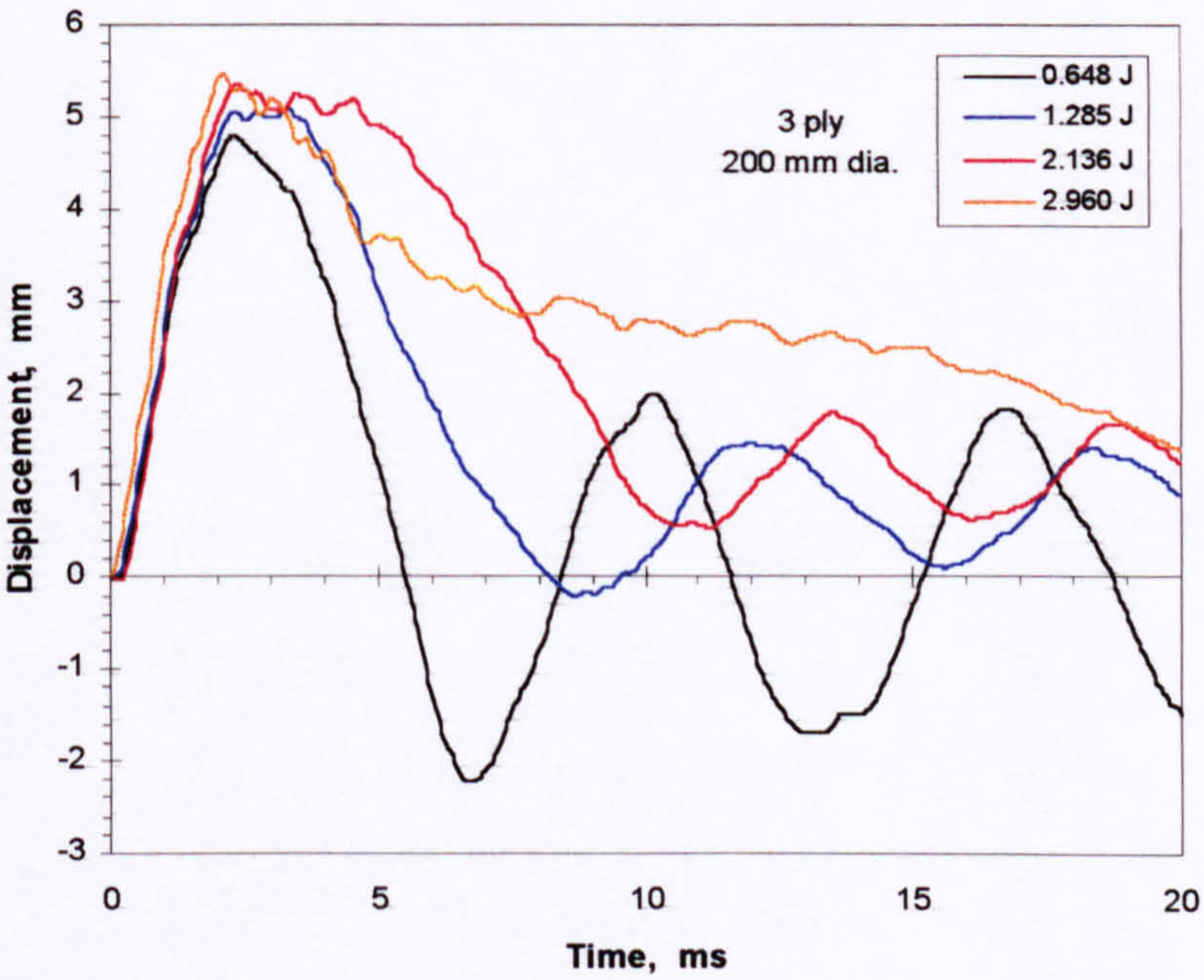

Figure. 4.25. Displacement history for the 3 ply, 200-mm dia. plain panels.

4.4 IMPACT DAMAGE DEVELOPMENT AND GROWTH

4.4.1 GENERAL CHARACTERISTICS

Measurement of the projected delaminated area, the total backface crack length and the permanent indentation on the frontface of the panel provided a means of monitoring the development and growth of damage in the impacted panels. The results of these measurements for the 100-mm diameter panels are presented as damage maps in Figures 4.26 to 4.28. In Figure 4.26 the projected delaminated area is seen to grow with incident impact energy and the rate of growth appears to increase with the energy. This gives the trend of the data in the figure a concave-upwards shape up to the impact penetration energy. At and above the penetration energy, the size of the projected delaminated oscillates about a fixed value and appears to become independent of the incident energy. The effect of panel thickness can also be clearly seen, with thicker panels requiring larger incident energies to penetrate it and having noticeably larger maximum projected delaminated areas.

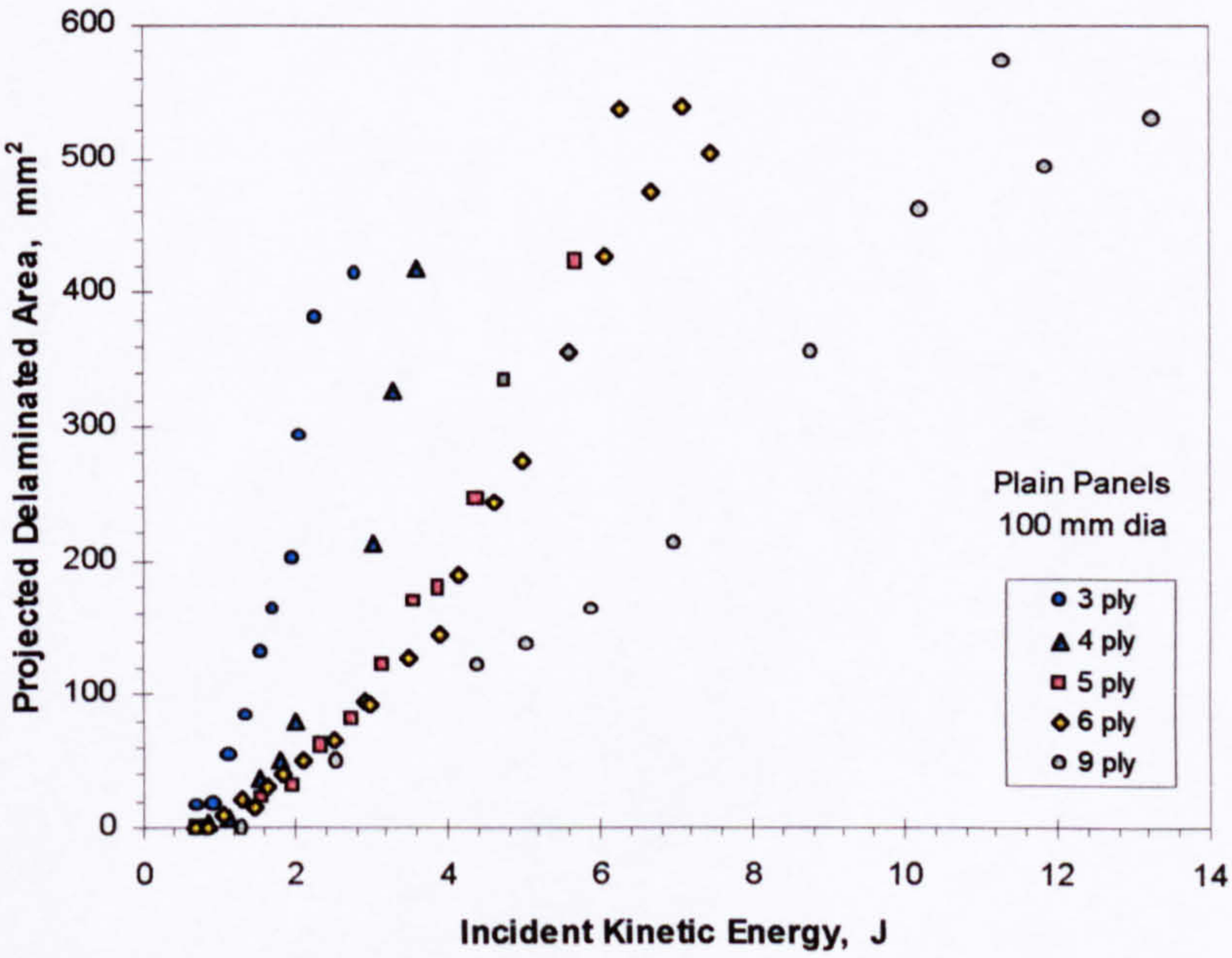

Figure 4.26. Increase in the projected delaminated area with impact energy for the 100-mm diameter, plain panels.

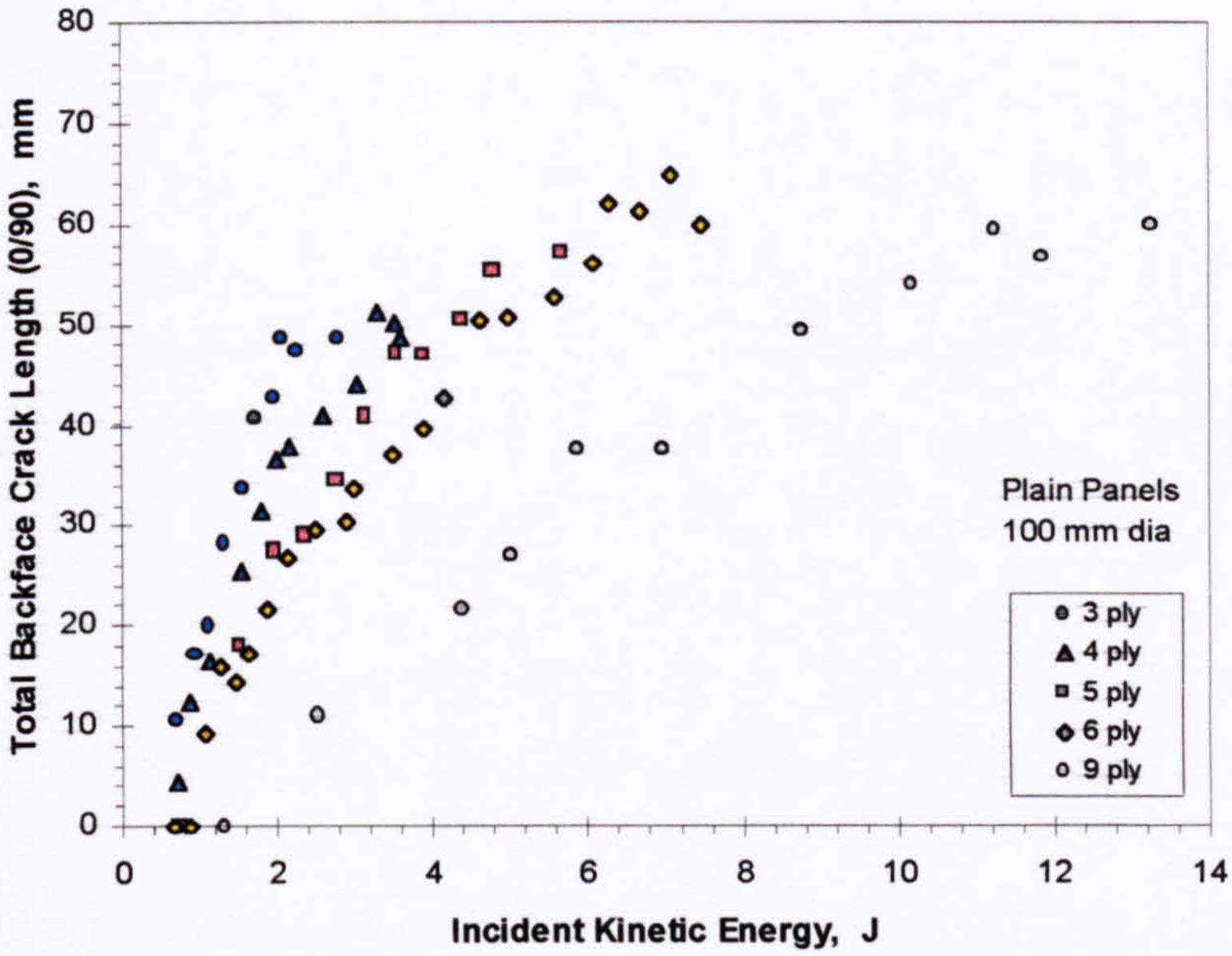

Figure 4.27. Increase in the total backface crack length with impact energy for the 100-mm diameter, plain panels.

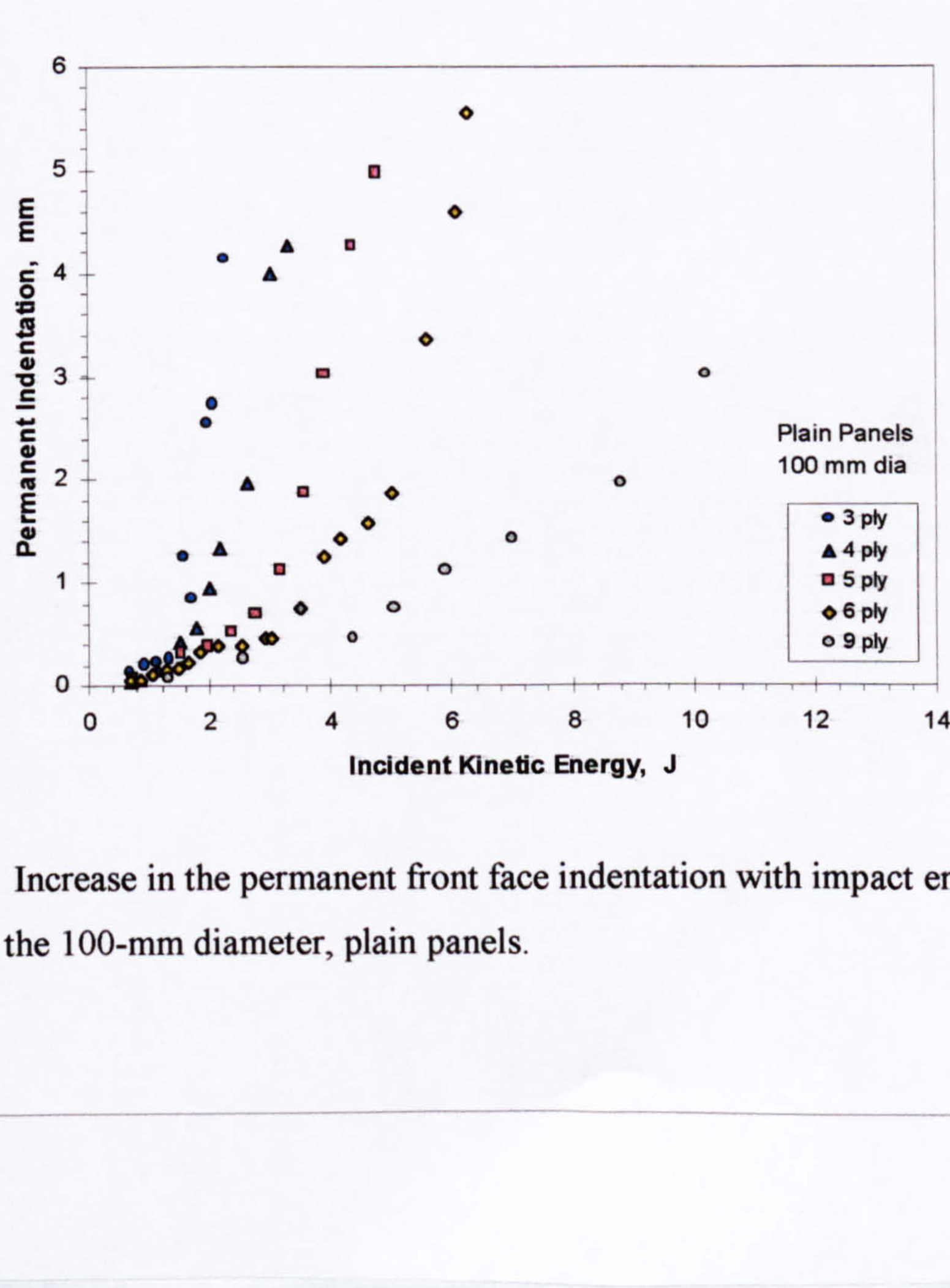

Figure 4.28. Increase in the permanent front face indentation with impact energy for the 100-mm diameter, plain panels.

The same observations made for the growth of delaminations can be applied to the increase in total backface crack length with impact energy shown in Figure 4.27 with the exception that the crack length growth rate decreases with impact energy. Because of this the trend of the data in Figure 4.27 has a concave-downward shape in contrast to the concave-upward trend indicated in Figure 4.26. Like the projected delaminated area the total backface crack length reaches a plateau at and above the penetration energy. These observations imply that once the impacting body possesses enough energy to penetrate the panel the maximum size of the damage will have been attained and any further increase in incident impact energy would create no further damage.

The trend in the increase in permanent frontface indentation with impact energy for the 100-mm diameter plain panels is shown in Figure 4.28. Like the projected delaminated area, the trend of the data has a concave-upwards shape indicating increasingly rapid growth of indentation with impact energy brought about by damage to the panels. It was surprising to find that the indentation can exceed the panel thickness. This is thought to be due to the significant local deformation of the panel in the vicinity of the load application point. At and above the impact penetration energy the front face indentation becomes undefined because the diameter of the hole created in the panel becomes independent of the depth of penetration by the hemispherical-nose indentor.

The variations in projected delaminated areas, total backface crack lengths, permanent frontface indentations with impact energy for the 200-mm and 300-mm diameter panels are shown in Figures 4.29 to 4.34. The data in these figures are not as extensive as that for the 100-mm diameter panels but the same observations mentioned above apply to it as well. Comparing the corresponding figures for delaminations, crack lengths and indentations, the effect of panel size can be clearly seen: For the same panel thickness, increasing the panel diameter increases the impact energy to create the same damage size.

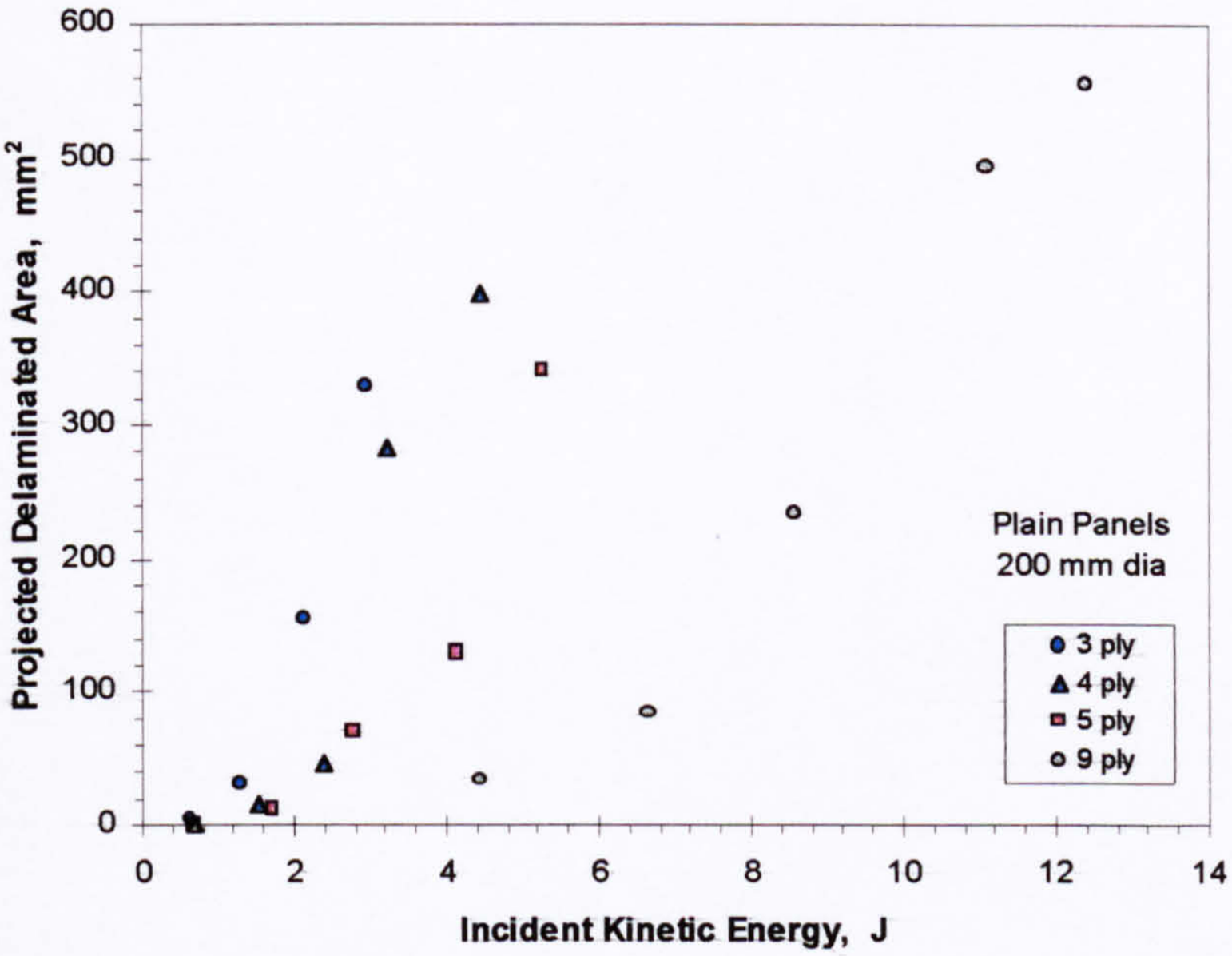

Figure 4.29. Increase in the projected delaminated area with impact energy for the 200-mm diameter, plain panels.

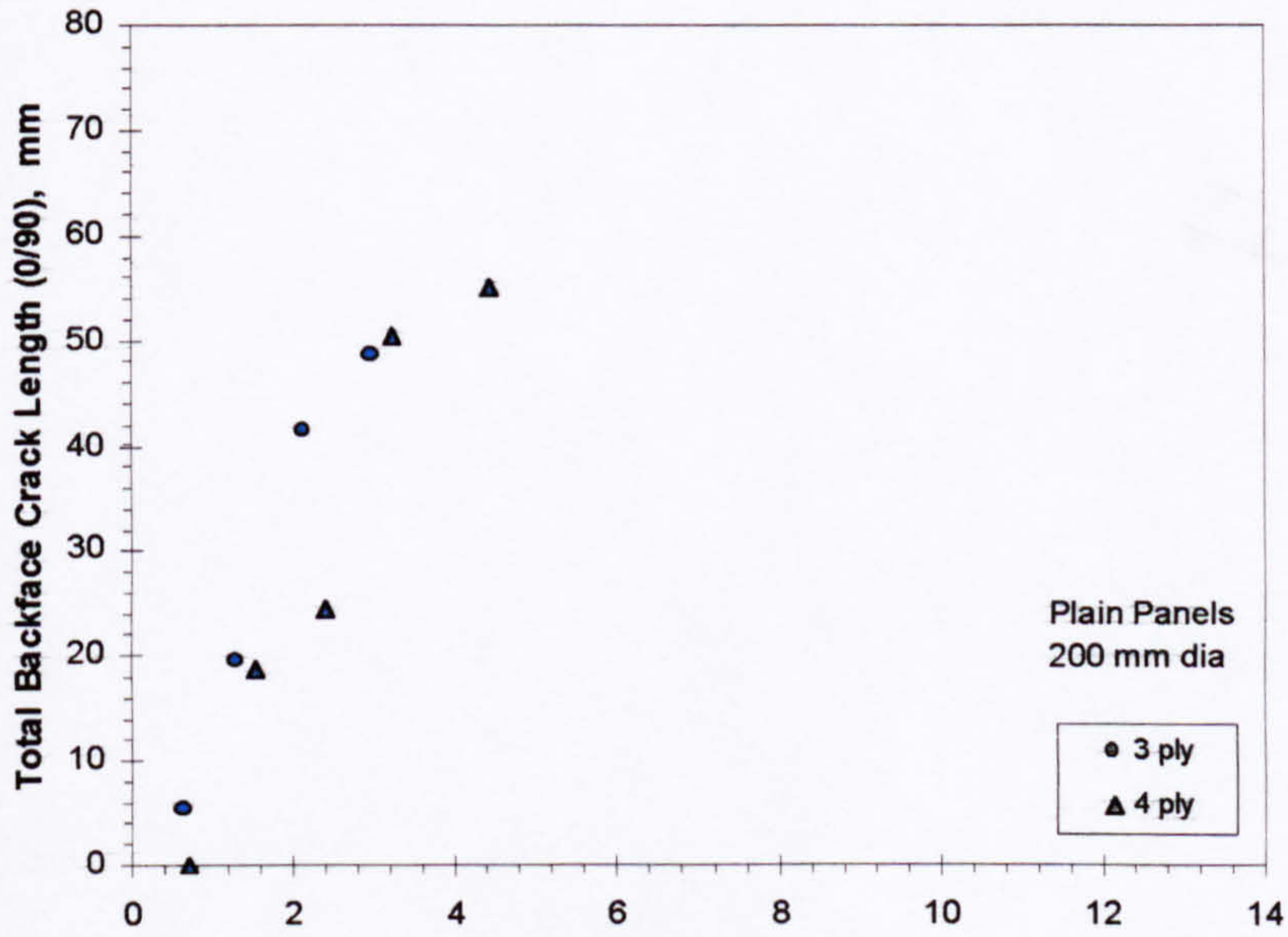

Figure 4.30. Increase in the total backface crack length with impact energy for the 200-mm diameter, plain panels.

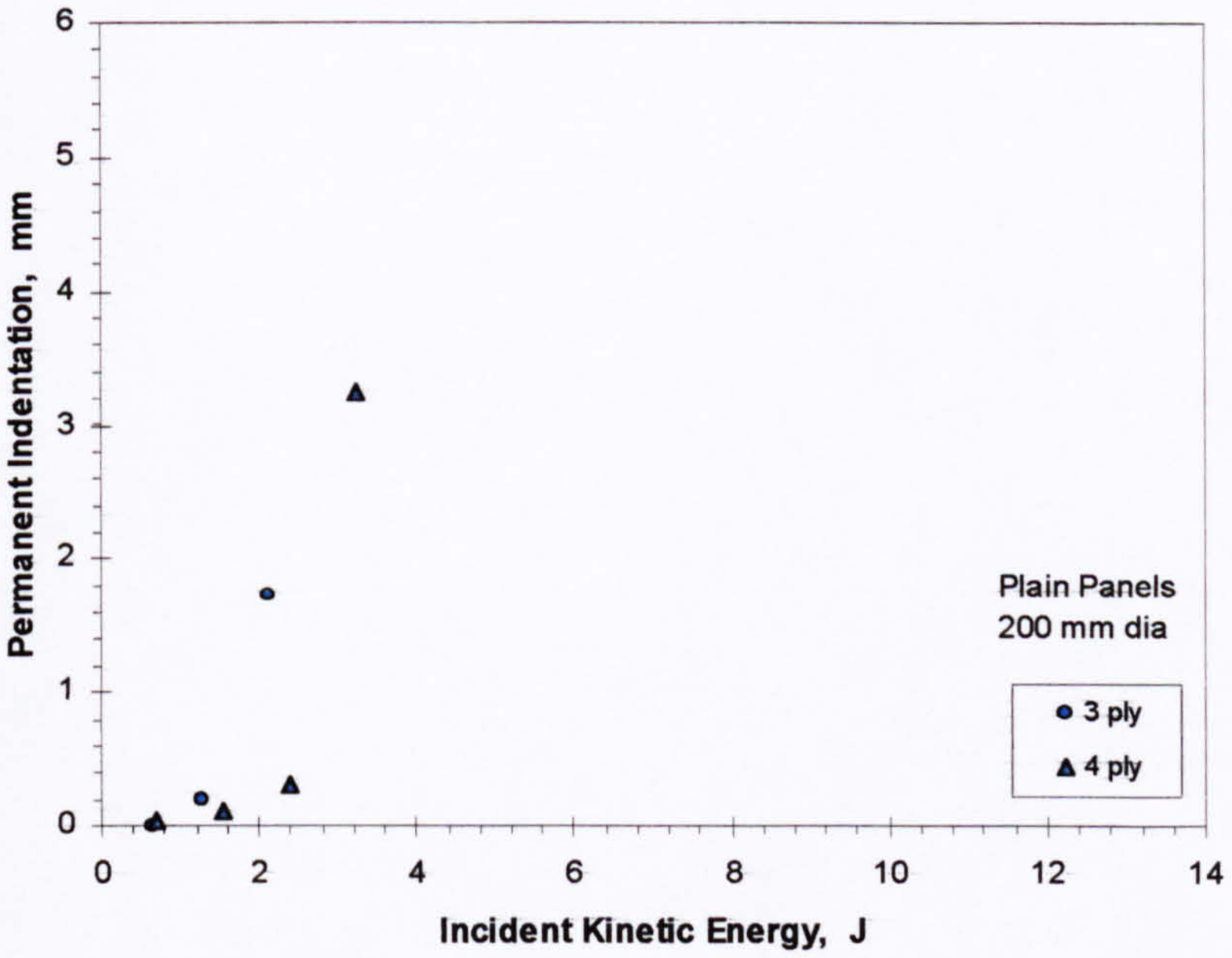

Figure 4.31. Increase in the permanent frontface indentation with impact energy for the 200-mm diameter, plain panels.

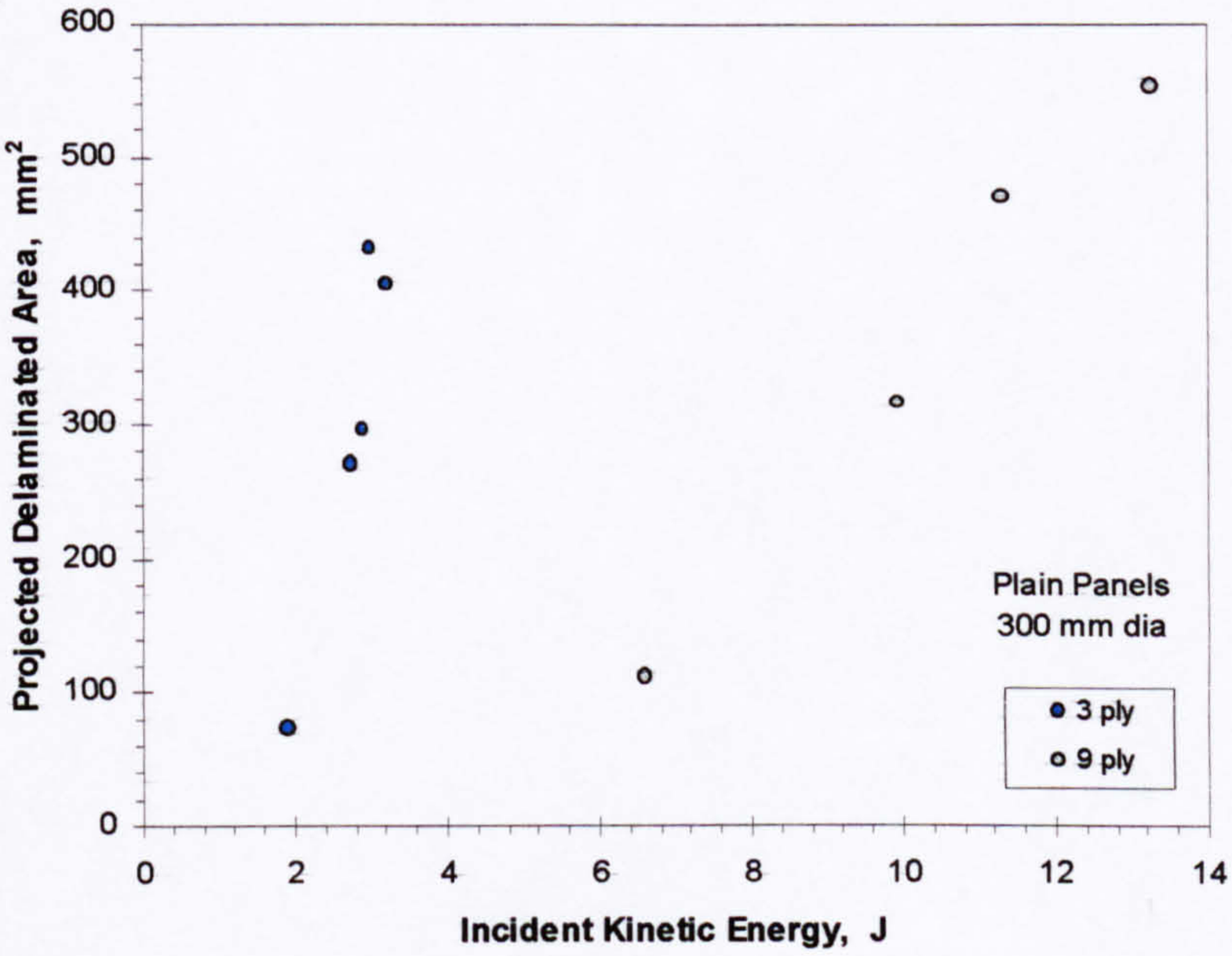

Figure 4.32. Increase in the projected delaminated area with impact energy for the 300-mm diameter, plain panels.

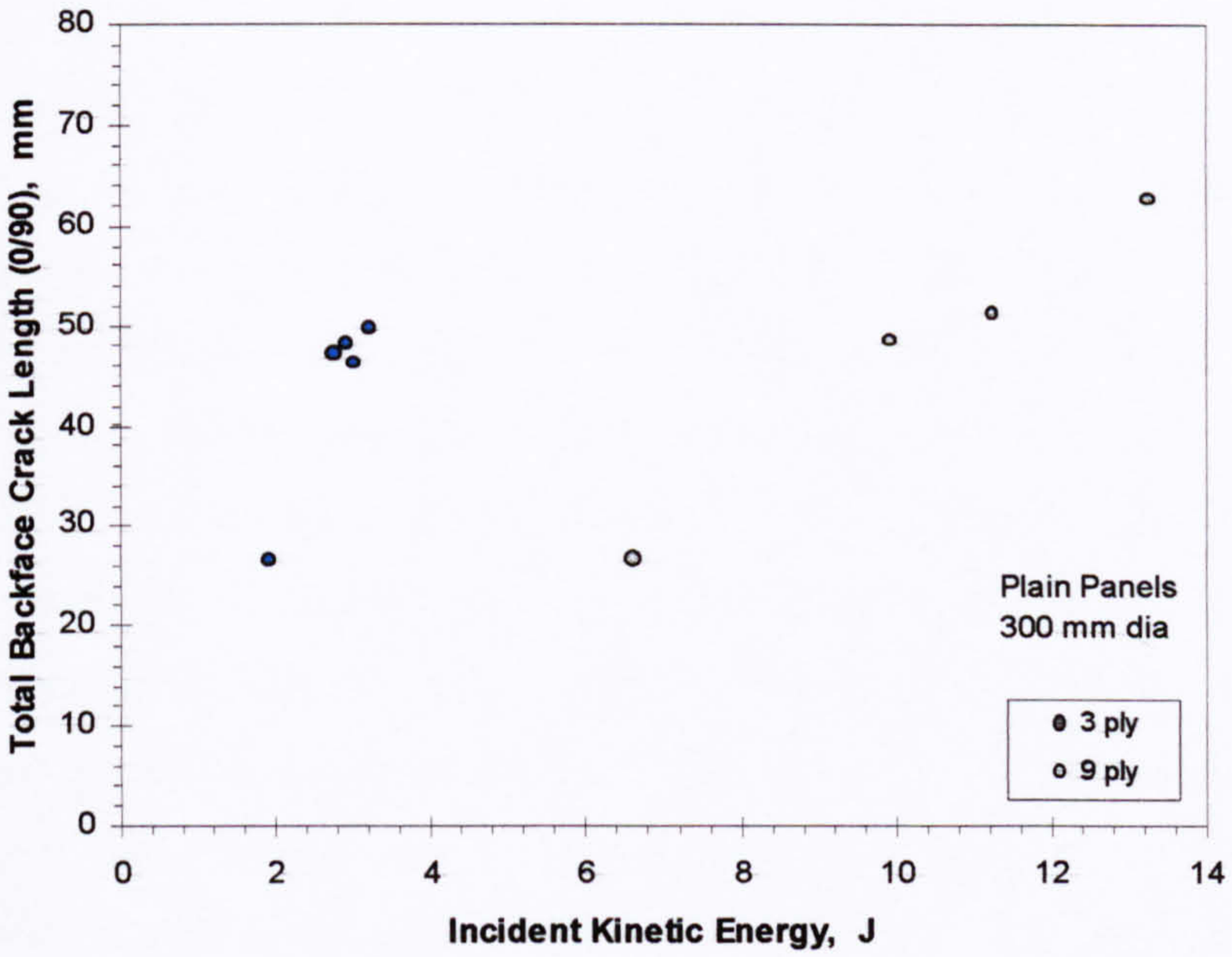

Figure 4.33. Increase in the total backface crack length with impact energy for the 300-mm diameter, plain panels.

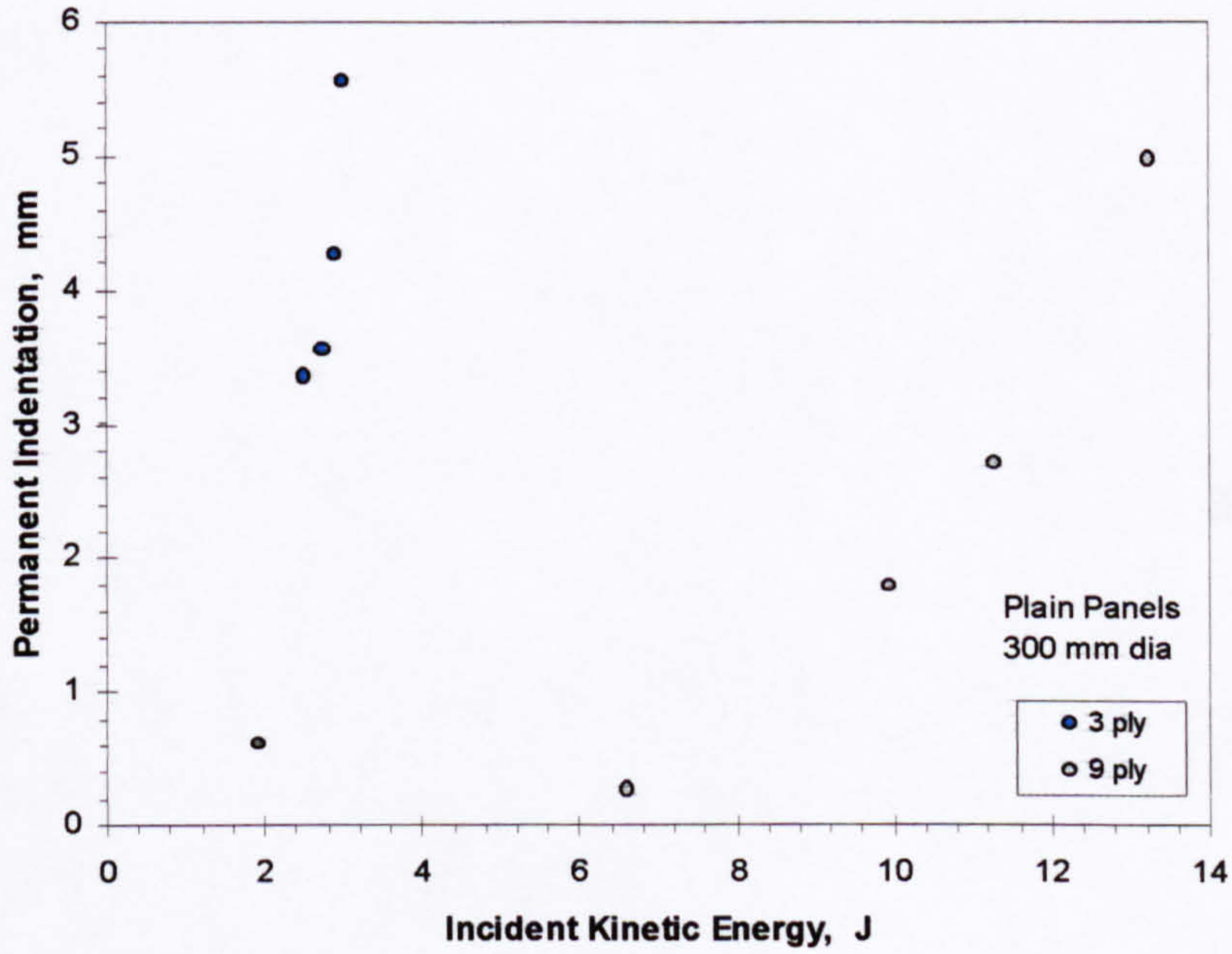

Figure 4.34. Increase in the permanent frontface indentation with impact energy for the 300-mm diameter, plain panels.

A closer examination of the damage maps for projected delaminated area and total backface crack length offers some insights into the damage mechanism occuring in the panels. To illustrate this notion, the delaminated area and backface crack length for the 6 ply, 100-mm diameter panel is cast into one plot as shown in Figure 4.35. In Figure 4.35 region A encompasses the range of data dominated primarily by backface crack growth. In this region the backface cracks grow with incident kinetic energy at a significantly larger rate than do the delaminations. In region B changes in the damage growth rates appears to result in the cracks and delaminations growing at essentially the same rate with respect to impact energy. This seems to suggest that this region marks the transition from a damage mechanism dominated largely by backface cracking to one in which the interlaminar delaminations become more significant. In region C the crack growth rate appears to reduce further coupled with a rapid increase in the delamination growth with incident kinetic energy. This region is also characterised by severe fibre fracture in the material especially in the plies nearest the backface and the shearing of the upper plies near the frontface of the panel. In region D the damage growth rates become essentially zero and the damage sizes appears to oscillate about a constant value. Region D represents the states where the panel has been penetrated through by the indentor (i.e. the indentor was embedded in the panel).

The procedure discussed above was applied to the damage maps for the other panels and similar trends and patterns in the damage assessment data were observed. It could therefore be concluded that the observations and conclusions obtained from Figure 4.35 may apply to the other damage maps as well. Typical projected delamination patterns are shown in Appendix D page 176.

It is interesting to note that the damage patterns observed in regions A, B to C, and D in Figure 4.35 show some correspondence to the states of damage in curves B-C, C-D, and D-E in Figure 4.6 (Refer also to Figure 4.6-1).

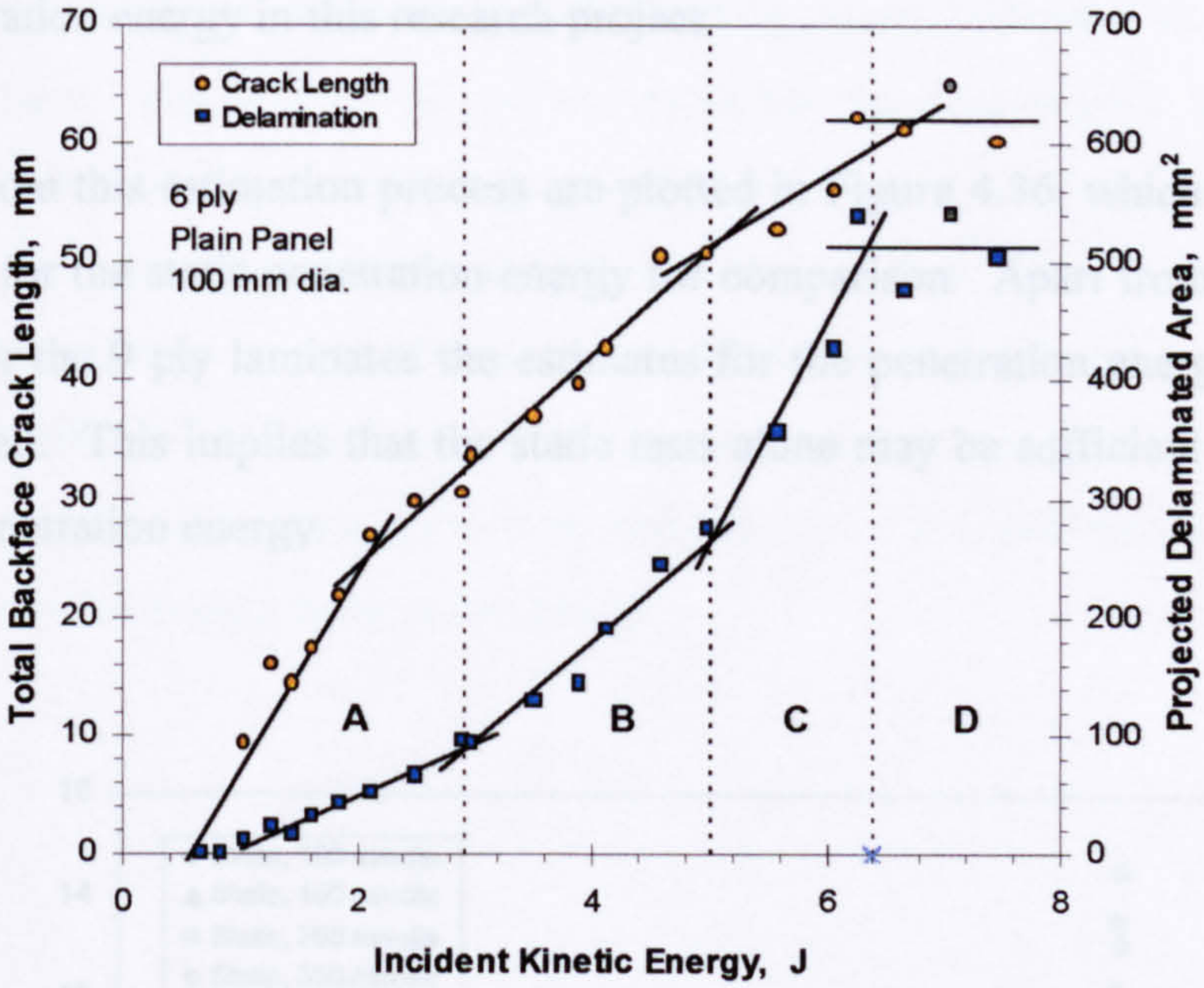

Figure 4.35. Projected delaminated area and total backface crack length for the 6 ply 100 mm diameter panel.

4.4.2 IMPACT PENETRATION

As was discussed in the previous section impact energies at and above the penetration threshold results in a damage size that can practically be taken to be constant with increasing incident energy. This characteristic can be used to estimate the impact penetration energy from the impact damage maps. Using Figure 4.35 as a basis, the impact penetration energy for the 6 ply, 100-mm diameter panel can be estimated from the intersection of the best-fit line through the delamination data in region C and the horizontal line representing the average delamination size in region D. The value of the impact energy at the intersection point can be taken to be the minimum energy required to penetrate the panel. The same analysis can be applied to the crack data in Figure 4.35 to obtain an estimate of the penetration energy, but this was found not to be as consistent as that found by using the delamination data. The reason for this is that the slope of the best-fit line through the crack data in region C is quite small and small changes in this slope results in large changes in the location of the intersection

point. For this reason it is the delamination data that is used in the estimation of the impact penetration energy in this research project.

The results from this estimation process are plotted in Figure 4.36, which also includes the estimates for the static penetration energy for comparison. Apart from some scatter in the data for the 9 ply laminates the estimates for the penetration energies appear to agree very well. This implies that the static tests alone may be sufficient in estimating the impact penetration energy.

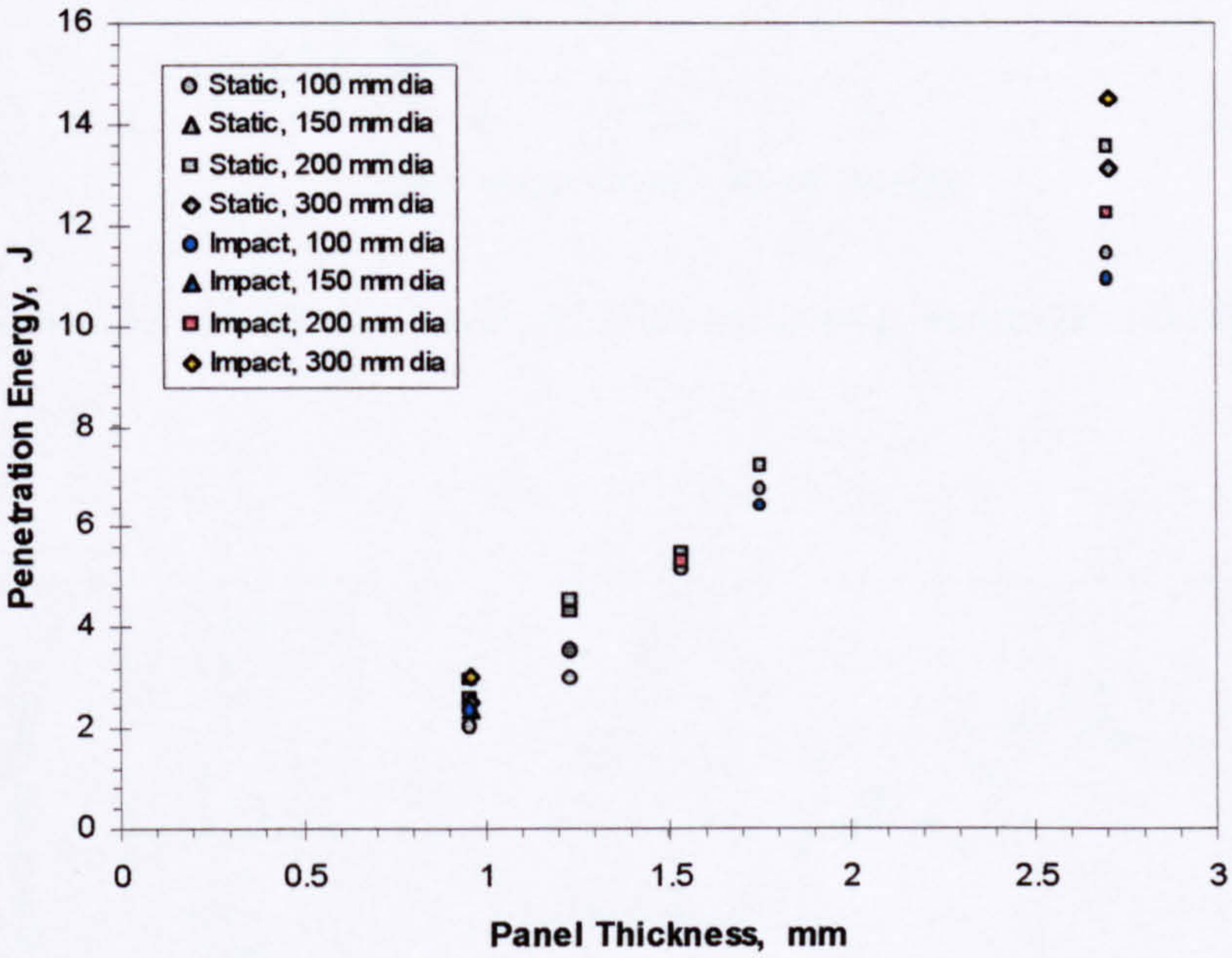

Figure 4.36. Impact and static penetration energies for the plain panels.

Having observed similar trends in the damage maps and having obtained estimates of the penetration energy from the delamination data, the damage maps for the panels were normalised with respect to their corresponding maximum values of damage size and their corresponding values of impact penetration energy. The exception to this procedure is the data on permanent indentation, which was normalised with respect to panel thickness. These were done in order to compare the differing data more easily. The results of this normalisation process are plotted in Figures 4.37 to 4.39.

Figures 4.37 and 4.38 show the normalised data for delaminations and crack lengths and it was quite surprising to discover that all the data points collapsed into narrow and well-defined band. Perhaps it was just fortuitous for the data to have done so but it could very possibly be due to behaviour governed by some laws of similarity. If this is the case, then the impact penetration energy and the maximum possible damage size are important parameters to be considered. From the trend of the band of data in these figures it is possible to identify the regions where the damage mechanism change as was done in Figure 4.35. The data appears to indicate that the transitions occur at about 50% and 80% of the impact penetration energy.

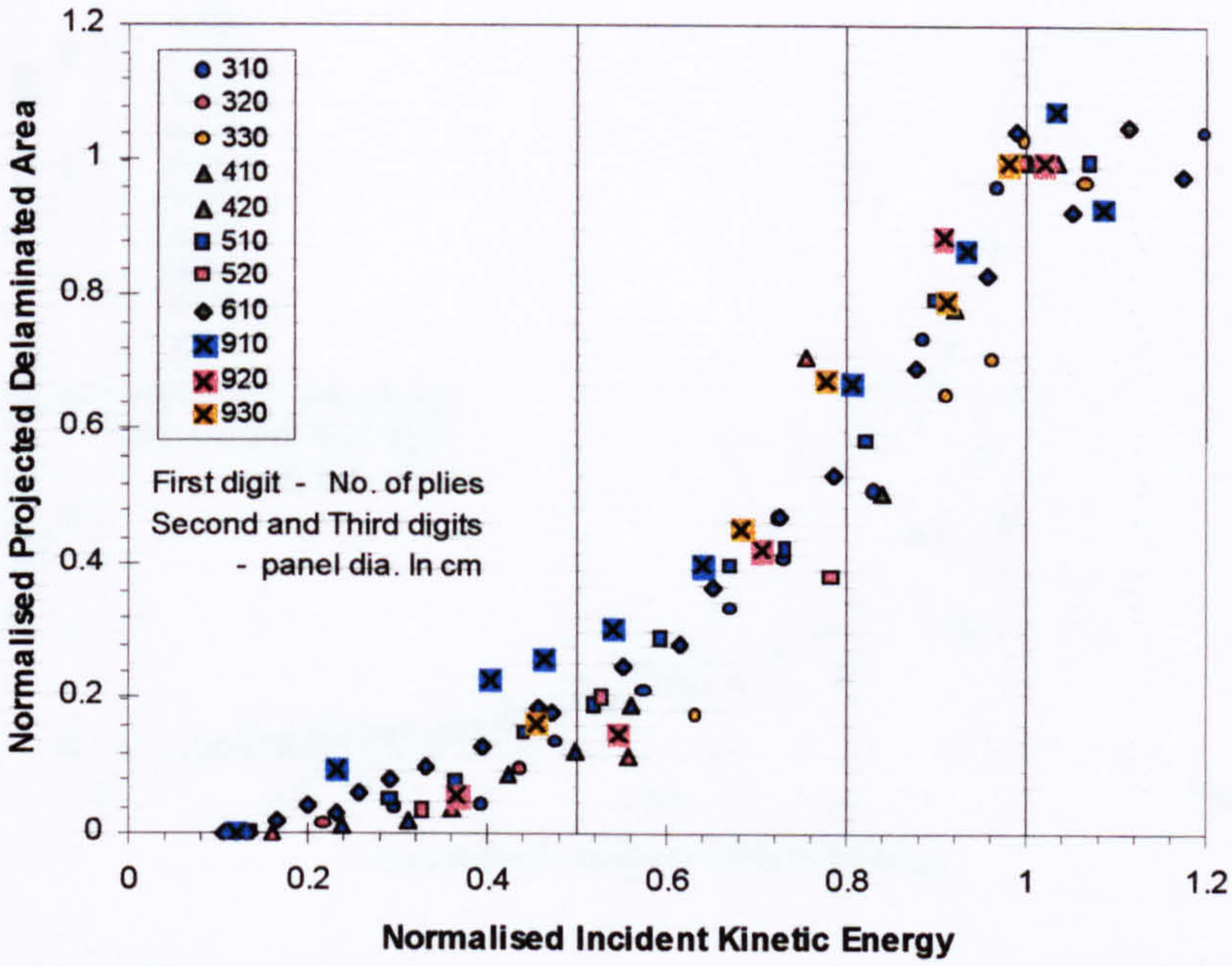

Figure 4.37. Normalised delamination vs. normalised kinetic energy

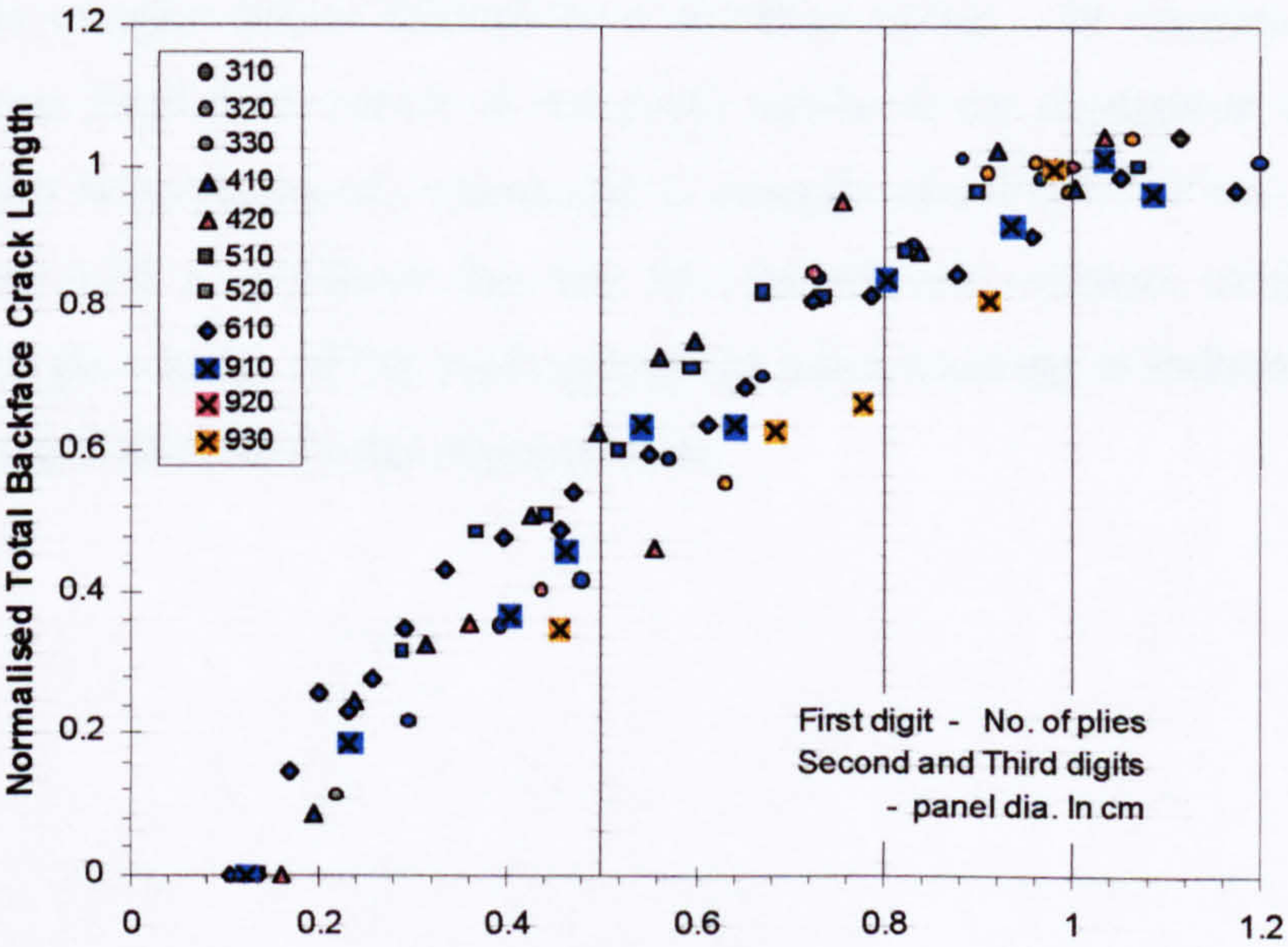

Figure 4.38. Normalised crack length vs. normalised kinetic energy

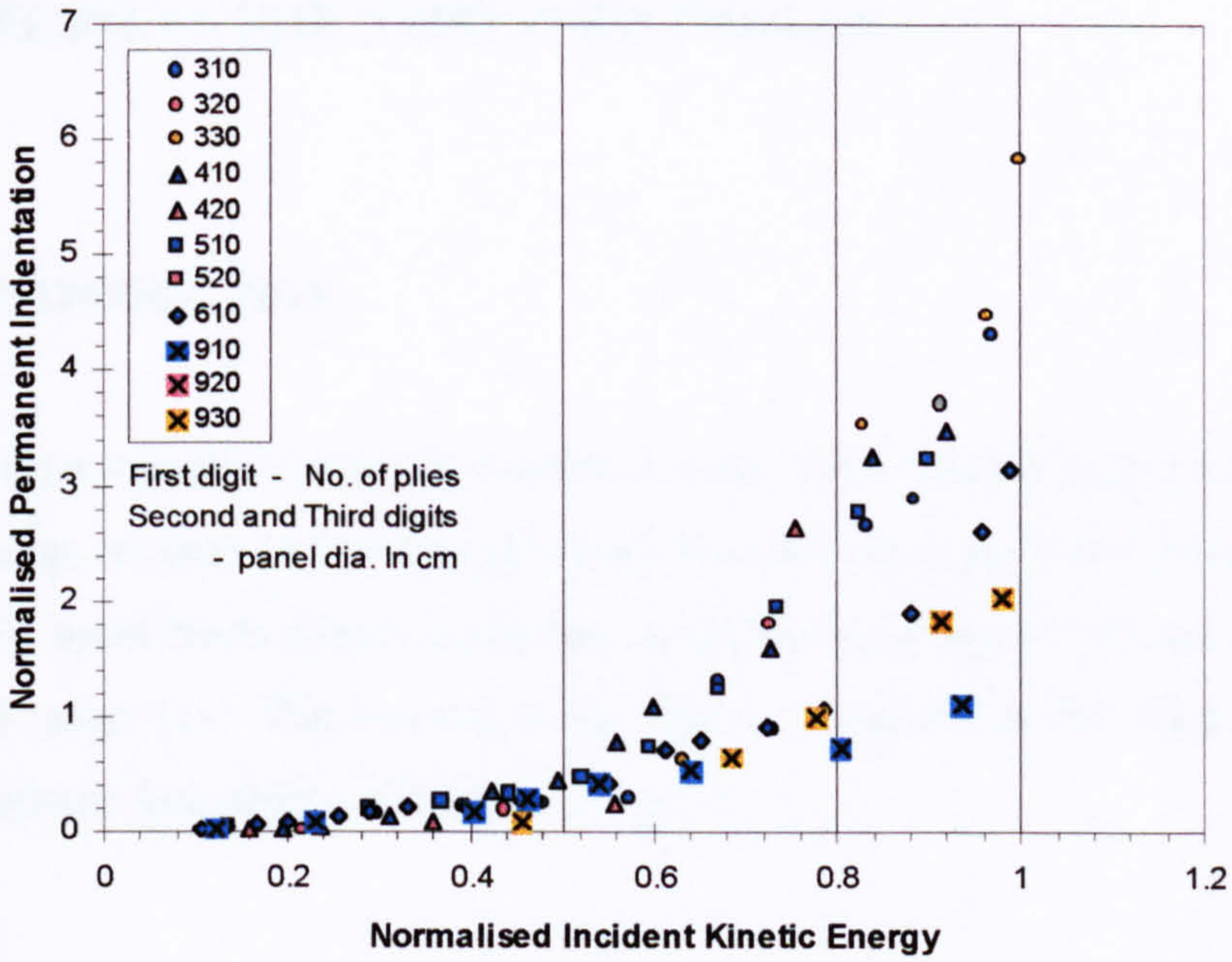

Figure 4.39. Normalised indentation vs. normalised kinetic energy

In Figure 4.39 the normalised indentation data appear to collapse into a narrow band only at impact energies below 50% of the penetration energy. At energies above this value significant local deformation of the panel results in the divergence of the data. This divergence becomes more pronounced at energies above 80% of the penetration energy. Figure 4.39 also shows that the thin panels can undergo extensive local deformation in the vicinity of the load application point resulting in indentations up to six times the panel thickness prior to penetration.

5 RESULTS FOR STIFFENED PANELS

5.1 INTRODUCTION

This chapter discusses the results obtained from tests conducted on 3 ply blade-stiffened panels and compares them with those obtained from the plain panels of similar size and thickness. The multi-blade panels tested have a stiffener spacing of 100 mm (see Figure 3.1, Chapter3, page 31). The legends in the figures presented in this chapter uses the data coding system described in Chapter 3, page 32.

5.2 STATIC LOADING RESPONSE

The static load-deflection characteristics of a 100-mm diameter panel loaded on the stiffener and a 150-mm diameter panel loaded in the bay are shown in Figures 5.1 and 5.2 respectively. Examination of these figures reveal that the effect of the stiffeners on the static loading response depends on where the load is applied relative to the stiffeners. Referring to Figure 5.1, we find that when the load is applied directly above the stiffener blade the stiffener largely dominates the initial response and the load-deflection response is essentially linear. As the indentor is driven further into the panel the resulting force attains a value that causes rapid failure of the blade resulting in the sudden loss of panel stiffness which manifest itself as the severe discontinuity (point 1 in Figure 5.1) in the curve. The blade or web of the stiffener failed via a vertical crack running from its free edge to its root. Driving the indentor beyond the failure point of the stiffener again results in the increase of the load with indentor displacement until failure of the panel skin occurs at which the force seems to level out at some maximum value. Driving the indentor even further results in the penetration of the panel with the load decreasing as the indentor displacement is increased.

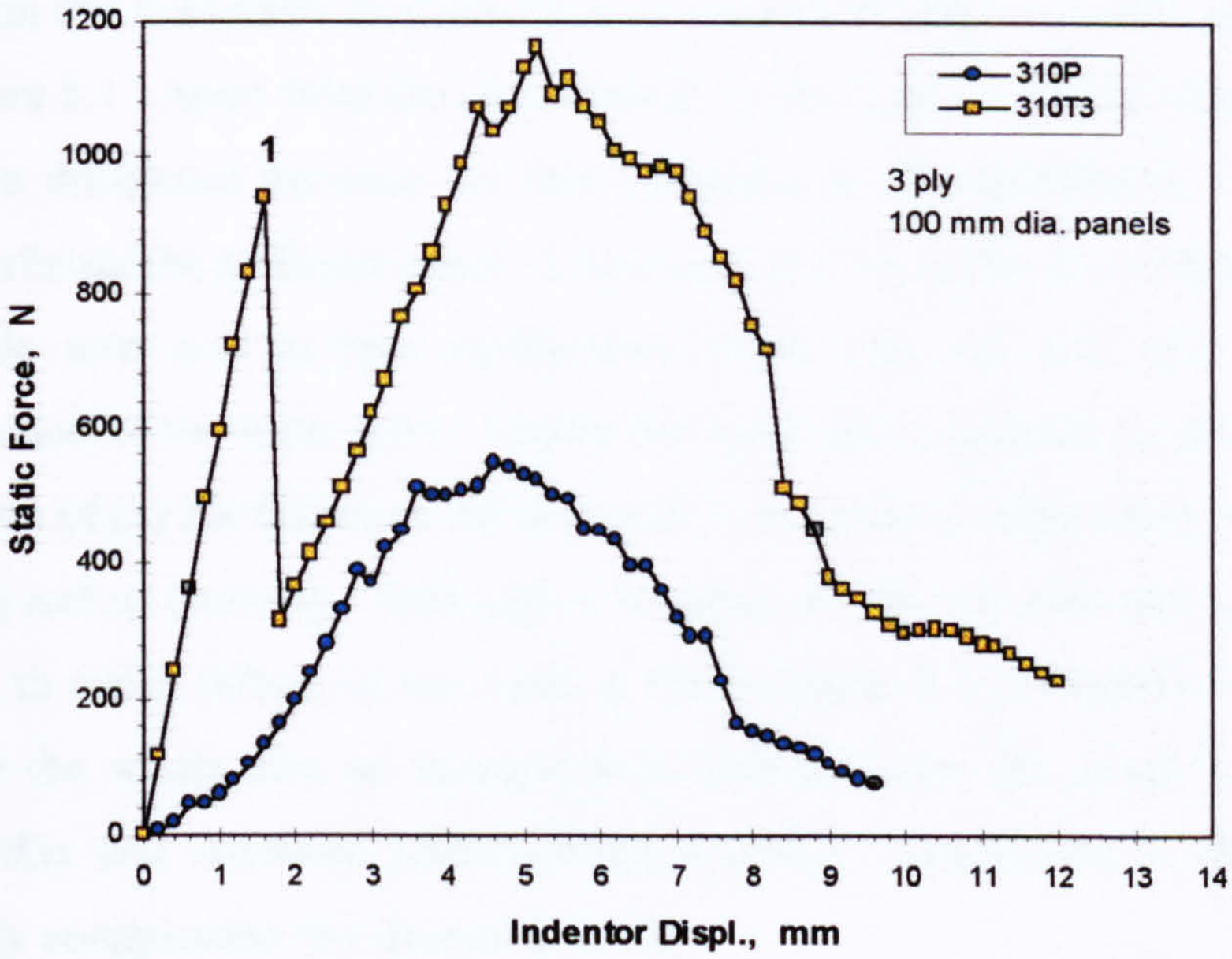

Figure 5.1. Static load-deflection response for the 100-mm diameter plain and stiffened panel

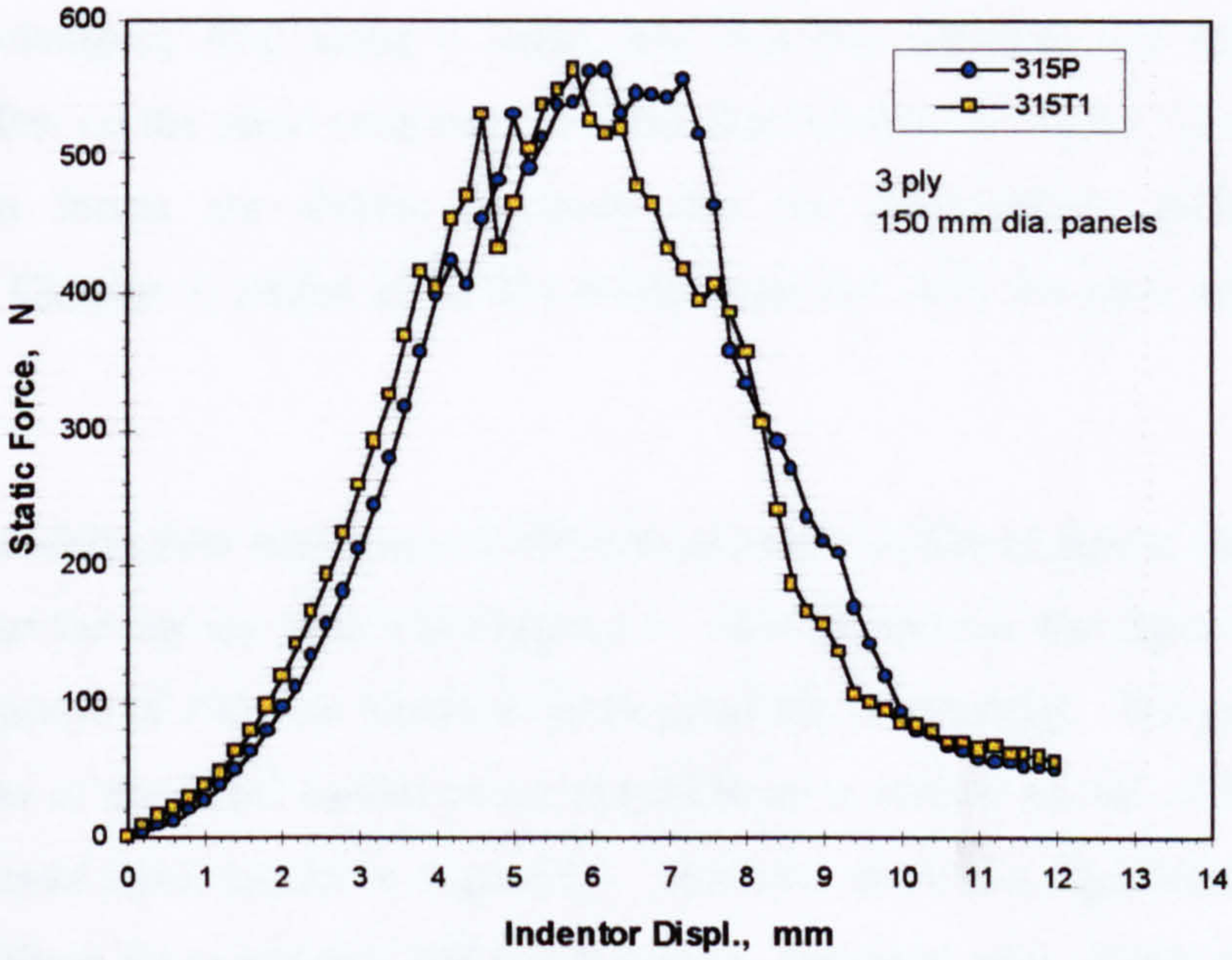

Figure 5.2. Static load-deflection response for the 150-mm diameter plain and stiffened panel

For comparison the load-deflection response of a 100-mm diameter plain panel is also shown in Figure 5.1. Apart from the discontinuity in the response of the stiffened panel, the other main difference between the two responses is the significantly larger force required to perforate the stiffened panel. The reason for this is that the stiffener with the fractured blade now acts as two cantilevered beams that are still able to carry a significant portion of the static load. Unlike the plain panel perforation now occurs as the combination of (1) the failure of the skin and (2) the failure of the fractured blade by local buckling and or crushing. Although it is apparent that it would take considerably larger energy to cause failure of the panel at the stiffener it is a situation that is best avoided since the whole idea of incorporating stiffeners into the panel is to provide structural rigidity and increased load carrying capacity. Any failure in the stiffeners would severely compromise this design criterion.

The load-deflection response of a 150-mm diameter stiffened panel loaded in the bay and that of a plain panel of the same size are shown in Figure 5.2. Apart from the apparently stiffer response of the stiffened panel there is almost no difference between the two curves. It may be the fact that the stiffeners are only 25 mm away from the edge of the clamping ring along a radial line that the stiffeners are not having a significant effect on the panel response. Further examination of Figure 5.2 reveals that the maximum forces are similar implying that the delamination initiation force (discussed in Chapter 2, pages 22 to 23) is the same for both the plain and stiffened panel.

The static load-deflection responses of 300-mm diameter stiffened panels loaded on the stiffener and on the bay are shown in Figure 5.3. Also included in the figure is the load-deflection response of 300-mm diameter plane panel for comparison. The general trend of the response of the panel loaded above the stiffener is similar to that of the 100-mm diameter stiffened panel shown in Figure 5.1. However there is a significant difference in the blade failure force and this difference will be discussed later in this section. For the panel loaded in the bay the effect of the stiffeners gives a load-deflection response that is noticeably stiffer than that for the plain panel. Again we find that the maximum

force is similar to that in the plain panel, agreeing with observations made in the 150-mm diameter panels discussed previously.

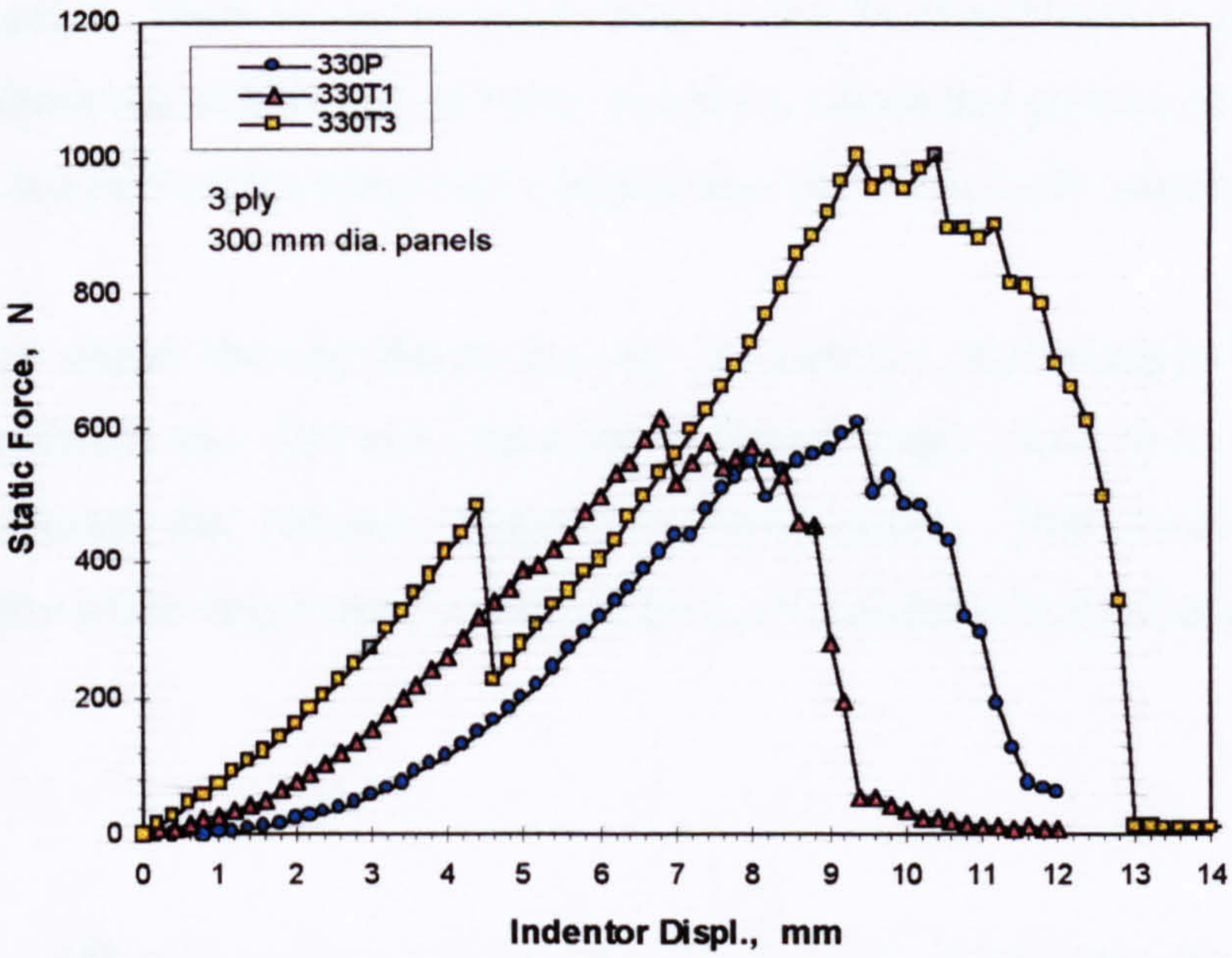

Figure 5.3. Static load-deflection response for the 300-mm diameter plain and stiffened panel

Figure 5.4 compares the load-deflection responses of 100-mm diameter and 300-mm diameter stiffened panels loaded above the stiffener. The most significant difference between the two responses is the failure of the stiffener blade in the larger panel at a much lower value of static force. It appears that the effect of increasing the panel size is to reduce the failure load of the stiffener. This can be explained by considering the stiffener alone as a beam that is cantilevered at both ends. For a concentrated load P in the mid-span of such a beam, elementary beam theory dictates that the maximum bending moment will occur at the mid-span and at the cantilevered ends. Because of this and because of the geometry of the stiffener, which in this case may be approximated by a T section, the maximum tensile stress will be found in the outermost fibre of the web or blade under the load application point. Keeping the load P constant and increasing the span of the beam proportionately increases the maximum bending

moment and therefore the maximum tensile stress. Failure of the blade occurs when the maximum tensile stress exceeds the tensile strength of the material. These are the reasons why the blades in the stiffened panels fails in the manner mentioned above and why the blade in the larger panel fails at a much lower applied load than does the blade in the smaller panel. There is also reason to believe that the failed blade in the stiffened panel loaded above the stiffener is still able to carry a substantial portion of the applied load resulting in a perforation force that is higher than that for a 3-ply, plain panel.

Figure 5.4 also shows the significant increase in indentor displacement required to completely perforate the 300-mm diameter stiffened panel over that required to completely perforate the 100-mm diameter stiffened panel. This could imply the increasing ability of the larger panel to absorb more energy than the smaller panel.

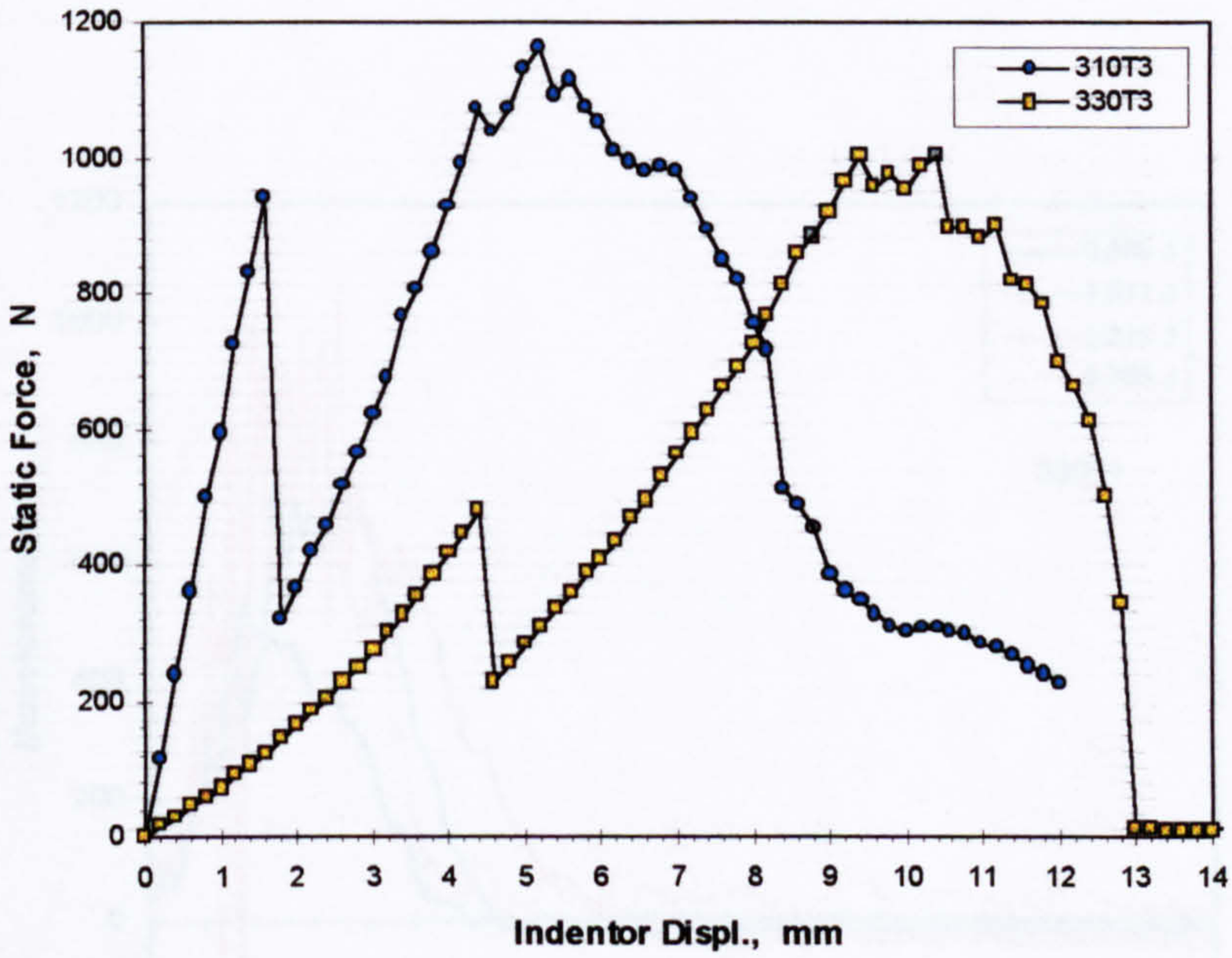

Figure 5.4. Static load-deflection response for the stiffened panels loaded on the stiffener

5.3 IMPACT RESPONSE

5.3.1 IMPACT BETWEEN THE STIFFENERS

The accelerometer force history, load cell force history and displacement history for the 300-mm diameter, stiffened panels impacted on the bay are shown in Figures 5.5, 5.6 and 5.7 respectively. The accelerometer force history in Figure 5.5 displays the same high frequency, high amplitude oscillations brought about by impulsive loading that was also observed in the impact data for the plain panels (see Figures 4.21 to 4.23 in pages 65 and 66 of Chapter 3). From the load cell force history in Figure 5.6 it is apparent that for impact energies at and above 1.517 J, the forces generated are at the level of the delamination initiation force resulting in the creation of substantial damage in the panel and in the levelling-out of peak forces.

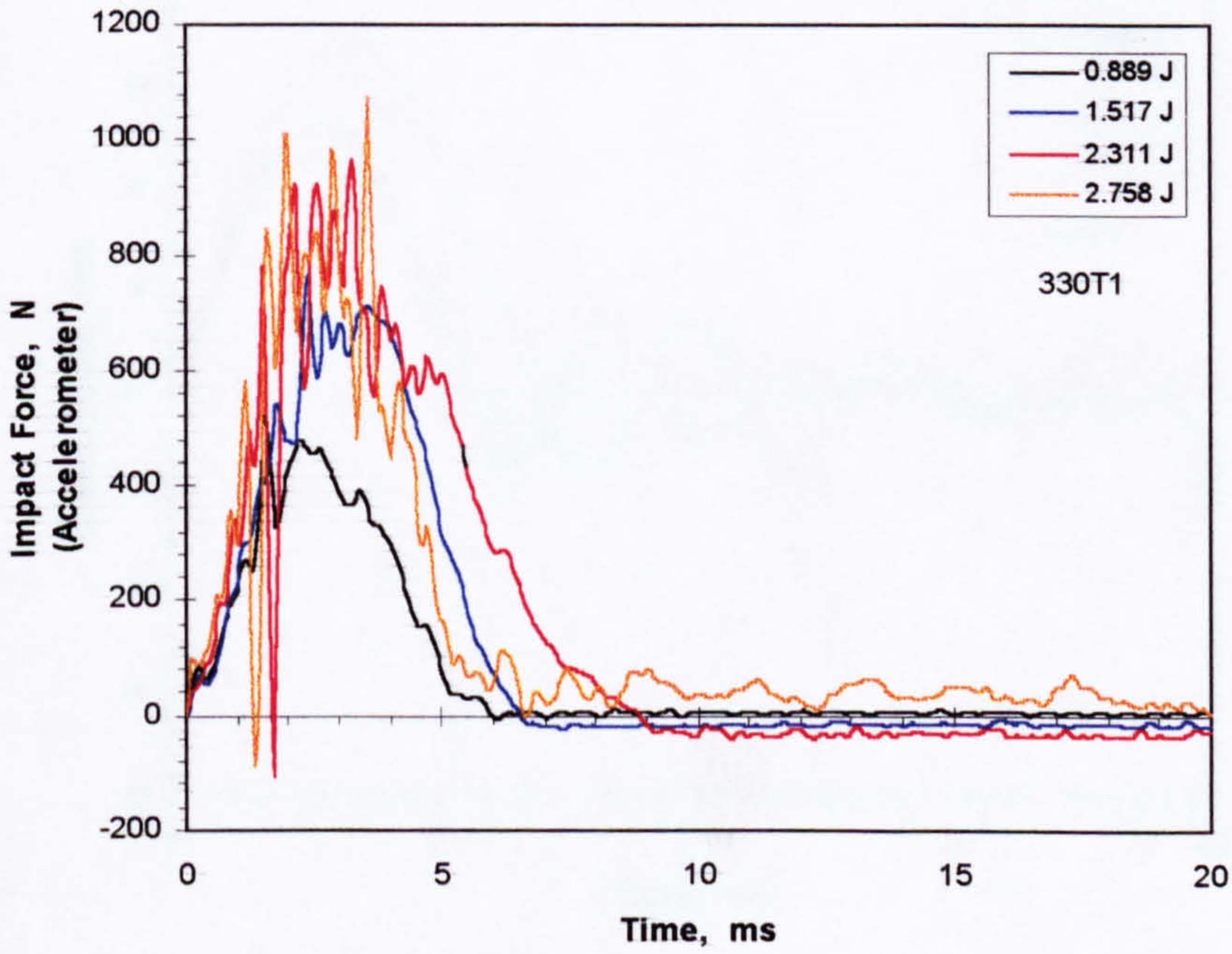

Figure 5.5. Accelerometer force history for the 300-mm diameter panels impacted on the bay

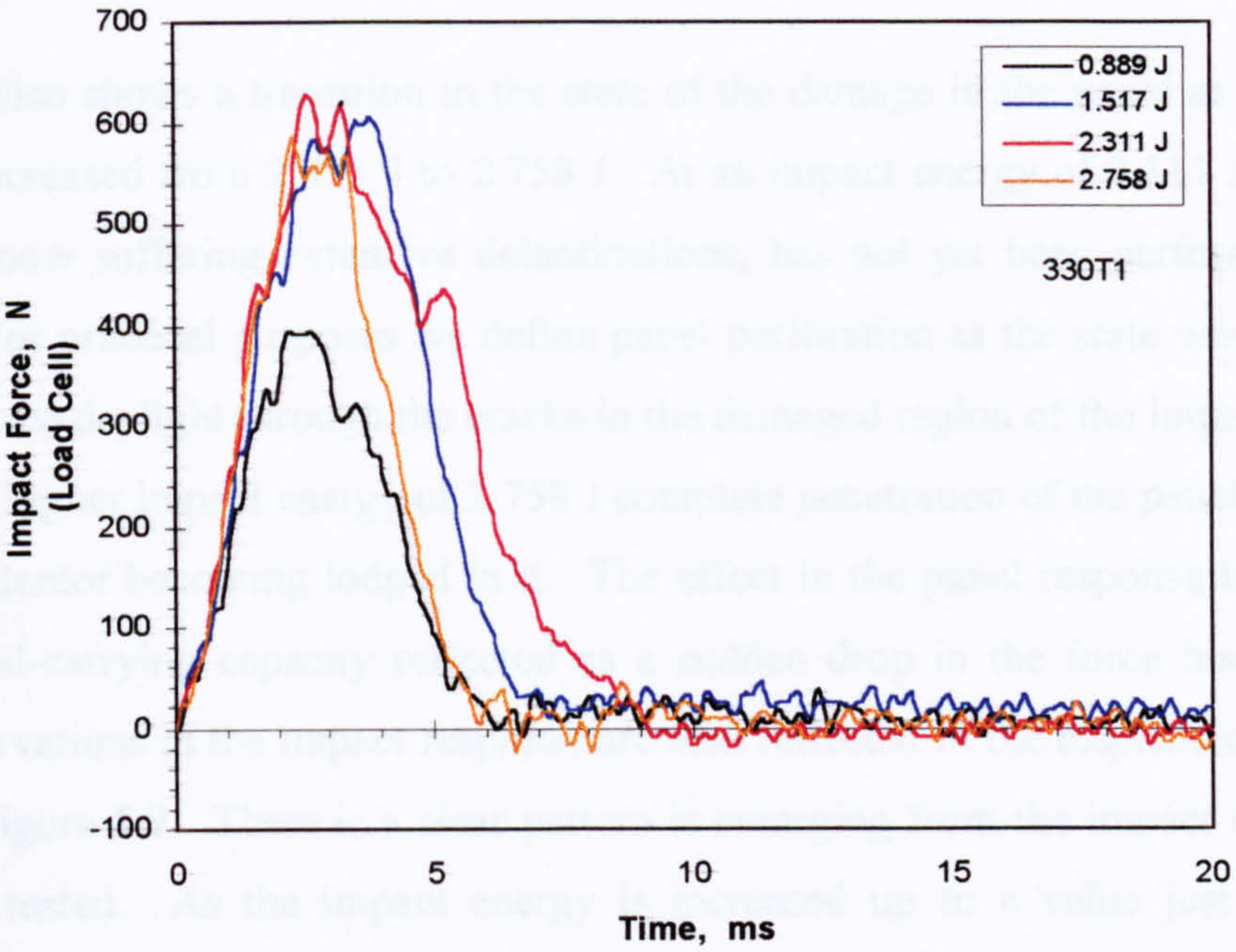

Figure 5.6. Load cell force history for the 300-mm diameter panels impacted on the bay

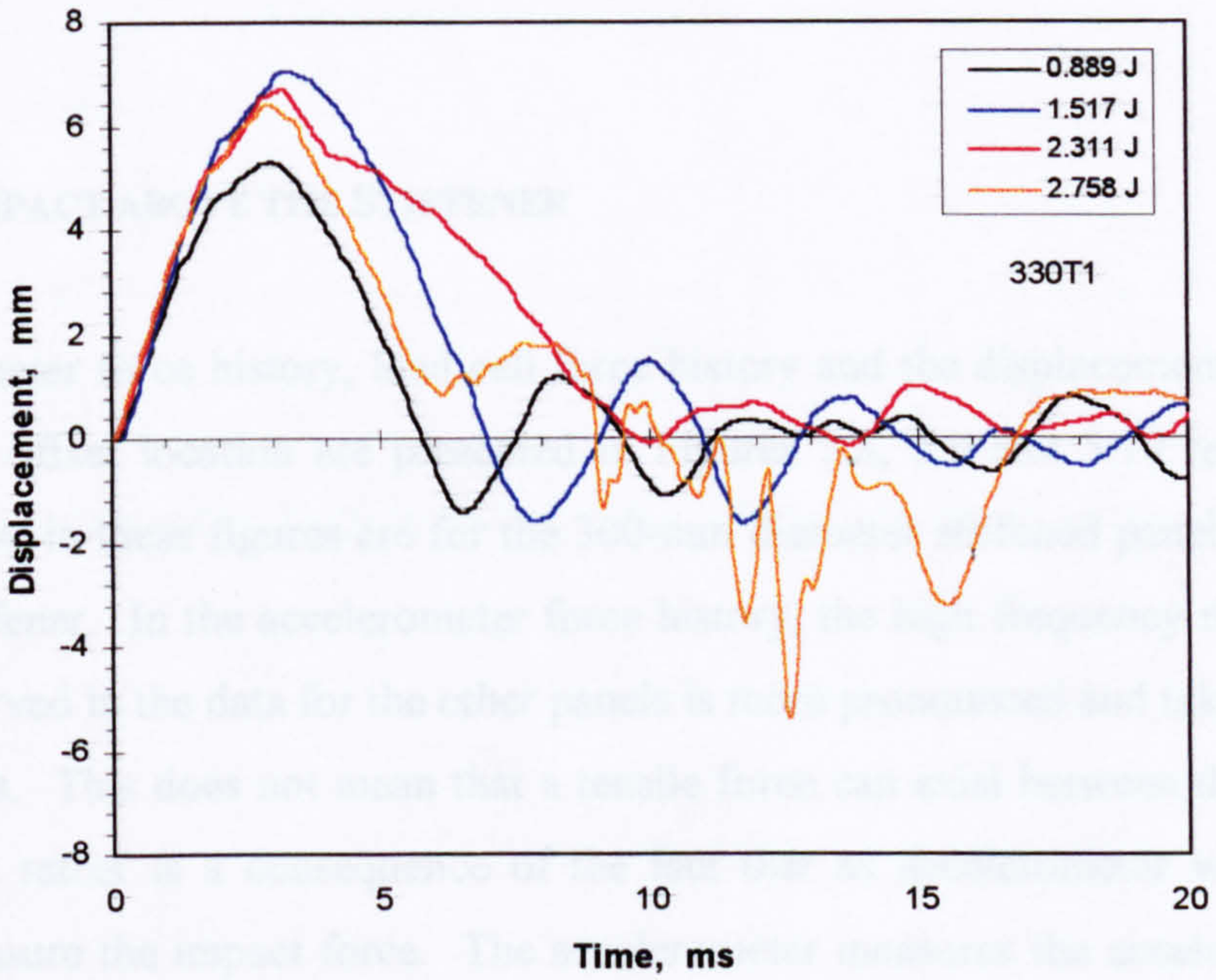

Figure 5.7. Displacemment history for the 300-mm diameter panels impacted on the bay

Figure 5.6 also shows a transition in the state of the damage in the panel as the impact energy is increased from 2.331 J to 2.758 J. At an impact energy of 2.311 J the panel, though by now suffering extensive delaminations, has not yet been perforated by the indentor. For practical purposes we define panel perforation as the state where you are just able to see daylight through the cracks in the damaged region of the impacted panel. At the next higher impact energy of 2.758 J complete penetration of the panel is attained with the indentor becoming lodged in it. The effect in the panel response is an abrupt drop in load-carrying capacity reflected as a sudden drop in the force history curve. These observations in the impact response are also reflected in the displacement history shown in Figure 5.7. There is a clear pattern is emerging from the impact response of the panels tested. As the impact energy is increased up to a value just below the perforation threshold, the impact duration increases and so do the peak forces developed. The peak forces become limited to a maximum value as delaminations in the panel become the significant mode of damage. Above the perforation energy the impact duration suddenly decreases and a new dynamic mode is created resulting from the imbedding of the indentor in the panel.

5.3.2 IMPACT ABOVE THE STIFFENER

The accelerometer force history, load cell force history and the displacement history at the IR sensor offset location are presented in Figures 5.8, 5.9 and 5.10 respectively. The data shown in these figures are for the 300-mm diameter stiffened panels impacted above the stiffener. In the accelerometer force history, the high frequency ringing that was also observed in the data for the other panels is more pronounced and takes on large negative peaks. This does not mean that a tensile force can exist between the indentor and panel but rather is a consequence of the fact that an accelerometer was used to indirectly measure the impact force. The accelerometer measures the acceleration of a mass resulting from net force acting on it. The significant ringing in the accelerometer force history is the result of the sudden failure of the stiffener blade that causes an equally sudden loss in the panel stiffness. This abrupt loss in panel stiffness constitutes

a very sharp impulsive load change that excites some of the high frequency modes of the indentor assembly that could create negative spikes in the accelerometer signal.

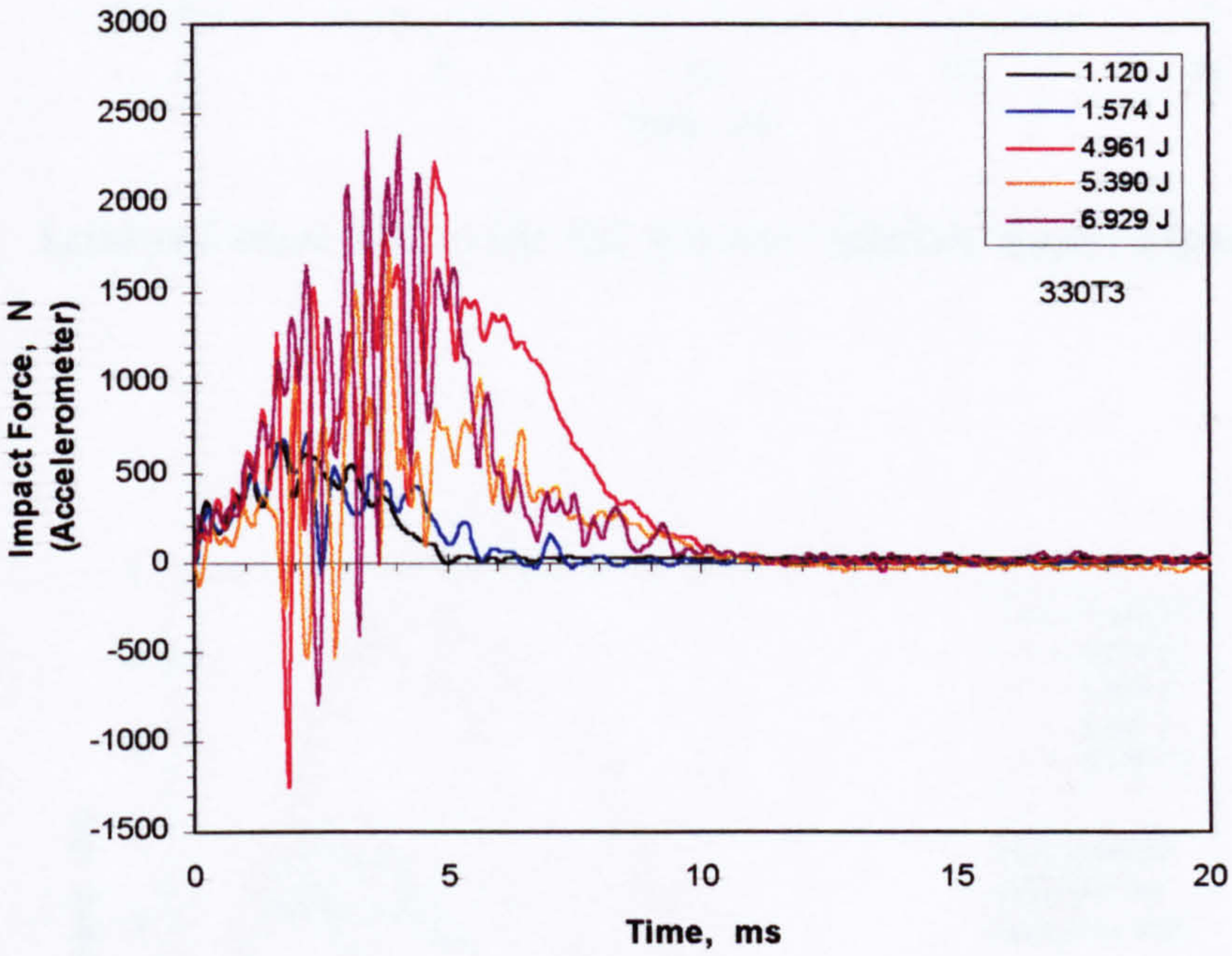

Figure 5.8. Accelerometer force history for the 300-mm diameter panels impacted on the stiffener

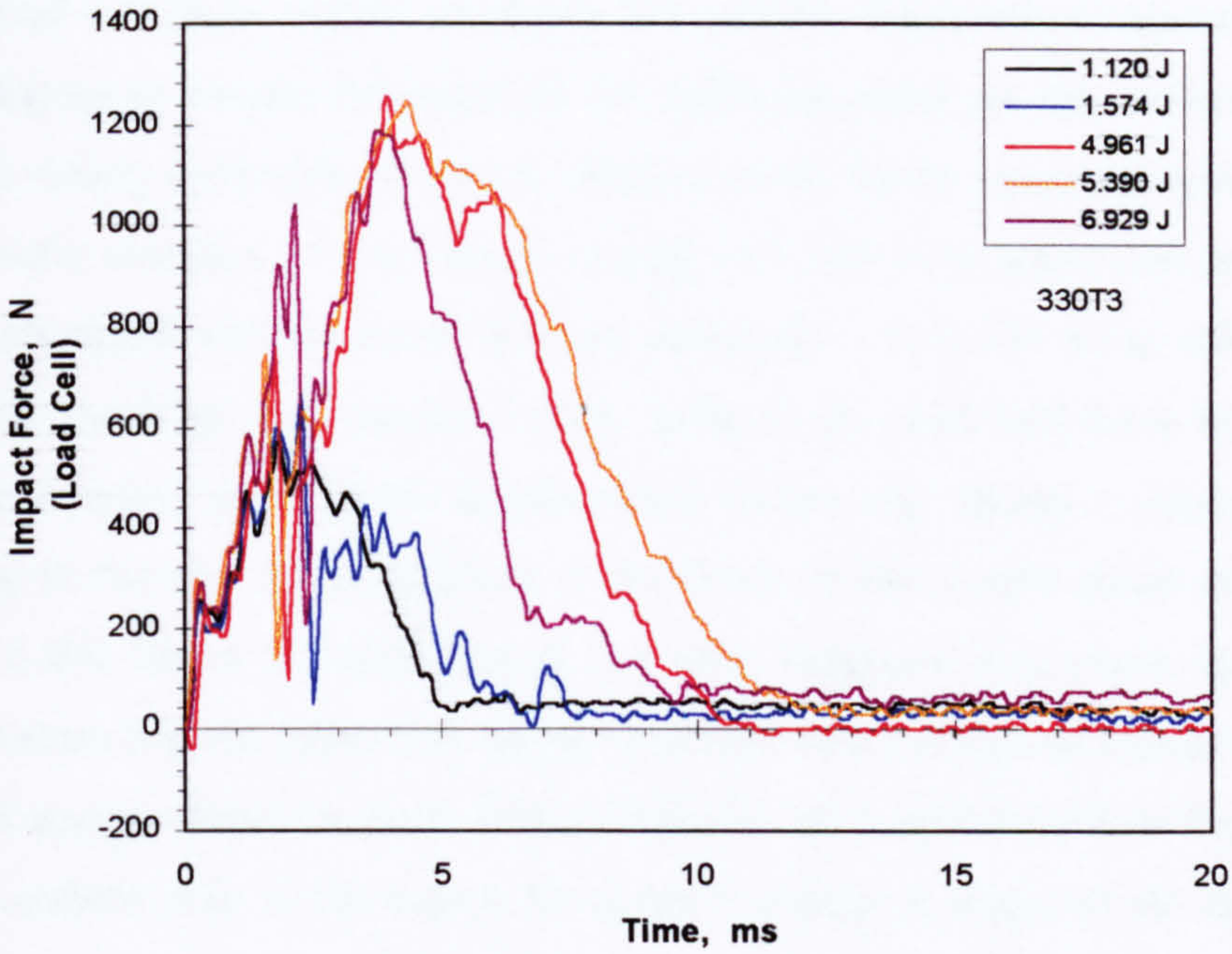

Figure 5.9. Load cell force history for the 300-mm diameter panels impacted on the stiffener.

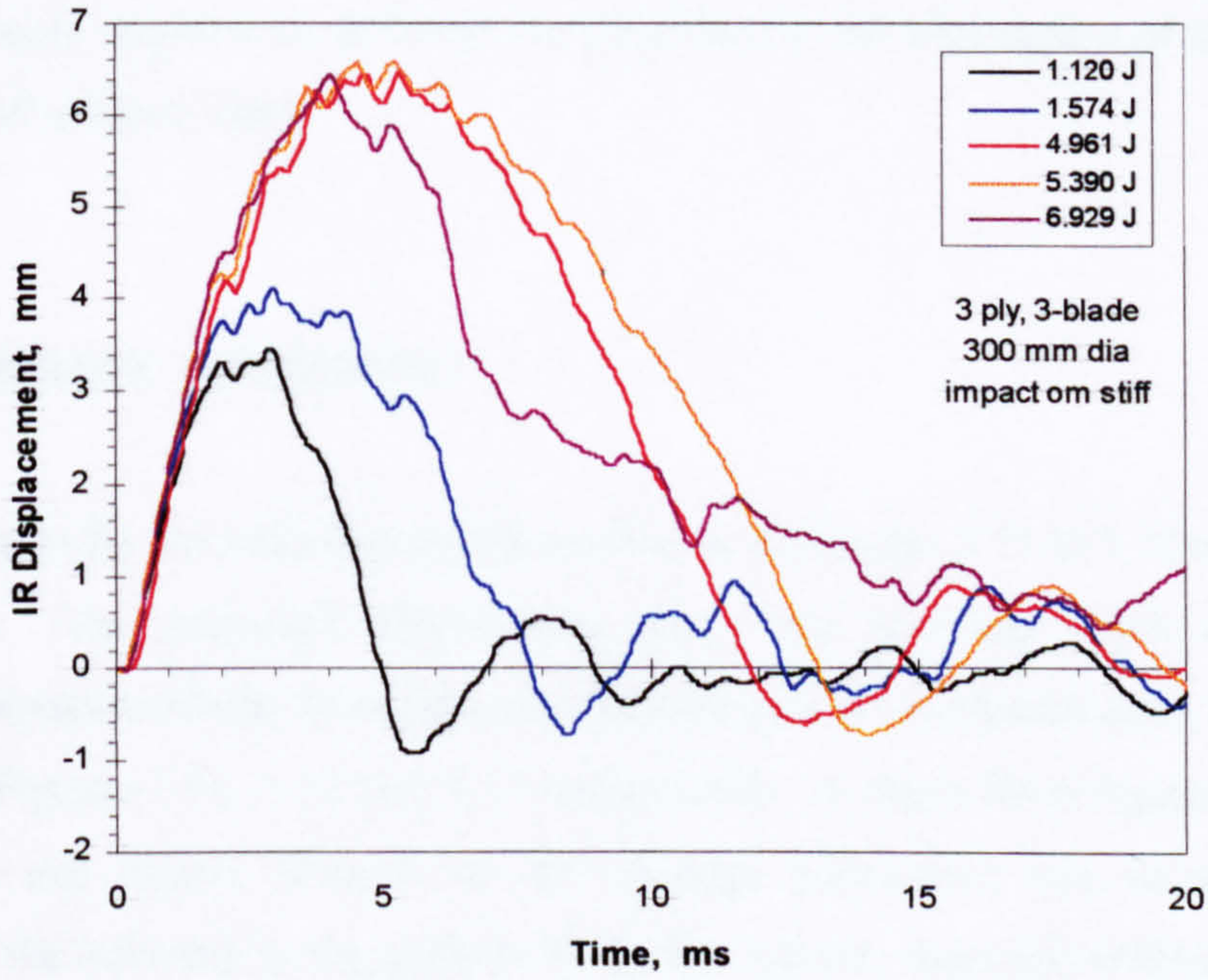

Figure 5.10. IR displacement history for the 300-mm diameter panels impacted on the stiffener.

From the load cell force history in Figure 5.9 and the displacement history in Figure 5.10 the change in impact response of the stiffened panel as the impact energy is increased is clearly discernible from the changes in the traces representing the different incident kinetic energies. At an impact energy of 1.120 J the panel skin and stiffener are both undamaged and the panel deforms elastically. At 1.574 J the stiffener blade fails abruptly resulting in a negative going spike in the load cell force history. The slope of the rebound phase in the displacement history also shows a reduced absolute slope owing to the loss of contribution of the blade to the overall panel stiffness. At 4.961 and 5.390 Joules the peak forces and peak displacements reach their limiting maximum values and the panel skin begins to experience substantial damage. At 6.929 J, an impact energy above the perforation threshold, the sudden breach of the panel skin results in a sudden drop in the impact force and a change in shape of the displacement trace from a concave downward shape to a concave upward shape. All these observations on the impact response are similar to those for the plain panels (see Figures 4.21 to 4.25 in Chapter 4) and to those for the stiffened panels impacted in the bay (see Figures 5.5 to 5.7). The only exceptions were the negative going spike in the force history corresponding to the failure of the stiffener blade and the significantly higher peak forces required to perforate the panel due to the obstruction of the indentor by the fractured stiffener blade.

5.4 DAMAGE ASSESSMENT

The damage maps for the stiffened panels are shown in Figures 5.11 to 5.13 and Figures 5.15 to 5.18. The projected delaminated area, total backface crack length and permanent indentation of the front face were plotted against incident kinetic energy and are shown in Figures 5.11, 5.12 and 5.13 respectively. In these three figures the effect of panel size and impact location on the damage parameters can be seen. The obstruction of the indentor by the stiffener blade for impacts above the stiffener (330T3) results in an average maximum delaminated area smaller than that for the other panels whilst the average maximum total backface crack lengths appear to be the same for all the panels. The obstruction of the indentor by the stiffener also results in the significant

increase of the impact energy required to perforate the 300-mm diameter stiffened panel even though the stiffener blade failed at an impact energy of less than 2 Joules.

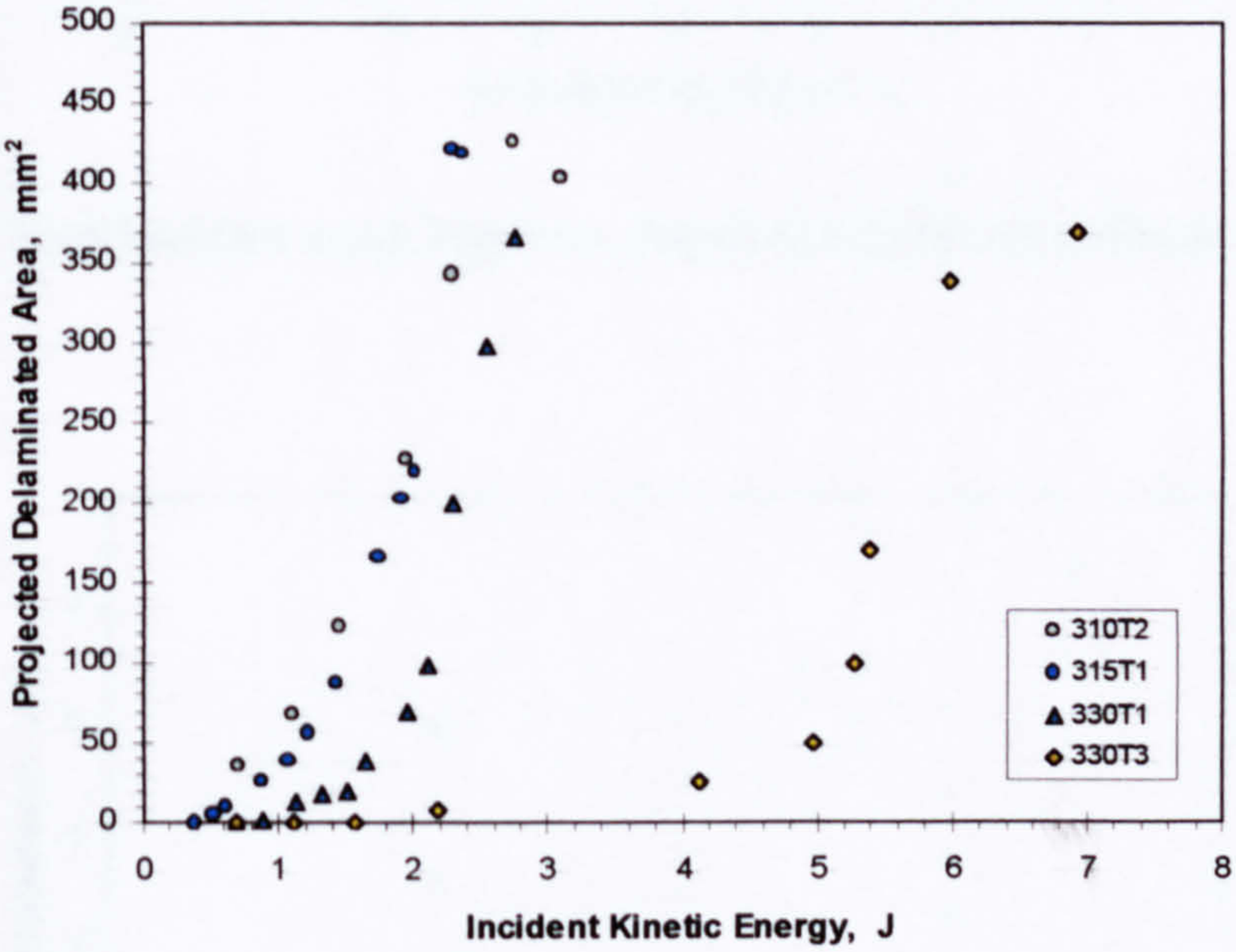

Figure 5.11. Projected delaminated area vs. impact energy for the stiffened panels.

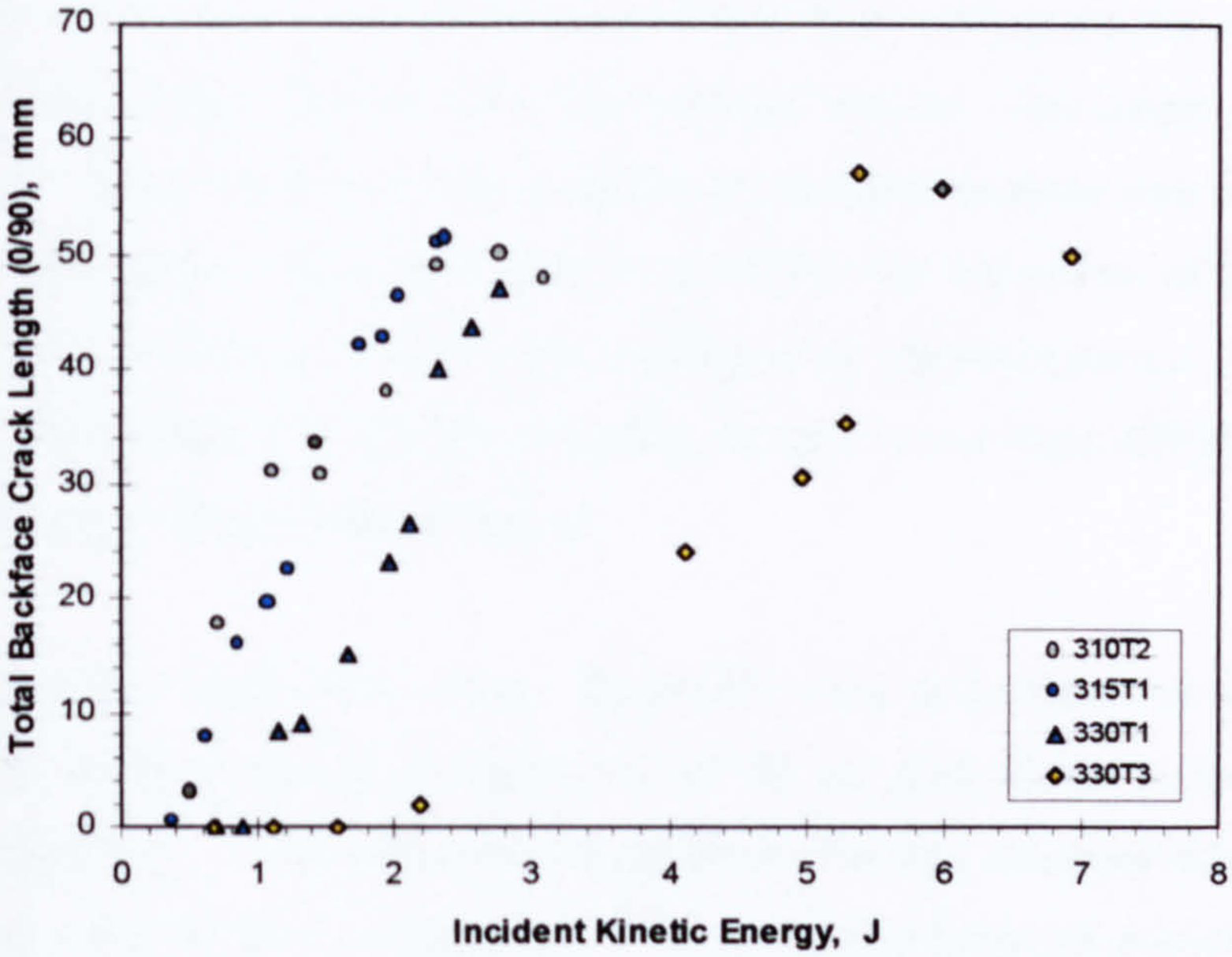

Figure 5.12. Total backface crack length vs. impact energy for the stiffened panels.

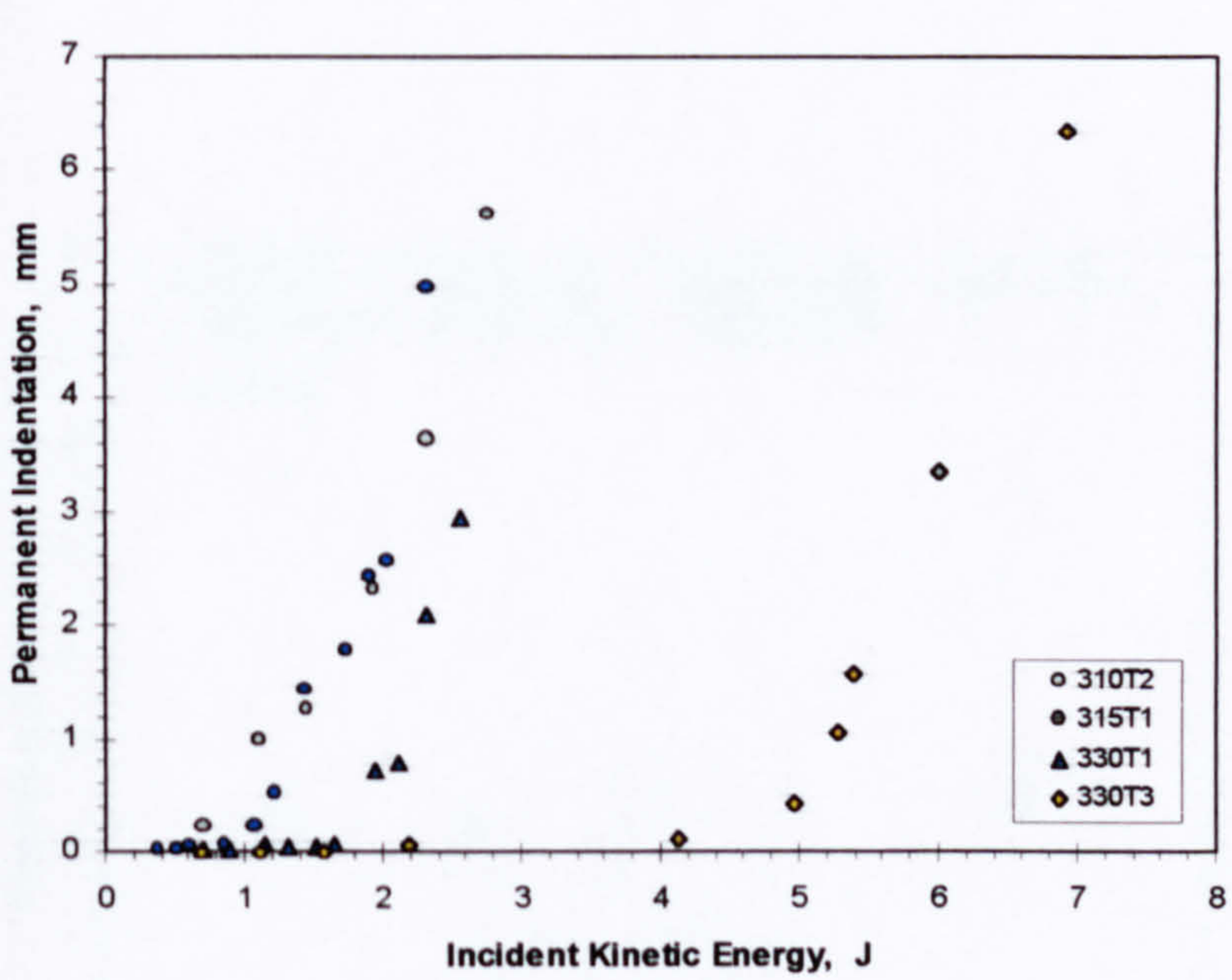

Figure 5.13. Permanent indentation vs. impact energy for the stiffened panels.

For impacts in the bay (315T1 and 330T1), the effect of increasing the panel size results in a more compliant panel that can store more elastic energy. The larger panel would therefore require larger incident kinetic energies to produce the same size of damage as that in the smaller panel. It is interesting to note that the behaviour of the stiffened panels impacted in the bay is similar to that exhibited by the plain panels. For impacts on the toe of the stiffener (310T2) the resulting damage is not very different from the 150-mm diameter panel impacted in the bay.

The static and impact penetration energy thresholds were determined for the stiffened panels using the methods discussed and employed for the plain panels in Sections 4.2.3 and 4.4.2 in Chapter 4. The static penetration threshold was obtained from the static load-deflection curve whilst the impact penetration threshold was determined from the delamination damage maps. These energy thresholds are plotted against panel diameter in Figure 5.14. This figure shows (where data are available) that the impact energy thresholds are only slightly higher than the static energy thresholds for panels of the same diameter.

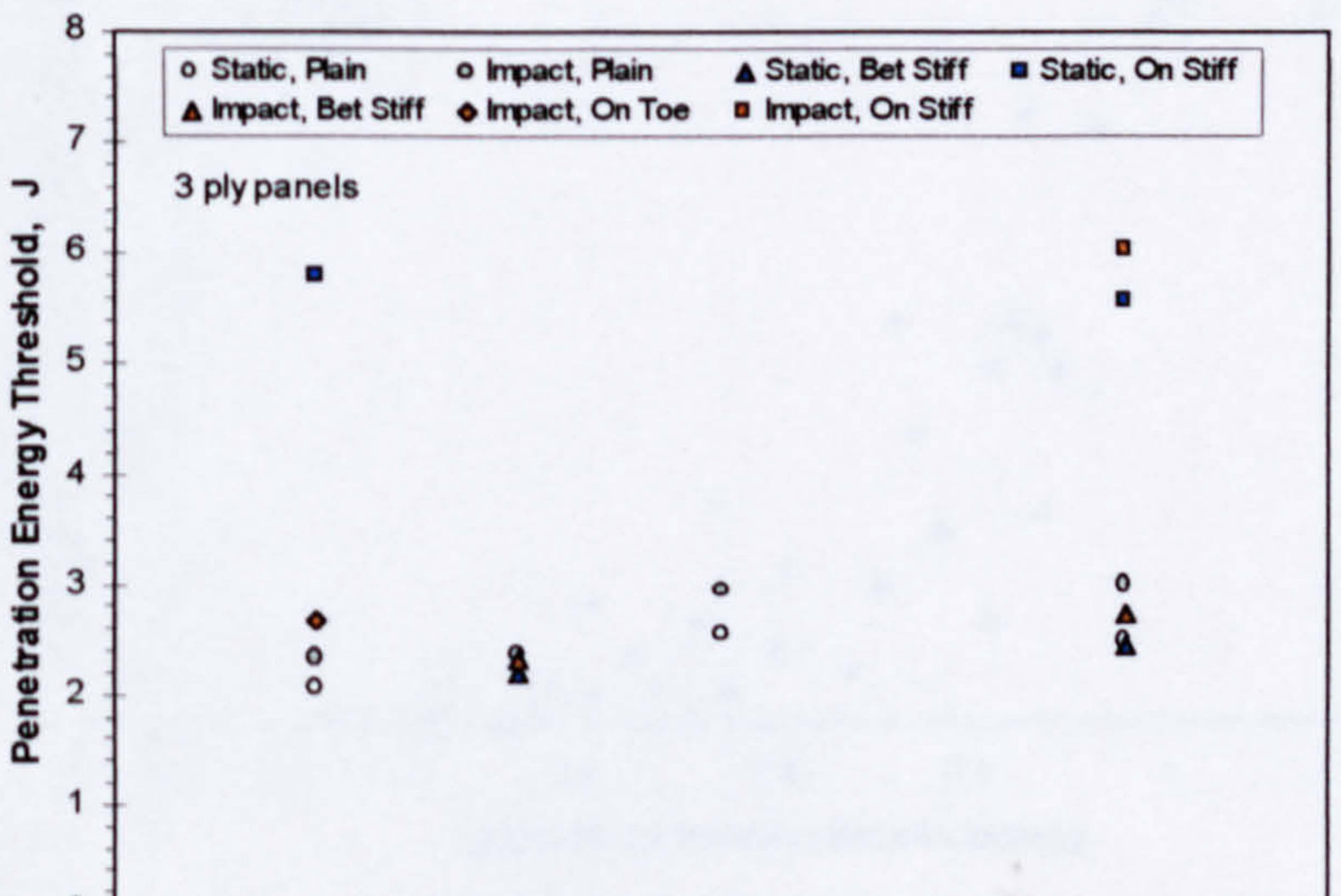

Figure 5.14. Penetration energy thresholds for the stiffened panels. Results for the plain panels are also shown for comparison.

Referring to Figure 5.14, for panel loads applied above the stiffener (310T3 and 330T3) the energy thresholds are much higher owing to the significant portion of the elastic energy stored in the stiffener. It was also surprising to find that, for the panels loaded above the stiffener, there is little difference between the static penetration thresholds even though the panel diameters differ by a factor of three. We can conclude from Figure 5.14 that the static penetration threshold is an accurate estimate of the impact penetration threshold at least for the 150-mm diameter and 300-mm diameter stiffened panels tested.

Using the information presented in Figure 5.14 and employing the damage data normalisation procedure discussed in Chapter 4 Section 4.4.2, normalised damage maps for the stiffened panels were generated. These normalised damage maps are presented in Figures 5.15 to 5.17.

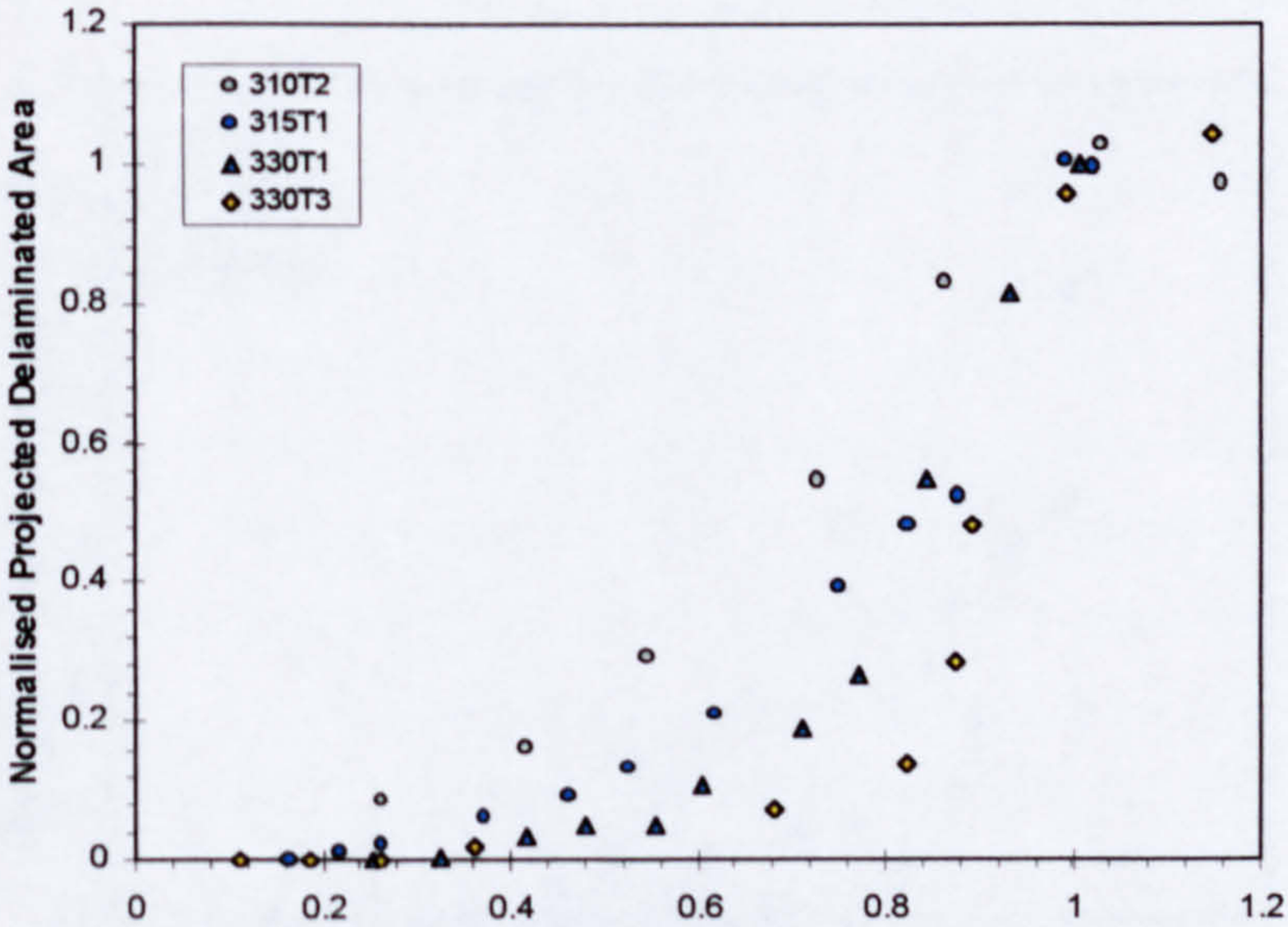

Figure 5.15. Normalised projected delaminated area vs. normalised impact energy for the stiffened panels.

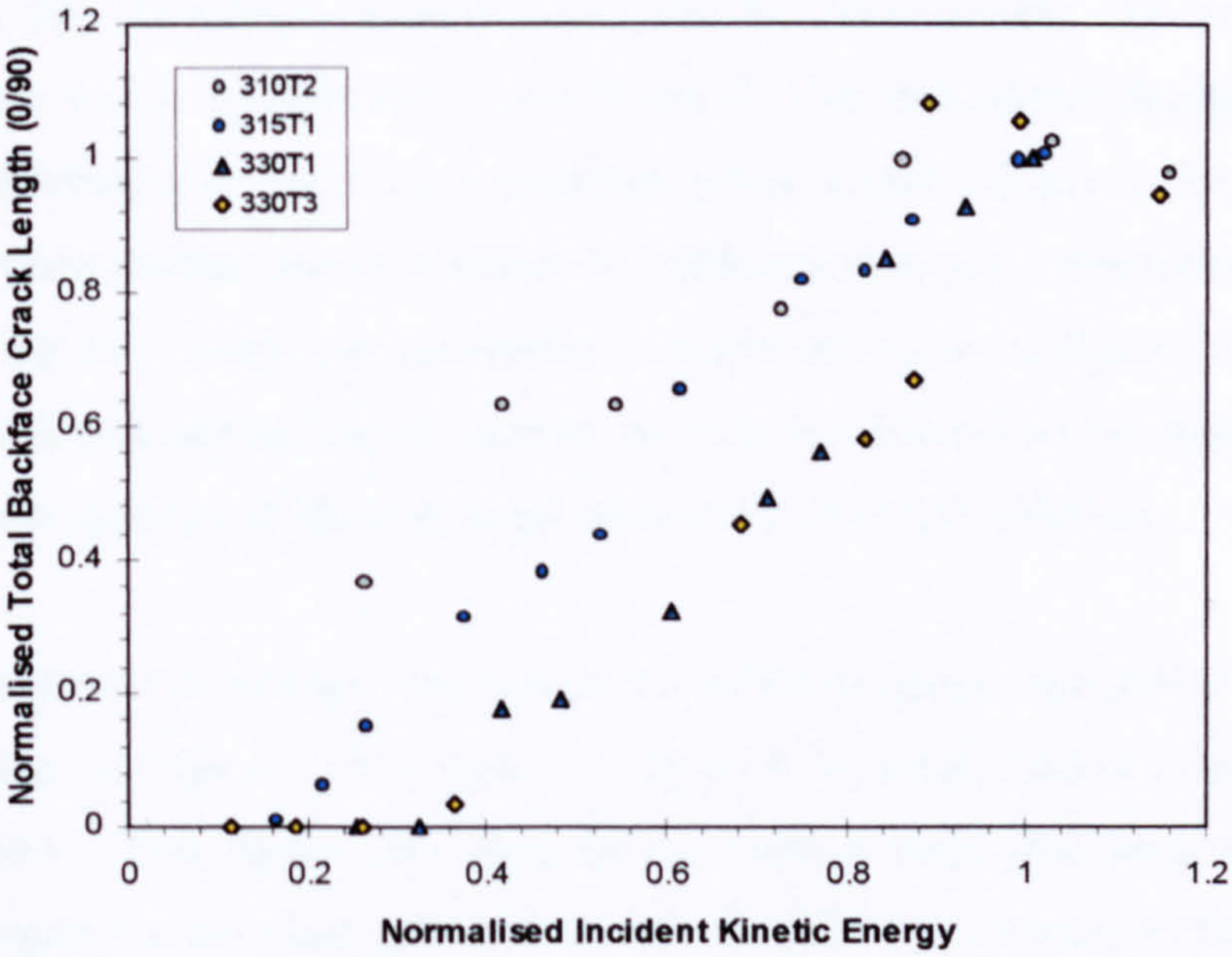

Figure 5.16. Normalised total backface crack length vs. normalised impact energy for the stiffened panels.

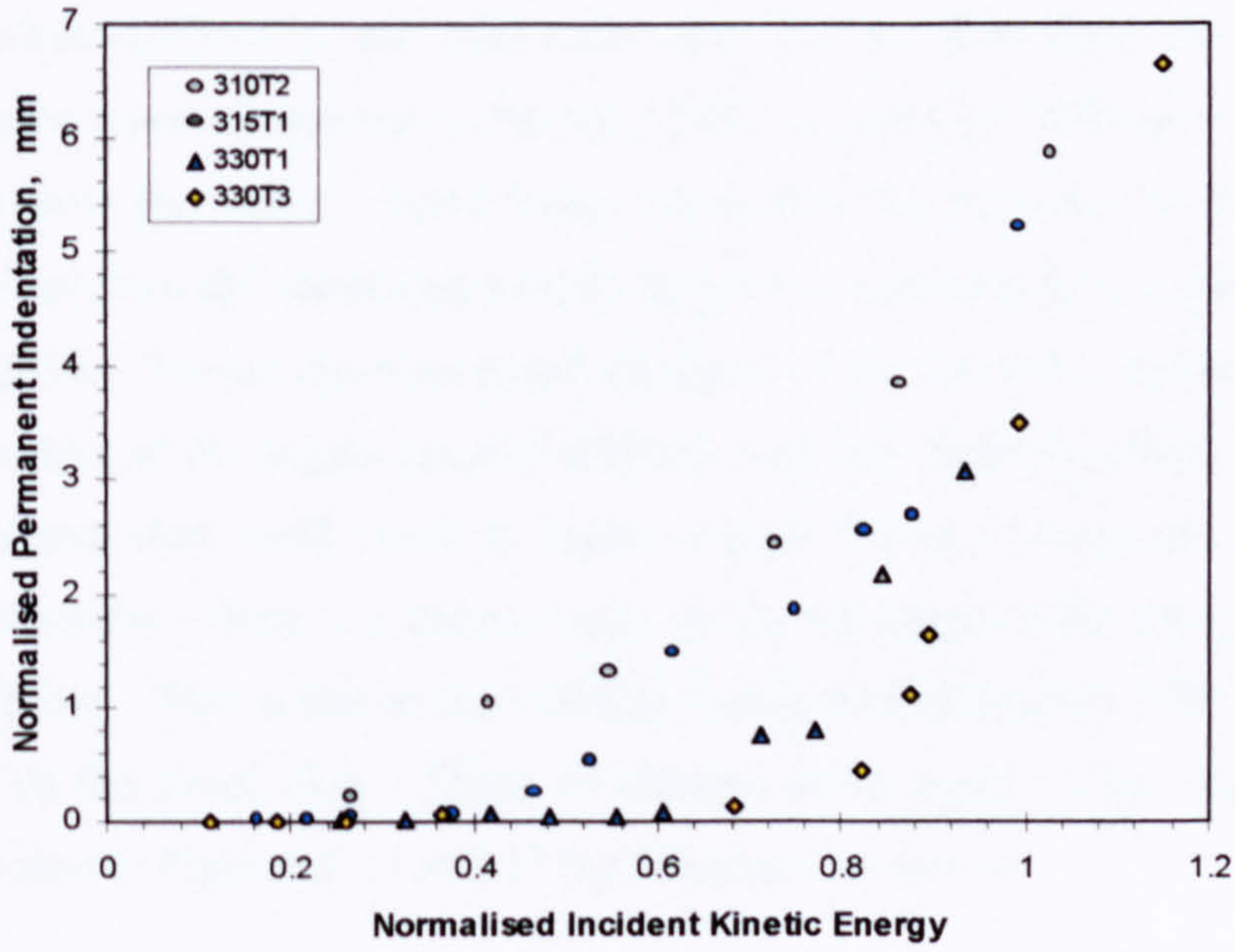

Figure 5.17. Normalised permanent indentation vs. normalised impact energy for the stiffened panels.

Compared to the normalised damage maps for the plain panels, the maps for the stiffened panels do not collapse into a narrow band. The normalised damage maps for projected delaminated area and total backface crack length (Figures 5.15 and 5.16 respectively) show distinct trends between the different data sets. Similar observations can be made for the normalised permanent indentation shown in figure 5.17. It also seems that the data is separating into distinctive sets that depend on the diameter of the panel and on the distance of the load application point from the stiffeners.

To better understand the damage response of the stiffened panels, the plot of normalised delaminated area in Figure 5.15 is recast in Figure 5.18, which includes data for the 3 ply plain panels. This figure also includes the vertical lines indicating the damage transition energies for the plain panels that were identified in Chapter 4, Section 4.4.2. In Figure 5.18, the data for the 150-mm diameter panel impacted between the stiffeners (315T1) falls within the narrow band defined by the plain panel data. This may be a consequence of the fact that the stiffeners in the panel are near the inner edge of the clamping ring so as to have only a little effect on the stiffness of the panel. The data for the 100-mm diameter panel impacted on the toe of the stiffener (310T2) lies to the left and above the band defined by the plain panel data. On the other hand, the data for the 300-mm diameter panels impacted on the bay (330T1) and on the stiffeners (330T3) lies to right and below this band. These trends show how the presence of the stiffeners effects deviations from the somewhat orderly behaviour displayed by the plain panels in Chapter 4. For the 100-mm diameter panel impacted on the toe of the stiffener (310T2), the close proximity of the impact point to stiffener web may have the effect of causing a very stiff response that could result in higher impact forces at relatively low impact energies. Furthermore there is a discontinuity in the thickness of the panel skin at the toe of the stiffener. This is due to the stiffener flange adding another 0/90 ply layer to the backface of the panel skin. These conditions could result in the larger relative damage sizes seen in Figures 5.15 to 5.17 for this panel geometry.

The suppression of the growth of delamination damage for the 300-mm diameter, stiffened panel impacted on the stiffener (330T3) because of the obstruction of the indentor by the fractured blade is evident in Figure 5.18. The data for this panel geometry show a relatively slow growth of delamination damage with impact energy up to 80 percent of the impact penetration energy. However, for impact energies 80 to 100 percent of the impact penetration energy, delamination growth increases rapidly suggesting catastrophic local failure of the panel.

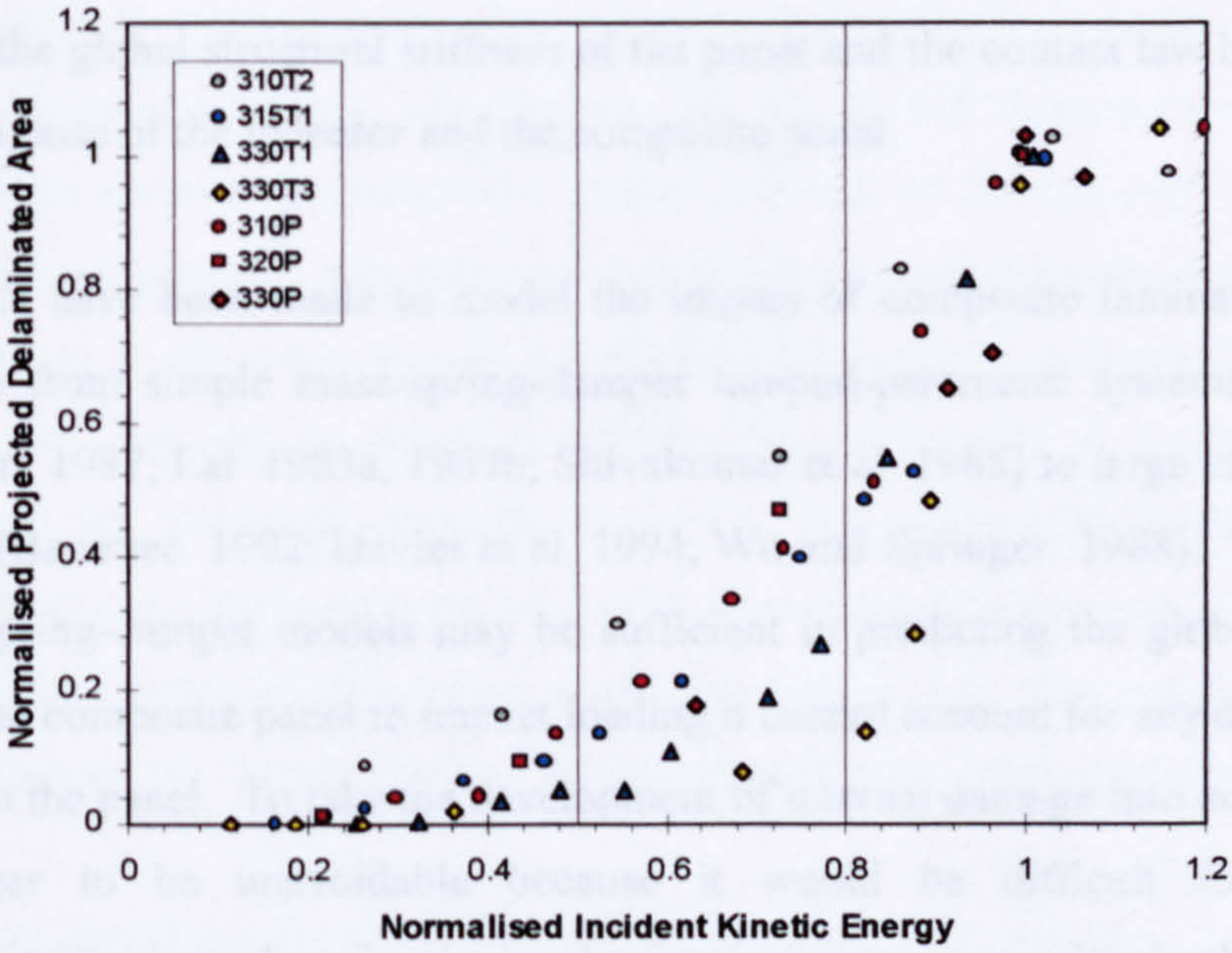

Figure 5.18. Normalised projected delaminated area vs. normalised impact energy for plain and stiffened panels.

6 MODELLING OF THE IMPACT RESPONSE OF CFRP

6.1 INTRODUCTION

An impact event requires the collision of at least two bodies. It is a complex phenomenon that is influenced by the impact velocity, the masses of the colliding bodies, the rigidity of the bodies, the contact area and the governing contact law (that determines the contact force developed between the two bodies). In this thesis the low-velocity impact event studied was that between a guided falling mass which we refer to as the indentor and a stationary target consisting of a composite panel held between two clamping rings. In this context the parameters of interest were the mass and velocity of the indentor, the global structural stiffness of the panel and the contact law between the hemispherical nose of the indentor and the composite panel.

Many attempts have been made to model the impact of composite laminates. These models range from simple mass-spring-damper lumped-parameter systems (Caprino. 1984; Sjoblom. 1987; Lal. 1983a, 1983b; Shivakumar et al. 1985) to large and complex FEA models (Banerjee. 1992; Davies et al. 1994; Wu and Springer. 1988). Though the linear mass-spring-damper models may be sufficient in predicting the global dynamic response of the composite panel to impact loading it cannot account for any damage that could occur in the panel. To take the development of internal damage into account FEA models appear to be unavoidable because it would be difficult for classical mathematical methods to describe the mechanisms of damage creation in the material. The results from these various models agree that the total response of the laminated panel consists of two parts: (a) a global structural response to the impact load and (b) a highly localised response that is confined to a small area around the impact point or contact zone. This localised response is the more complex of the two since it could include the creation of damage in the panel if the impact energy were sufficiently high. The superposition of these two responses and the dominance of one over the other are responsible for the varied and complex behaviour of the force-time and displacement-time histories obtained from experiments and numerical models of the impact event.

The attempt to use a lumped-parameter model to simulate the impact events studied in this research first grew out of a need to gauge the data obtained from the experiments and to determine the what digital filter parameter values are to be used in the processing of the data. Initial results from the model allowed us to better understand the impact event and assured us that the captured data represented actual dynamic events. Encouraged by these initial results the model was extended to include non-linear panel behaviour and the effects of panel damage on the impact response.

6.2 THE LUMPED-PARAMETER MASS-SPRING-DAMPER MODEL

The mechanical model of the dynamical system comprised of the drop-mass or indentor and target panel and was constructed of masses, springs and dampers configured as shown in Figure 6.1. In this model, M_j represents the masses, K_j the stiffness elements and C_j, the dampening elements. The elements M_0, M_1, K_0 and C_0 model the drop-mass assembly and the element K_1 models the contact stiffness of the indentor nose against the panel surface. Using the embedded pale model proposed by Ursenbach et al (1995) the local stiffness of the panel around the vicinity of the load application point was modelled by the elements K_2 and C_2. Finally, the panel itself is modelled by its equivalent mass, M_3, and by the elements K_3 and C_3. The choice of the model elements and the way they were interconnected was made after careful assessment of the impact problem and the model configuration shown in Figure 6.1 was found to give a dynamical response that closely matched the response observed from experimental data.

The differential equations governing this model shown in Figure 6.1 are:

$$M_0 \frac{d^2 y_0}{dt^2} = -C_0\left(\frac{dy_0}{dt} - \frac{dy_1}{dt}\right) - K_0(y_0 - y_1)$$

$$M_1 \frac{d^2 y_1}{dt^2} = -K_1(y_1 - y_2) + C_0\left(\frac{dy_0}{dt} - \frac{dy_1}{dt}\right) + K_0(y_0 - y_1)$$

$$M_3 \frac{d^2 y_3}{dt^2} = -C_3 \frac{dy_3}{dt} - K_3 y_3 + C_2\left(\frac{dy_2}{dt} - \frac{dy_3}{dt}\right) + K_2(y_2 - y_3)$$

Eqns. 6.1

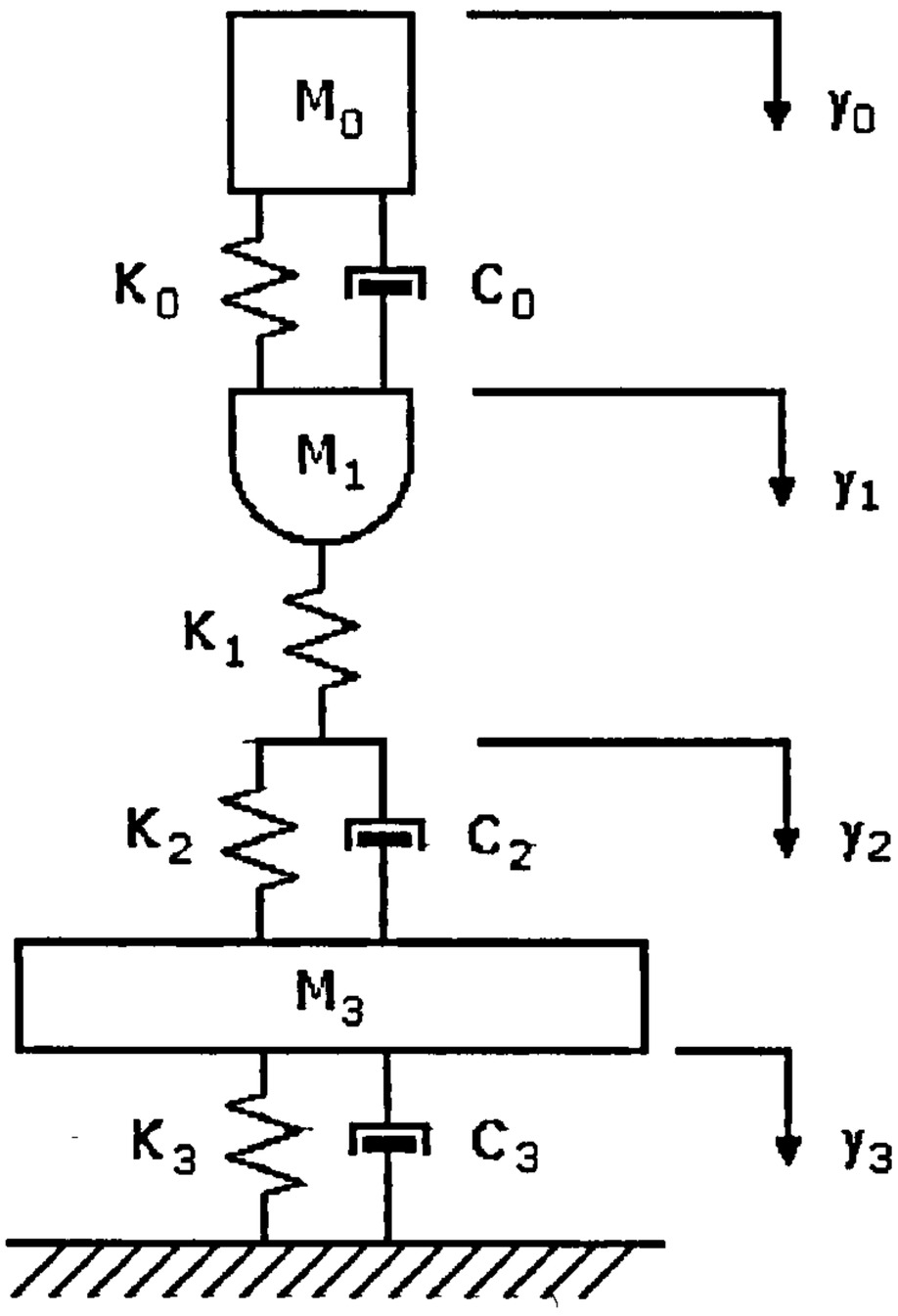

Figure 6.1. The mass-spring-damper model

Dynamic compatibility requires that

$$K_1(y_1 - y_2) = C_2\left(\frac{dy_2}{dt} - \frac{dy_3}{dt}\right) + K_2(y_2 - y_3)$$

where $K_1 = 0 \quad if \quad (y_1 - y_2) < 0$

and $C_2 = 0 \quad and \quad K_2 = 0 \quad if \quad (y_1 - y_2) < 0 \quad or \quad (y_2 - y_3) < 0$

Eqns. 6.2

Kinematic compatibility requires that

$$\frac{dy_2}{dt} = \frac{dy_3}{dt} - \frac{K_2}{C_2}(y_2 - y_3) + \frac{K_1}{C_2}(y_1 - y_2) \qquad \text{Eqn. 6.3}$$

In Equations 6.1 to 6.3 the positive direction was taken to be downwards. Furthermore the stiffness element parameters represented by K_j need not be constants and can be non-linear functions of the displacement parameters y_j.

6.2.1 LINEAR MODEL PARAMETERS

As a first approximation, a model with constant coefficients was tested to ascertain the suitability of the model configuration. At this stage no theoretical considerations were made in determining the model parameters. Instead a process of trial and error determined these parameters until an acceptable match was found between the model response and the impact response of the panel from test data. From this preliminary modelling of the impact event it was found that the impact response is a combination of three dynamic responses. These responses are (1) a main impact pulse that determines the duration of the impact event, (2) a high-frequency oscillatory response superposed on the main impact pulse and (3) the free vibration of the panel after the indentor breaks contact with the panel in the rebound phase. Figure 6.2 illustrate these three responses in terms of the impact force and panel displacement histories calculated for a low-energy impact (0.472 J at 2.578 m/s) on a 100-mm diameter, 3-ply panel. This figure shows that there is an important interaction between the indentor and panel during the impact event that is governed by the contact stiffness between these two bodies and by the global stiffness of the panel. The displacement history also shows that there is energy transferred to the panel during the impact event that excites transverse vibrations in the panel and that these vibrations persist well after the impact event.

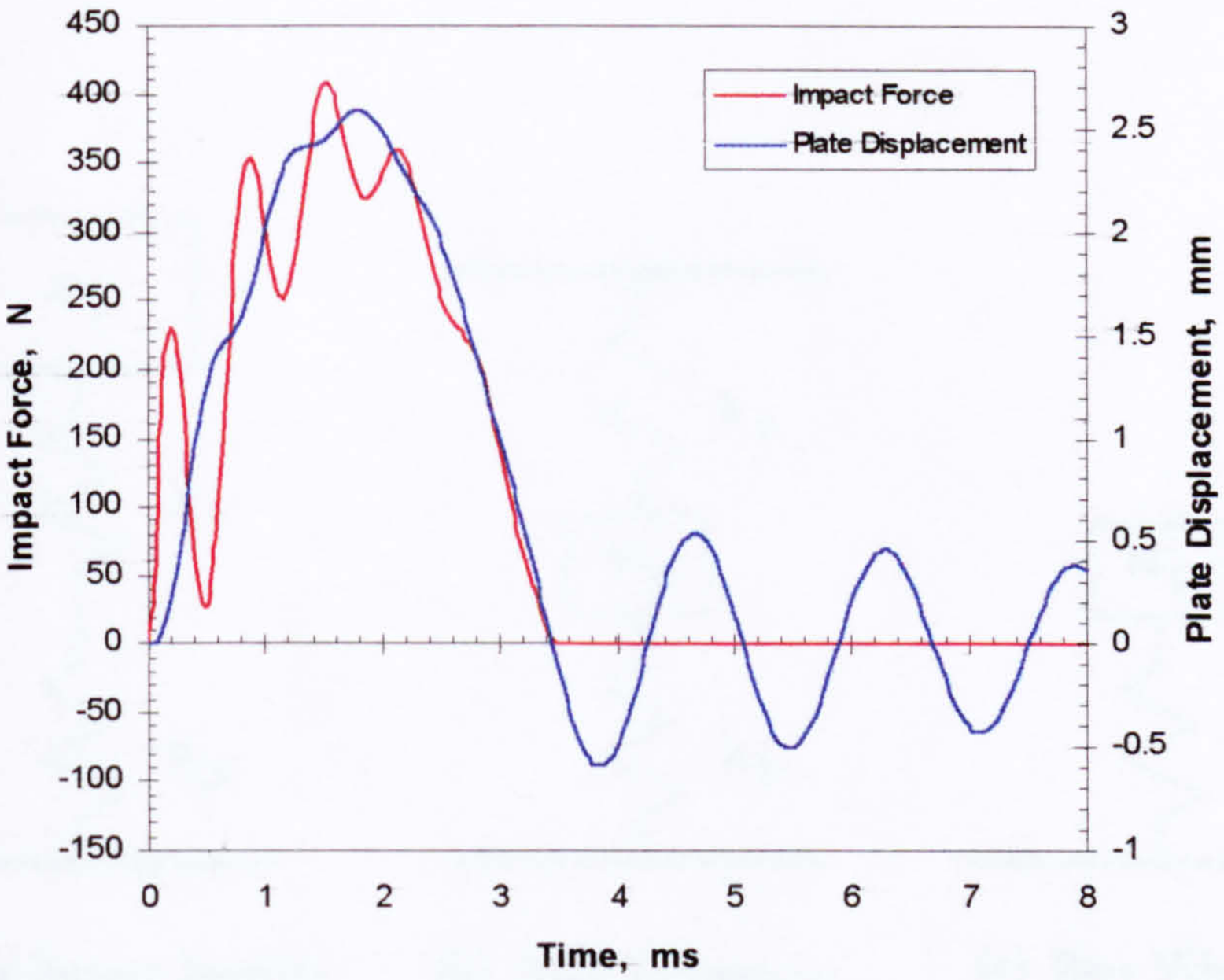

Figure 6.2. Impact force and panel displacement as calculated from the numerical model

The three impact response components are determined by how the different model elements interact with each other during the impact event. These element interactions and what they contribute to the total impact response are illustrated in Figure 6.3(a) to 6.3(c). The main impact pulse is governed by the mass of the indentor, m_i (which is many times larger than the mass of the panel), the equivalent contact stiffness between the indentor and panel, k_c, and the global panel stiffness, k_p. This implies that the impact duration for a non-damaging impact will scale as $\sqrt{\frac{m_i}{k_{equiv}}}$, where k_{equiv} is the combined stiffness of k_c and k_p. The high-frequency oscillation superposed on the main impact pulse is governed by the elements shown in Figure 6.2(b). This oscillation results from the panel vibrating against the indentor, through the equivalent contact stiffness k_c, during the impact event. The frequency of the oscillation is given by $\sqrt{\frac{k_c + k_p}{m_p}}$. Finally, after the indentor has rebounded from the panel, the panel response is one of free vibration as governed by the model elements shown in Figure 6.2(c).

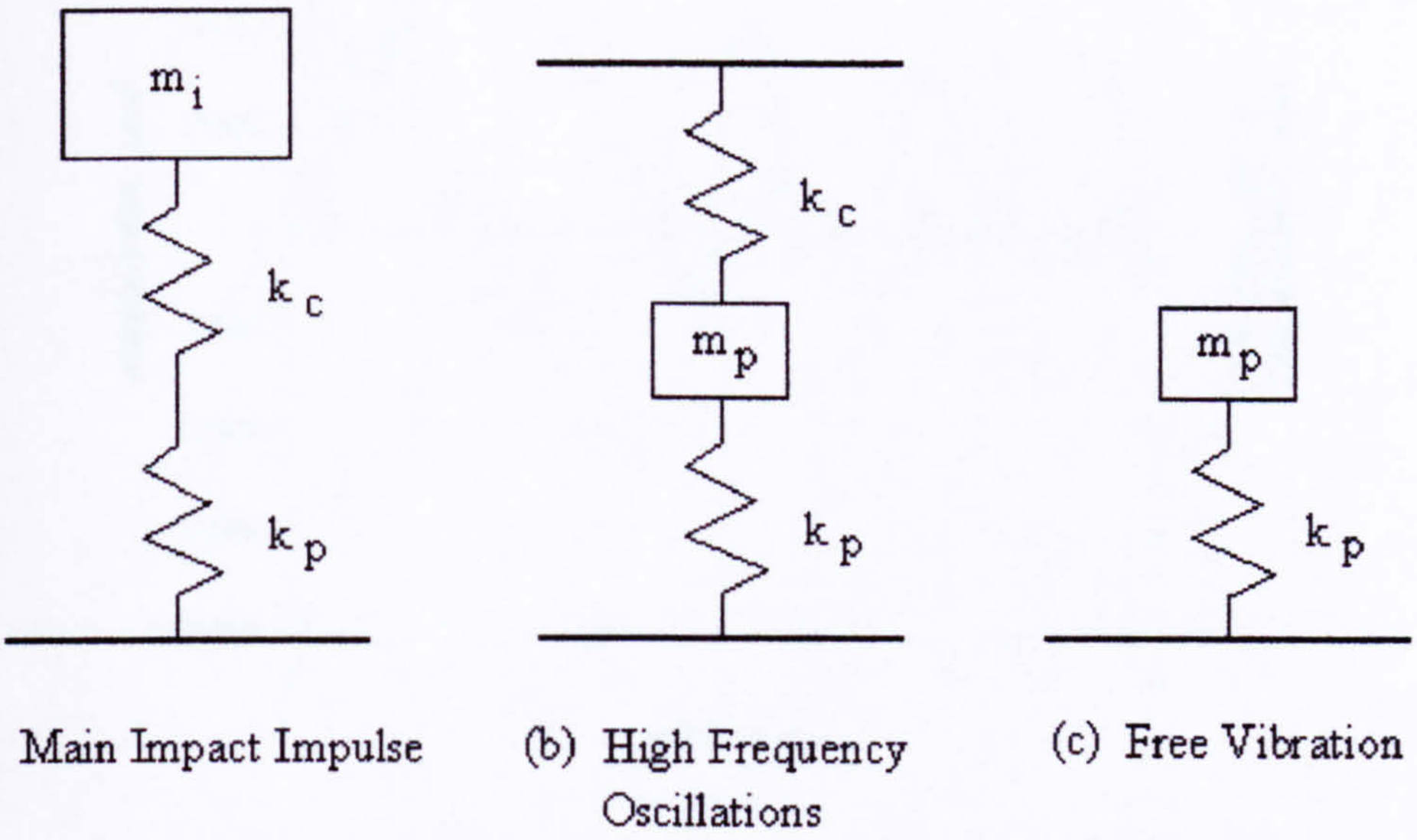

Figure 6.3. Model component responses

The acceleration, velocity and displacement histories of the panel as predicted by the model are presented in Figure 6.4. As expected, the acceleration of the panel is completely different from that of the indentor. This implies that the panel experiences entirely different dynamic forces from that experienced by the indentor during the impact event.

To verify the model prediction, the displacement history from test data for a 100-mm diameter, 3-ply plain panel subjected to an impact energy of 0.472 J was numerically differentiated twice to obtain the velocity and acceleration histories of the panel. Prior to numerical differentiation the data was first smoothed by passing it through a low-pass digital filter set a to a cut-off frequency of 3500 Hz and a cut-off transition width of 1000 Hz. The result of this calculation is presented in Figure 6.5. Comparing this figure with Figure 6.4, it is clear that the predicted behaviour of the panel agrees fairly well with the panel response observed in the tests.

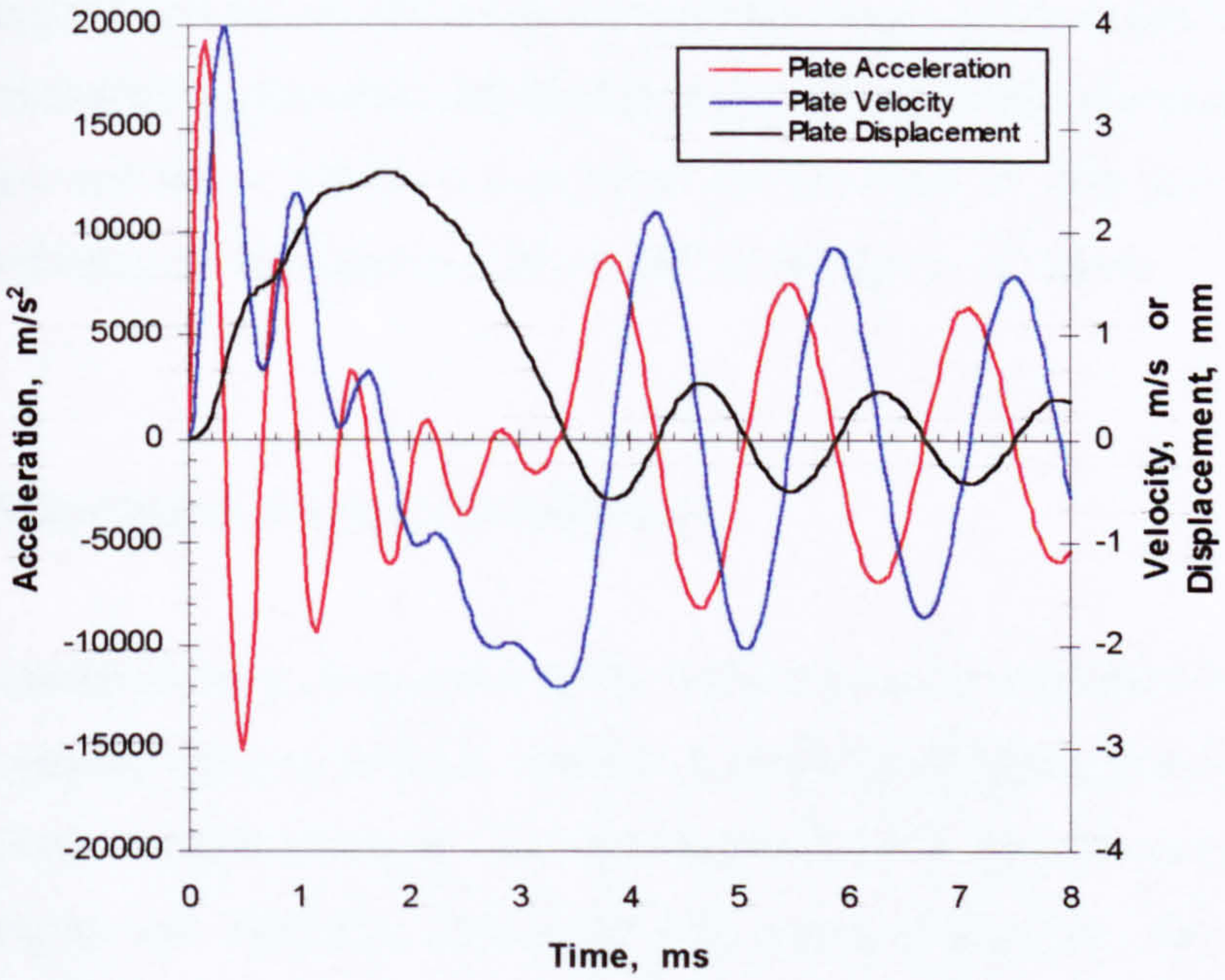

Figure 6.4. Acceleration, velocity and displacement of the panel as calculated from the numerical model

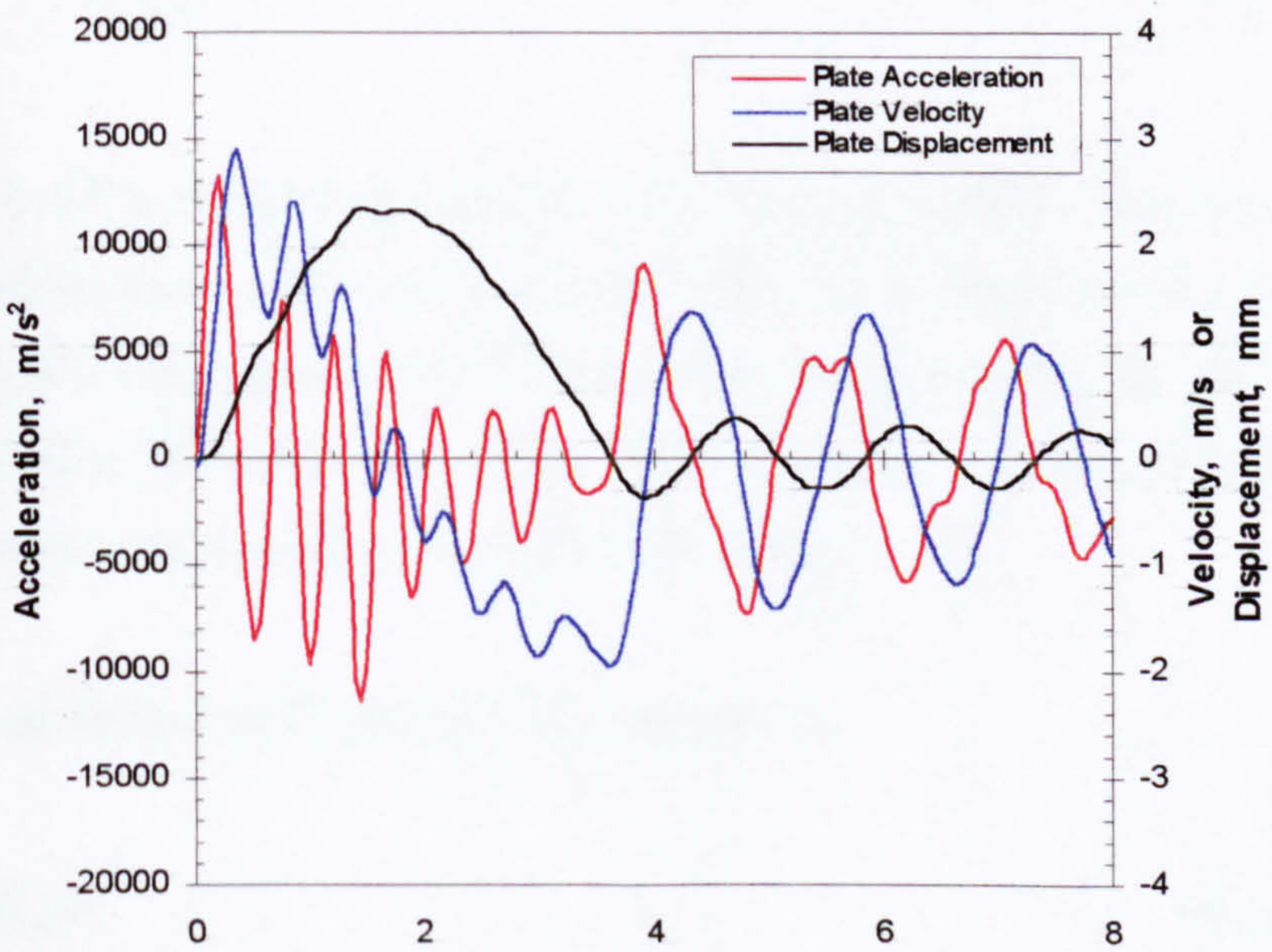

Figure 6.5. Acceleration, velocity and displacement of the panel as calculated from captured data

It must be emphasised that all the initial predictions based on the model considered in this section exclude the possibility of damage to the panel. In the succeeding section a more complex non-linear model is presented that attempts to take into account the membrane stiffening of the panel as well as impact damage to the panel.

6.2.2 NON-LINEAR MODEL PARAMETERS

In the linear model of the previous section the membrane stiffening effect was neglected and thus the validity of the model was limited to small panel deflections and to impacts at relatively low incident energies. In order to predict the impact response at larger incident energies and therefore larger resulting panel deflections, the approximate analysis for centrally loaded, circular, thin isotropic plates expressed in Equation 2.2 was used. For the benefit of discussion this equation is repeated below:

$$\frac{w}{h}+A\left(\frac{w}{h}\right)^3=B\frac{Pa^2}{Eh^4} \qquad \text{Eqn. 6.4}$$

In Equation 6.4 P is the applied force, E is the Young's modulus, a is the panel radius, h is the panel thickness and w is the central deflection of the panel due to the load P. The dimensionless constants A and B account for the edge constraints of the panel and are functions of the Poisson's ratio alone. The values for these constants for four edge constraints or boundary conditions are given in Table 6.1.

The panel load-deflection relation can be expressed as

$$P=K_b w+K_m w^3 \qquad \text{Eqns. 6.5}$$

where K_b is the bending stiffness and K_m is the membrane stiffness. Shivakumar et al (1985), drawing from the work by Volmir (1967), have shown that for an isotropic material, the stiffness parameters K_b and K_m can be expressed as functions of the

Young's modulus E, the Poisson's ratio ν, the panel radius a and the panel thickness h. These expressions for K_b and K_m are summarised in Table 6-2.

Table 6-1. Edge conditions and values for dimensionless constants A and B (Timoshenko and Wionowsky-Krieger. 1959)

Edge Conditions		A	B
Clamped, Immovable Edge	CIE	0.443	0.217
Clamped, Movable Edge	CME	0.200	0.217
Simply supported, Immovable Edge	SIE	1.430	0.552
Simply supported, Movable Edge	SME	0.272	0.552

Table 6-2. Edge conditions and corresponding expressions for K_b and K_m (Shivakumar et al. 1985). Edge conditions are as defined in Table 6.1 above

Edge Conditions	K_b	K_m
CME	$\frac{4\pi Eh^3}{3(1-\nu^2)a^2}$	$\frac{191\pi Eh}{648\,a^2}$
CIE	$\frac{4\pi Eh^3}{3(1-\nu^2)a^2}$	$\frac{(353-191\nu)\pi Eh}{648\,(1-\nu)a^2}$
SME	$\frac{4\pi Eh^3}{3(3+\nu)(1-\nu)a^2}$	$\frac{\pi Eh}{(3+\nu)^4 a^2}\left[\frac{191}{648}(1+\nu)^4+\frac{41}{27}(1+\nu)^3+\frac{32}{9}(1+\nu)^2+\frac{40}{9}(1+\nu)+\frac{8}{3}\right]$
SIE	$\frac{4\pi Eh^3}{3(3+\nu)(1-\nu)a^2}$	$\frac{\pi Eh}{(3+\nu)^4 a^2}\left[\frac{191}{648}(1+\nu)^4+\frac{41}{27}(1+\nu)^3+\frac{32}{9}(1+\nu)^2+\frac{40}{9}(1+\nu)+\frac{8}{3}\right]$ $+\frac{\pi Eh}{(3+\nu)^4(1-\nu)a^2}\left[\frac{(1+\nu)^4}{4}+2(1+\nu)^3+8(1+\nu)^2+16(1+\nu)+16\right]$

Using Equations 6.4 and 6.5 to solve for the edge constraint constants A and B in terms of the panel stiffness coefficients K_b and K_m we have:

$$A = \frac{K_m}{K_b} h^2$$

$$B = \frac{1}{K_b} \frac{Eh^3}{a^2}$$

Eqns. 6.6

By using the expressions in Table 6-2 to substitute for K_b and K_m in Equation 6.6 we find that the dimensionless constants A and B are functions of the Poisson's ratio only. The results of the calculations for the expressions for A and B in terms of ν for the different edge conditions are summarised in Table 6-3.

Table 6-3. Edge conditions and expressions for A and B in terms of ν. Edge conditions are as defined in Table 6.1

Edge Conditions	*A*	*B*
CIE	$\frac{(353-191\nu)}{648(1-\nu)}\frac{3}{4}(1-\nu^2)$	$\frac{3}{4\pi}(1-\nu^2)$
CME	$\frac{191}{648}\frac{3}{4}(1-\nu^2)$	$\frac{3}{4\pi}(1-\nu^2)$
SIE	$\frac{3}{4(3+\nu)^3}[(1-\nu)f(\nu)+g(\nu)]$ See notes *a, b*	$\frac{3}{4\pi}(3+\nu)(1-\nu)$
SME	$\frac{3}{4}\frac{(1-\nu)}{(3+\nu)^3}f(\nu)$ See note *a*	$\frac{3}{4\pi}(3+\nu)(1-\nu)$

Notes: *a.* $f(\nu) = \frac{191}{648}(1+\nu)^4 + \frac{41}{27}(1+\nu)^3 + \frac{32}{9}(1+\nu)^2 + \frac{40}{9}(1+\nu) + \frac{8}{3}$

b. $g(\nu) = \frac{(1+\nu)^4}{4} + 2(1+\nu)^3 + 8(1+\nu)^2 + 16(1+\nu) + 16$

To determine the sensitivity of the dimensionless constants ***A*** and ***B*** to changes in the Poisson's ratio, the expressions in Table 6-3 were evaluated over a range of values of Poisson's ratio. The results of these calculations are presented in Figure 6.6. From this figure we can see that for reasonable values of the Poisson's Ratio for carbon fibre-epoxy composites (between 0.3 and 0.4), the edge constants are not strong functions of the Poisson's ratio.

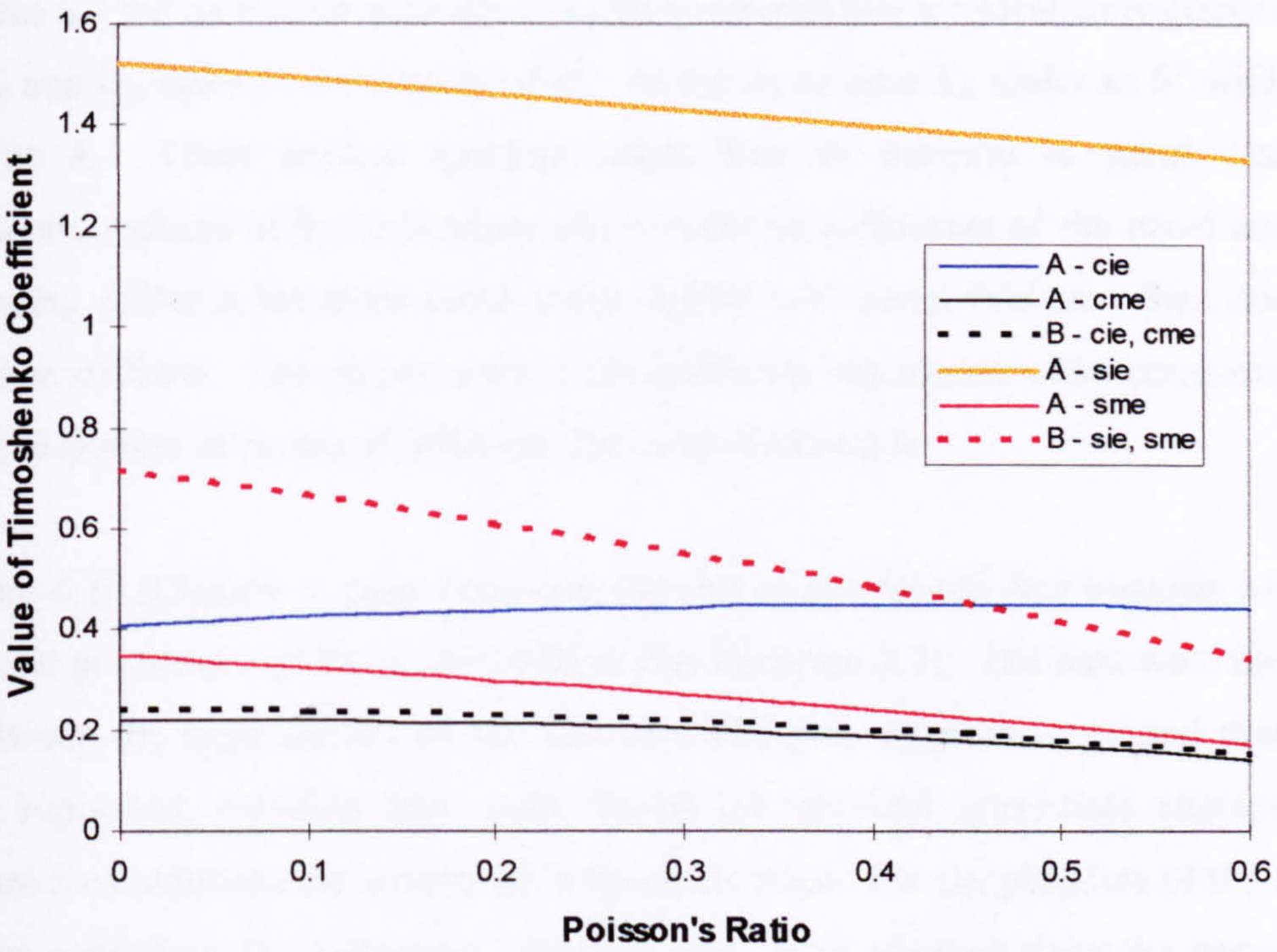

Figure 6.6. Variation of the Timoshenko panel coefficients *A* and *B* with Poisson's ratio

This implies that the large deflection response of thin isotropic panels is influenced mainly by the Young's modulus, the panel thickness and the panel radius and is much less affected by the Poisson's ratio.

We can rewrite Equations 6.6 to express the stiffness coefficients in terms of the constraint constants.

$$K_b = \frac{1}{B}\frac{Eh^3}{a^2}$$

$$K_m = \frac{A}{B}\frac{Eh}{a^2}$$

Eqns. 6.7

Equations 6.7 tell us that for a panels of a given material that are identically constrained, both K_b and K_m scale as the inverse of a^2. At the same time K_b scales as h^3 whilst K_m scales as h. These scaling relations imply that an increase in panel diameter significantly reduces both the bending and membrane stiffnesses of the panel and that the bending stiffness increases much more rapidly with panel thickness than does the membrane stiffness. This information is of significant importance when comparing the loading responses of panels of different sizes and thicknesses.

In Figure 4.10 (Chapter 4, page) was cast the plot of normalised data together with the theoretical predictions of Equation 6.4 (See also Equation 2.2). The data were found to fall between the edge conditions for that of a clamped, movable edge and that of a simply supported, movable edge even though the physical constraints attempted to duplicate the conditions for a clamped, immovable edge. For the purposes of the model the edge conditions for a clamped, movable edge were adopted since the normalised static test data (See Figure 4.10) appear to fall closer to the curve predicted by this set of constraints.

The contact stiffness between the nose of the indentor and the surface of the panel can be calculated from the Hertz contact law given in Equation 2.4 (Chapter 2, page 9) For an isotropic indentor with a hemispherical nose of radius R_I and a transversely isotropic composite panel Shivakumar et al (1985) citing Conway and Angew gives the expression for **n** as

$$n = \frac{4\sqrt{R_I}}{3\pi\left(Kn_I + Kn_2\right)} \qquad \text{Eqn. 6.8}$$

where

$$Kn_I = \left(\frac{1-\nu_I{}^2}{\pi E_I}\right) \qquad \text{Eqn. 6.9}$$

and

$$Kn_2 = \frac{\sqrt{A_{22}}\left[\left(\sqrt{A_{11}A_{22}} + G_{zr}\right)^2 - \left(A_{12} + G_{zr}\right)^2\right]^{\frac{1}{2}}}{2\pi\sqrt{G_{zr}}\left(A_{11}A_{22} - A_{12}{}^2\right)}$$

$$A_{11} = E_z\beta\left(1-\nu_r\right) \qquad A_{22} = \frac{E_r\beta\left(1-\delta\nu_{zr}{}^2\right)}{1+\nu_r} \qquad A_{12} = E_r\beta\nu_{zr}$$

$$\beta = \frac{1}{1-\nu_r - 2\delta\nu_{zr}{}^2} \qquad \delta = \frac{E_r}{E_z}$$

Eqns. 6.10

In Equations 6.9 to 6.10 the constants E, G and ν are the Young's modulus, shear modulus and Poisson's ratio respectively. The subscripts r and z respectively refer to the radial (or in-plane) and thickness directions of the panel.

For the case where shear deformation in the panel cannot be neglected, Shivakumar et al (1985) expressed the load-deflection relation in the form

$$P = K_{bs}w + K_m w^3 \qquad \text{Eqn. 6.11}$$

where K_{bs},the equivalent stiffness due to bending and shear deformations, is given by:

$$K_{bs} = \frac{K_b K_s}{K_b + K_s} \qquad \text{Eqn. 6.12}$$

In Equation 6.12 the shear stiffness can be determined from the expressions

$$K_s = \frac{4\pi}{3} G_{rz} h \left[\frac{E_r}{E_r - 4\nu_{rz} G_{rz}}\right] \left[\frac{1}{\frac{4}{3} + \ln \frac{a}{a_c}}\right]$$

$$a_c = \left[\frac{3\pi}{4}\left(Kn_I + Kn_2\right) R_I \; P\right]^{\frac{1}{3}}$$

Eqns. 6.13

where a_c is the contact radius.

We then can use Equations 6.11 to 6.13 and the expressions in Table 6-2 to define an equation for the non-linear global panel stiffness:

$$K_3 = K_{bs} + K_m {y_3}^2 \qquad \text{Eqn. 6.14}$$

and we can substitute the right hand side of this equation for K_3 in the differential equations governing the model (Equations 6.1 to 6.3).

Similarly we can express the contact stiffness between the indentor nose and panel as

$$K_1 = n(y_1 - y_2)^{1/2} \qquad \text{Eqn. 6.15}$$

where n is defined by Equation 6.8.

Equations 6.7 to 6.15 give us the theoretical basis for calculating for the model parameters that account for non-linear panel behaviour. At this stage the non-linear model neglects the effects of damage in the panel. The next section discusses a way of incorporating the effects of damage into the model.

6.2.3 Modelling the Effects of Material Damage on the Impact Response

For the mass-spring-damper model developed in this research project the effect of impact damage on the dynamic response was attempted by modifying the elements representing contact stiffness (K_1 in Figure 6.1) and the local panel stiffness (K_2 and C_2 in Figure 6.1). As the lumped-parameter model cannot take into account the mechanics of damage creation in the panel some amount of empiricism was unavoidable and was in fact resorted to.

The test data show that the maximum extent of the damage seems to oscillate about a fixed size or diameter for a given panel thickness. Furthermore these maximum damage sizes did not appear to be significantly influenced by the diameter of the panel (see Figure 6.6-1). So it was natural to assume that the effects of damage would be confined to the small region around the load application point. From the test data and the damage assessment of the impacted panels it was determined that this damaged region is no larger than 30 mm in diameter. Using this value for the diameter of the embedded plate in the model proposed by Ursenbach et al (1995), the bending stiffness of the local panel region can be calculated from Equations 6.7 assuming a clamped, immovable edge. Owing to the small diameter of this local region the membrane stiffness is insignificant compared to the bending stiffness and can be ignored.

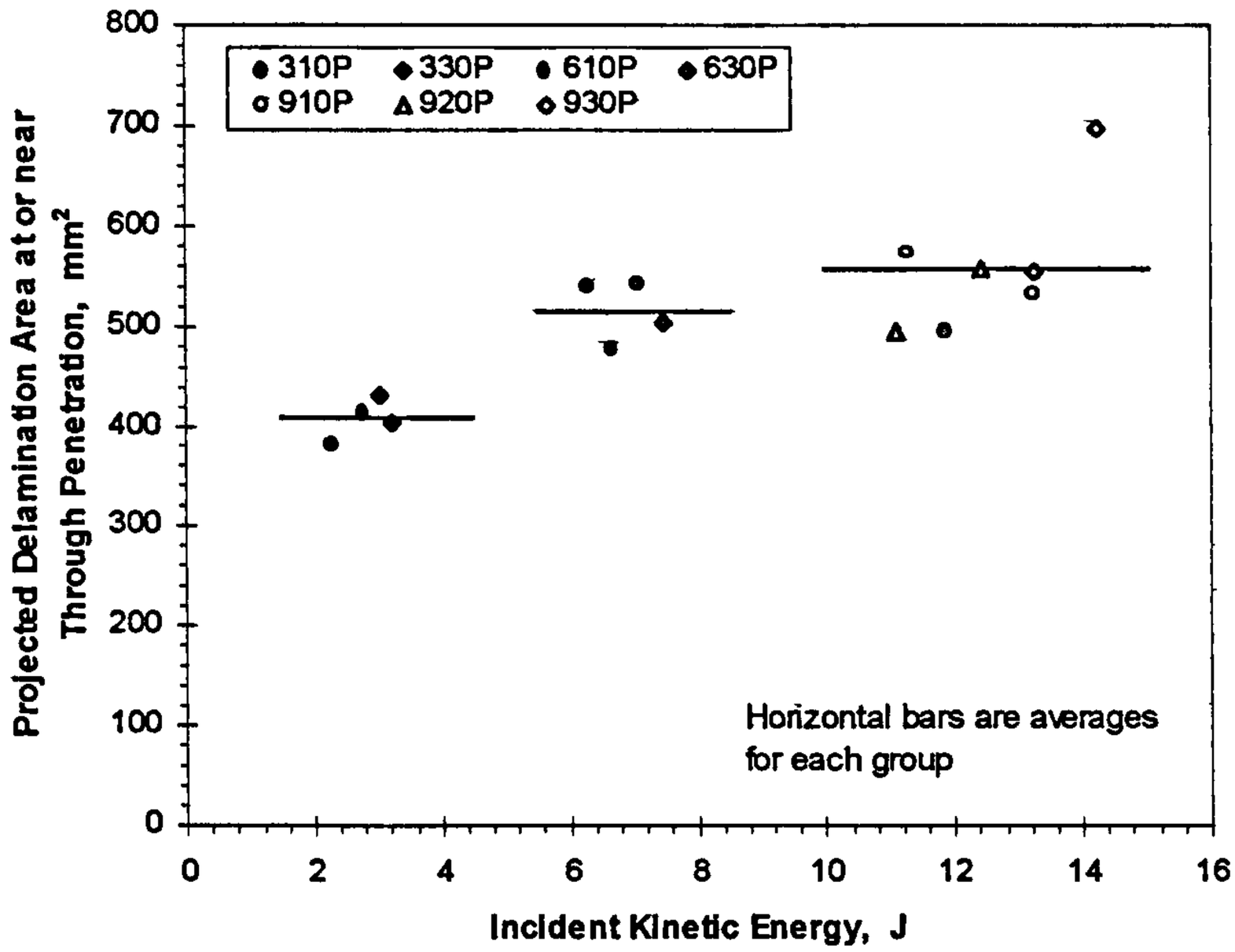

Figure 6.6-1. Maximum projected delamination areas for 3-, 6-, and 9-ply plain panels. Panel diameters represented are 100-, 200-, and 300-mm in diameter.

The load at which the first backface cracks in the panel occurs was obtained from the best-fit curve through the static test data plotted in Figure 6.7. The equation for this best-fit curve is:

$$P_{bfc} = 400\, h^{\frac{5}{3}} \qquad \text{Eqn. 6.16}$$

where P_{bfc} is the applied load to initiate the first backface cracks and h is the panel thickness.

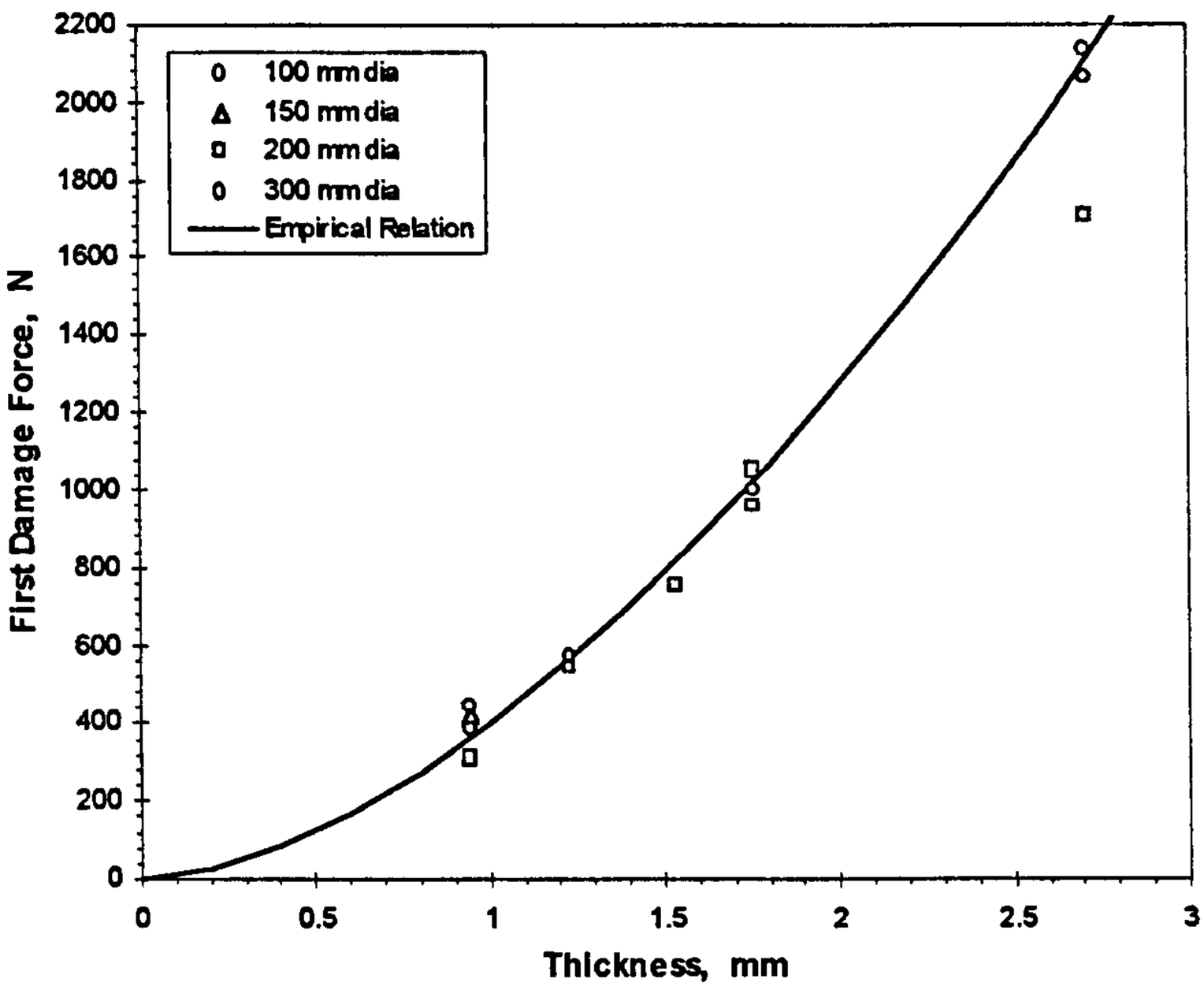

Figure 6.7. Magnitude of the static force at the onset of the first backface cracks.

The reduction in panel stiffness due to the occurrence of the first backface cracks was accounted for in the model by reducing the laminate thickness in the local panel region. The reduction in thickness was arbitrarily taken to be multiple of the ply thickness due to a lack of a theoretical expression to calculate for this quantity. In the 3-ply panels the model results best follow the test data if the reduction thickness is equal to one-half the

thickness of a ply. For the 9-ply panels this reduction in thickness is three times the thickness of a ply.

The onset of delamination damage and its effect on the impact response was accounted for through the use of Equations 2.12 and 2.13 (Section 2.6, page 23) and the use of the data presented in Figure 4.20 (Section 4.2.3, page 63). This entailed the modification of the element K_1 (see Figure 6.1) which represents the contact force so that it can only transmit a load at around the magnitude of the delamination initiation force defined by Equation 2.12. The expression for the contact force when the panel is delaminating can be written as:

$$P_{del} = P_c + C_{del}\left(\frac{dy_1}{dt} - \frac{dy_2}{dt}\right) \qquad \text{Eqn. 6.17}$$

where P_c is the critical delamination force defined by Equation 2.12 and C_{del} is a dampening coefficient that is used to account for any rate effects.

With maximum contact force limited to the value of the delamination initiation force because of the weakening of the material in the local contact region, the indentor can rapidly penetrate through the panel if its initial kinetic energy was sufficiently high. When the indentor traverses a distance through the material equal to the thickness of the panel, perforation of the panel by the indentor is deemed to occur. In actual tests where the indentor just possesses enough kinetic energy to perforate the panel, this condition is manifested by the ability to see daylight through the cracks in the damaged panel. Complete penetration of the panel is assumed when the indentor traverses a distance through the material of panel equal to the radius of the indentor nose.

The most difficult part of the damaged response to model was the penetration phase, which is that portion of the static indentation response where the static load decreases

with increasing indentor displacement (Curve D-E in Figure 4.6 and Figure 4.17). The empirical expression for the penetrating force that gives model results that best fit the test data was found to be of the form

$$P_{pen} = P_c \left(1 - \left[\frac{(y_1 - y_2) - h}{R_I - h}\right]^{\frac{5}{4}}\right) \qquad \text{Eqn. 6.18}$$

where P_c is the critical delamination force defined by Equation 2.12, R_I is the indentor nose radius and h is the thickness of the panel. Equation 6.18 represents the maximum force that the panel being penetrated can carry as the indentor is driven into it.

As implemented in the model, Equation 6.18 is non-zero only when the following conditions are met:

$$h \le (y_1 - y_2) \le R_I$$

$$\frac{dy_1}{dt} - \frac{dy_2}{dt} \ge 0$$

Eqns. 6.19

These sets of model equations comprise an initial value problem and were solved using a software package implementing a fourth-order Runge-Kutta time-integration algorithm.

6.2.4 MODELLING SUMMARY

The sets of non-linear model equations (Equations 6.4 to 6.19 in Section 6.2.2) were used in combination with the differential equations of motion (Equations 6.1 to 6.3 in Section 6.2) to describe the response of the panels to both static and impact loading. The model equations comprise an initial value problem and were solved using MathCad (by MathSoft), a software package that includes, among many of its tools and features, a fourth-order Runge-Kutta time-integration utility. Equations 6.1 to 6.19 were cast into MathCad script form so the software may interpret and solve them. The equations, however, are quite general and there is no reason why they could not be implemented successfully in other numerical analysis software packages.

The input parameters to the MathCad program were the mass, nose geometry, and engineering properties of the indentor; the equivalent mass, geometry, and engineering properties of the panel. Leissa (1969) suggested, for the case of vibration of an isotropic circular plate with a centrally attached mass, that the equivalent mass of the panel should be about 25 percent of the total mass of the panel.

All initial conditions in the governing differential equations were set to zero except for the indentor velocity, which was set equal to the incident impact velocity just before the indentor strikes the panel in a particular impact test.

In the simulation of a static test, the same procedure that was applied to an impact test simulation was used except that the indentor velocity was set to a very low value (no more than 0.2 mm/s) and held constant. This was made possible by disregarding the first two differential equations in Eqns. 6.1 and considering only the dynamics of the panel.

6.3 Model Results and its Comparison with Experimental Data

6.3.1 Results for Plain Panels

6.3.1.1 Static Test Modelling Results

Figures 6.8 to 6.11 show the results of the numerical simulations of the static tests on the 3-ply and 9-ply plain panels. For the comparative purposes actual test data were cast together with the model results in the plots shown in these figures. In general the model appears to be able to predict the static indentation behaviour when the panel diameter-to-thickness ratio is large. For the 3-ply panels where this ratio is at least 104 the model results follow the trend in the data quite closely. This is observation is also true for the 9-ply, 300-mm diameter panel (whose diameter to thickness-ratio-is about 110). Significant differences between the model results and the data can be observed for the 9-ply, 100-mm diameter panel whose diameter-to-thickness ratio is just under 37. Based on these observations it seems that the model developed in this thesis is best applicable to "thin" panels with diameter-to-thickness ratios of 100 or greater. For "thick" panels (with diameter-to-thickness ratios less than 100) through the thickness effects, which were not considered in the model, appear to introduce other modes of damaged response.

The results of the static test modelling overestimates the applied static loads and underestimates the panel displacements. This is a consequence of the theoretical clamped and movable edge constraints imposed on the non-linear model being stiffer than actual constraints experienced by the test panels (See Figure 4.10). The overestimation of the loads and the underestimation of the displacements are more pronounced for the thicker panels. This is due to the stiffness of the thicker panels becoming comparable to the actual physical stiffness of the edge constraints and thus resulting in a load-deflection response that was more compliant than that for a theoretical configuration where the edge constraints have infinite stiffness.

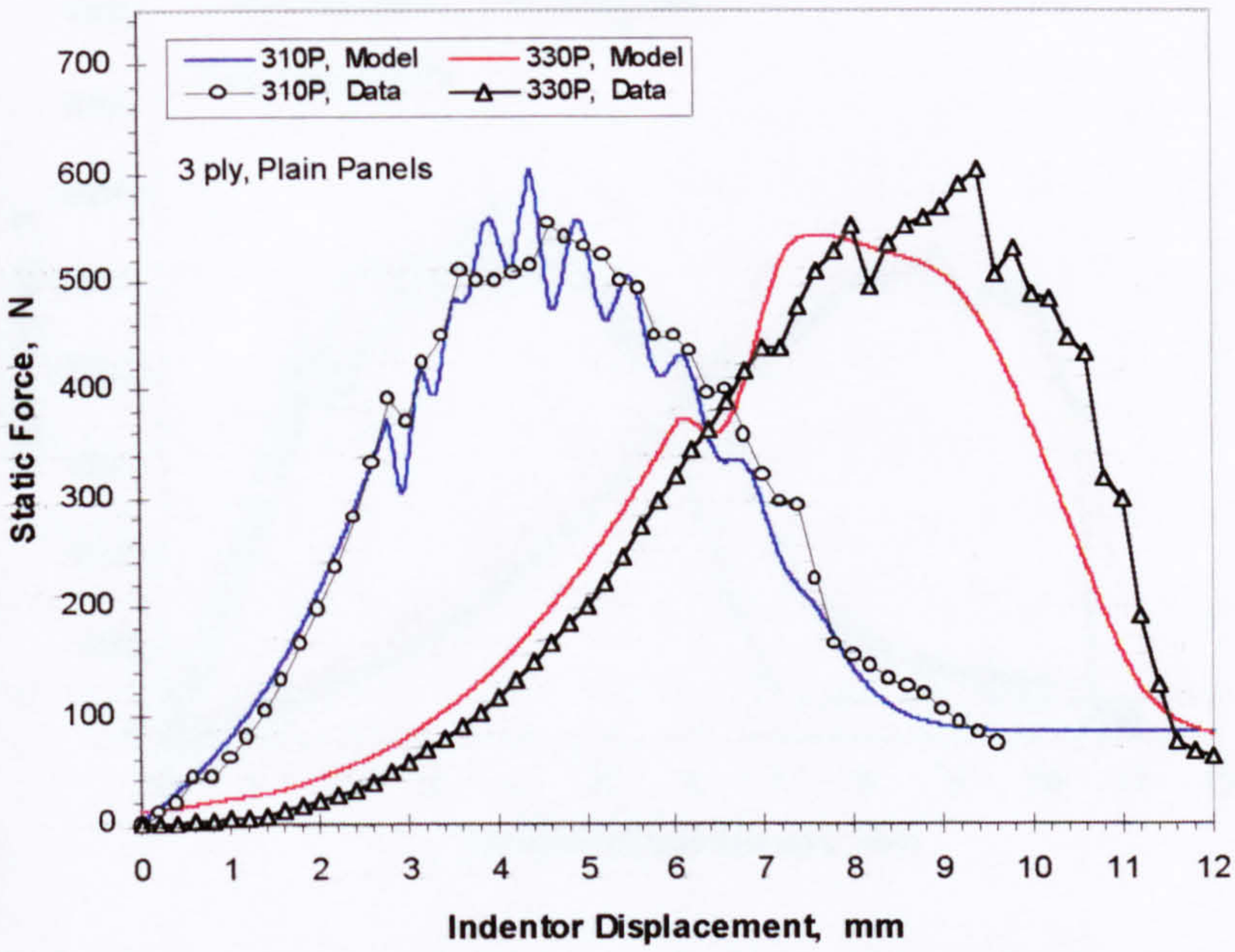

Figure 6.8. Static force v.s. indentor displacement for the 3-ply, plain panels.

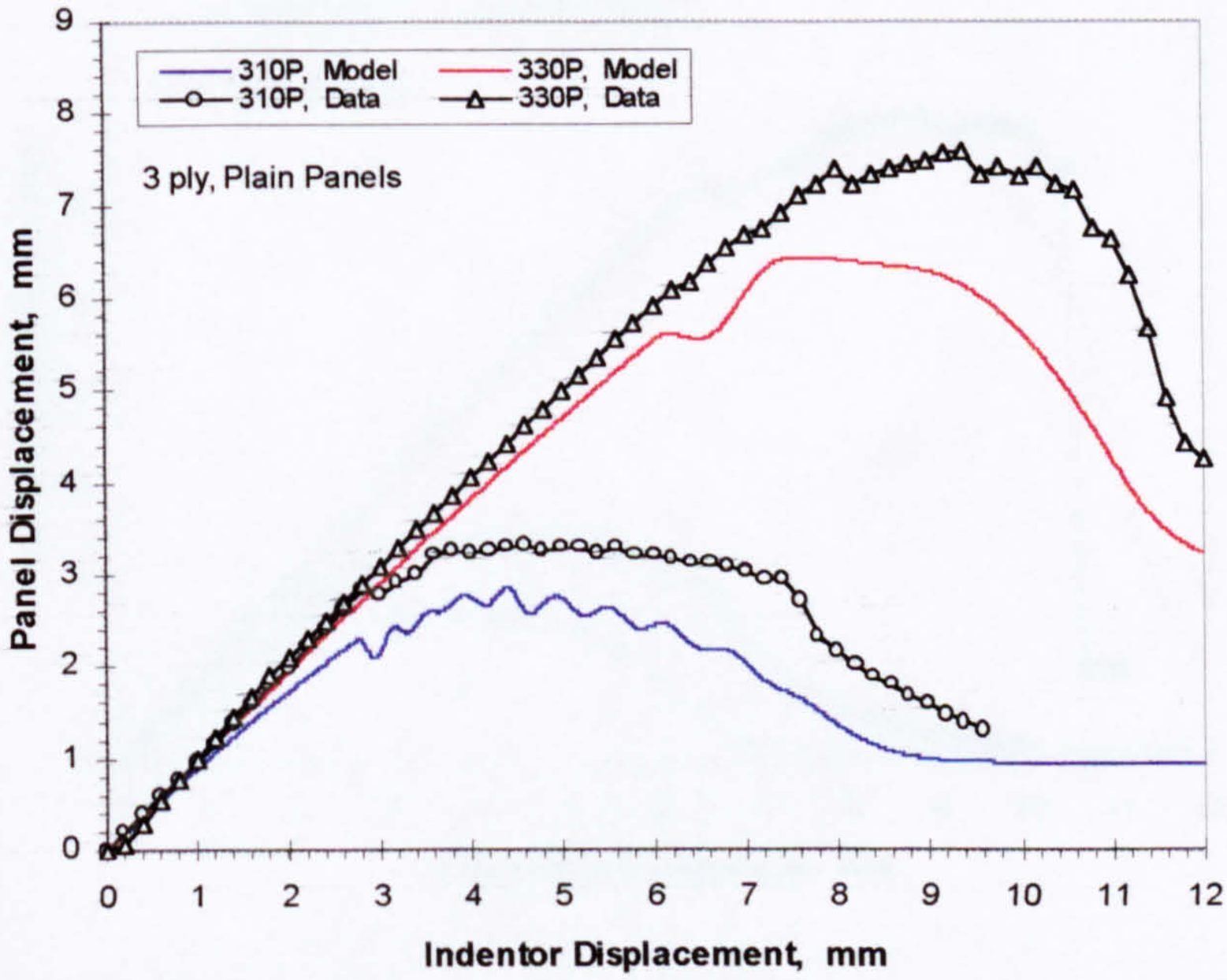

Figure 6.9. Panel displacement v.s. indentor displacement for the 3-ply, plain panels.

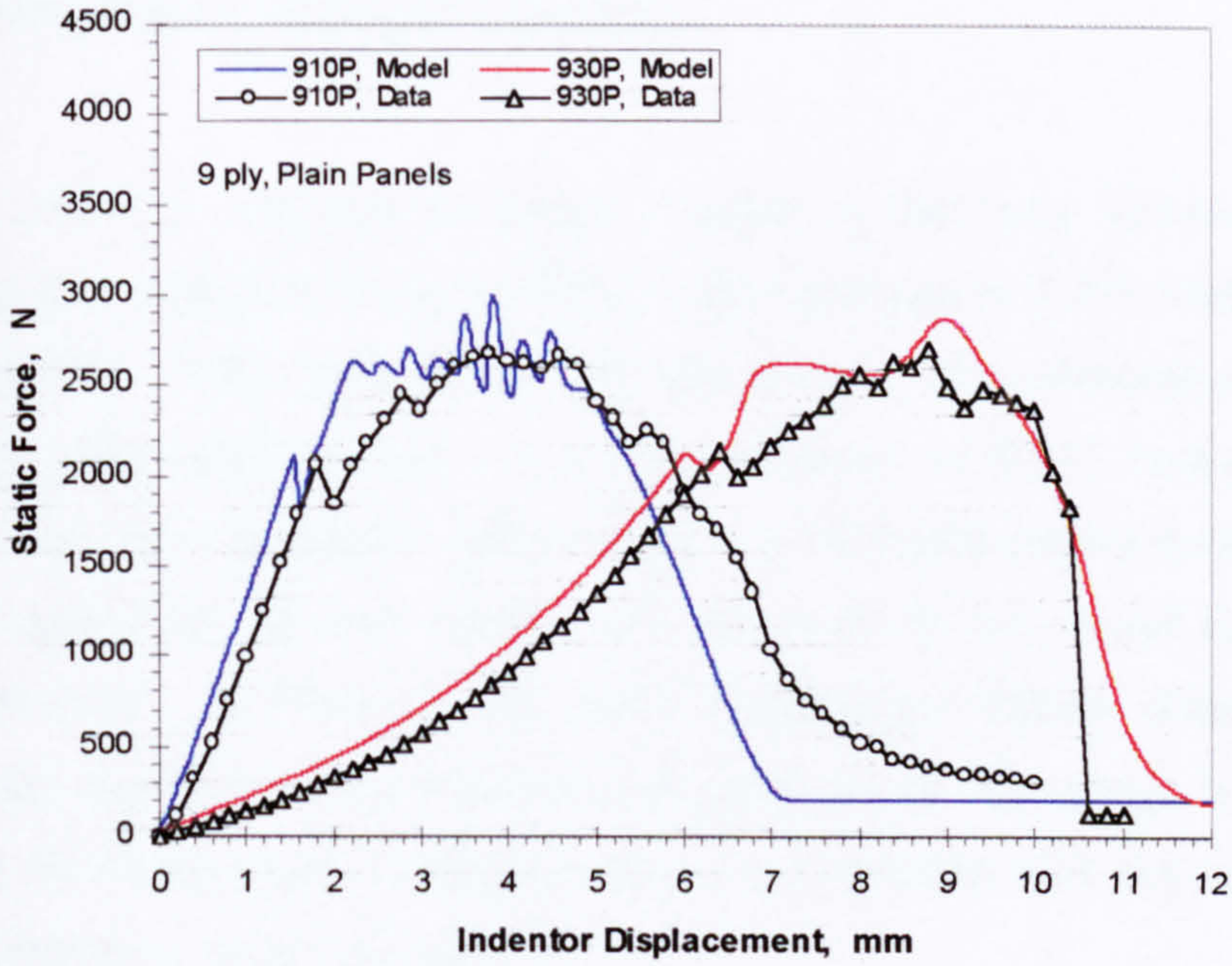

Figure 6.10. Static force v.s. indentor displacement for the 9-ply, plain panels.

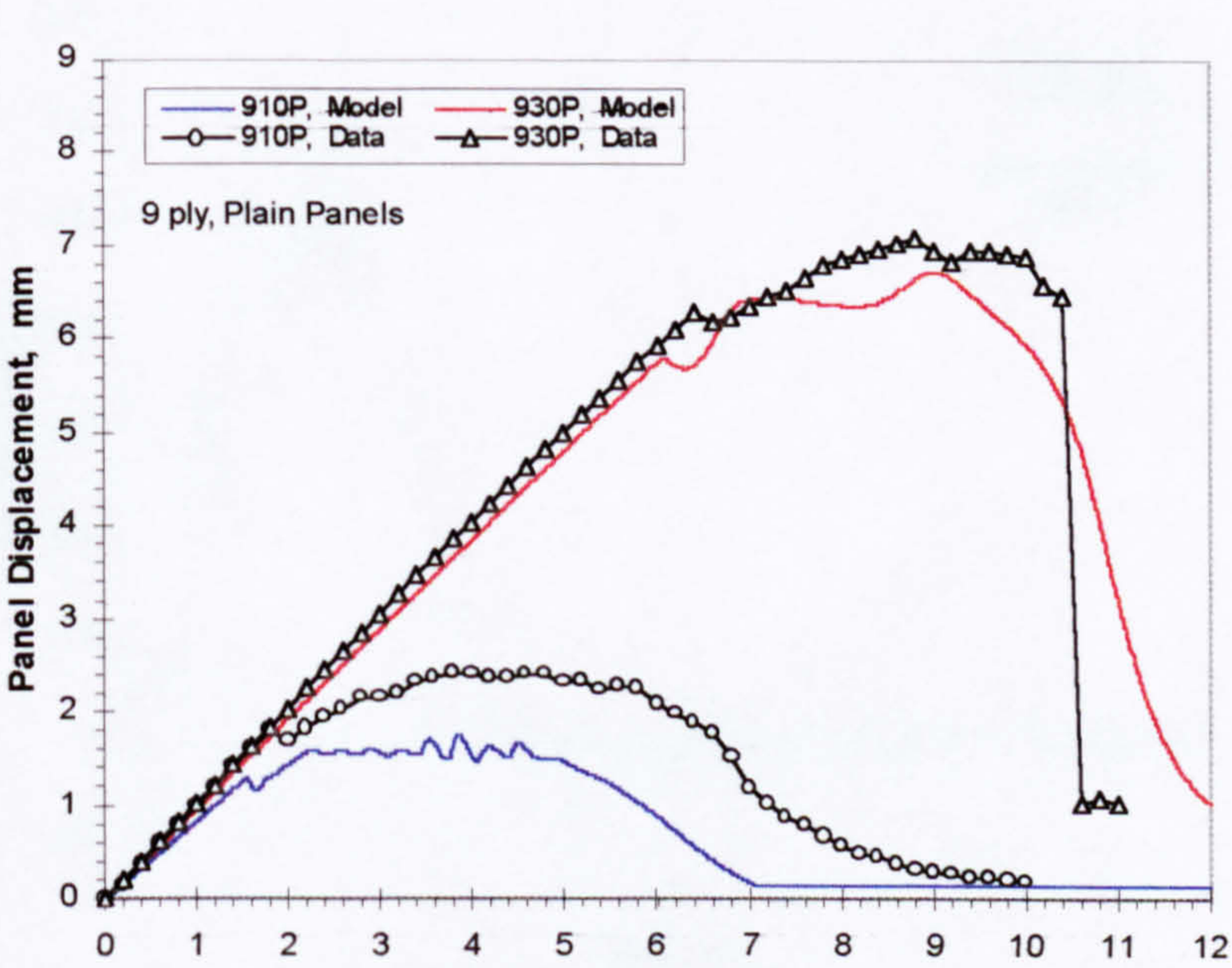

Figure 6.11. Panel displacement v.s. indentor displacement for the 9-ply, plain panels.

6.3.1.2 IMPACT TEST MODELLING RESULTS

Figures 6.12 and 6.13 compares the impact response of the 3-ply, 100-mm diameter, plain panel to that predicted by the model at impact energies of 0.697 Joule and 2.270 Joules respectively. These figures show the time histories of accelerometer force load cell force and panel displacement. At an impact energy of 0.697 Joules the model results are in very good agreement with the data. At the higher impact energy of 2.270 Joules good agreement between model and data could be still found for the force histories. However, deviations in the panel displacement history (Figure 6.13(c)) between model results and data become more apparent at this energy level. These deviations in the displacement history appear to be consistent with the results of the static indentation tests shown in Figure 6.9.

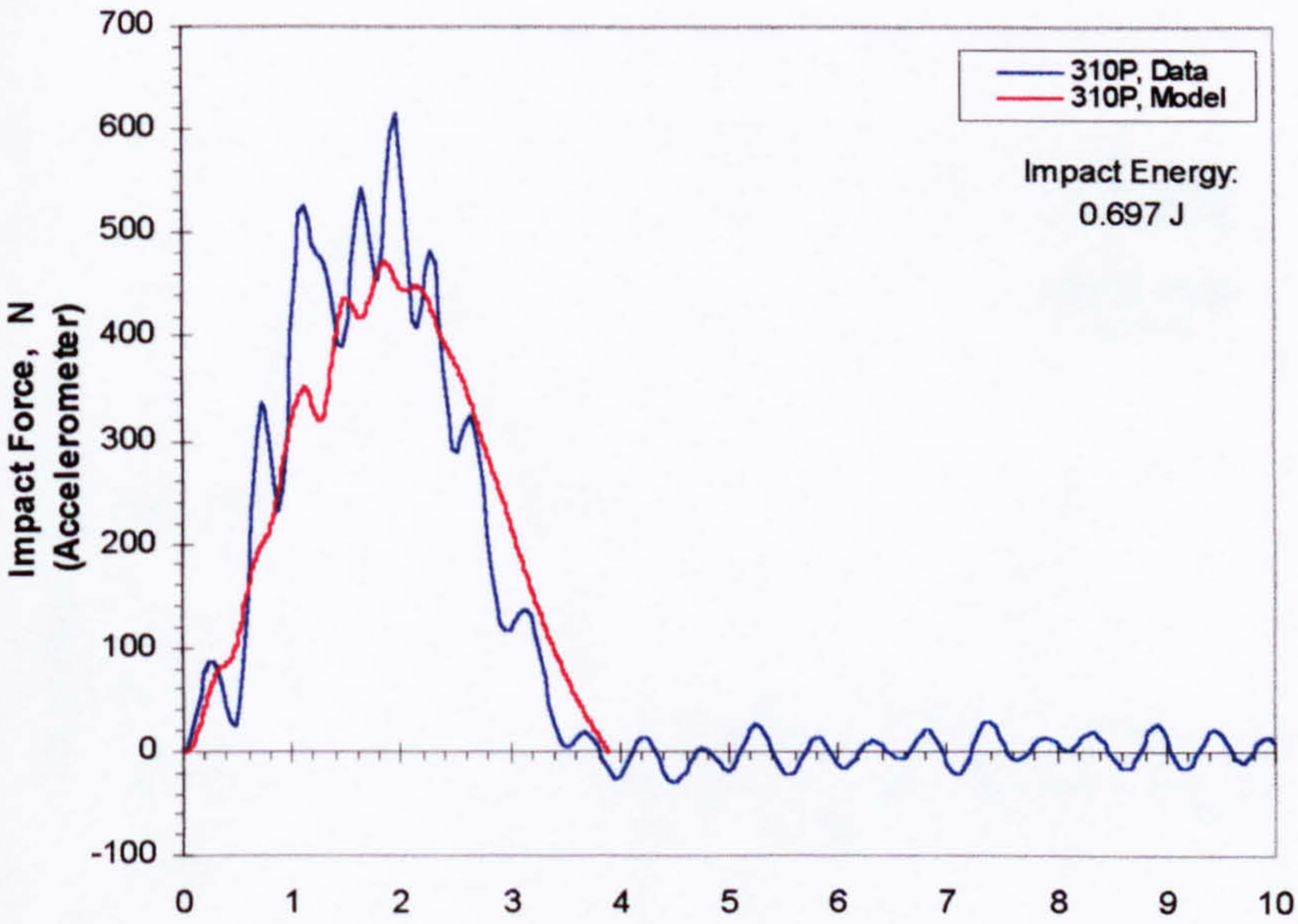

Figure 6.12(a). Accelerometer force history for the 3-ply, 100-mm diameter, plain panel at an impact energy of 0.697 Joule (29.8% of the impact penetration energy).

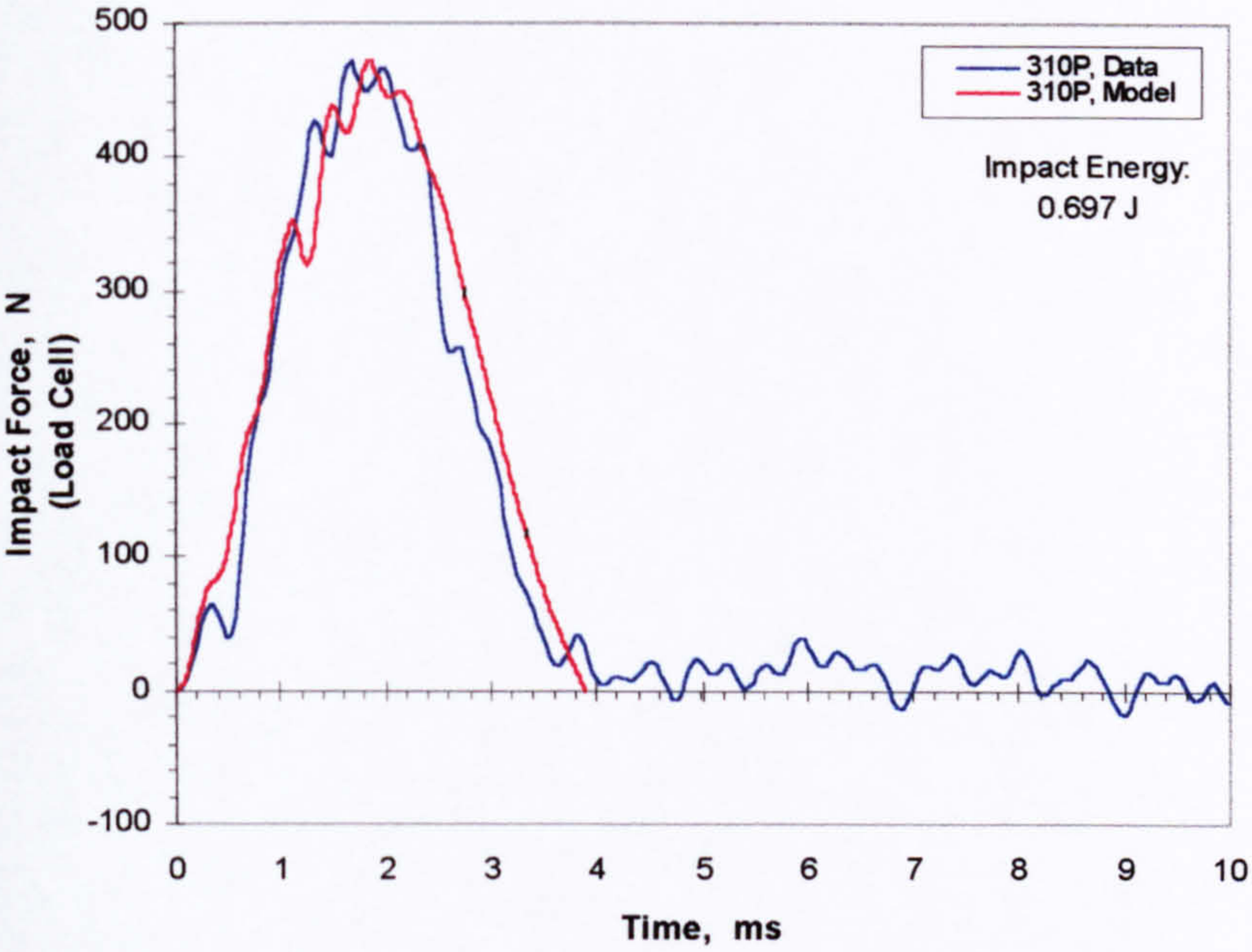

Figure 6.12(b). Load cell force history for the 3-ply, 100-mm diameter, plain panel at an impact energy of 0.697 Joule (29.8% of the impact penetration energy).

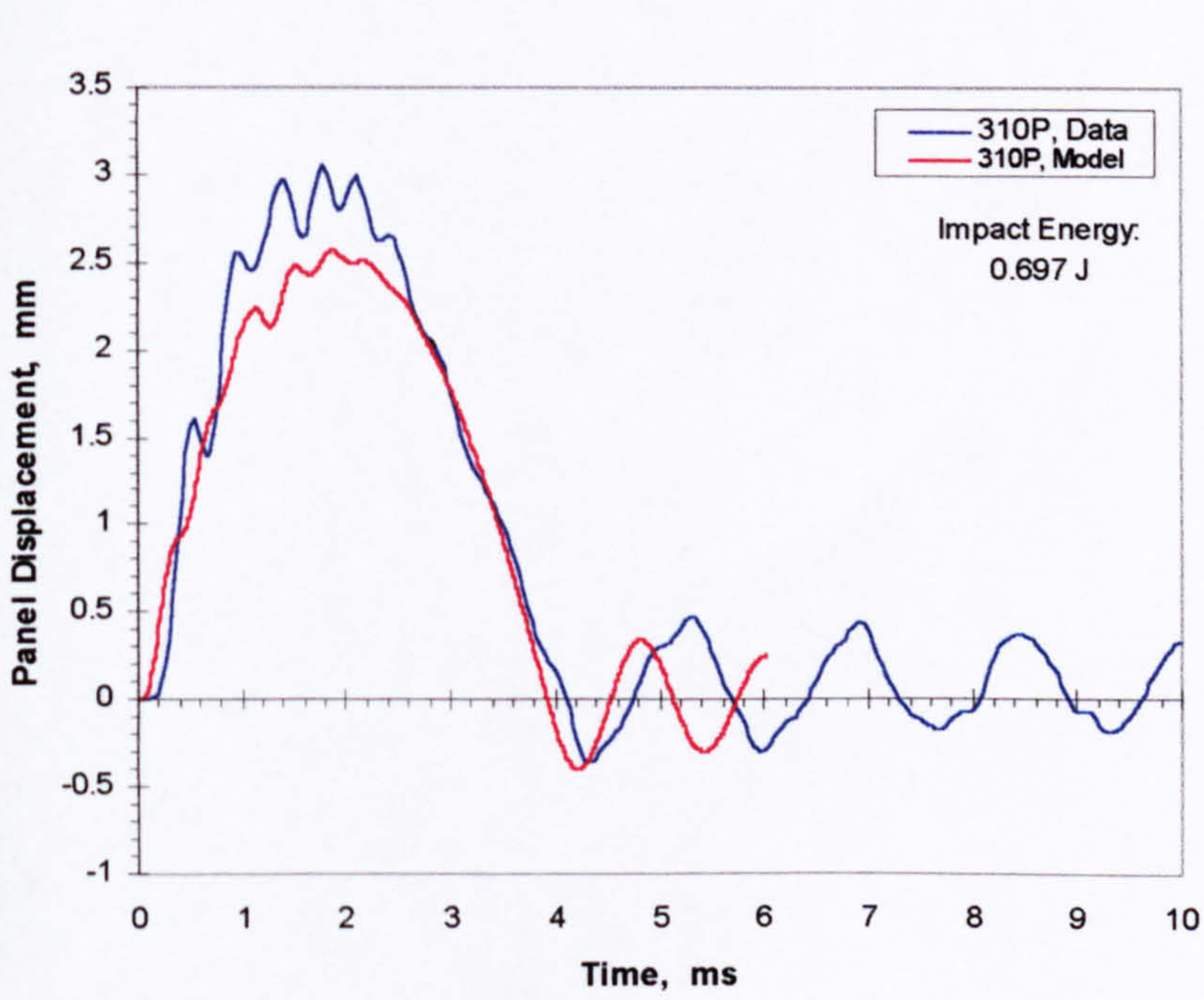

Figure 6.12(c). Displacement history for the 3-ply, 100-mm diameter, plain panel at an impact energy of 0.697 Joule (29.8% of the impact penetration energy).

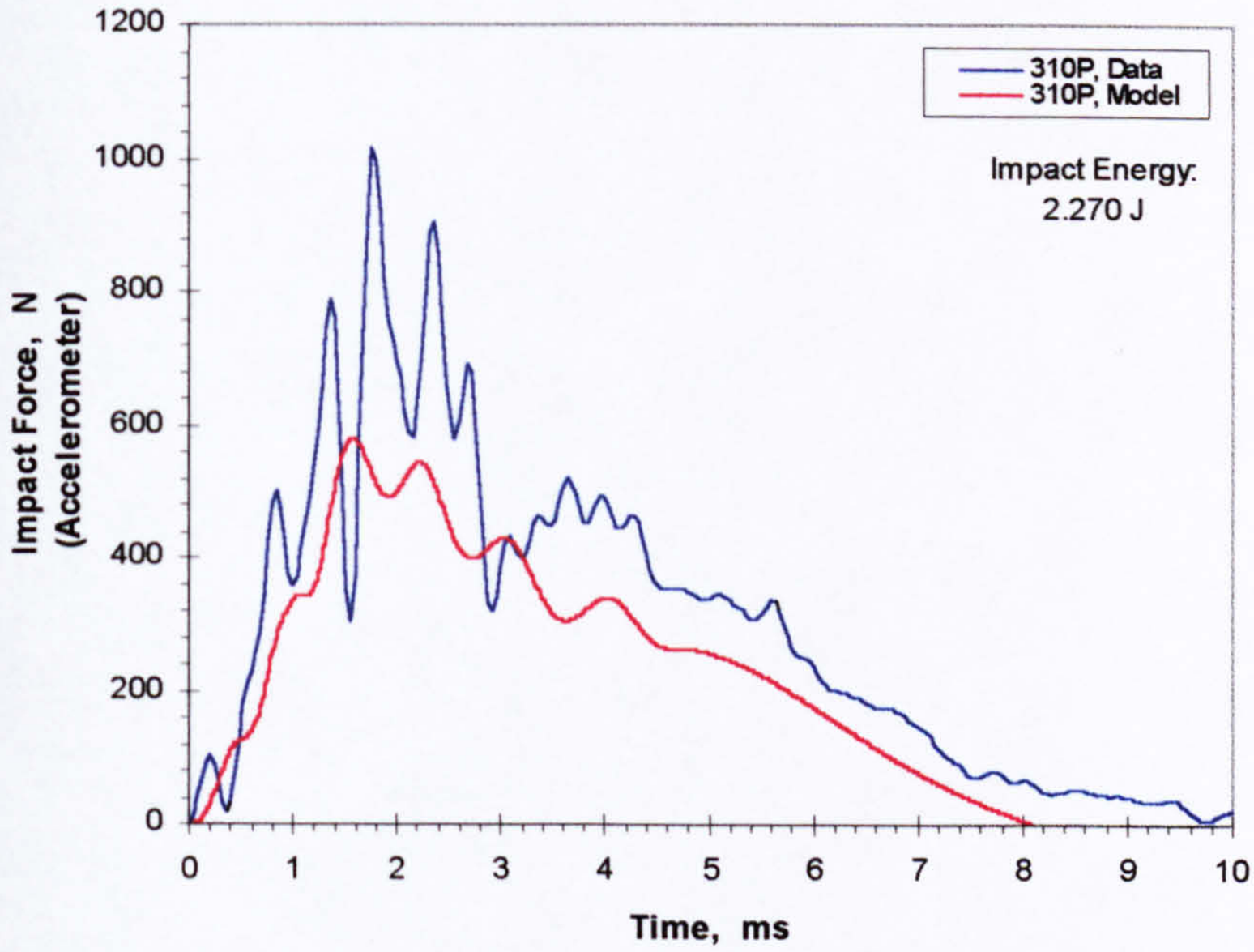

Figure 6.13(a). Accelerometer force history for the 3-ply, 100-mm diameter, plain panel at an impact energy of 2.270 Joules (96.9% of the impact penetration energy).

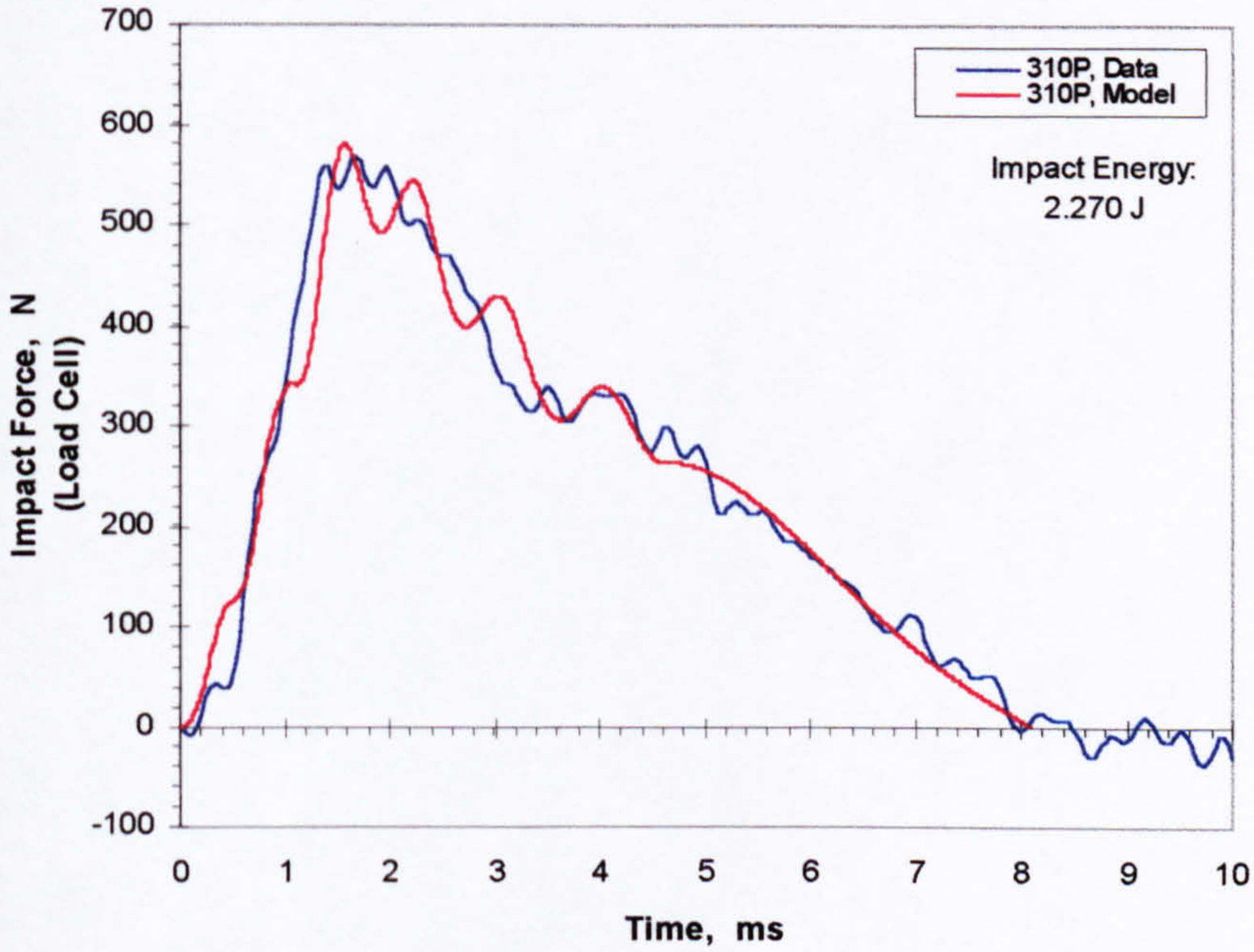

Figure 6.13(b). Load cell force history for the 3-ply, 100-mm diameter, plain panel at an impact energy of 2.270 Joules (96.9% of the impact penetration energy).

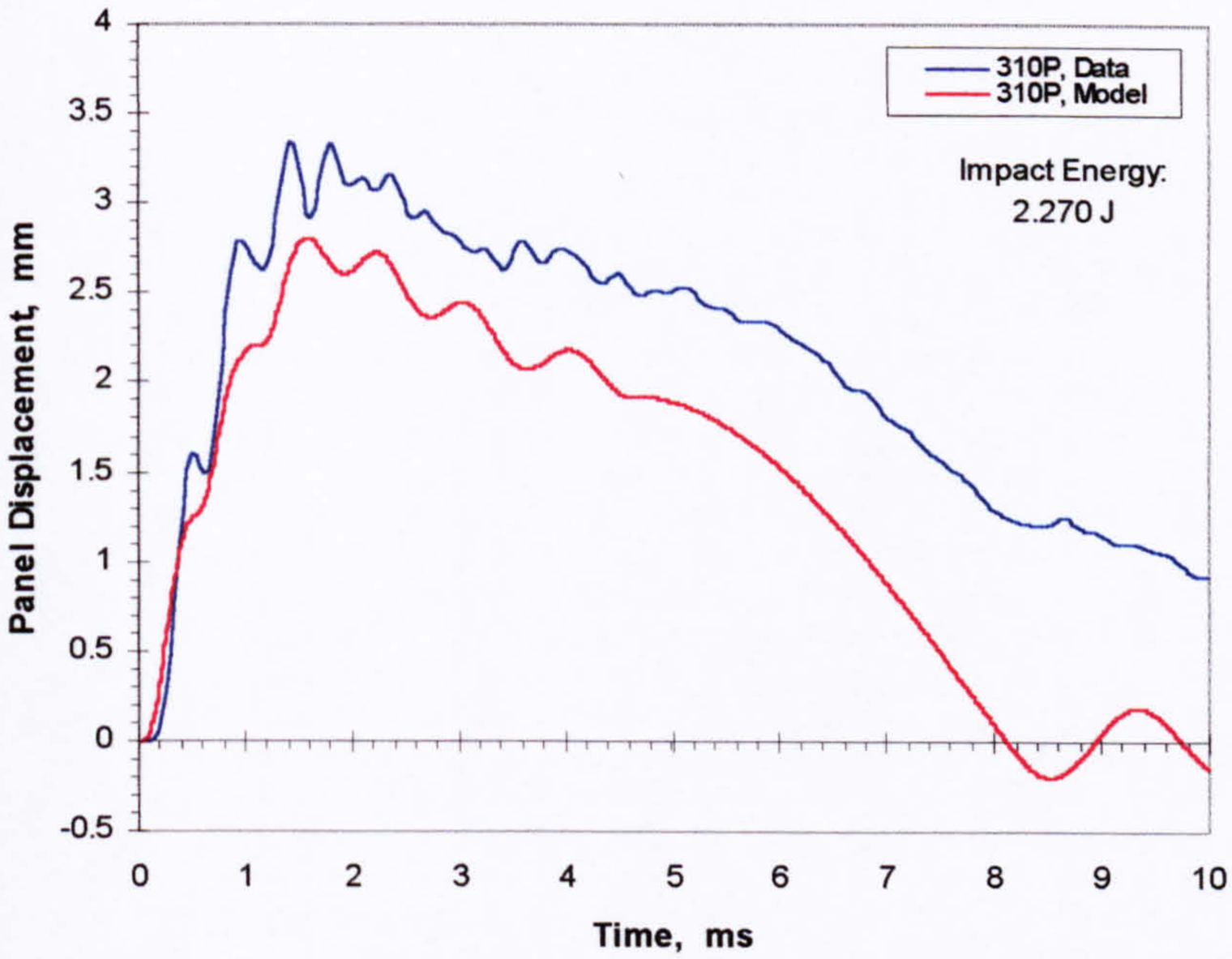

Figure 6.13(c). Displacement history for the 3-ply, 100-mm diameter, plain panel at an impact energy of 2.270 Joules (96.9% of the impact penetration energy).

The comparison between model results and impact data for the 3-ply, 300-mm diameter plain panels are presented in Figures 6.14 and 6.15. The impact energies indicated in these figures are 1.914 Joules and 2.510 Joules respectively. Like Figures 6.12 and 6.13 above, the time histories for accelerometer force, load cell force (if the data were available) and panel displacement are shown. Good agreement could again be found between model results and actual data in the impact force history. Significant underestimation of the panel displacement by the model occurs at the higher impact energy of 2.510 Joules. It appears that permanent deformation of the panel due to material damage and/or non-recoverable deformation due to membrane stretching is influencing the actual panel displacement response. This also appears to be true of the displacement response of the 3-ply, 100-mm diameter panels discussed earlier in this section.

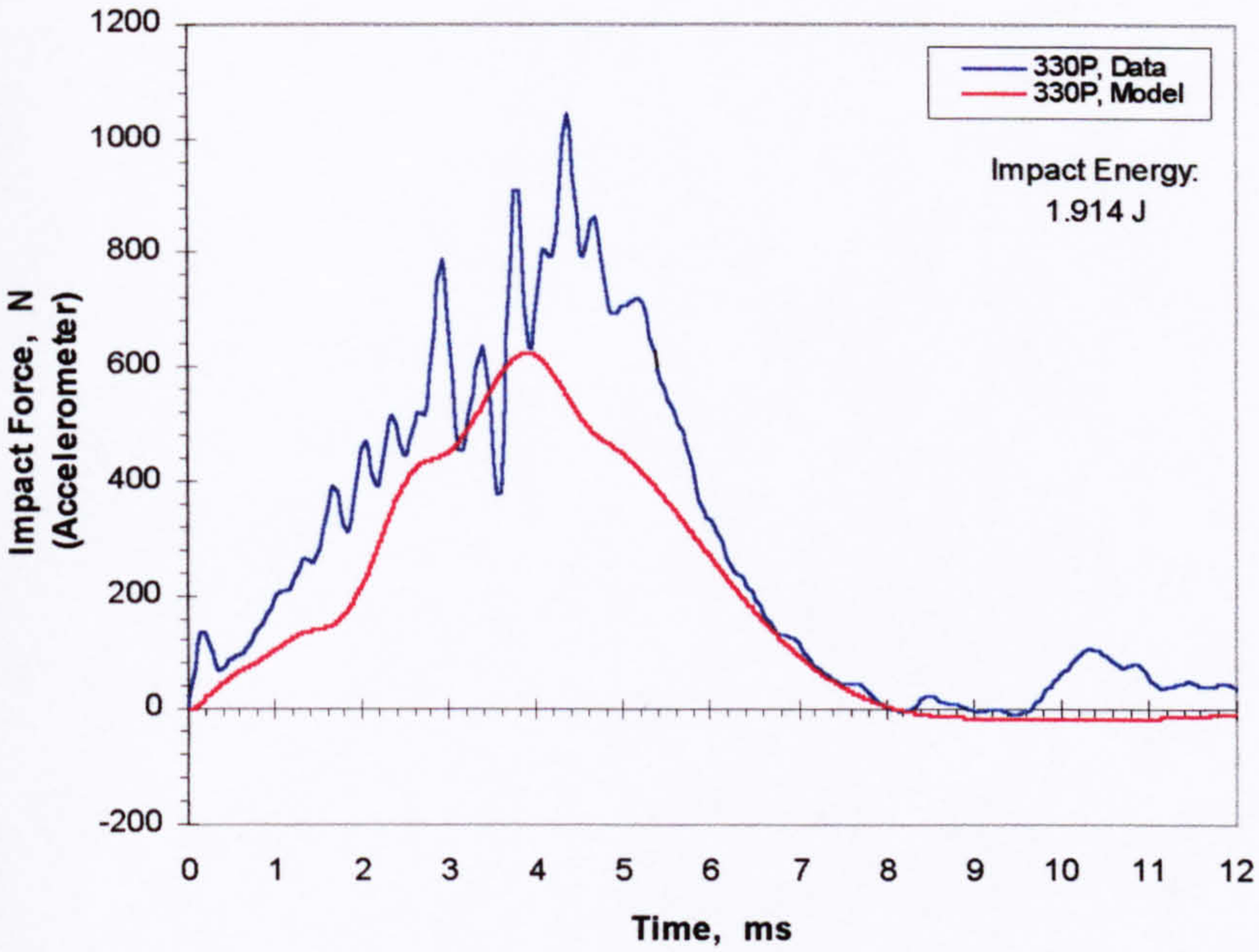

Figure 6.14(a). Accelerometer force history for the 3-ply, 300-mm diameter, plain panel at an impact energy of 1.914 Joules (63.3% of the impact penetration energy).

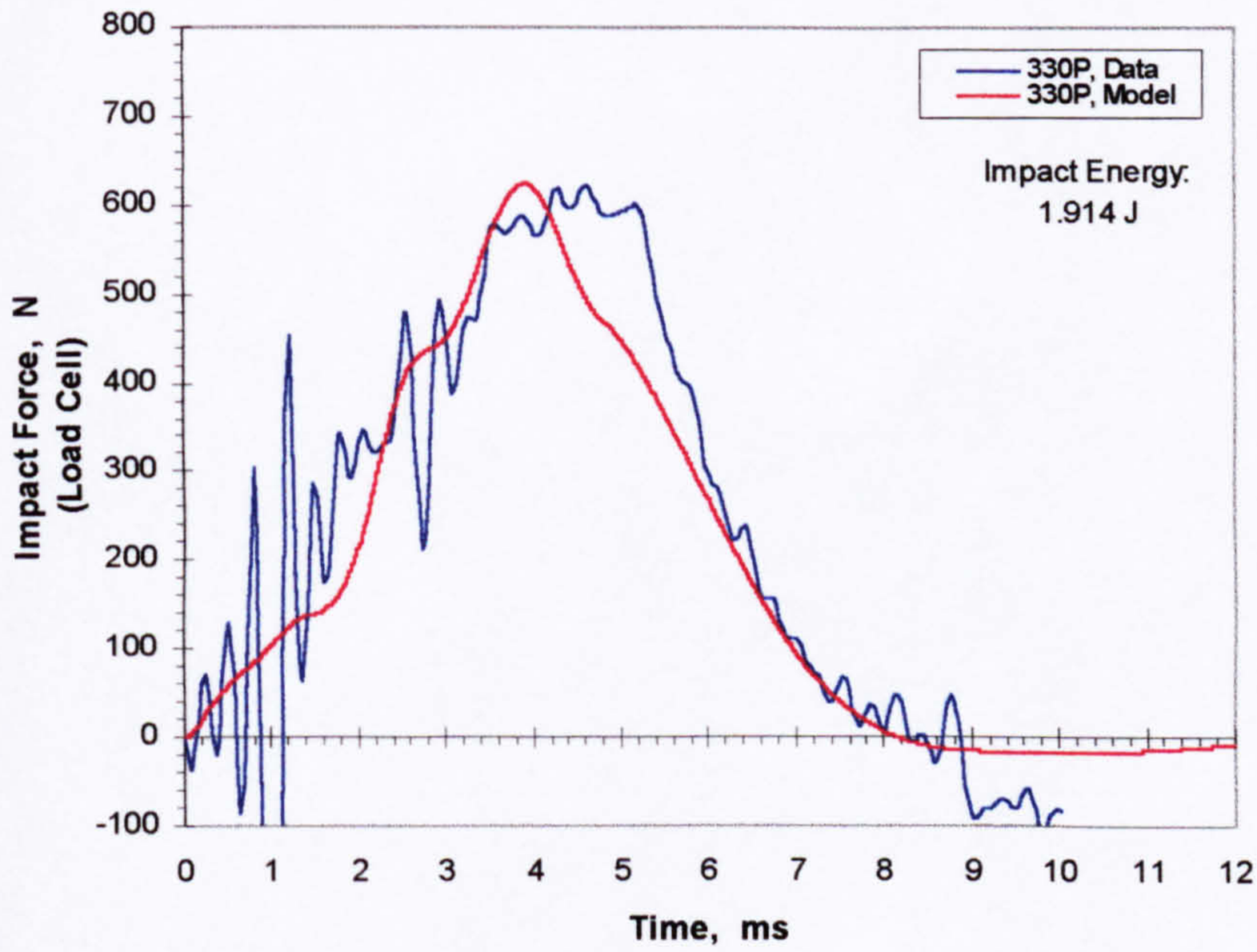

Figure 6.14(b). Load cell force history for the 3-ply, 300-mm diameter, plain panel at an impact energy of 1.914 Joules (63.3% of the impact penetration energy).

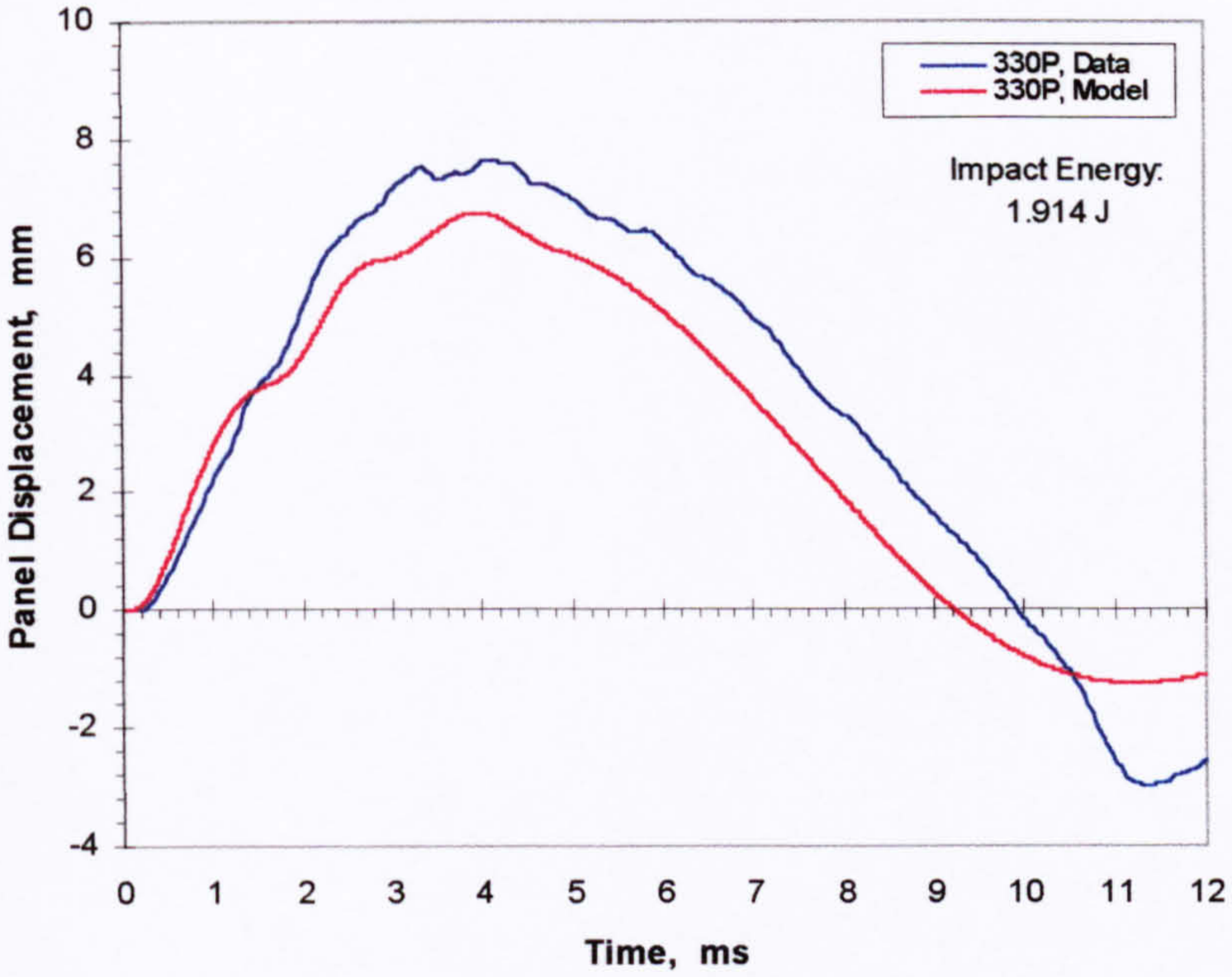

Figure 6.14(c). Displacement history for the 3-ply, 300-mm diameter, plain panel at an impact energy of 1.914 Joules (63.3% of the impact penetration energy).

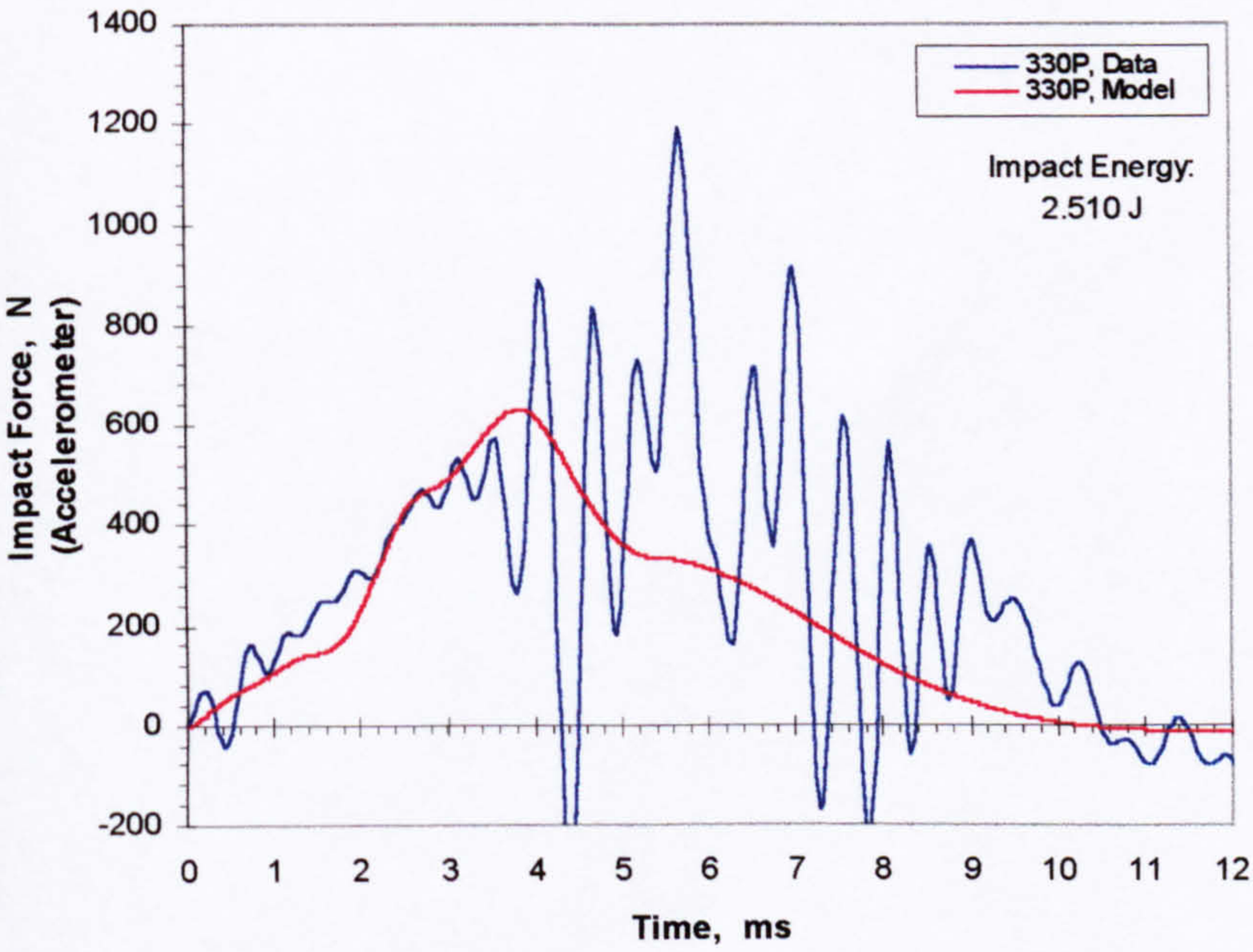

Figure 6.15(a). Accelerometer force history for the 3-ply, 300-mm diameter, plain panel at an impact energy of 2.510 Joules (83.0% of the impact penetration energy).

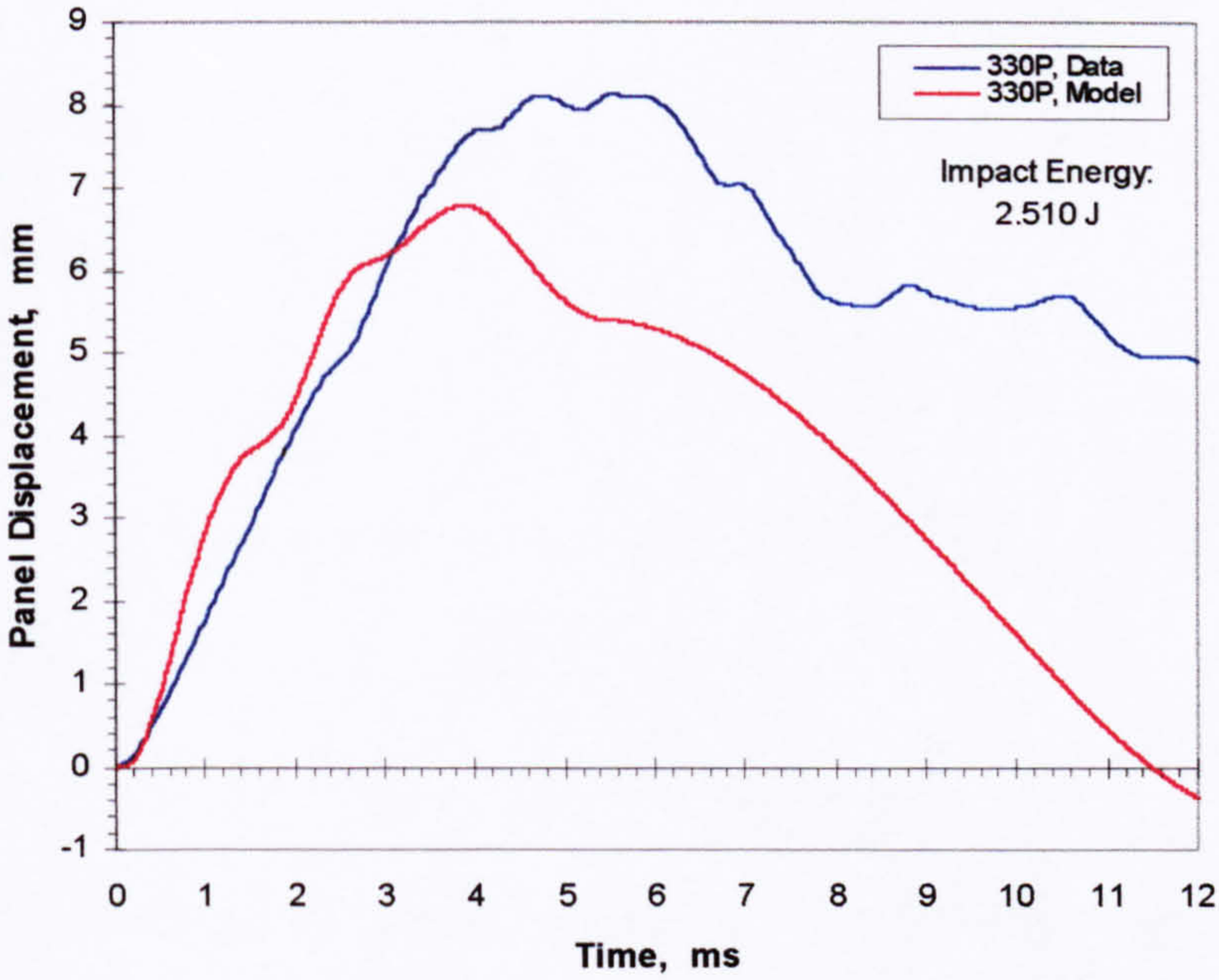

Figure 6.15(b). Displacement history for the 3-ply, 300-mm diameter, plain panel at an impact energy of 2.510 Joules (83.0% of the impact penetration energy).

The model results for the 9-ply, 100-mm diameter panels are shown in Figures 6.16 and 6.17. The impact energies indicted in these figures are 1.323 Joules and 4.396 Joules respectively. The largest deviations between model results and actual data can be found in these figures. The model results predict a response that is considerably stiffer than that indicated by the data. This reinforces the observation made in Section 6.3.1.1 that "thick" panels (or panels with small diameter-to-thickness ratios) are more sensitive to the rigidity or physical stiffness of the actual boundary conditions. In addition, through the thickness phenomenon in the contact region are more likely to influence the damage response of thick panels than it would thin panels. These are the possibilities that could account for the differences between model results and actual data presented in Figures 6.16 and 6.17.

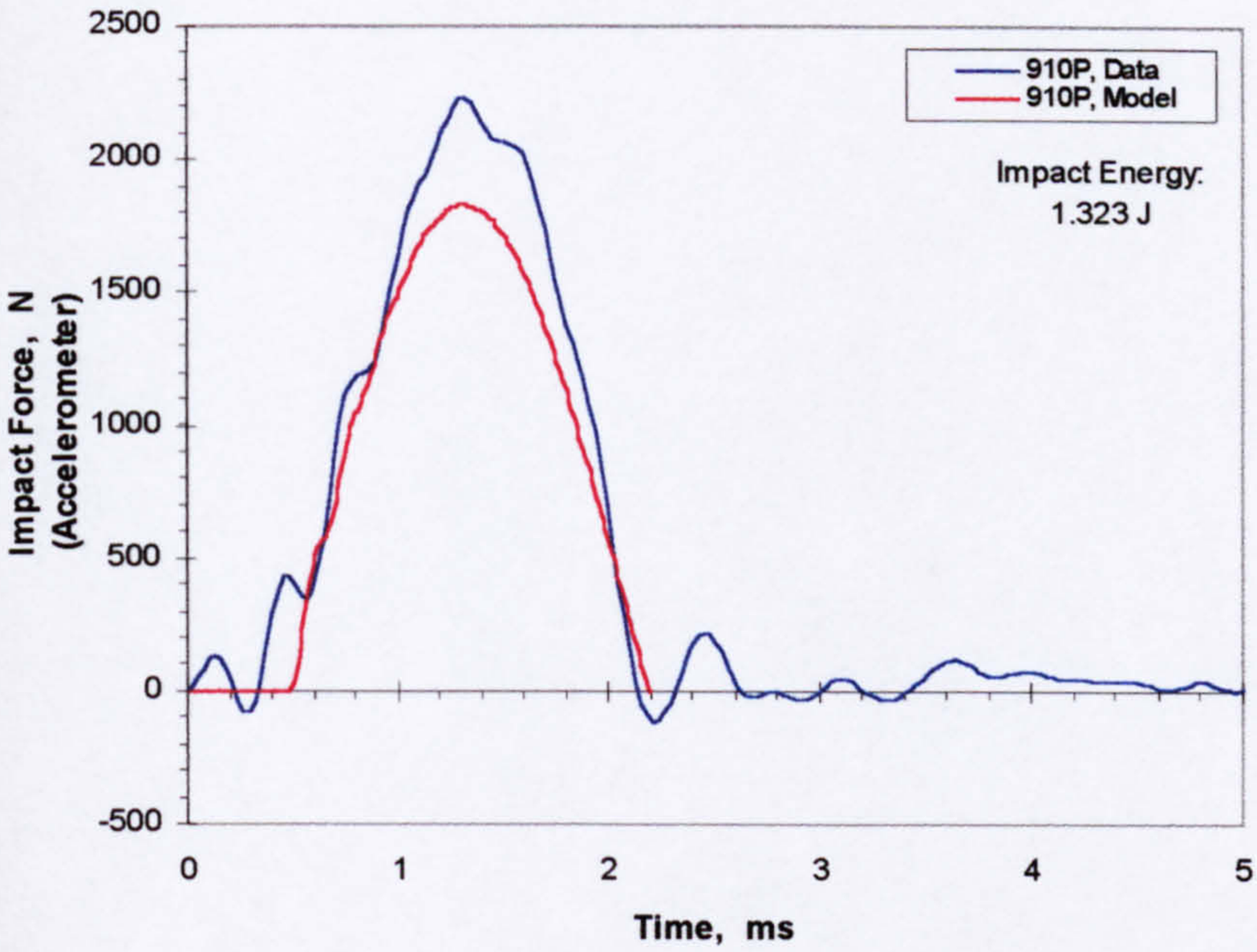

Figure 6.16(a). Accelerometer force history for the 9-ply, 100-mm diameter, plain panel at an impact energy of 1.323 Joules (12.1% of the impact penetration energy).

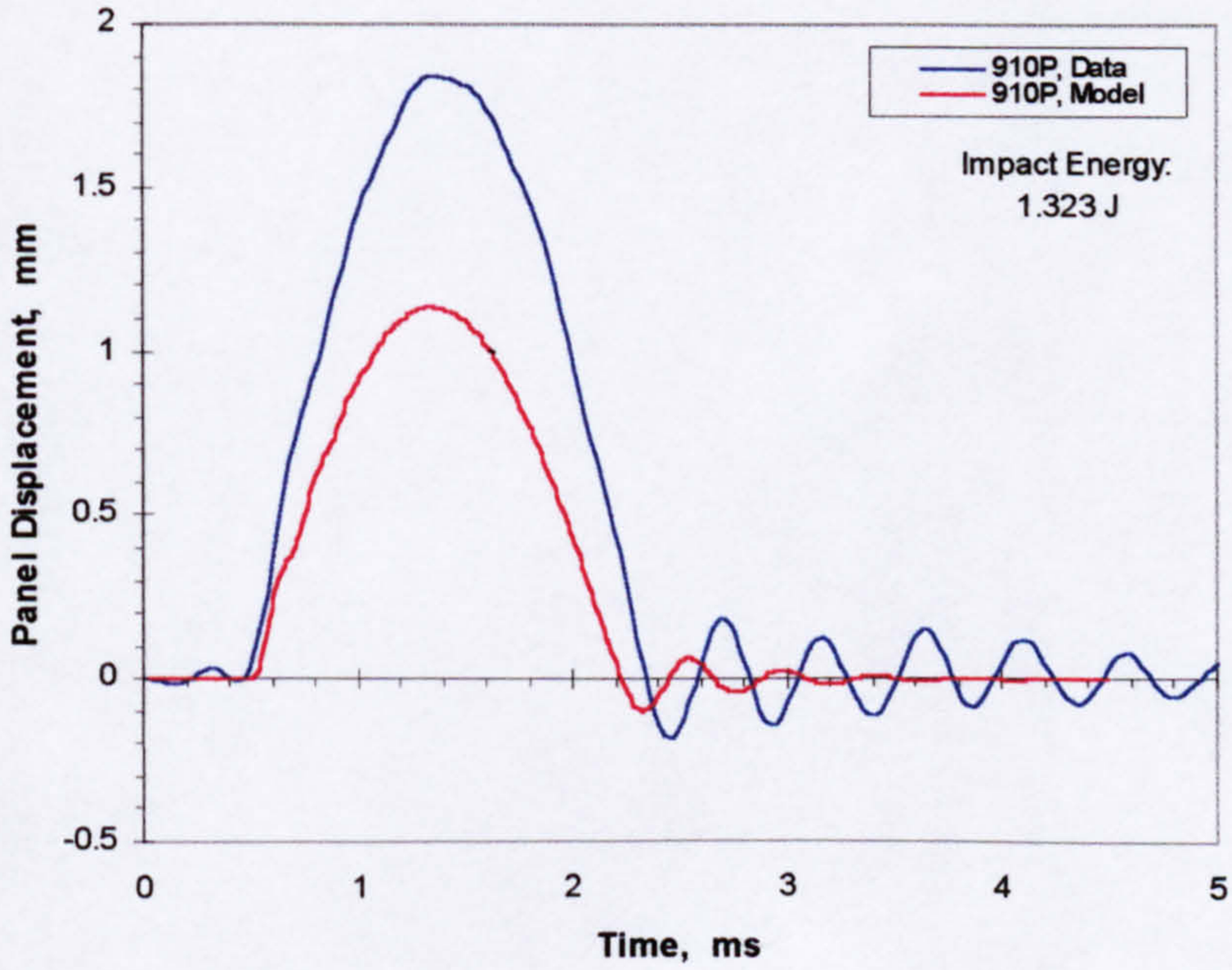

Figure 6.16(b). Displacement history for the 9-ply, 100-mm diameter, plain panel at an impact energy of 1.323 Joules (12.1% of the impact penetration energy).

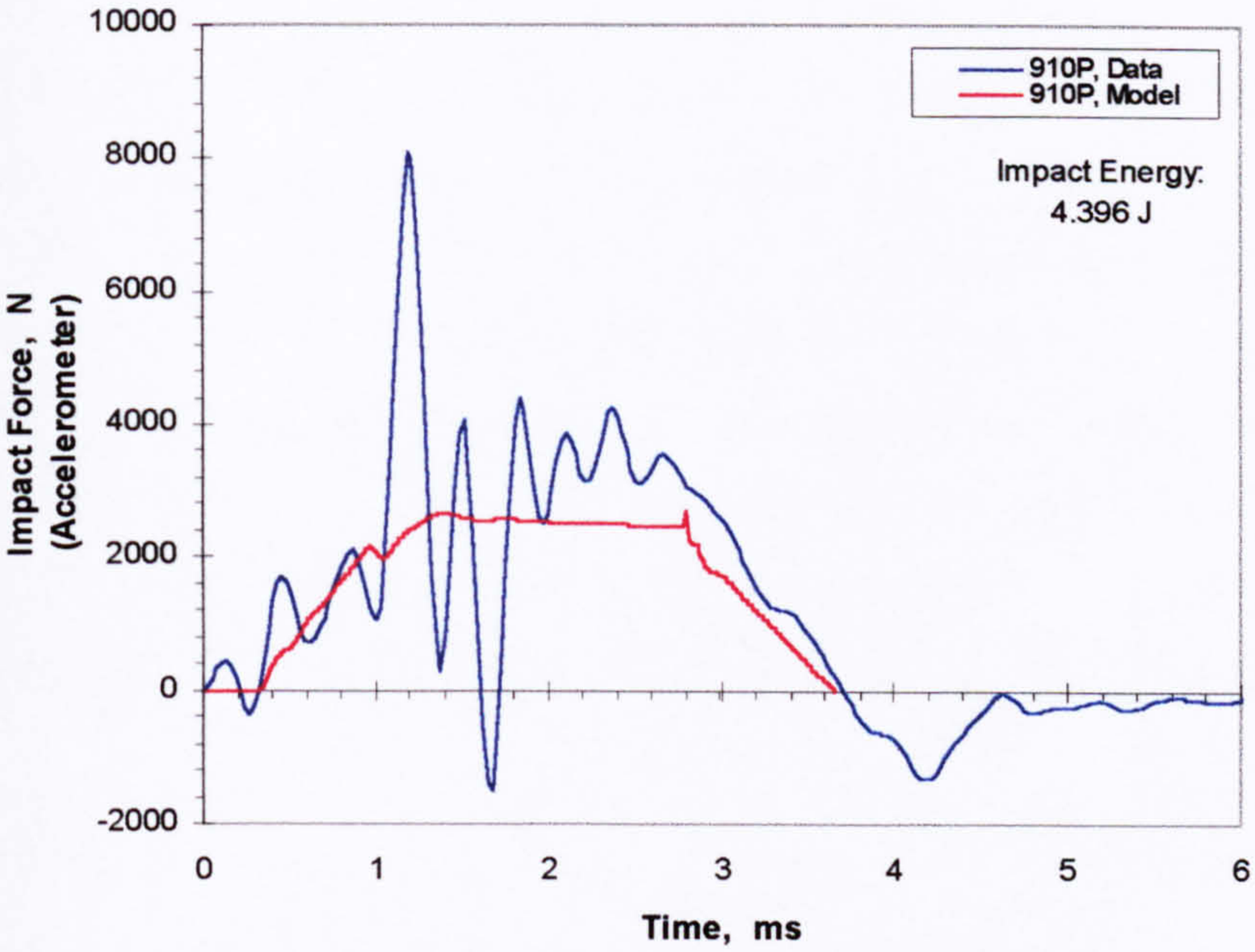

Figure 6.17(a). Accelerometer force history for the 9-ply, 100-mm diameter, plain panel at an impact energy of 4.396 Joules (40.3% of the impact penetration energy).

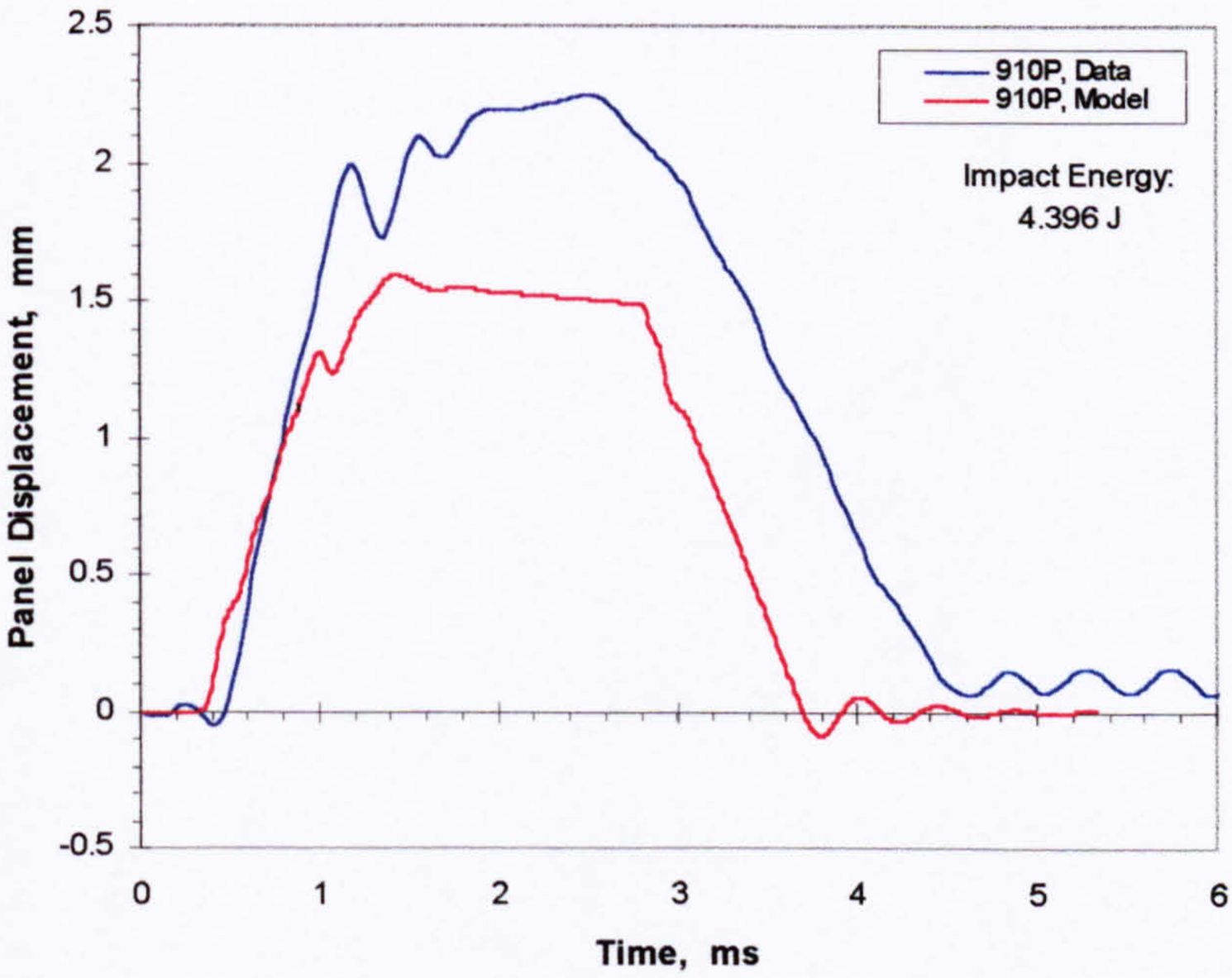

Figure 6.17(b). Displacement history for the 9-ply, 100-mm diameter, plain panel at an impact energy of 4.396 Joules (40.3% of the impact penetration energy).

Figures 6.18(a) and 6.18(b) show the model results for a 9-ply, 300-mm diameter, plain panel subjected to an impact energy of 6.616 Joules. Again we find close agreement between model results and actual data just as we found close agreement between model results and actual data for the 3-ply plain panels. This close agreement can be explained by the fact that the 9-ply, 100-mm diameter panel has a diameter-to-thickness ratio of a little over 110. This makes its impact behaviour more akin to that of "thin" panel. The results so far presented confirm that the model is best applicable to "thin" panels with diameter-to-thickness ratios greater than 100 (an idea that was first proposed in Section 6.3.1.1).

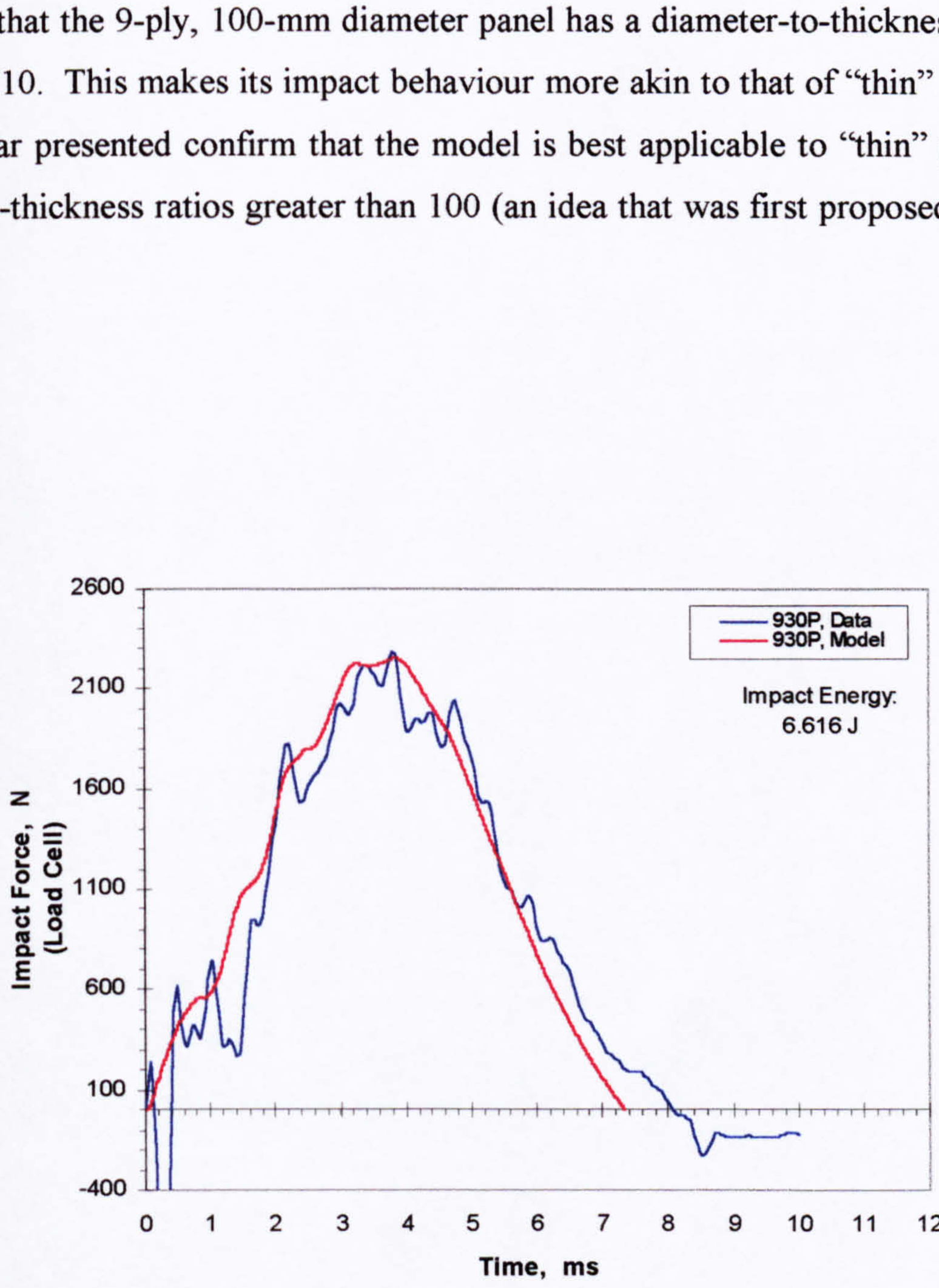

Figure 6.18(a). Load cell force history for the 9-ply, 300-mm diameter, plain panel at an impact energy of 6.616 Joules (45.6% of the impact penetration energy).

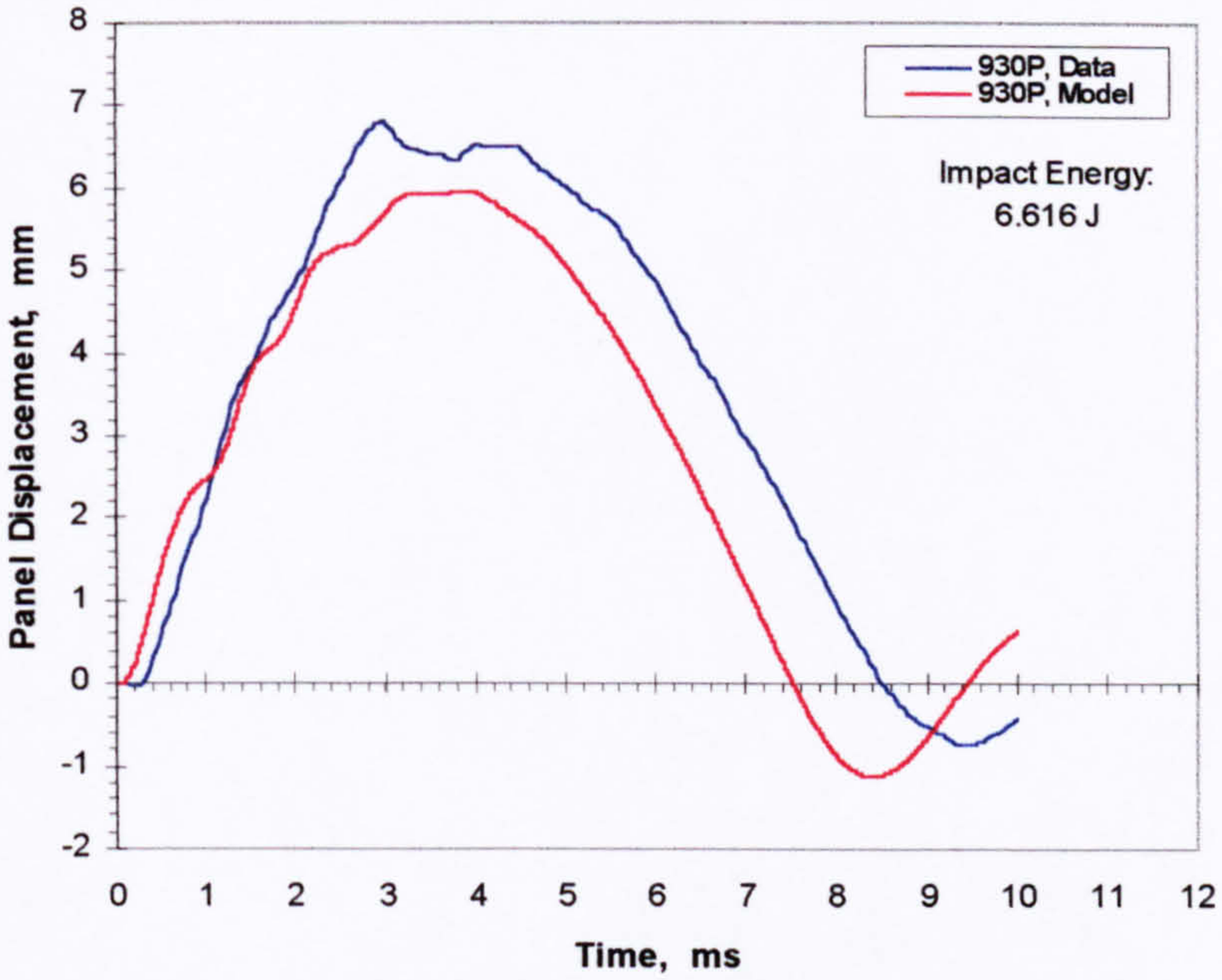

Figure 6.18(b). Displacement history for the 9-ply, 300-mm diameter, plain panel at an impact energy of 6.616 Joules (45.6% of the impact penetration energy).

6.3.2 RESULTS FOR THE STIFFENED PANELS

For the modelling of the 3-ply stiffened panels, the expression for the global panel stiffness K_3 in Equations 6.1 and 6.14 was modified by using the principle of superposition to include the additional stiffness contributed by the presence of the stiffeners. With the modifications, the global panel stiffness is

$$K_3 = K_{bs} + K_m y_3^{\,2} + K_{T1} + K_{T3} \qquad \text{Eqn. 6.20}$$

where K_{T1} is the equivalent stiffness coefficient due to the stiffeners on either side of the load application point and K_{T3} is the equivalent stiffness coefficient due to the stiffener directly below the load application point. An attempt was made to calculate for these stiffness coefficients using the material properties and elementary beam theory. However, the values obtained were far larger than what was required to account for the

panel response exhibited in the static test data. Because of this K_{T1} and K_{T3} were estimated from static test results. The estimated values for these parameters are summarised in Table 6.4

Table 6.4. Estimates of the equivalent stiffness coefficients K_{T1} and K_{T3} (N/mm).

Panel Configuration	K_{T1}	K_{T3}
Plain	0	0
310T3 – 3-ply, 100-mm diameter. Load on the stiffener	0	505.28
330T3 – 3-ply, 300-mm diameter. Load on the stiffener	19.69	55.74
330T1 – 3-ply, 300-mm diameter. Load on the bay	38.92	0

When the stiffener below the load application point fails by tensile fracture of the web, the resulting support geometry would result in two cantilevered beams that are in contact at their free ends. This configuration is illustrated in Figure 6.19(B). Elementary beam theory dictates that the stiffness of such a configuration will be one-fourth of the stiffness of the intact beam shown in Figure 6.19(A). As such the values for K_{T3} in Table 6.4 are reduced accordingly when fracture of the stiffener web occurs. The force at which the stiffener directly below the load application point fails by fracture of the web was taken from experimental data since theoretical calculations using the material properties gives results that are very large to be consistent with test data. From the data the estimated values of the stiffener web failure force are 810 Newtons for the 100-mm diameter panels and 250 Newtons for the 300-mm diameter panels.

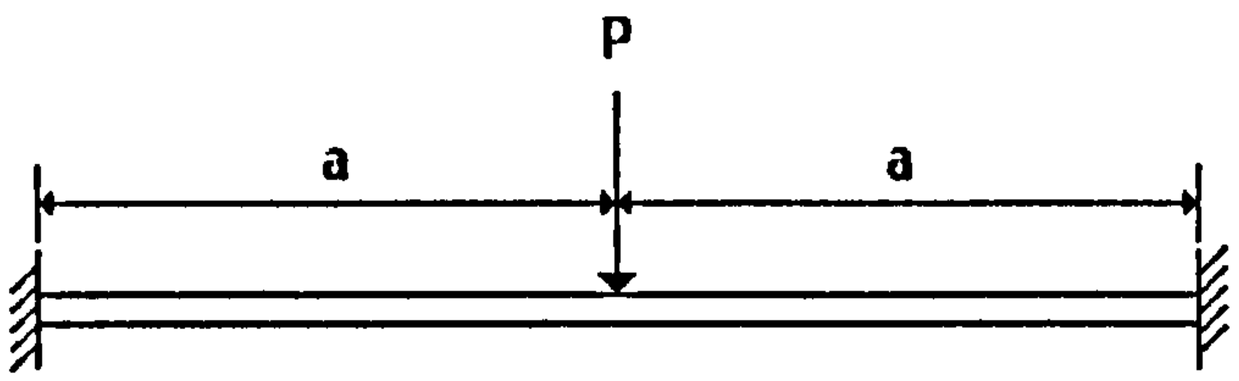

(A)

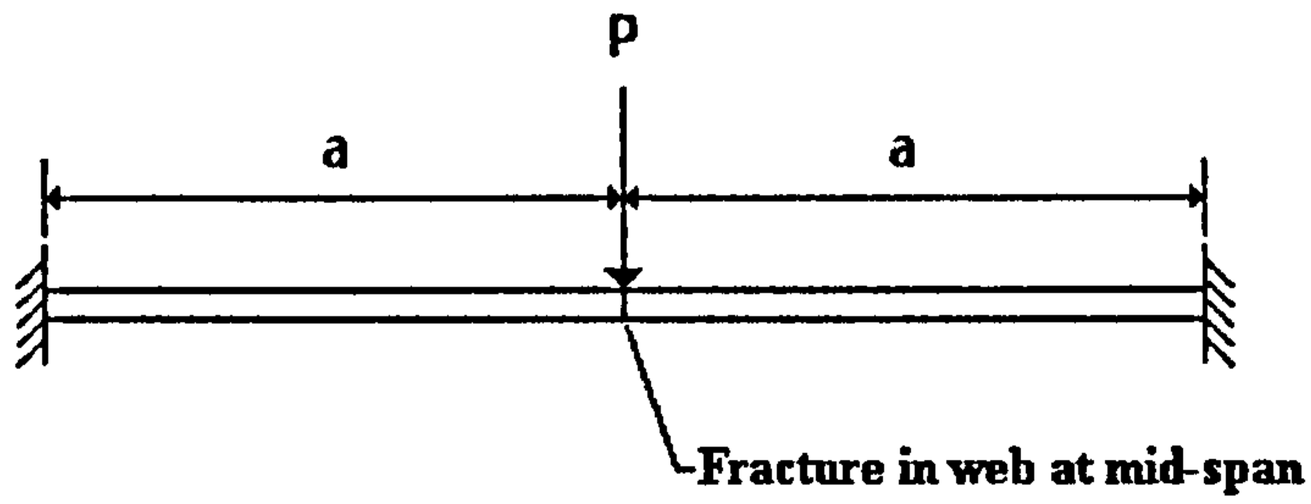

(B)

Figure 6.19. Illustration of an (A) intact stiffener and (B) fractured stiffener.

6.3.2.1 STATIC TEST MODELLING RESULTS

The static test modelling results for the 3-ply, 300-mm diameter stiffened panels are presented in Figures 6.20 and 6.21. For comparison static test data from the experiments were also cast in the same plots. Good agreement between model results and actual data could be found for both static load force and panel displacement up to an indentor displacement of just below 7 mm. This is the range where the load force is below 529 Newtons, the critical delamination force for a 3-ply panel. This suggests that the assumption of the applicability of the principle of superposition to the model for the stiffened panels appear to be valid. The results shown in Figures 6.20 and 6.21 also suggest that the presence of the stiffeners have a significant reinforcing effect on the stiffness of the panel.

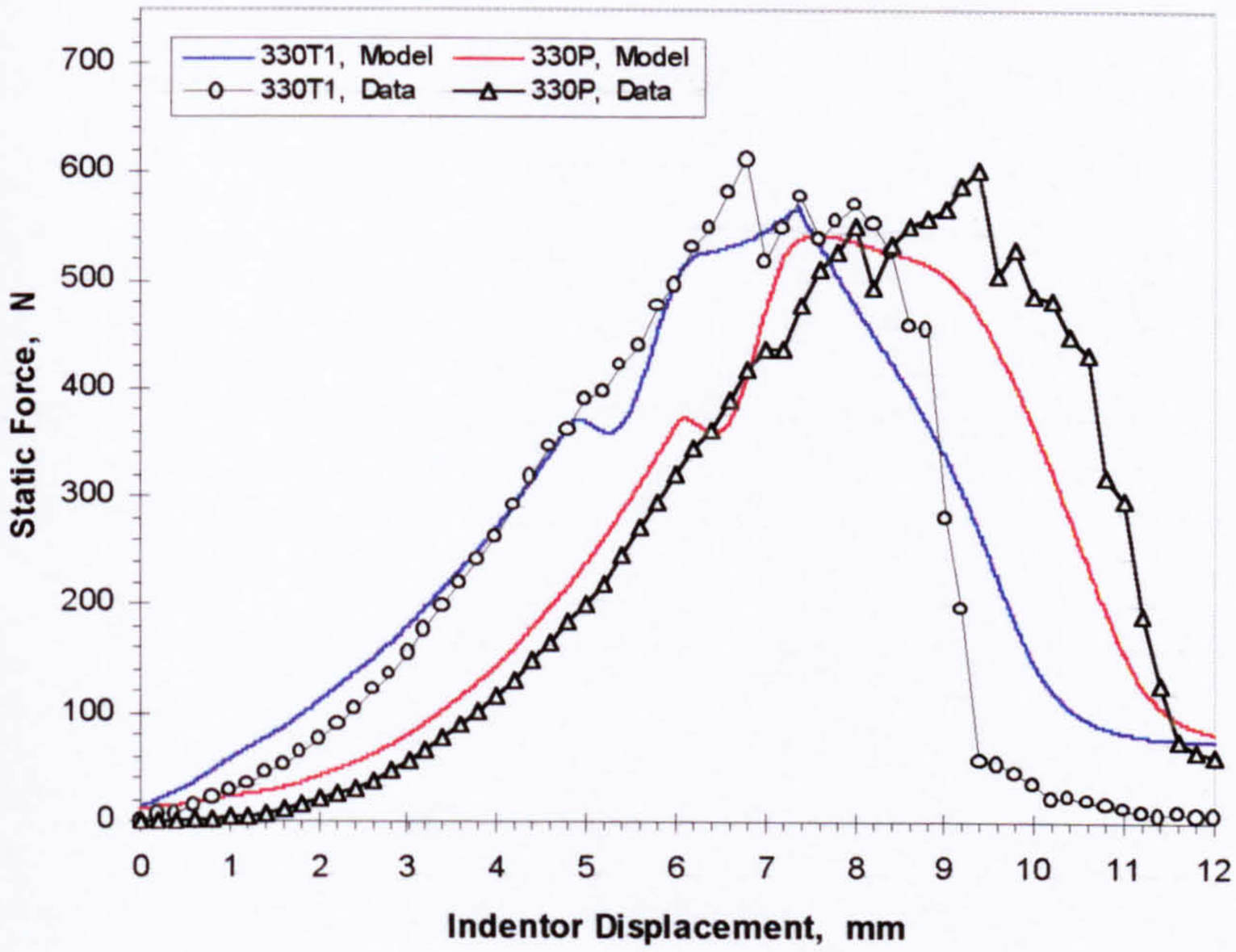

Figure 6.20. Static force v.s. indentor displacement for the 3-ply, 300-mm diameter, stiffened panel loaded on the bay (between the stiffeners).

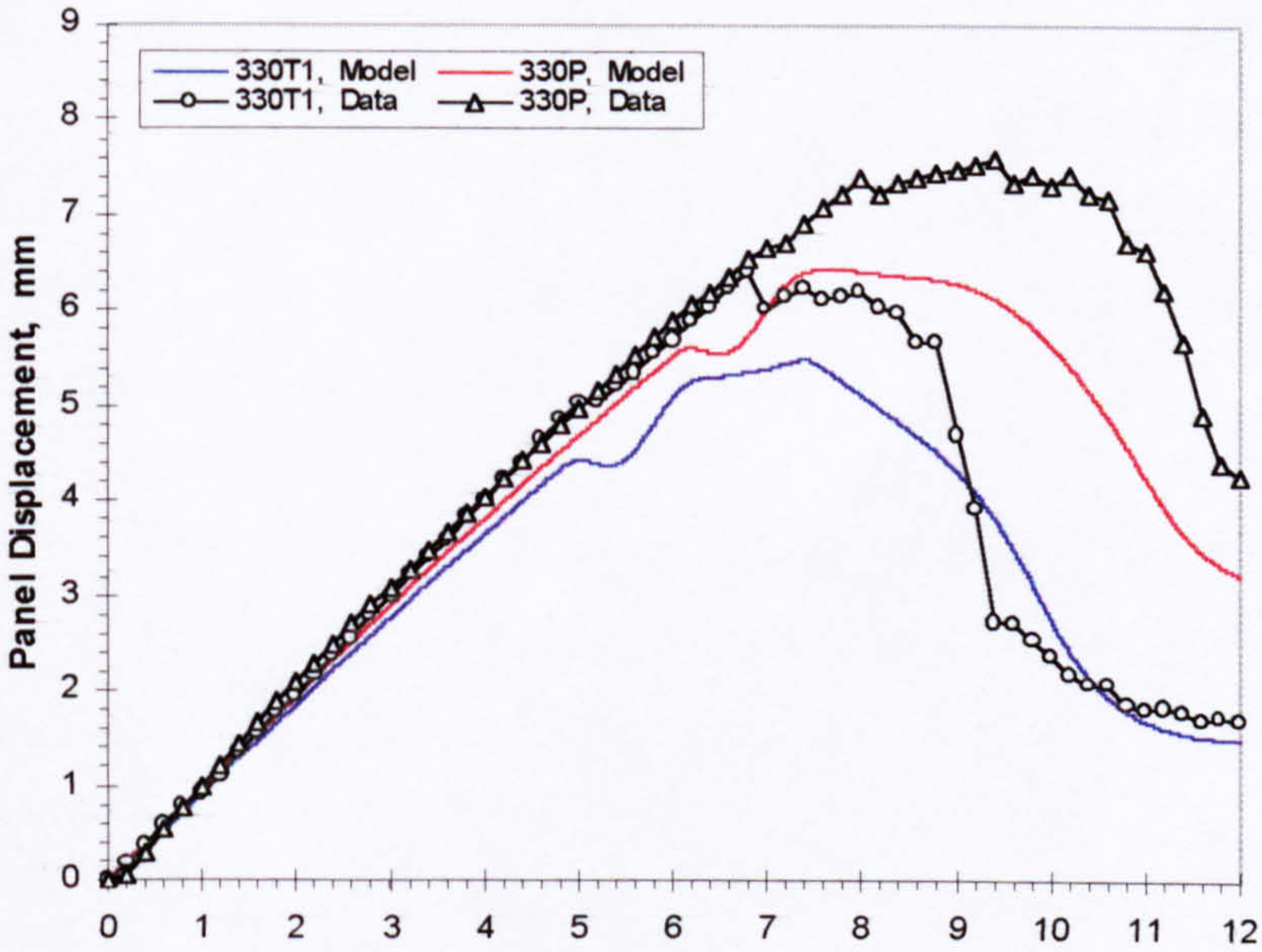

Figure 6.21. Panel displacement v.s. indentor displacement for the 3-ply, 300-mm diameter, stiffened panel loaded on the bay (between the stiffeners).

In Figures 6.22 and 6.23 are cast the results of the static test simulations for the 3-ply, 100-mm diameter panel and 300-mm diameter panel, respectively, both of which were loaded above the stiffener. In the same plots were cast data for the plain panels of the same diameter from the experiments for comparison. Two model results were also presented for the stiffened panels in these diagrams to illustrate the effect of presence of the stiffeners on the membrane stiffness of the panel.

The results of Model1 (for both 100-mm and 300-mm diameter panels) assume no reduction in membrane stiffness due to the presence of the stiffeners. Using Model1 results in a significantly stiffer predicted panel response after the stiffener web failure point. These can be clearly seen in the orange-coloured traces in Figures 6.22 and 6.23. This implies that for the stiffened panels loaded on the stiffener, the presence of the central stiffener suppresses the membrane action of the panel by providing in-plane reinforcement in addition to the desired transverse reinforcement of the panel. To take into account this suppression of the membrane effect, Model2a and Model2b were used in numerical simulations. Model2a assumes a 20 percent reduction of the membrane stiffness for the 100-mm diameter panel whilst Model2b assumes a 45 percent reduction in membrane stiffness for the 300-mm diameter panel. These values for the percentage reductions of the membrane stiffness were determined by trial and error to best fit to the experimental data. The results from using Model2a and Model2b are shown by the red-coloured traces in Figures 6.22 and 6.23.

For the stiffened panels loaded above the stiffener, the penetration force is much greater than the critical delamination initiation force. It appears that the presence of the fractured stiffener web below the load application point (see Figure 6.19(B)) provides enough of an obstruction to the progress of the indentor as it is driven into the plate. From the results of the static indentation tests the penetration force for the 3-ply, stiffened panels loaded on the stiffener is about 500 Newtons more than the critical delamination initiation force. This gives a value for the penetration force of about 1029 Newtons.

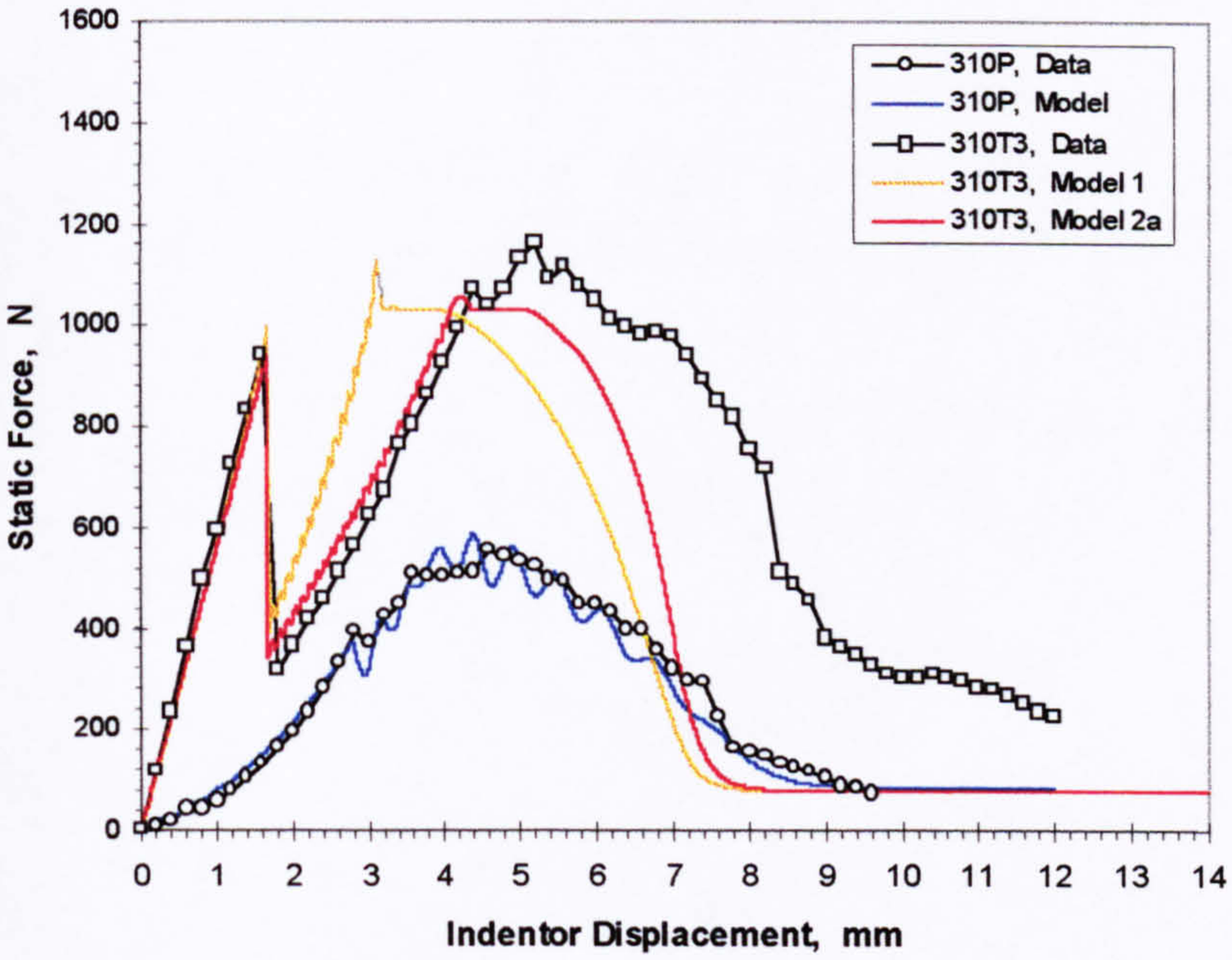

Figure 6.22. Static force v.s. indentor displacement for the 3-ply, 100-mm diameter, stiffened panel loaded on the stiffener.

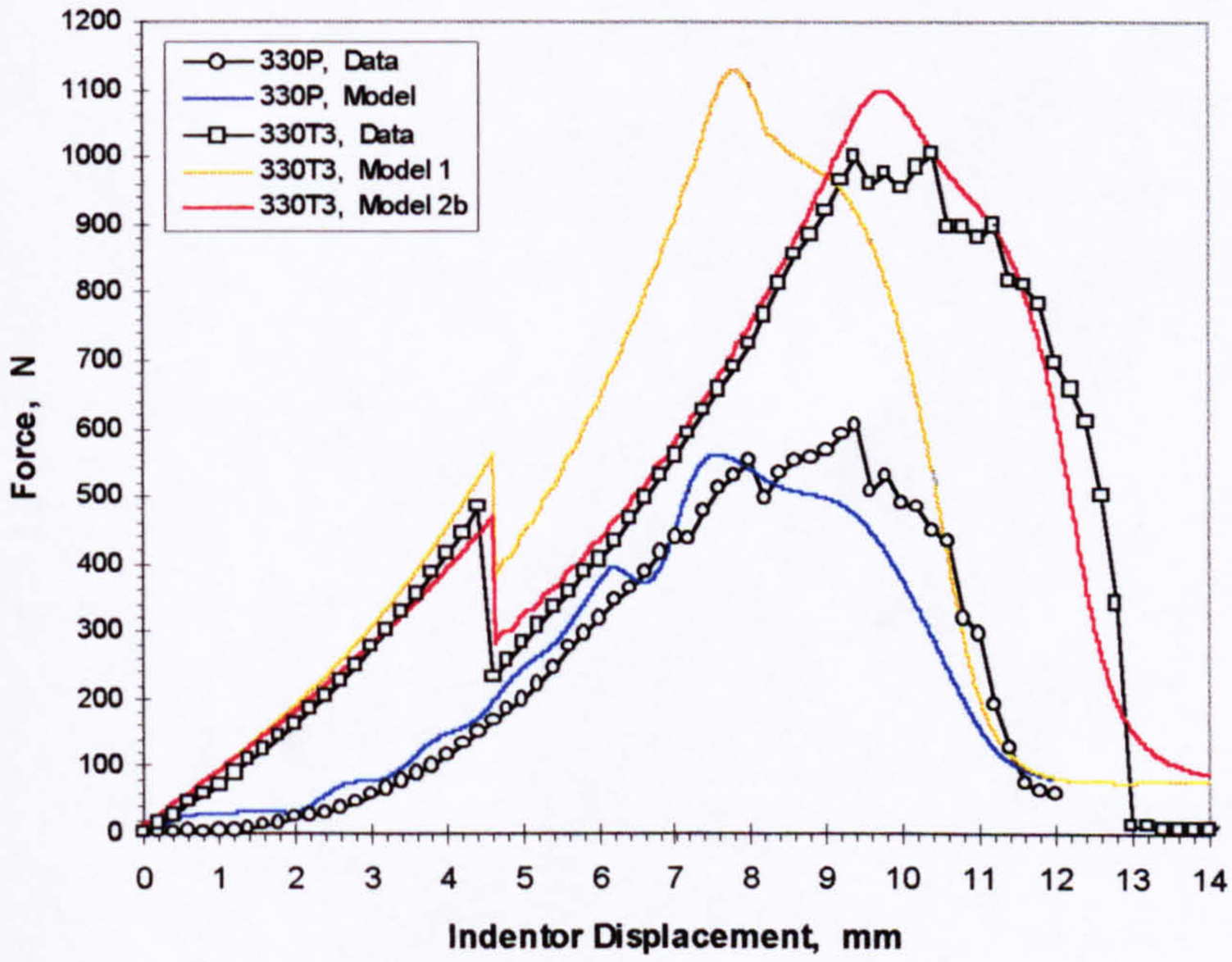

Figure 6.23. Static force v.s. indentor displacement for the 3-ply, 300-mm diameter, stiffened panel loaded on the stiffener.

The results of the modelling for the stiffened panels loaded above the stiffener drew heavily from data obtained from the experiments. This was done since no suitable theoretical relations were available for the calculation of some of the parameters. Despite this, the results obtained from the models are still useful since they allow a description of the quantities that influence the panel response. At the very least the models can be used as a guide into the development of more complex models that more accurately describe the impact response of panels of complex geometry.

6.3.2.2 IMPACT TEST MODELLING RESULTS

Figures 6.24 and 6.25 show the impact test modelling results for the 3-ply, 300-mm diameter, stiffened panels loaded on the bay at impact energies of 1.517 Joules and 2.311 Joules respectively. The model results shown in these figures show good agreement with data for the force histories and only fair agreement between model and data for the displacement histories. Like in the plain panels, it may be the stiffer prescribed boundary conditions on the model that are causing these observed deviations.

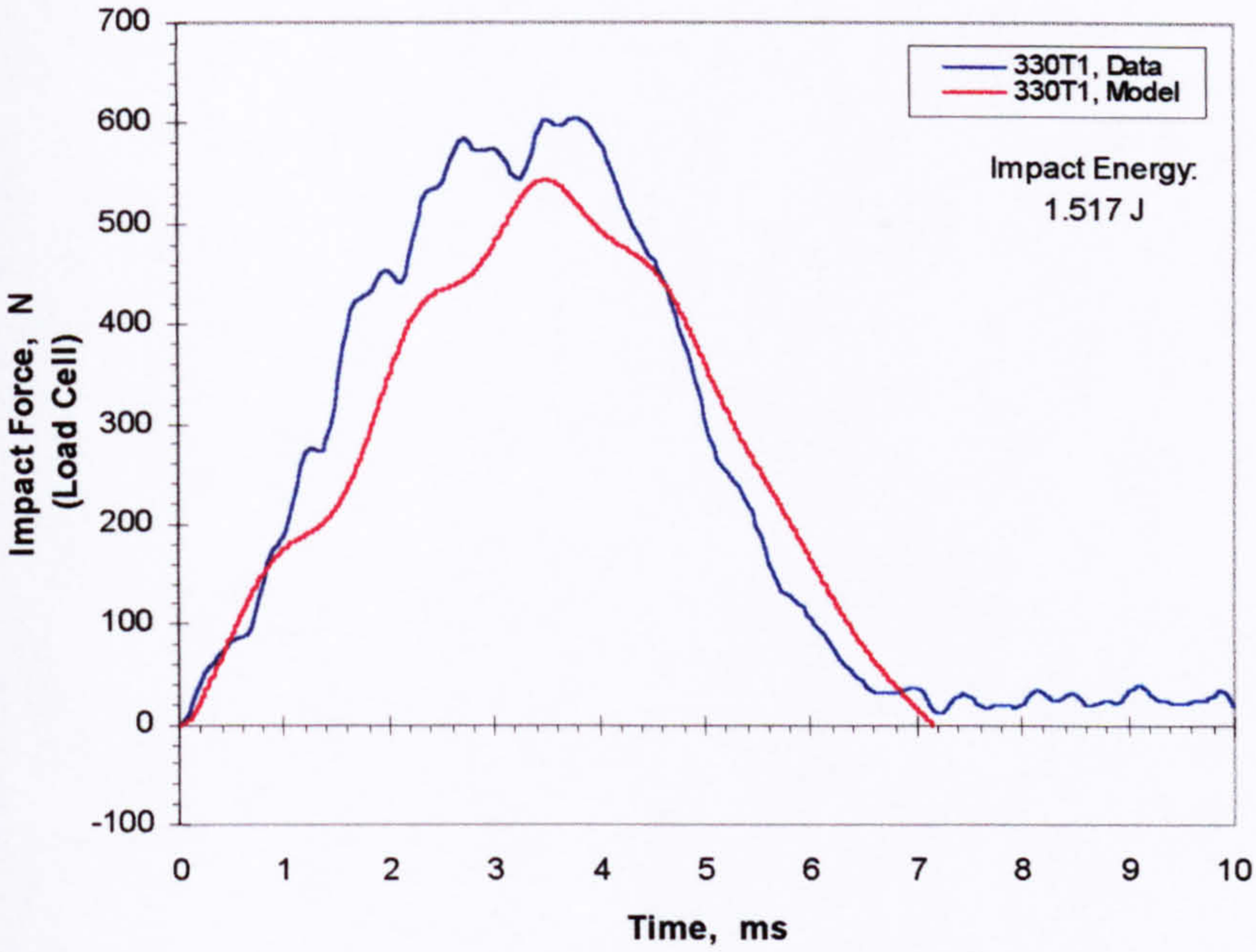

Figure 6.24(a). Force history for the 3-ply, 300-mm diameter, stiffened panel loaded on the bay at an impact energy of 1.517 J (55.4% of the impact penetration energy).

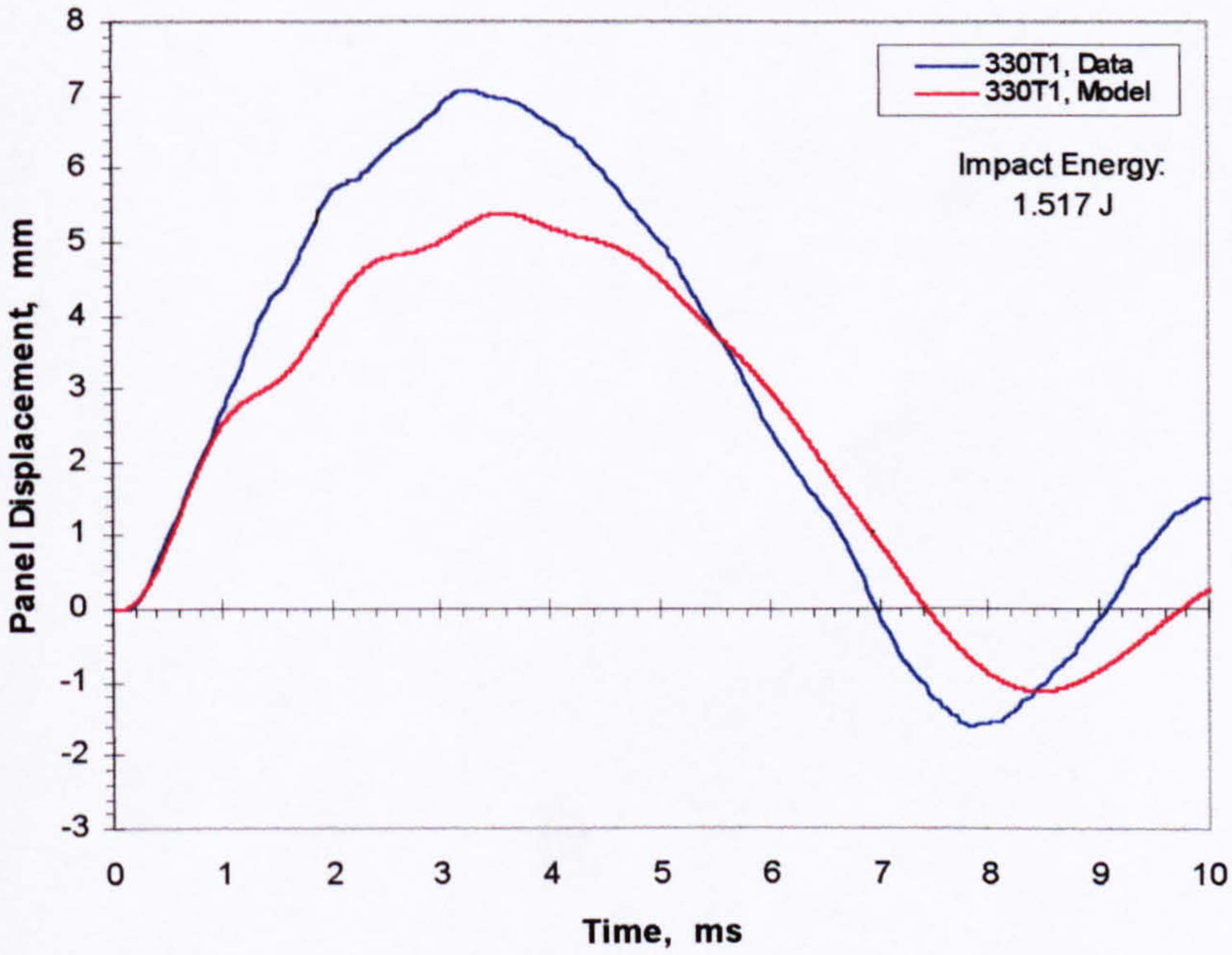

Figure 6.24(b). Displacement history for the 3-ply, 300-mm diameter, stiffened panel loaded on the bay at an impact energy of 1.517 J (55.4% of the impact penetration energy).

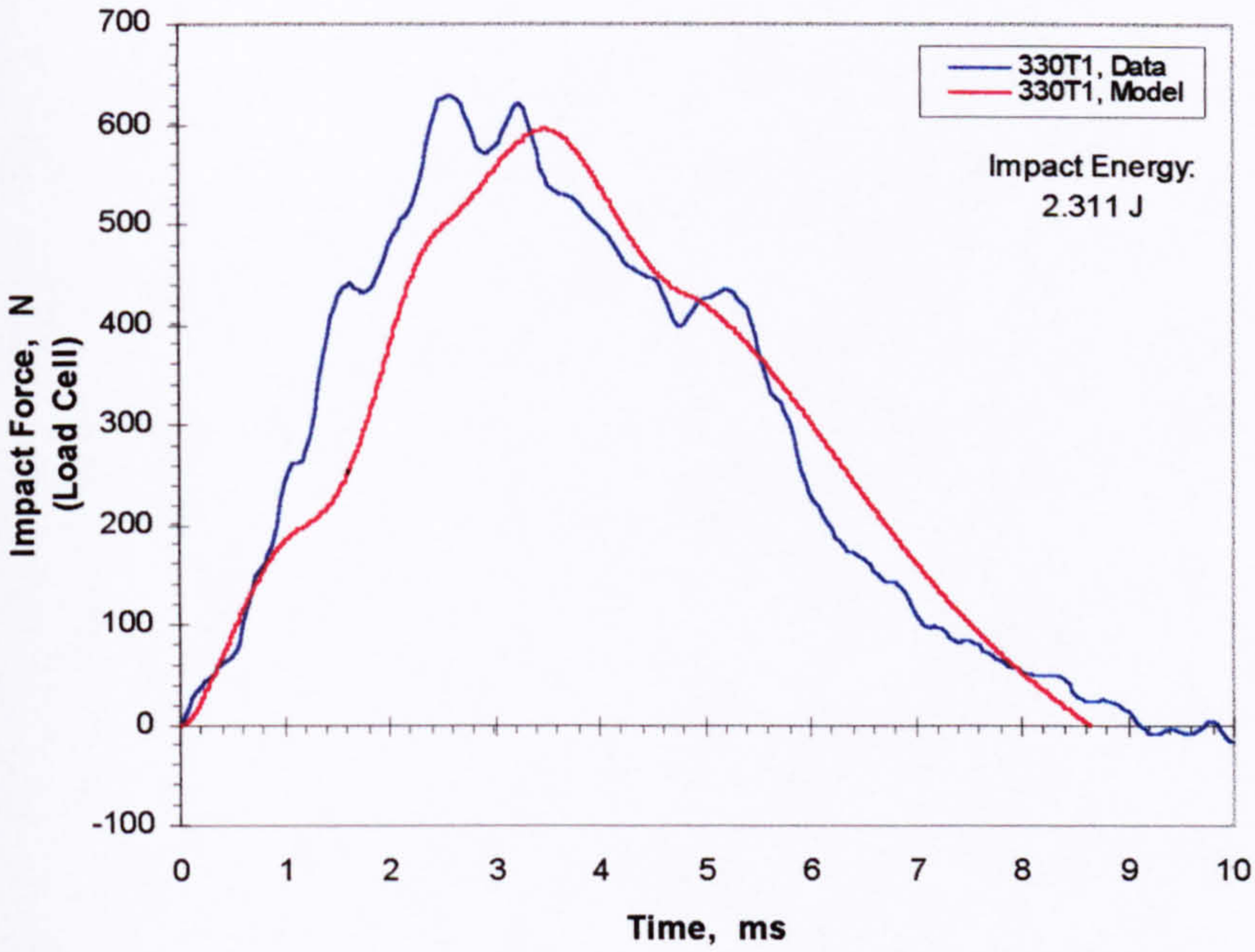

Figure 6.25(a). Force history for the 3-ply, 300-mm diameter, stiffened panel loaded on the bay at an impact energy of 2.311 J (84.4% of the impact penetration energy).

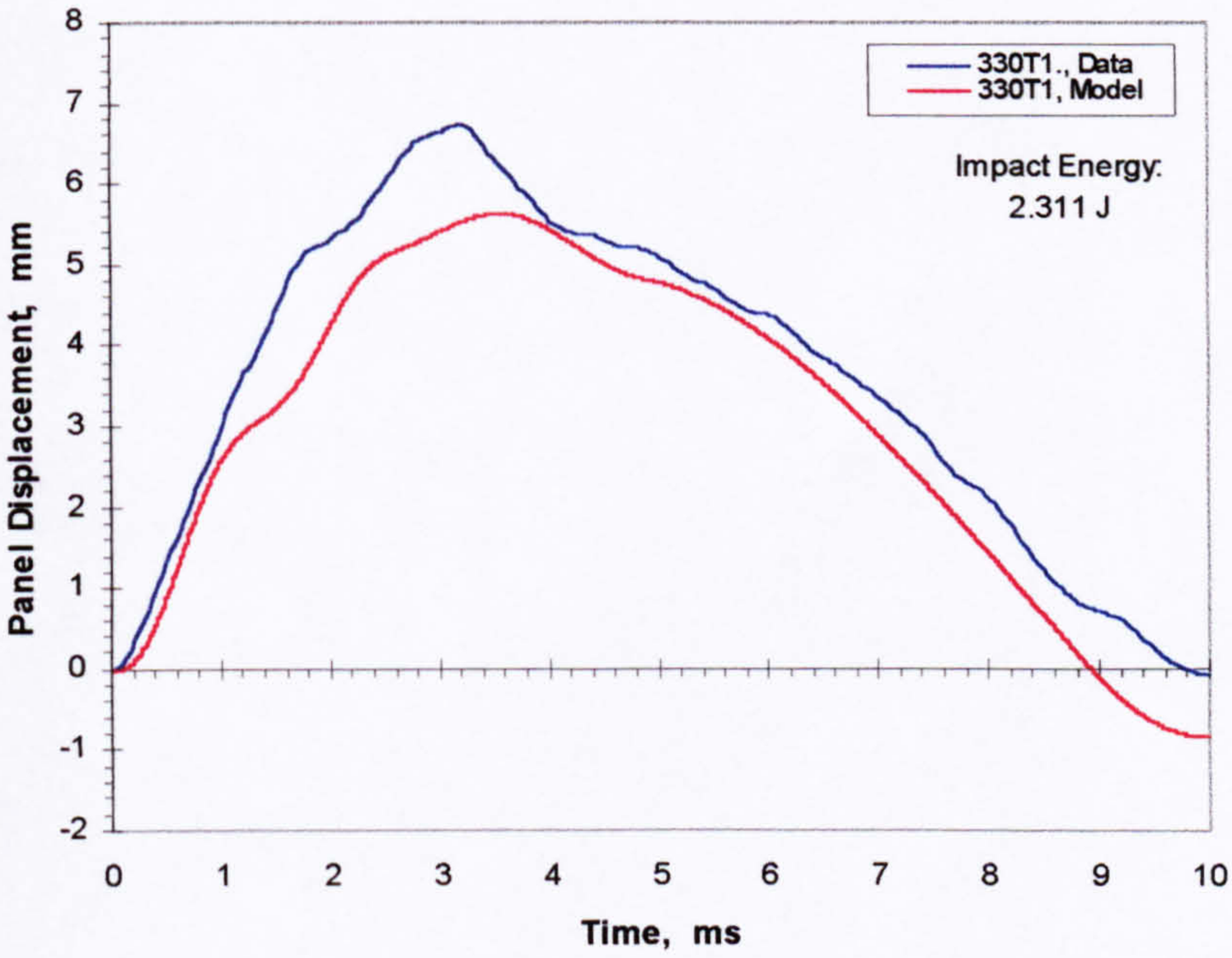

Figure 6.25(b). Displacement history for the 3-ply, 300-mm diameter, stiffened panel loaded on the bay at an impact energy of 2.311 J (84.4% of the impact penetration energy).

In Figures 6.26 and 6.27 are shown the results of the impact test modelling for the 3-ply, 300-mm diameter, stiffened panels loaded above the stiffener at impact energies of 1.574 Joules and 4.961 Joules respectively. The model used in these simulations corresponds to Model2b described earlier in Section 6.3.2.1. Because Model2b was "tuned" to best fit the static test data, it is not surprising to find very good agreement between model results and test data in the figures shown.

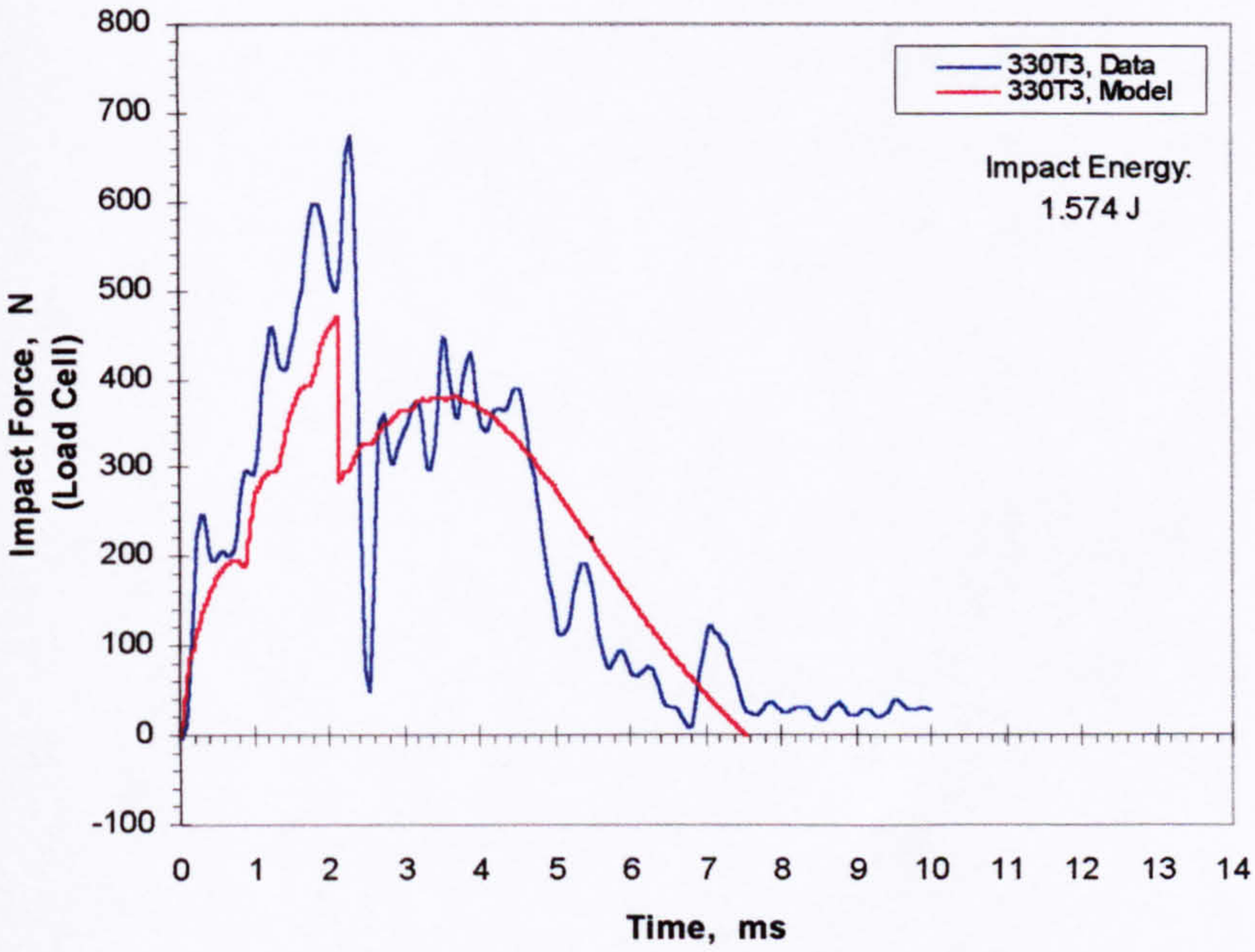

Figure 6.26(a). Force history for the 3-ply, 300-mm diameter, stiffened panel loaded on the stiffener at an impact energy of 1.574 J (26.1% of the impact penetration energy).

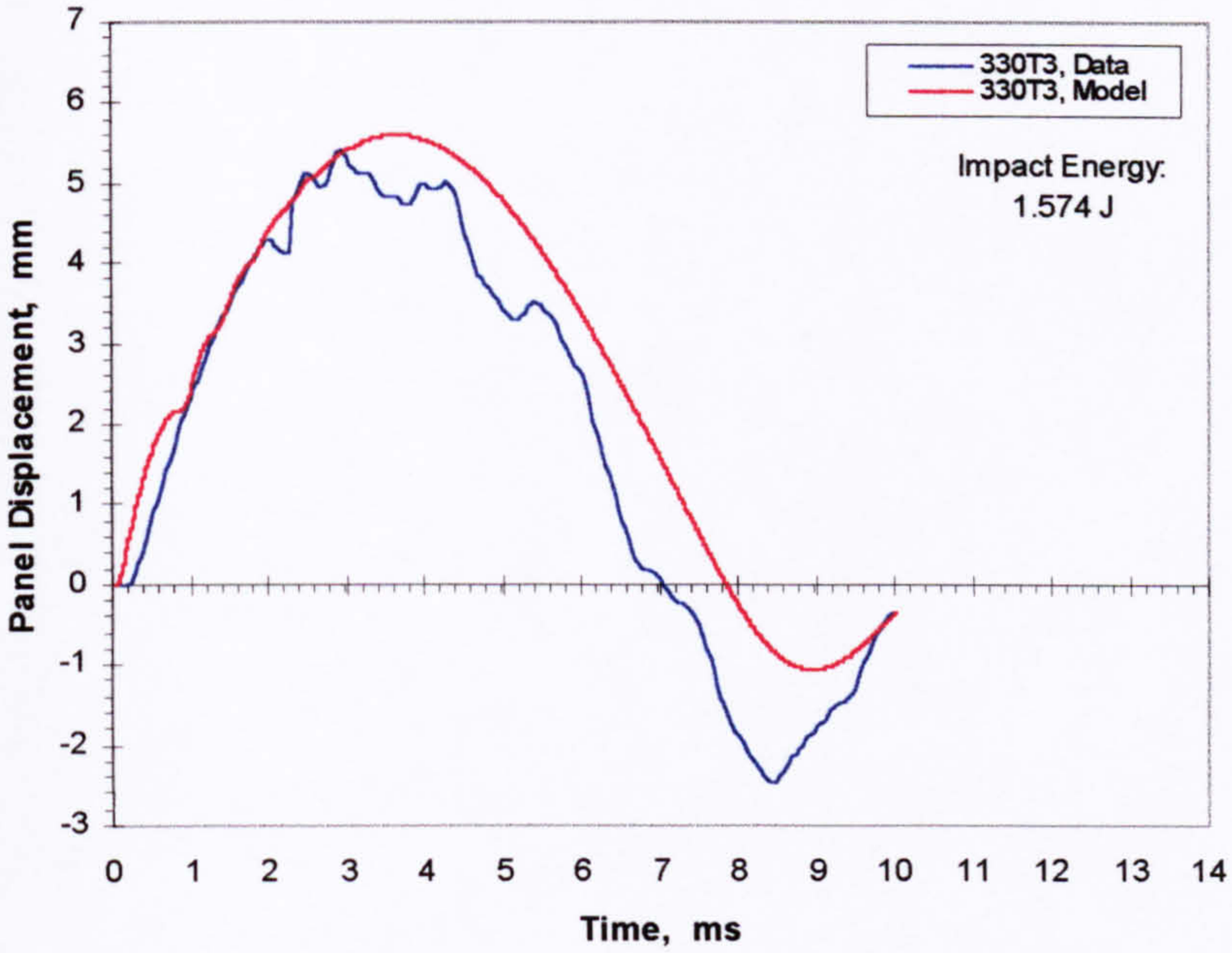

Figure 6.26(b). Displacement history for the 3-ply, 300-mm diameter, stiffened panel loaded on the stiffener at an impact energy of 1.574 J (26.1% of the impact penetration energy).

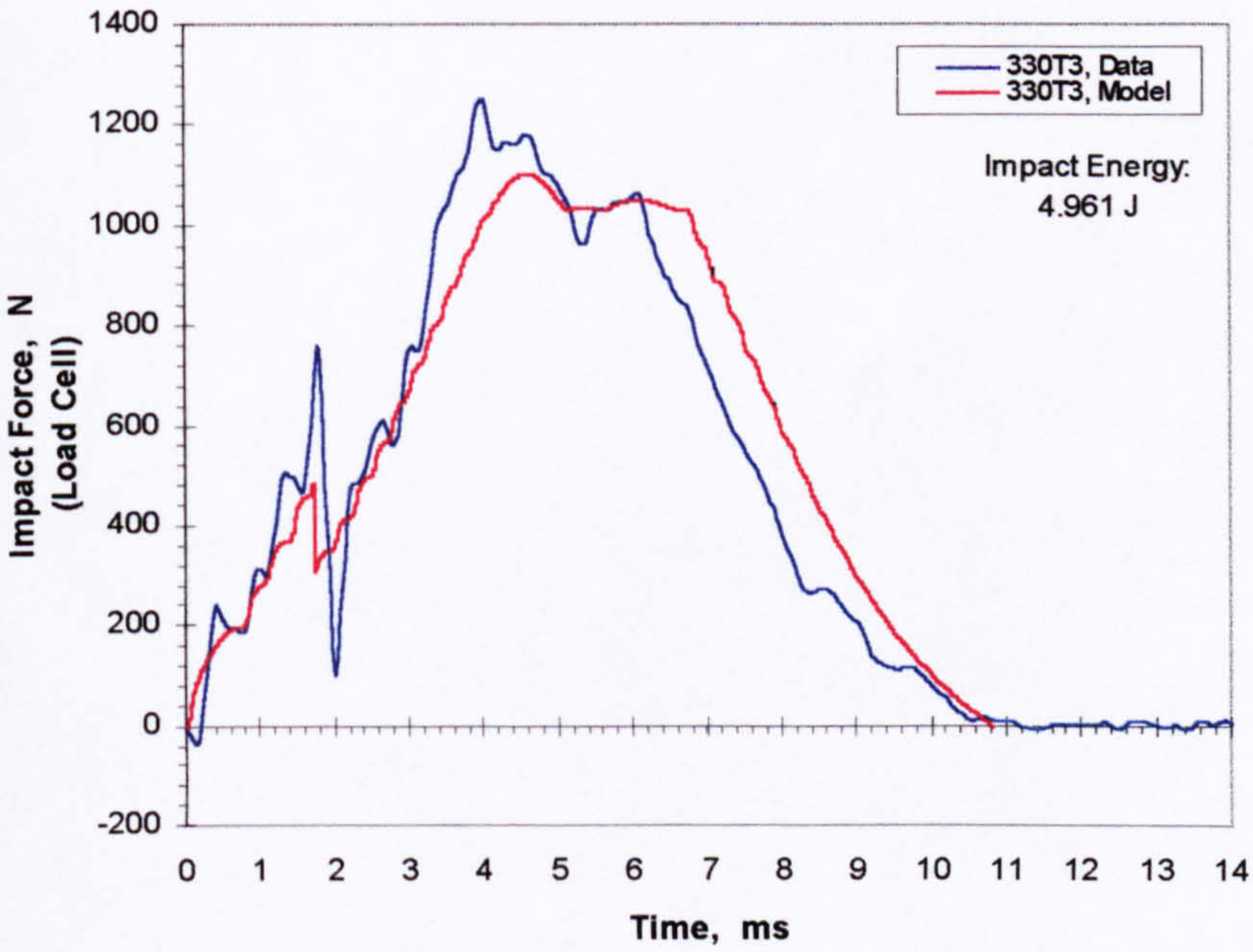

Figure 6.27(a). Force history for the 3-ply, 300-mm diameter, stiffened panel loaded on the stiffener at an impact energy of 4.961 J (82.2% of the impact penetration energy).

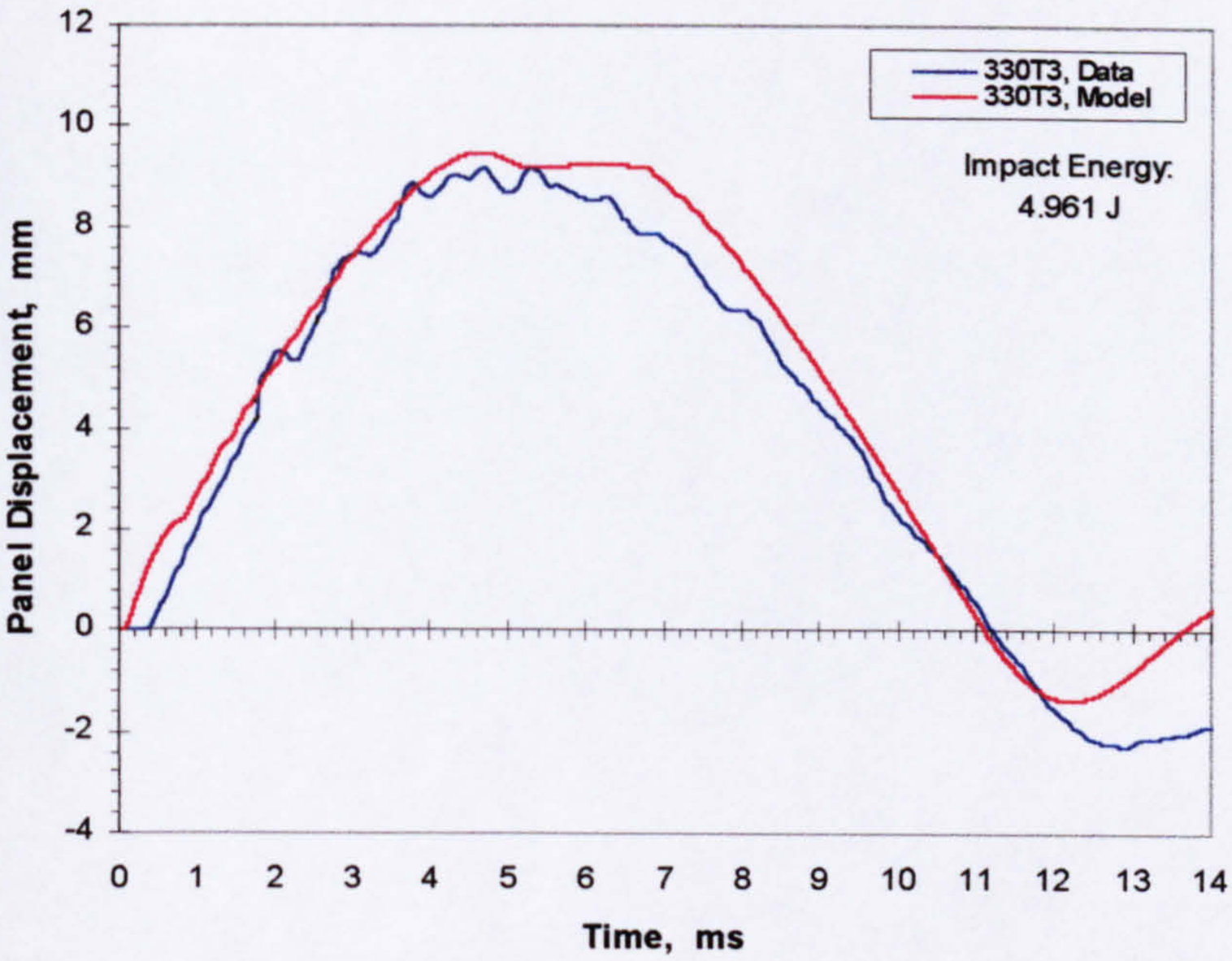

Figure 6.27(b). Displacement history for the 3-ply, 300-mm diameter, stiffened panel loaded on the stiffener at an impact energy of 4.961 J (82.2% of the impact penetration energy).

6.4 SUMMARY

The non-linear, lumped-parameter, mass-spring-damper model developed in this thesis is capable (with acceptable accuracy) of simulating the impact response of plain panels up to 2.7125 mm thick (9-ply panel). It appears to be best applicable to thin panels with diameter-to-thickness ratios of 100 or greater. For thick panels, the influence of the boundary conditions on the panel stiffness and material through the thickness effects in the panel causes significant deviations between model results and test data.

The model attempted to incorporate the effects of material damage on the impact response through the use of relevant theoretical relations (if available) as well as through the use of empirical relations drawn from experimental data. The exercise

helped identify the relevant quantities that affect local and global panel stiffness parameters due to degradation caused by damage to the material of the panel.

Finally the model was extended to include the effects of built-in stiffeners in the panel. It was found that the principle of superposition could be used to account for the additional stiffness brought in by the presence of the stiffeners. It was also found that membrane stiffness could be significantly suppressed by the presence of stiffeners especially if the load application point is above a stiffener. It is thought that the stiffeners not only reinforce the panel in the transverse direction but in the direction of the plane of the panel as well. This prevents the stretching of the panel when it is transversely loaded and thus reduces the membrane effects.

7 Discussion of Results

7.1 INTRODUCTION

The results of the tests conducted in this research project were presented in Chapters 4 and 5 whilst the results of the modelling work were reported in Chapter 6. The purpose of this chapter is to analyse and compare these results with relevant work reviewed in Chapter 2.

7.2 MODELLING

7.2.1 PLATE MODELS

The static loading test results in Chapter 4 suggests that the behaviour of the plain, quasi-isotropic CFRP panel is consistent with the large deformation theory of isotropic plates proposed by Timoshenko and Woinowsky-Krieger (1959). Test results show that the mid-plane stresses causes membrane stiffening of the panel resulting in an undamaged force-deflection response that is concave upwards. This effect is most readily observed in the thin, large-diameter panels where the bending stiffness is relatively smaller. Furthermore if the test data are cast into the non-dimensional form suggested by Equation 2.2 in page 5 of Chapter 2, the data collapses into a narrow band of points as shown in Figure 4.10 (Chapter 4, page 55).

For impulsive loading of plates, Mindlin (1951) and Whitney and Pagano (1970) have shown that rotary inertia and transverse shear deformation can result in significant deviations from classical plate theory. Mindlin (1951) also found that under certain circumstances transverse shear deformation could account for nearly all of this deviation. This deviation however was found to reduce significantly by Whitney and Pagano (1970) when the ratio of the diameter of the plate to its thickness is 30 or greater. In the tests carried out in this project the smallest diameter-to-thickness ratio encountered is about 36.8 corresponding to the case of the 9-ply panel held between

100-mm diameter rings. Based on this criterion all of the data obtained in this research should lie outside the range were transverse shear deformation becomes significant. To verify this, the variations in the bending stiffness, K_b, and the equivalent stiffness due to bending and shear deformations, K_{bs}, with contact force are plotted in Figures 7.1 and 7.2. Figure 7.1 shows the variations for a 9-ply, 100-mm diameter plain panel whilst Figure 7.2 shows the variations for a 9-ply, 300-mm diameter panel. The greatest difference between K_b and K_{bs} can be found for the 9–ply 100-mm diameter panel (Figure 7.1). For this panel geometry K_{bs} is about 16.5 percent smaller than K_b for small values of the contact force. The difference between K_b and K_{bs} is also seen to decrease slightly as the contact force increases. For the 9-ply, 300-mm diameter panel (Figure 7.2), K_{bs} is at most 3 percent smaller than K_b for low values of the contact force. From these we see that the diameter-to-thickness ratio of the panel is an important parameter in determining the overall panel stiffness, which in turn greatly influences the panel response.

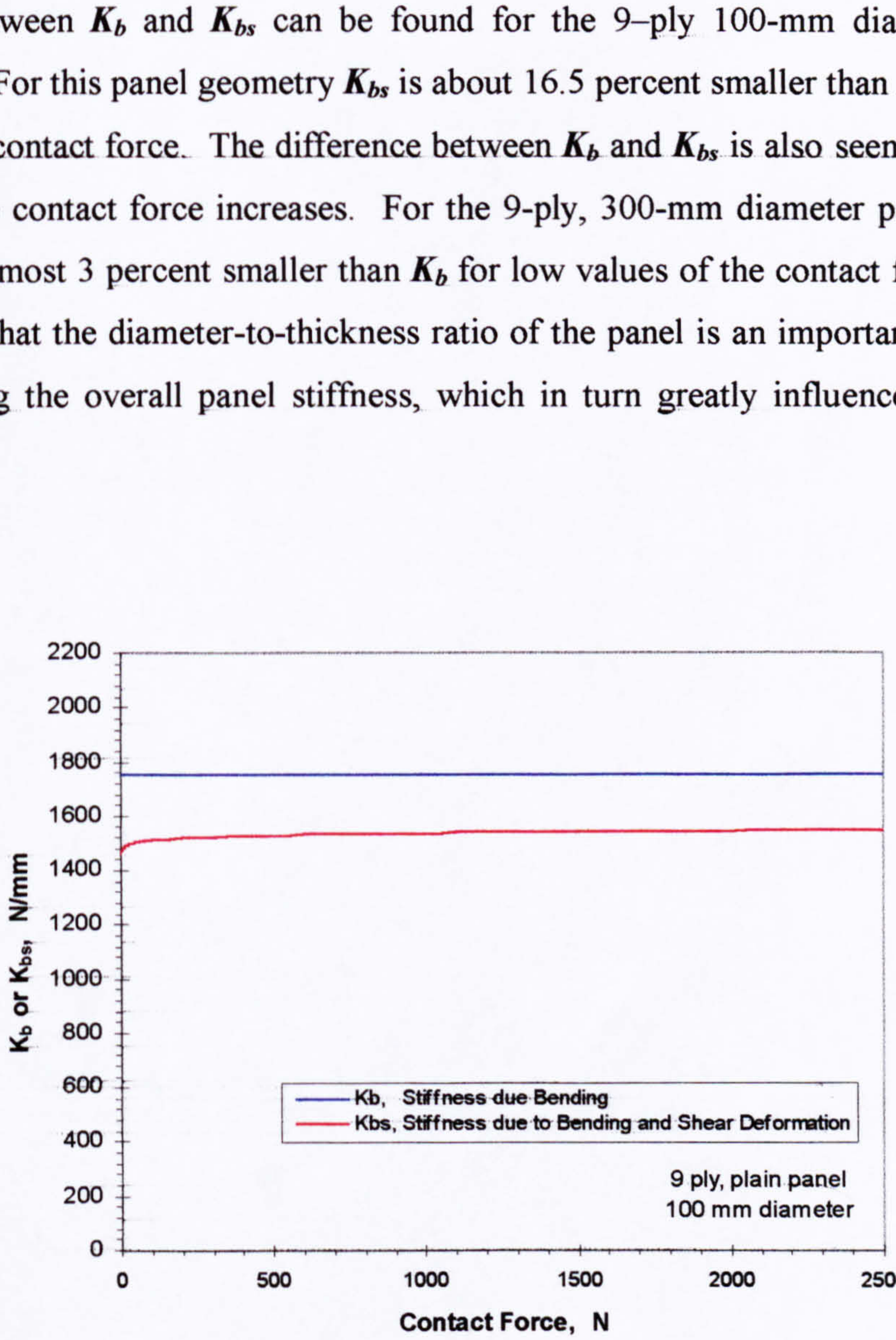

Figure 7.1. Variations in the panel bending stiffness and panel equivalent stiffness due to bending and shear for the 9-ply, 100-mm diameter plain panel.

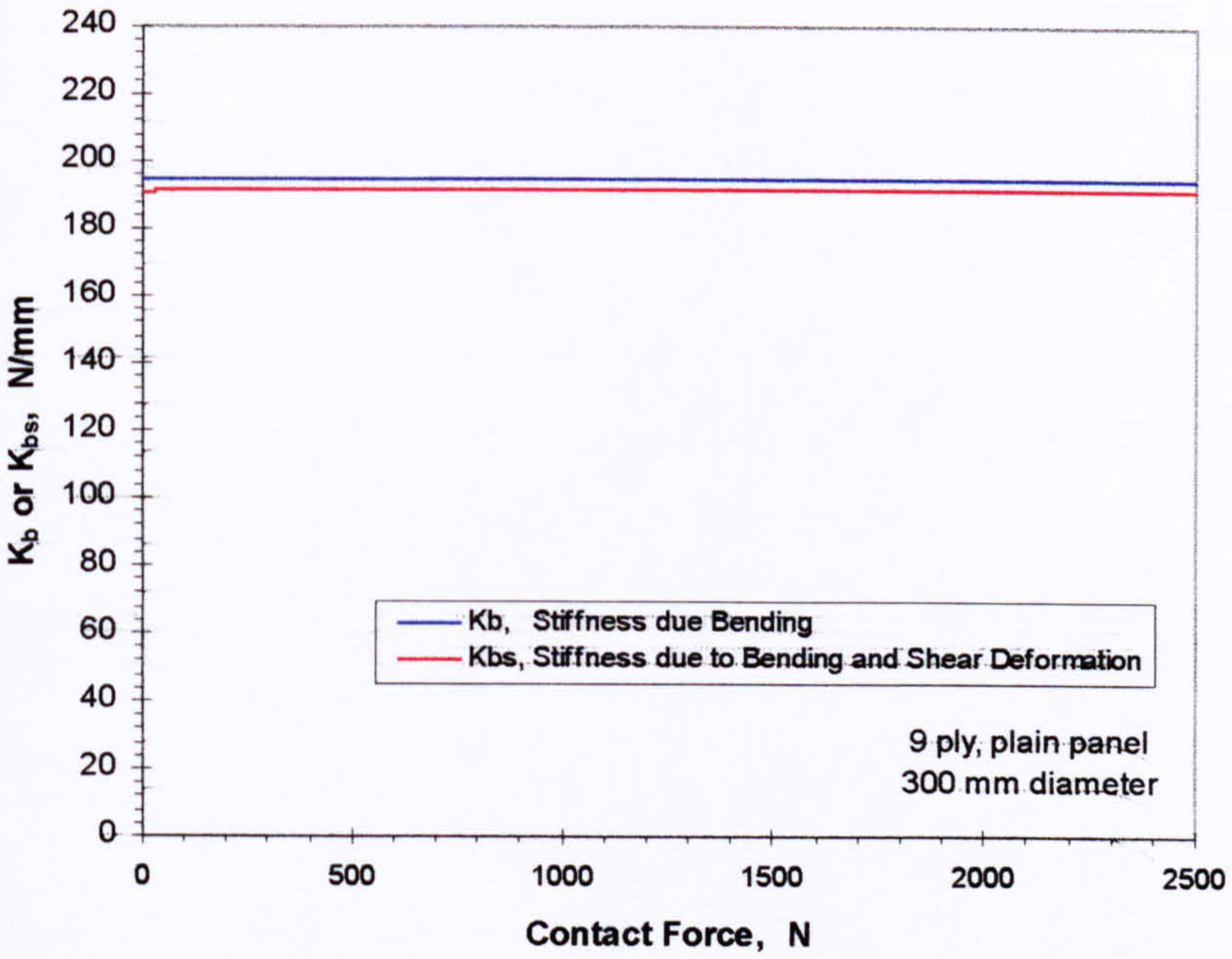

Figure 7.2. Variations in the panel bending stiffness and panel equivalent stiffness due to bending and shear for the 9-ply, 300-mm diameter plain panel.

The question of whether to use a quasi-static plate model or a more complex plate model such as that described by Equation 2.6 or its variants depends on whether the impact event is "low-velocity" or "high-velocity." In low-velocity impacts the projectile or indentor velocity must be significantly smaller than the velocity of the stress wave that propagates most slowly in the impacted material in order for the panel to respond in a quasi-static manner. Robinson and Davies (1992) suggested an upper bound of 10 to 20 m/s to low-velocity impacts based on the compressive failure strain and the speed of sound in common epoxy composites (see Equation 2.8 on page 12 of Chapter 2). The impact velocity in the tests carried out in this project was held constant at approximately 2.7 m/s, which is well below the upper limit suggested above. It therefore seems justifiable to use the quasi-static plate model in the low-velocity impact response of CFRP panels and it is no surprise to find that such a model was used by many other investigators in the field and these models produced results that are in satisfactory agreement with experiments. The suitability of the application of the quasi-static model to low-velocity impact was also corroborated by the test results presented in Chapters 4 and 5.

7.2.2 IMPACT MODELS

In Chapter 2, Section 2.4 different impact models for CFRP plates were discussed. These models ranged from simple mass-spring-damper systems to complex FEA models. The mass-spring-damper models were found to be satisfactory when modelling the low-velocity impact response of CFRP panels where the impact response can be considered as a quasi-static process. Furthermore, if the panel is of quasi-isotropic lay-up, the panel bending and membrane stiffness can be obtained from laminate theory (Jones. 1975; Tsai. 1985; Tsai and Hahn. 1980) and from the constitutive equations describing the large deformation theory of isotropic plates (Timoshenko and Woinowsky-Krieger. 1959). These principles have been used by several investigators (Lal.1983a, 1983b; Shivakumar et al 1985) in predicting the impact duration and response of plain CFRP panels. In as much as the mass-spring-damper models give accurate predictions of the impact response when compared to test data, their application was limited to non-damaging impacts.

Investigations into the development and growth of impact damage in CFRP almost always resort to FEA techniques in order to surmount the difficulty in determining the through the thickness stress fields in the material. The calculated magnitudes of these stresses are compared with appropriate damage criteria in order to determine the initiation and subsequent growth of impact damage in the material. From the work on FEA impact modelling reviewed in chapter 2, it is apparent that 3-D elements are necessary in order to model the development of damage in the material since 2-D plate elements could not model transverse stresses accurately. The capability of 3-D FEA modelling in predicting dynamic response and damage development cannot be denied, however, because of the complexity of the model and the computational resources it requires (especially when modelling structures built of anisotropic materials), it is an expensive and time consuming method.

In an attempt to take advantage of the simplicity of mass-spring-damper models and their suitability to low-velocity impact response analysis, a mass-spring-damper model

was developed in this thesis that attempted to in corporate the effects of material damage on the low-impact response of thin CFRP panels. The constitutive equations used in the model were based on the large deformation theory of plates. Damage in the panel was modelled by drawing from careful observations of the panel response in the static and impact tests. The damage thresholds identified and discussed in Chapters 4 and 5 were also incorporated into the model. These considerations resulted in the mass-spring-damper configuration shown in Figure 6.1 (Chapter 6, page 100). In the case where no theoretical relation can be found to describe the damaged panel response, empirical relations were used that were tuned to fit the experimental data. Nonetheless, numerical results from this model show close agreement with most of the test data obtained in this research project. The results also show that, with a thorough understanding how internal damage influences both local and global panel stiffness, even relatively simple and less computationally intensive models can accurately predict panel response to low-velocity impact loading up to kinetic energies that could result in the penetration of the panel. This is not to say, however, that the model can predict the development and growth of internal damage in the material. What the model does is take into consideration the effect of material damage on the local stiffness of the panel around the load application point by degrading the local material stiffness in that region. The details of this model and the results obtained from it were presented and discussed in Chapter 6.

7.3 TEST RESULTS

7.3.1 PLAIN PANELS

Analysis of the static test results for the plain panels led to the identification of the four response phases that were discussed in page 51 of Chapter 4. These four phases corresponded to the different stages in the state of damage in the panel during the static test. It also exemplifies how the local area around the indentor greatly influences the global panel response even though the damage is limited only to this relatively small region. This is because that any load that is transmitted to the rest of the panel has to be

transmitted through this region. Any loss of integrity in this local region would certainly affect the load carrying capacity of the entire panel.

The static test results also indicated the existence of two critical force thresholds: that for the initiation of backface cracking and that for the onset of extensive delaminations. The critical load that marks the onset of delaminations was identified by Davies and Zhang (1995) and is calculated from Equation 2.12 (Chapter 2, page 23). This equation shows that the delamination initiation force is a function of panel thickness alone for a given material. The predicted values of this force were plotted together with the test data in Figure 4.20 (Chapter 4, page 64). One can see the very good correlation between theory and experiments in this plot.

The appearance of the first backface cracks suggests that tensile failure occurs in the face of the panel directly opposite the load application point. The force to initiate this condition may be estimated from the approximate expression for the maximum backface tensile stress for a clamped isotropic plate subjected to strong load concentration (Timoshenko and Woinowsky-Krieger. 1959). This stress is given by:

$$\sigma_{\max} = \frac{P}{h^2}(1+\nu)\left(0.485\ln\frac{a}{h}+0.52\right) \qquad \text{Eqn. 7.1}$$

where σ_{max} is the maximum tensile stress, P is the applied central load, ν is the Poisson's rato, h is the thickness of the plate and a is its radius. Equation 7.1 can be solved for P and expressed as:

$$P = C'h^2$$

where $$C' = \frac{\sigma_{\max}}{(1+\nu)\left(0.485\ln\frac{a}{h}+0.52\right)}$$

Eqns. 7.2

Equations 7.1 and 7.2 show that the stress and the force to initiate backface cracking is influenced by the diameter and thickness of the panel unlike Equation 2.12 which is influenced by the panel thickness alone.

If we substitute the maximum allowable tensile stress for the material (750 MPa) into σ_{max}, then Equation 7.2 can be solved for the force to initiate the first backface cracks (in the outermost ply opposite the load application point) as a function of the panel thickness and radius. The predicted vales of the critical force to initiate the first backface cracks are plotted together with those determined from the static tests in Figure 7.3. From this figure the theoretical curves are seen to predict substantially lower values of the initiation force for panel thickness below 2.5 mm. We must remember however that the theoretical expression was developed for isotropic plates and the anisotropy of the panels used in this study may have introduced variables that were not considered in the theory. Despite the shortcomings of the theoretical expression it appears to indicate general trends in the data in Figure 7.1. Figure 7.1 also shows the plot of the empirical relation used in Chapter 6 (Equation 6.16) to predict the onset of backface cracking.

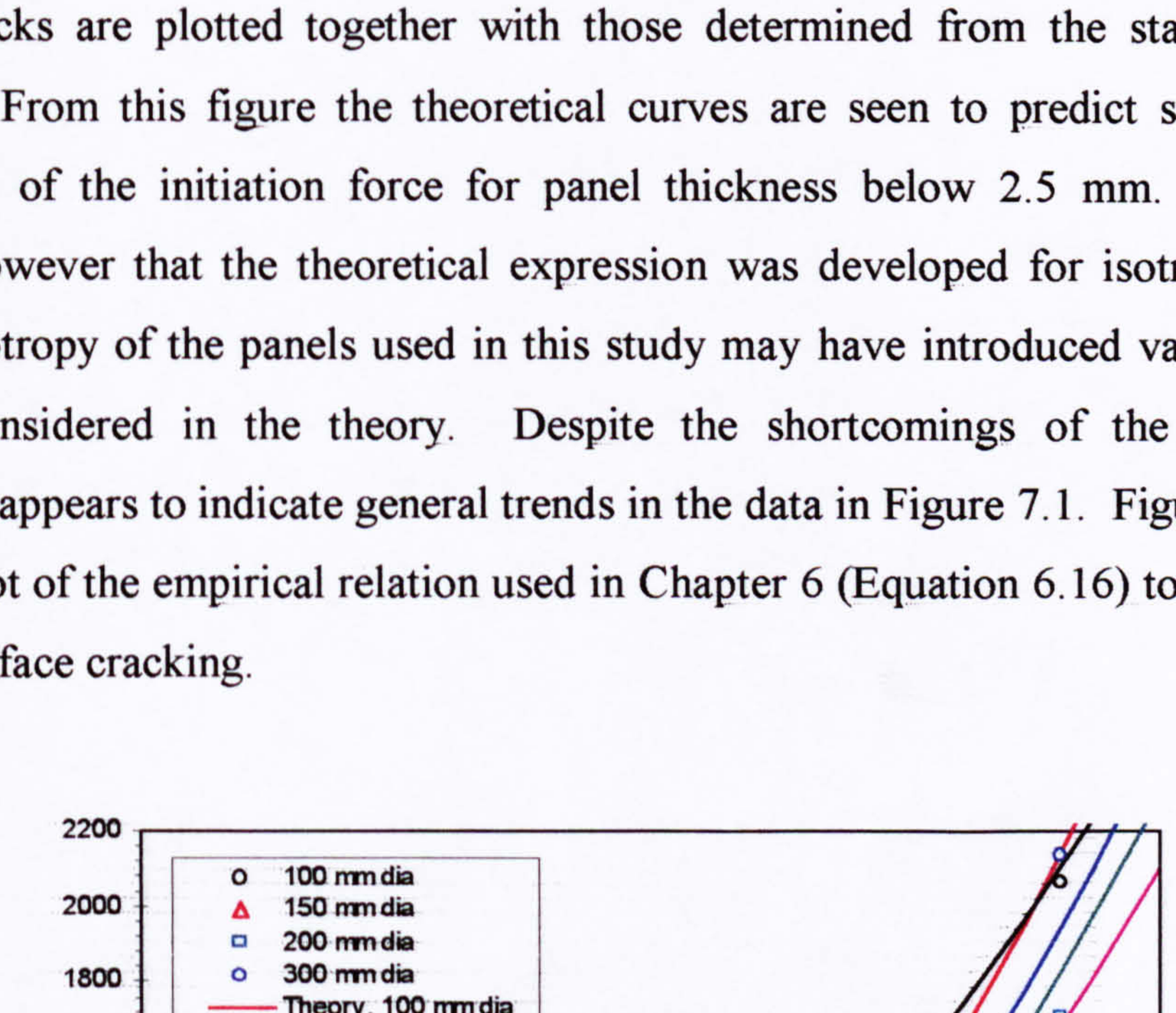

Figure 7.3. Static force to initiate the first occurrence of backface cracks in the plain panels.

7.3.2 STIFFENED PANELS

The static loading response of the stiffened panels depends very much on where the load application point is situated relative to the stiffeners. For loading on the bay or between the stiffeners, the response is similar to that of a plain panel but for the increased global stiffness due to the presence of the stiffeners. Figure 7.4 is a plot of the all the 3-ply static test data except for the stiffened panels loaded on the stiffener. Included in the figure is the horizontal line representing the critical delamination force threshold for a 3-ply panel as calculated from Equation 2.12. This critical force can be interpreted as the penetration force of the panel skin. It is clear from this figure that the presence of the stiffeners does not influence the magnitude the penetration force. This attests to the fact that the expression in Equation 2.12 does not contain any terms involving the boundary conditions imposed on the panel. This also implies that the damage to the panel is highly localised and should not be affected by the presence of the stiffeners provided that the load application point is sufficiently far from a stiffener so as not to encounter discontinuities in the thickness of the panel skin.

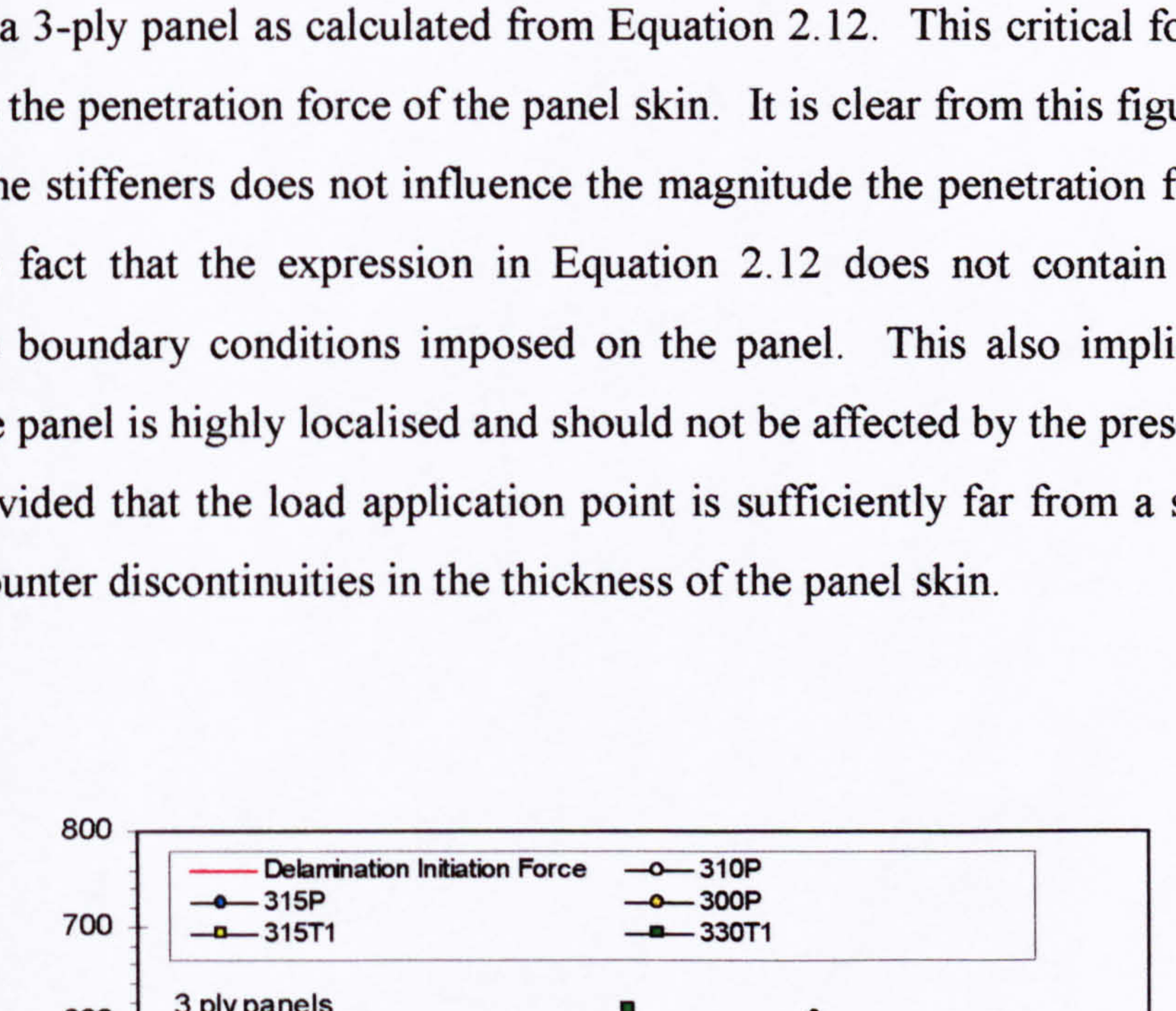

Figure 7.4. Static loading responses of 3-ply plain and stiffened panels loaded in the bay.

For loading above a stiffener the response is initially dominated by the bending stiffness of the stiffener blade until bending stresses in the blade causes it to fracture completely. This state is shown as points **1** and **2** in Figure 7.5. The failure of the stiffener is characterised by the complete fracture of the web or blade via a vertical crack from its outer edge to its root at the flange. This splitting of the blade causes an abrupt redistribution of the load shared between the panel skin and stiffener as well as a sudden loss in global panel stiffness. These events are clearly manifested as the sudden drop in the static load immediately after points **1** and **2** in Figure 7.5. Once the blade of the stiffener has split the resulting supporting structure can be interpreted as two cantilevered beams that are touching at their free ends. From this instance on the total applied load is now shared between the panel skin and these two beams. Driving the indentor into the panel beyond the point of blade failure results in increasing the load further until penetration of the panel occurs, at which point the load begins to decrease with indentor displacement. It is interesting to note that the penetration force for the panels loaded on the stiffener are significantly higher than the penetration force for the panel skin alone. The implication of this is that the two cantilevered beams can still carry a substantial portion of the applied load, therefore delaying the onset of significant delamination damage in the panel skin that usually results in the perforation of the panel by the indentor. It is also very likely that the presence of the fractured stiffener blade underneath the load application point obstructs the progress of the indentor as it is driven into the panel skin. This condition may also contribute to increasing the force required for the indentor to penetrate the panel skin.

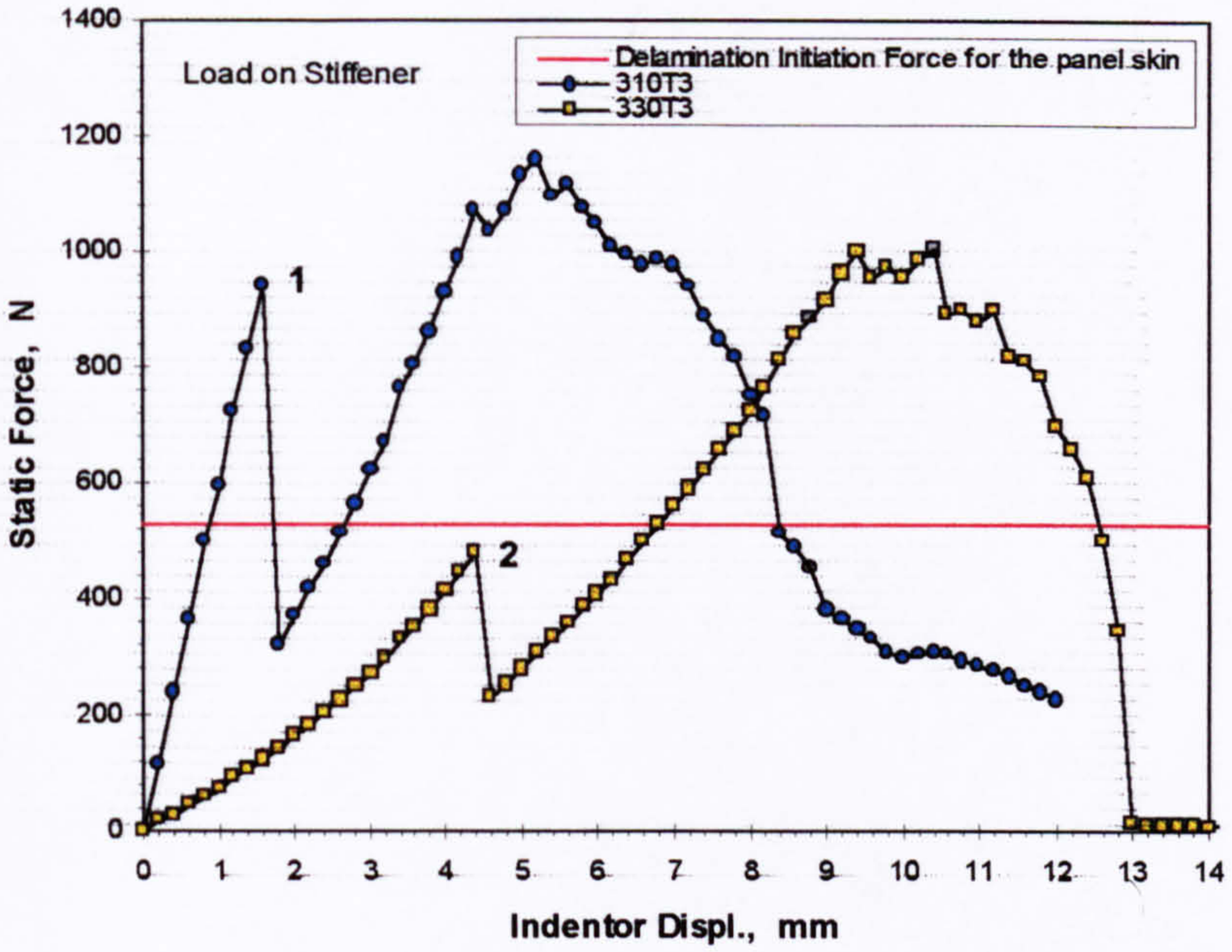

Figure 7.5. Static loading responses for 3-ply panels loaded above a stiffener.

The behaviour of the static loading response of the stiffened panels shown in Figure 7.5 can be explained by looking at how the applied load is shared between the stiffener and panel skin. As was done in Chapter 6, it was assumed that the principle of superposition could be applied to the loads carried by the stiffener and panel skin. For loads below the blade failure load the stiffener can be taken to be a beam that is clamped at both ends. From elementary beam theory (Shigley. 1963) the bending moment at the mid-span of such a beam with a centrally applied transverse load is (see Figure 6.19(A) on page 131):

$$M = \frac{Pa}{4} \qquad \text{Eqn. 7.3}$$

where P is the magnitude of the load and a is half the length of the beam.

The maximum bending stress at mid-span is given by the expression

$$\sigma = \frac{Mc}{I} \qquad \text{Eqn. 7.4}$$

where I is the moment of inertia of the beam cross-section about the neutral axis and c is the perpendicular distance from the neutral plane to the outermost fibre at the edge of the blade.

Equations 7.3 and 7.4 can be solved for the breaking load in terms of the failure stress of the beam material and this is:

$$P_f = \frac{4I\sigma_f}{ca} \qquad \text{Eqn. 7.5}$$

where P_f is the failure or breaking load of the beam and σ_f is the failure stress.

Equation 7.5 tells us that for a given beam material and geometry the failure load is inversely proportional to the span of the beam. Therefore a longer beam will have a lower failure load than that of for shorter one. Furthermore the failure loads will scale as the inverse ratio of the beam lengths or

$$\frac{P'_f}{P_f} = \frac{a}{a'} \qquad \text{Eqn. 7.6}$$

In Figure 7.5 we find that the smaller stiffened panel indeed fails at a much higher load than the larger panel in conformity with the prediction of Equation 7.5. However the breaking forces do not scale according to the expression in Equation 7.6 because the applied load is not carried by the stiffener alone, but is actually shared between the stiffener and panel skin.

For both plain and stiffened panels, the panel response due to impact loading is similar to the static loading response because of the quasi-static behaviour under low-velocity impact of the panels studied in this thesis. Strong evidence for this similarity were given in Figure 4.36 (Chapter 4, page 77) and Figure 5.14 (Chapter 5, page 93) which shows the static perforation energy having values quite close to the impact perforation energy.

7.4 ENERGY ABSORPTION BY THE PANEL

For constant panel thickness, larger diameter panels are able to store more elastic energy prior to failure. This can be best explained with reference to Figure 7.6. In this figure, the force-displacement responses of two different sized panels of the same thickness are shown. The maximum force for both panels are limited by $\mathbf{P_{crit}}$, the critical delamination force, and the elastic energy stored in the smaller panel and the larger panel are the areas **A1** and **A2** respectively. Area **A2** will always be greater than **A1** if the panels are of the same material and thickness. Since **A2** represents the elastic energy of the larger panel, it follows that the larger panel will be able to absorb more energy (through storage as elastic energy) before it reaches the levels of force that initiate damage in the material.

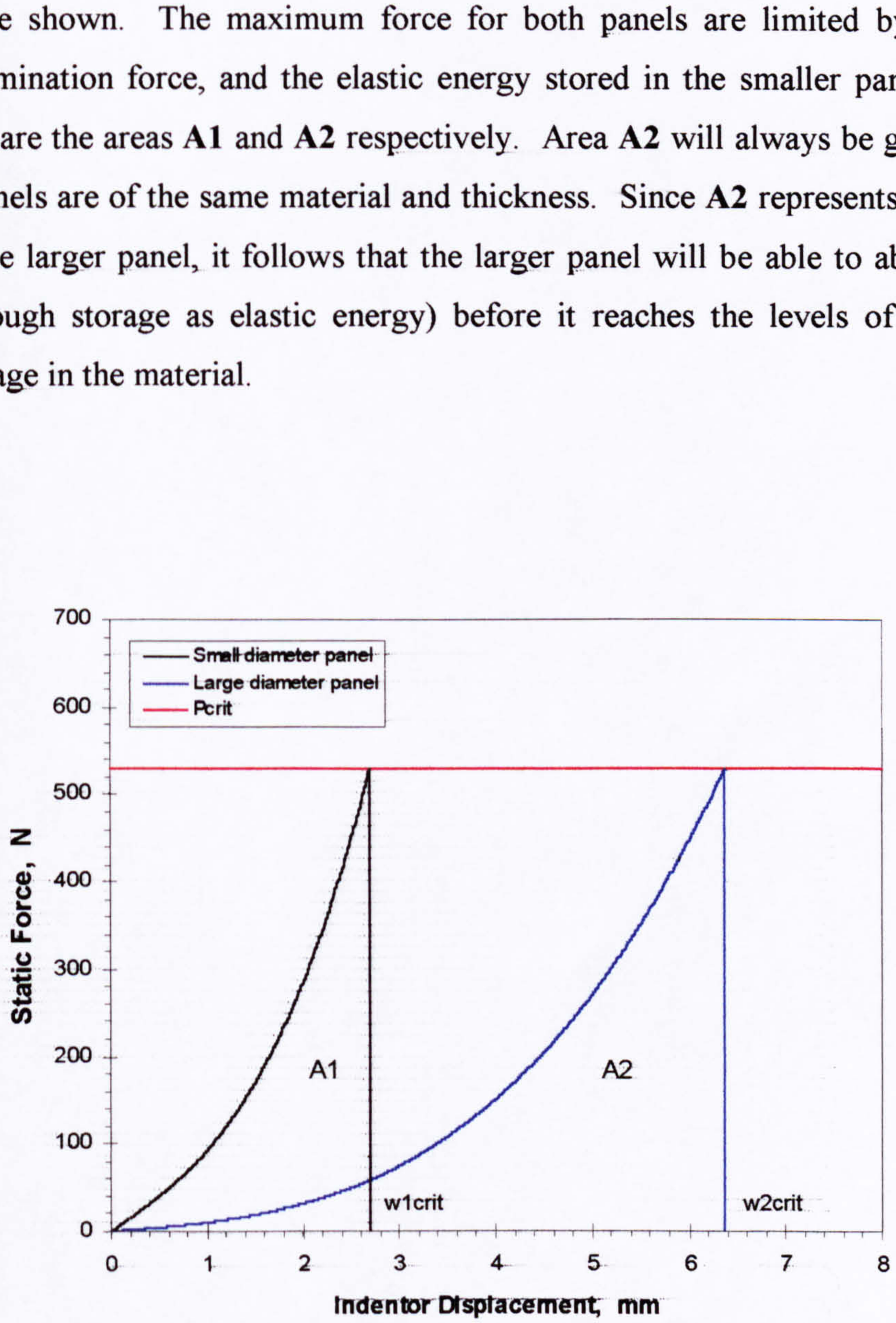

Figure 7.6. Static force-displacement responses of two panels of different diameters. Both panels are of identical material and thickness.

A more formal (but indirect) proof of this notion will now be presented. Rewriting Equation 2.2 to express the load-deflection characteristic for a circular, isotropic, plain panel loaded at the centre, we obtain the equation:

$$P = w\,(h^2 + A\,w^2)\,\frac{Eh}{Ba^2} \qquad \text{Eqn. 7.7}$$

where P is the applied load at the centre of the panel, w is the deflection of the panel at the load application point, E is the Young's Modulus, A and B are the edge constraint constants, h is the thickness of the panel and a is the radius of the panel. Equation 7.7 can be integrated with respect to w to obtain an expression for the elastic energy stored in the panel.

$$W = \frac{w^2}{2}\left(h^2 + A\frac{w^2}{2}\right)\frac{Eh}{Ba^2} \qquad \text{Eqn. 7.8}$$

where W can be interpreted to be the work done by an indentor that is driven against the panel a distance of w.

In Figure 7.6 the panels carry a load equivalent to the critical load P_{crit} when their deflections are at their respective critical values w_{crit}. The critical deflection can be solved for in terms of the critical force by inverting Equation 7.7 and considering only the real root of the resulting expression. This results in the equation:

$$w_{crit} = C - \frac{h^2}{3\,A\,C}$$

where

$$C = \left[\frac{1}{2}\left(\frac{Ba^2 P_{crit}}{AEh}\right) + \frac{1}{6}\sqrt{\frac{4}{3}\left(\frac{h^2}{A}\right) + 9\left(\frac{Ba^2 P_{crit}}{AEh}\right)^2}\right]^{\frac{1}{3}}$$

Eqns. 7.9

For panels of a given material and thickness that are also identically constrained, Equations 7.7 and 7.8 are functions of the panel radius and deflection only whilst Equation 7.9 is a function of the critical force and panel radius only. Solving for w_{crit} in Equation 7.9 and substituting it into w in Equation 7.8 results in a value for W that is always the largest for the panel with the biggest diameter. This proves that larger diameter panels can store more elastic energy prior to the initiation of material damage

7.5 PANEL PENETRATION

A method of calculating the static penetration energy was described in Section 4.2.3 of Chapter 4. The method described required the use of the static test data. In this section we introduce a theoretical method of calculating for the static penetration energy without recourse to the static tests. The method can be best explained by referring to Figure 7.7 which shows the theoretical static load-displacement response of a 3-ply, plain panel that is clamped at the edges. In this figure the portion of the curve from 0 to 1 is the panel load-deflection response according to Equation 7.7. The portion of the curve from 1 to 2 is the theoretical load-deflection response when the load the panel is carrying is at the critical delamination force given by Equation 2.12 (Chapter 2, page 23). The area under the curve 0-1-2 in Figure 7.7 represents the work done by the indentor when it is driven into the panel.

Over the portion 0-1 of the load-deflection curve, the panel responds elastically and there little or no indentation of the panel surface. The reason for this is that the contact stiffness, as calculated from Equation 6.8, is many times greater (by at least one order of magnitude) than the bending stiffness of the panel. As a result the panel has to be loaded by an appreciable amount before significant surface indentation occurs. To illustrate the calculated panel deflections and front face indentations for a given panel static load are presented in Figures 7.7-1 and 7.7-2. Figure 7.7-1 compares the transverse panel deflection to the front face indentation for a 3-ply, 100-mm diameter panel whilst Figure 7.7-2 compares the same parameters for the case of a 9-ply, 100-mm diameter panel.

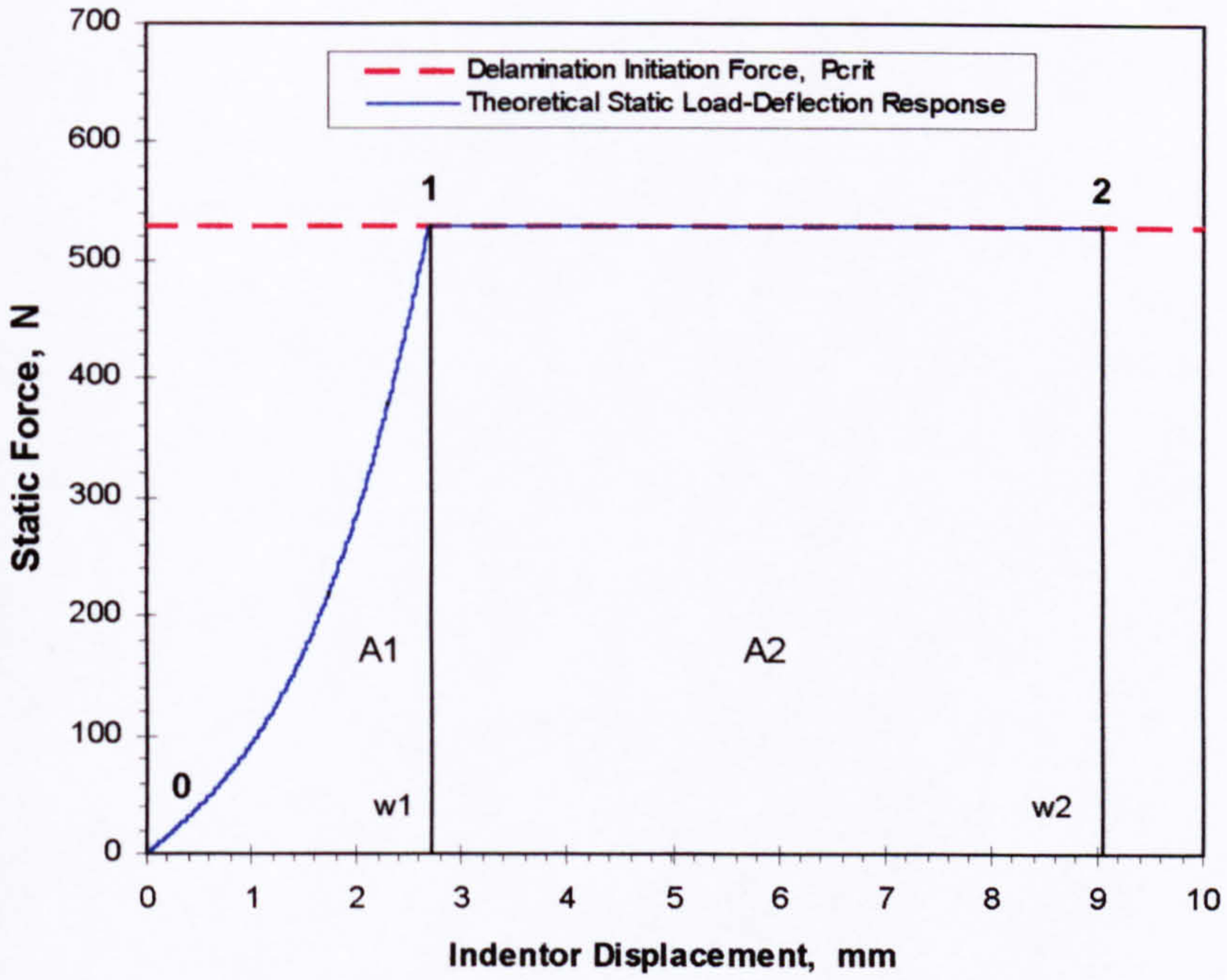

Figure 7.7. Theoretical static force-displacement response for a 3-ply panel.

Figures 7.7-1 and 7.7-2 show that the front face indentation is very small compared to the transverse displacement even for the much stiffer 9-ply, 100-mm diameter plain panel. Consequently, calculations have shown that the work of contact indentation, or what may be called the plastic work, is insignificant compared to the elastic work over curve 0-1 in Figure 7.7.

Over the portion 1-2 of the load-deflection curve in Figure 7.7, the static load remains at the critical delamination force threshold and results in the severe local damage to the panel and the relatively rapid penetration of the panel by the indentor. When the panel is delaminating, the indentor penetration distance or the horizontal distance between points 1 and 2 (w_2-w_1 in Figure 7.7) cannot exceed the radius of the indentor nose. This implies that there is an upper limit to the theoretical static indentation work that depends only on the panel material properties, the panel edge constraints and the radius of the indentor nose. This also suggests that the indentation work may depend on the size and shape of the indentor nose as well.

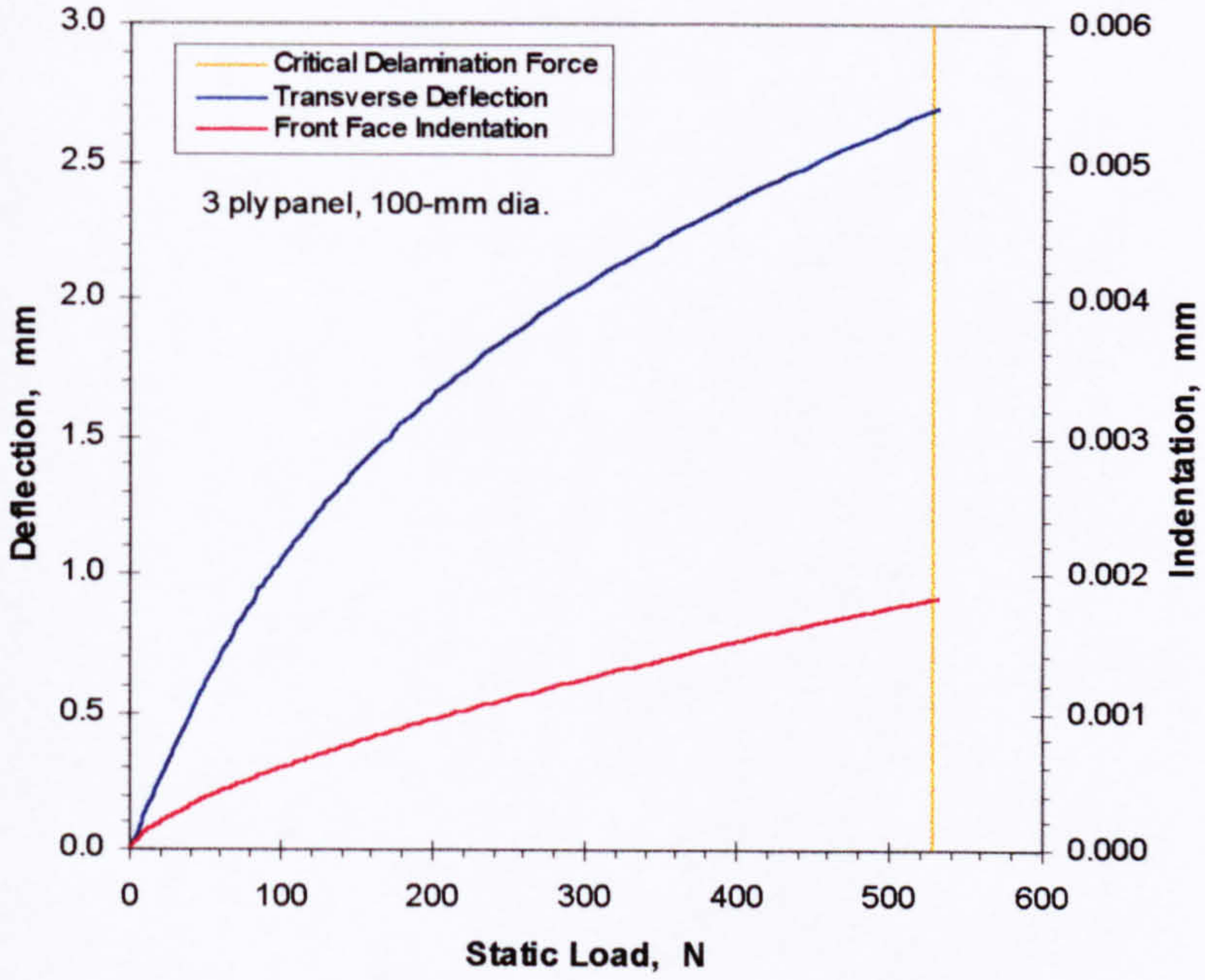

Figure 7.7-1. Panel deflection and indentation v.s. static load for the 3-ply, 100-mm diameter plain panel.

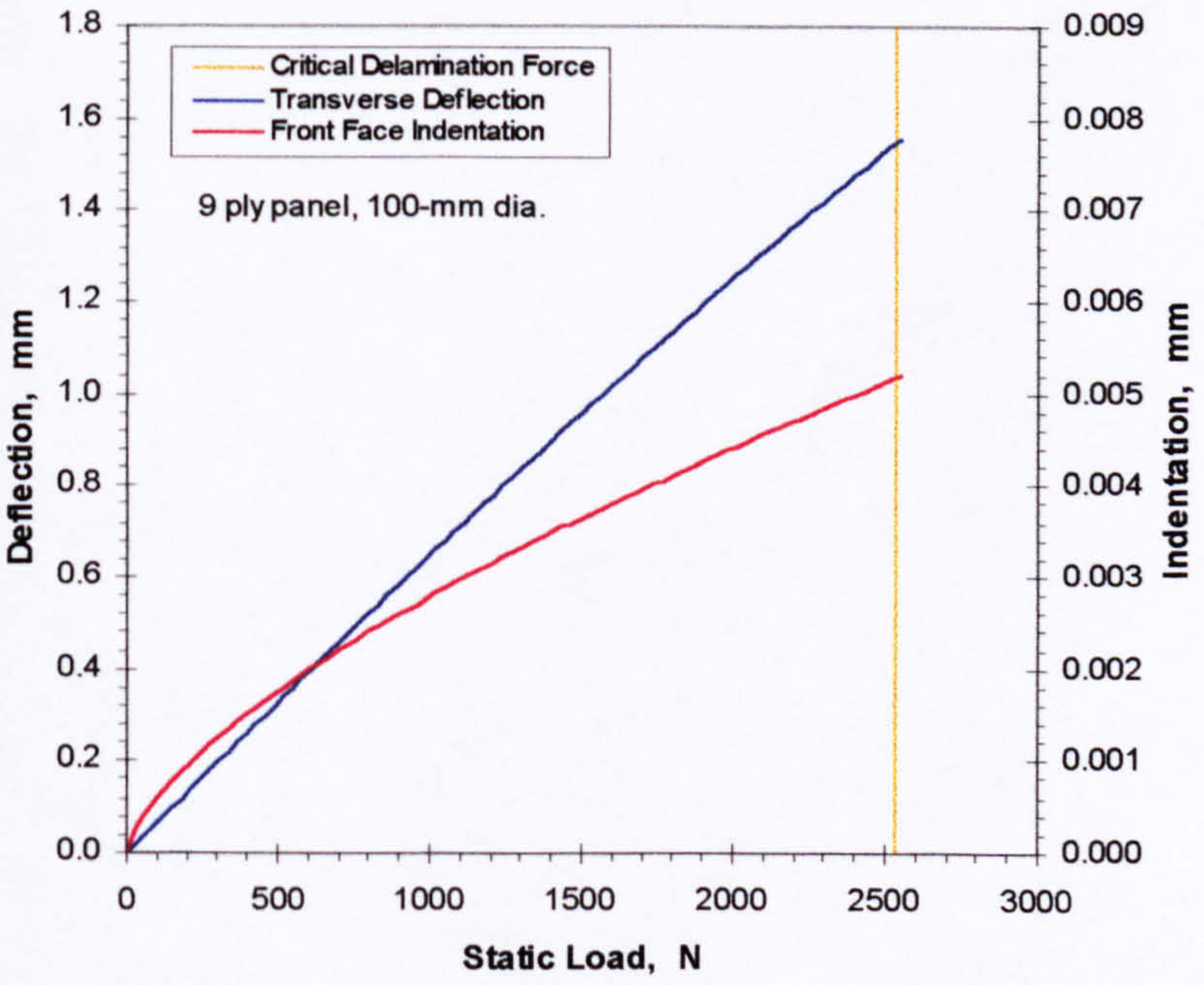

Figure 7.7-2. Panel deflection and indentation v.s. static load for the 9-ply, 100-mm diameter plain panel.

Using the method described above we can calculate for the static penetration energy of the plain panels starting from fundamental principles. In the first attempt, the penetration energies were calculated assuming w_2-w_1 in Figure 7.7 was equal to the radius of the indentor nose. This produced results that were significantly higher than the static penetration energies obtained from the static test data. These results were not surprising since in the actual static tests the panels were found to quickly lose their load carrying capability before the indentor could completely penetrate them (see Figures 4.1 to 4.5 in Chapter 4, pages 48 to 50). This implies that w_2-w_1 must be somewhat less than the radius of the indentor nose. It was found that the calculated penetration energies closely match those obtained from the static tests when w_2-w_1 was made equal to one-half the indentor nose radius. The results of these later calculations are shown in Figure 7.8

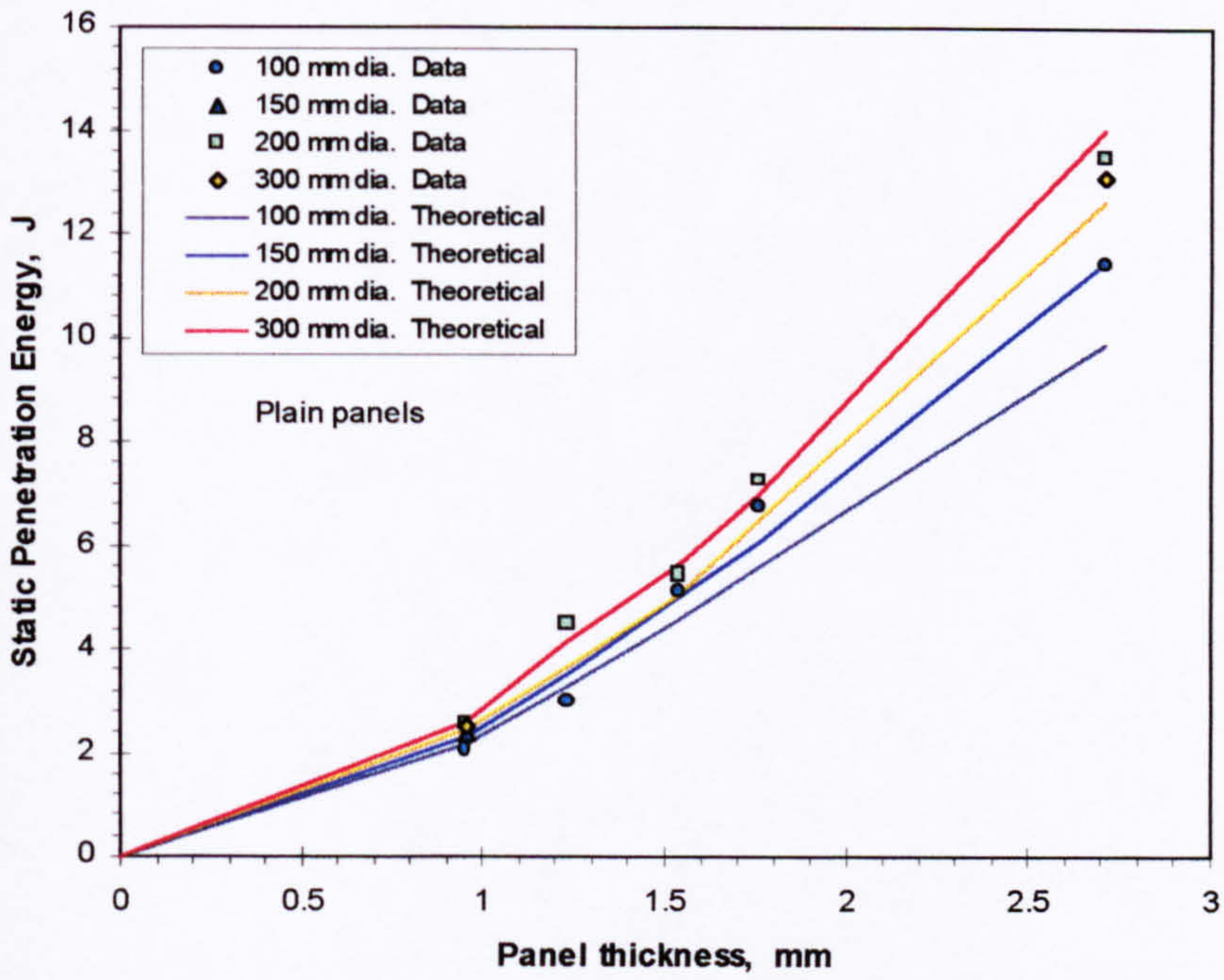

Figure 7.8. Theoretical and actual static penetration energy thresholds for the plain panels.

An explanation as to why the predicted penetration energies closely matches the experimentally determined static penetration energies when the indentor penetration w_2-w_1 is one-half the indentor nose radius must now be made. Figure 7.9 shows a diagram of the indentor penetrating the panel to a depth of one-half the nose radius. At this depth of penetration the size of the hole created in the panel is about 86.6 percent of the diameter of the indentor shank. In this state, most of the transmitted load from the indentor to the panel will be directed radially outward from the hole, in the direction of the plane of the panel, rather than in the transverse direction. This kind of force distribution could encourage the failure of the material around the edge of the hole in the panel by material crushing and/or local buckling. This in turn could lead to the rapid degradation of the panel load carrying capacity that was evident in the static test data (Figures 4.1 to 4.5). For penetration depths greater than one-half the nose radius, the situation becomes more adverse as the size of the hole created in the panel approaches the diameter of the indentor shank resulting in less available material to

physically impede the progress of the penetration process. The events discussed above could explain why the critical panel load could not be sustained over the full radius of the indentor nose and why the indentor penetration w_2-w_1 in Figure 7.7 has to be less than the full radius of the indentor nose.

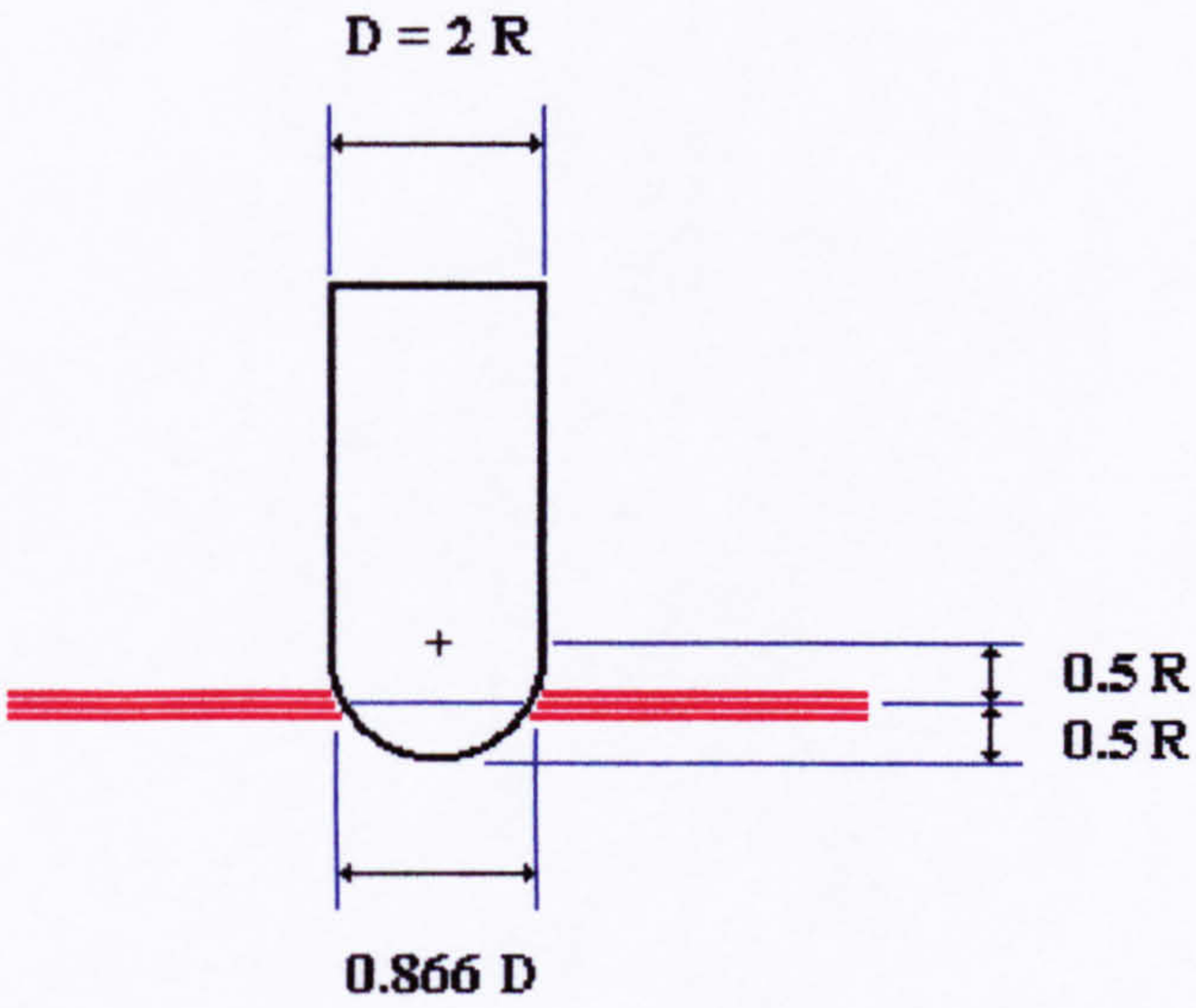

Figure 7.9. Panel penetration by the hemispherical-nosed indentor.

Figure 7.8 is recast in Figure 7.10 to include the penetration energies determined from the impact tests on the plain panels. The close agreement between the theoretical penetration energies and the experimentally determined static penetration energies is seen to extend to the impact data.

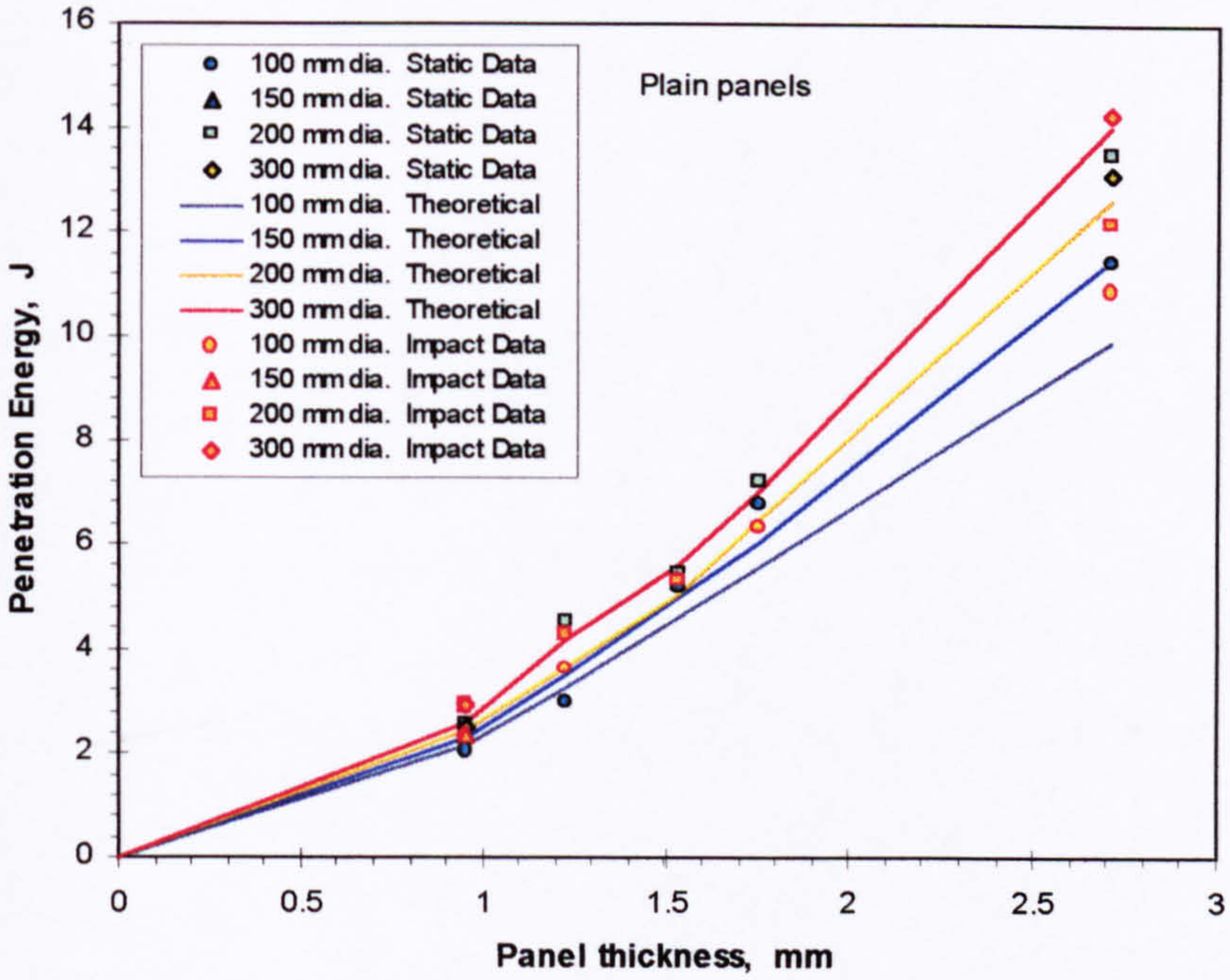

Figure 7.10. Theoretical, actual static and actual impact penetration energy thresholds for the plane panels.

7.6 DAMAGE TRANSITION ENERGY THRESHOLDS

In Chapters 4 and 5 normalised damage maps were presented that helped identify the damage transition energy thresholds. The damage transition energy thresholds differentiated between changes in damage mechanism and were seen to occur at about 50 percent and 80 percent of the impact penetration energy. These thresholds will now be shown to also manifest themselves in the plots of normalised static force against normalised indentor work as shown in Figures 7.10 to 7.12. The data for the plain panels and stiffened panels loaded on the bay was normalised by dividing the static force by the critical delamination force threshold (calculated from Equation 2.12) and by dividing the indentor work by the static penetration energy. In Figure 7.11 the normalised static test data for the plain panels are seen to collapse into a narrow and well-defined band. The same observation could also be made for the normalised data shown in Figure 7.12, which is for the panels loaded on the bay. Also cast in these figures are the vertical lines representing the damage transition energy thresholds at 50

percent and 80 percent of the penetration energy. Closer examination of Figures 7.11 and 7.12 reveal that they correlate very well with the normalised damage maps presented in Chapters 4 and 5. For the range of normalised indentor work below 0.50 the normalised curves all have a generally positive slope. In the damage maps, this range corresponds to the range where backface cracking is the dominant damage mode. For the range of normalised indentor work between 0.50 and 0.80 the normalised curves all tend to flatten out. From the damage maps this range marks the region of rapid delamination growth. When the normalised indentor work is between 0.8 and 1.0 the normalised static force curves now all have negative slope implying the loss of panel integrity in the contact region. In the damage maps this range corresponds to the range of very the rapid growth of delamination damage, the occurrence of fibre fracture and severe matrix damage, and the start of the penetration of the panel. The conclusion that can be drawn from these observations is that in the low-velocity impact response of CFRP panels, it may not be necessary to conduct impact tests at all. The static indentation tests alone can provide sufficient information to determine the penetration energy and the energy levels at which transitions between damage mechanisms occur.

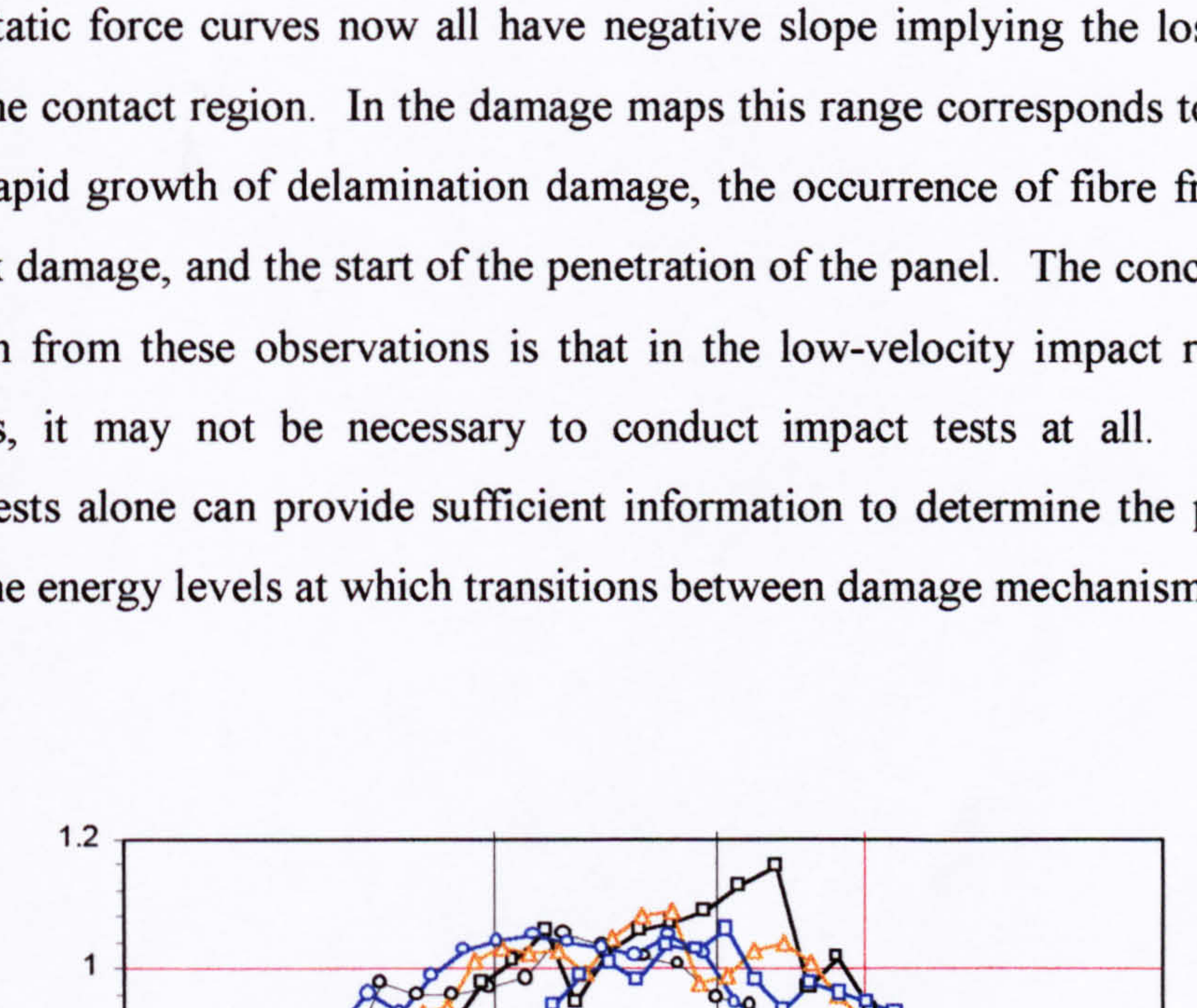

Figure 7.11. Normalised static force v.s. normalised indentor work for the plain panels.

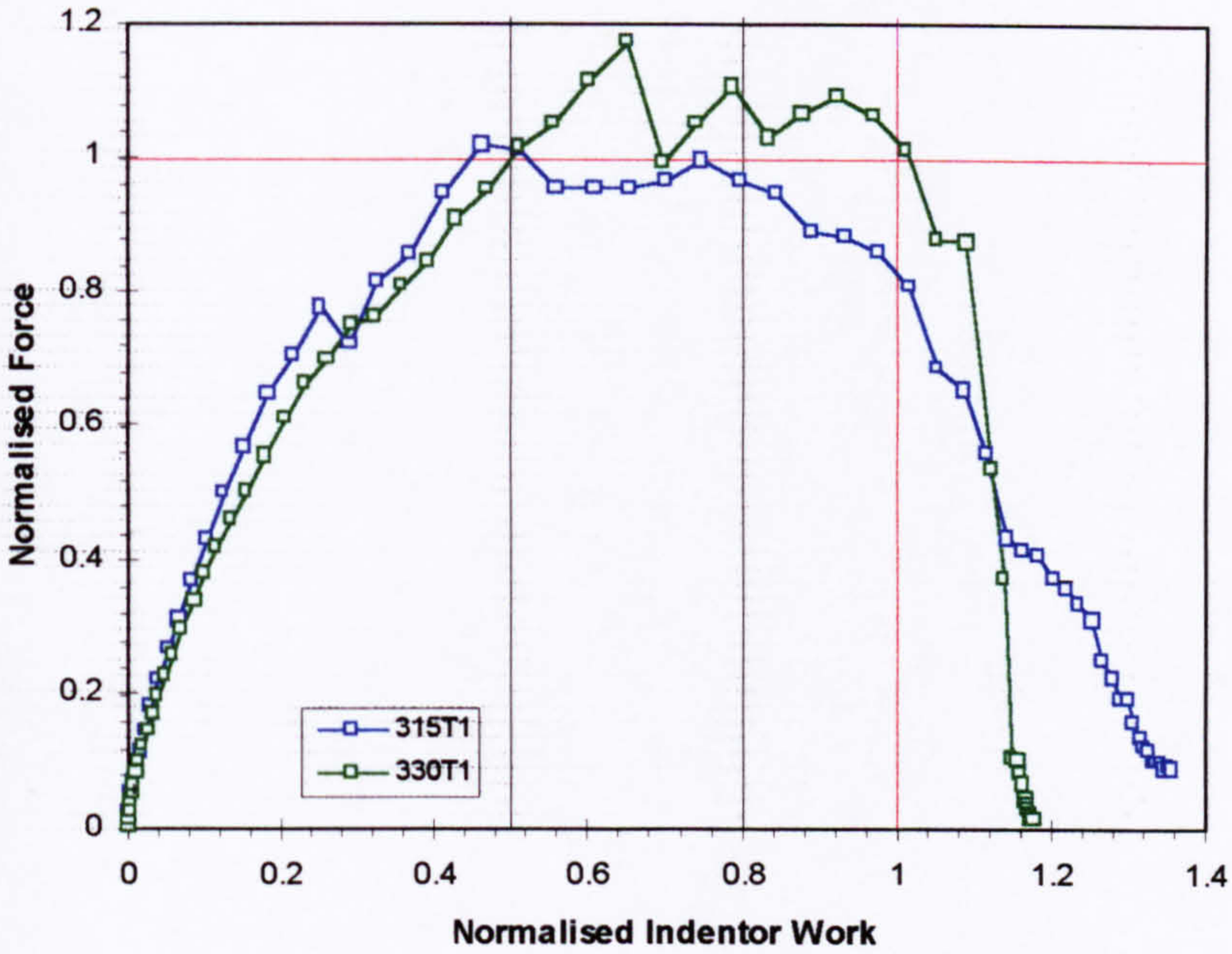

Figure 7.12. Normalised static force v.s. normalised indentor work for the stiffened panels loaded on the bay.

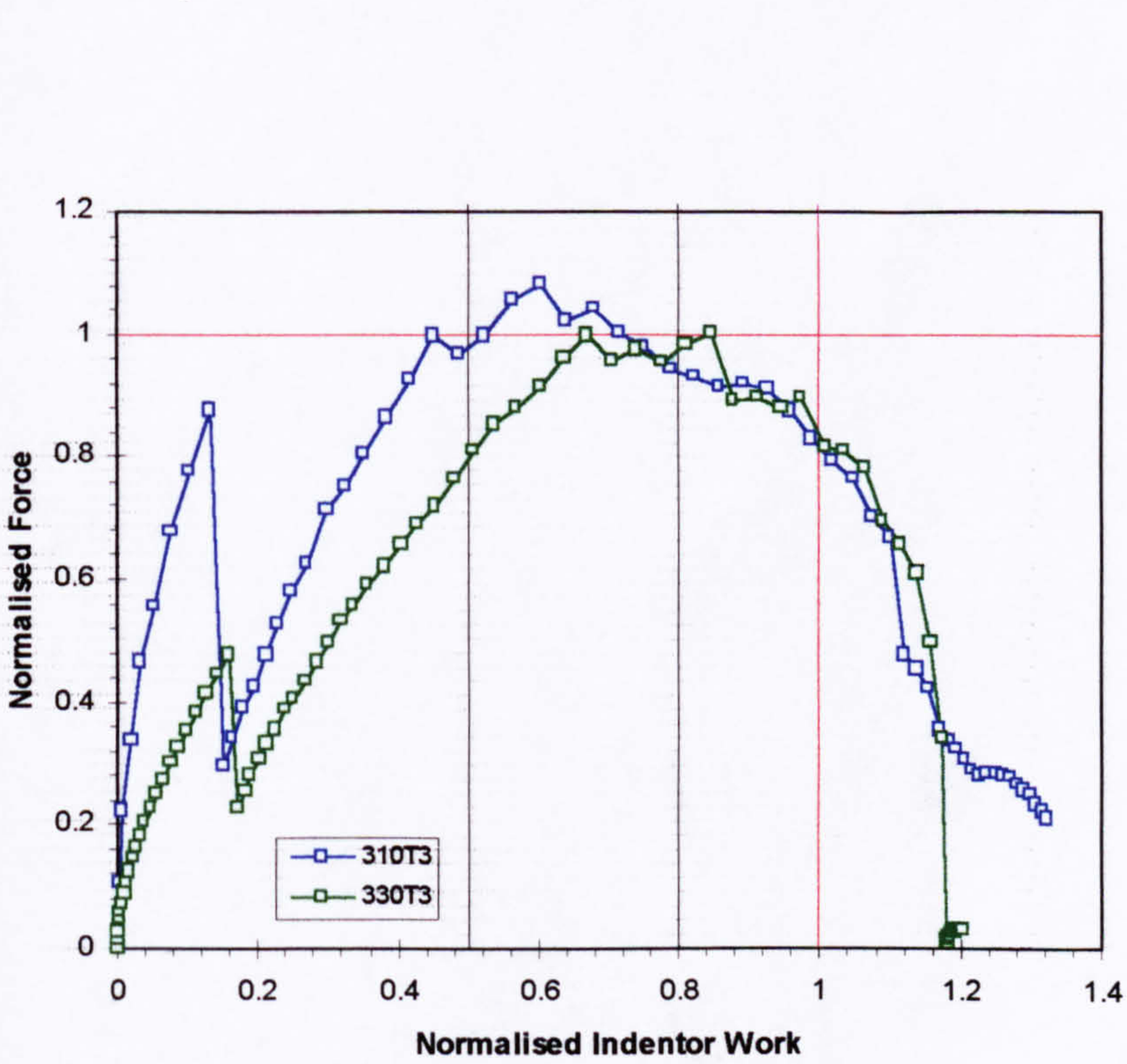

Figure 7.13. Normalised static force v.s. normalised indentor work for the stiffened panels loaded on the stiffener.

Figure 7.13 shows the plot of Normalised static force against normalised indentor work for the stiffened panels loaded on the stiffener. The static force in this plot was normalised against the force at which the panel starts to perforate. From the static test data this force is about 500 Newtons more than the critical delamination force threshold. As was mentioned in Section 7.3.2 the obstruction of the indentor by the stiffener blade contribute to increasing the force necessary to penetrate the panel. The same general patterns and trends in the data shown in Figures 7.11 to 7.12 can also be seen in Figure 7.13 apart from the severe discontinuity in the curves shown in Figure 7.13. This discontinuity is due to the failure of the stiffener blade.

8 CONCLUSIONS AND RECOMMENDATIONS

8.1 INTRODUCTION

This thesis was the result of an extensive study of the static and low-velocity impact response of plain and stiffened CFRP panels. The following conclusions can be drawn from the results of this study:

8.2 GENERAL CONCLUSIONS

- Low-velocity impact on CFRP panels can be treated as a quasi-static process particularly when the mass of the impacting body is much larger than the mass of the panel. The first mode of vibration need only be considered and all other higher order modes can be safely ignored.
- The static indentation response can be used to estimate the impact penetration energy with reasonable accuracy. This is a consequence of the quasi-static nature of the low-velocity impact event.
- Damage maps in the form of plots of projected delamination areas, total backface crack lengths and permanent indentation against incident kinetic energy are instrumental in discerning the different damage development phases and in identifying the energy levels at which changes in damage mechanism occur.
- Changes in damage mechanism were seen to occur at 50 percent and 80 percent of the penetration energy.
- Three forms of damage development were identified from the impact tests on the plain panels. These are: (1) matrix cracking on the backface of the laminate for impact energies up to 50 percent of the penetration energy, (2) the growth of internal delaminations for impact energies between 50 to 80 percent of the penetration energy, and (3) severe material damage in form of matrix cracks, extensive delaminations, fibre fracture, fibre pull out and laminate fragmentation for impact energies between 80 to 100 percent of the penetration energy.

- No significant growth of damage in the panels could be observed for impact energies above the penetration energy threshold. This suggests that damage creation is a highly localised event and that there is an upper limit to the size of the damage created in the panel.
- Panels with the ability to store more elastic energy are capable of resisting impact damage by delaying the onset of the damage initiation forces.
- Relatively simple one degree-of-freedom mass-damper-spring systems using plate constitutive relations drawn from large-deflection isotropic plate theory are adequate in modelling the low-velocity impact response of quasi-isotropic CFRP panels particularly in the case of non-damaging impacts.
- The effects of shear deformation can be neglected for panel diameter-to-thickness ratios greater than 100.
- For constant velocity impact, the increase in the impact duration because of an increase in incident kinetic energy is largely due to the increase in the mass of the indentor. This is particularly true for non-damaging low-energy impacts.

8.3 PARTICULAR CONCLUSIONS

8.3.1 PLAIN PANELS

- The critical force that initiates the first backface cracks appears to be a function of the panel thickness and diameter.
- The critical delamination initiation force is a function of the panel thickness.
- The peak impact force increases with impact energy but reaches a plateau at about the value of the delamination initiation force. Any further increase in kinetic energy only results in the increase of the impact duration until penetration of the panel and embedding of the indentor occurs.
- When the damage maps are normalised with respect to the impact penetration energy threshold and the maximum damage size, the data collapses in to a narrow and well-defined band. This suggests the existence of a scaling rule that governs the processes of damage creation.

8.3.2 STIFFENED PANELS

- The addition of stiffeners can significantly increase the transverse rigidity of the panels.
- For static loading on the bay the magnitude of the perforation force is about the value of the delamination initiation force for the panel skin.
- For impact loading on the bay, the response of the stiffened panels is essentially identical to that of the plain panels but for the effects of greater panel stiffness due to the presence of the blade stiffeners on either side of the impact point.
- For static loading on the stiffener the stiffener blade fails at a much higher applied load for 100-mm diameter panel than that for the 300-mm diameter panel. This was the consequence of the higher bending moments generated in the stiffener of the larger panel.
- For impact loading on the stiffener, the high bending resistance of the stiffener dominated the initial stage of the impact response. In this initial stage a very stiff response was first observed that was followed by an abrupt drop in stiffness corresponding to the fracture of the blade stiffener due to high tensile stresses brought about by high bending loads. As was also observed in the static tests, the fractured blade was still capable of carrying a substantial portion of the load resulting in the shifting of the damage initiation thresholds for the panel skin to higher impact energy values.
- For loading above a stiffener the obstruction of the indentor by the stiffener blade significantly increased the magnitude of the force required to penetrate the panel.
- Damage development and damage size do not appear to be significantly different from that observed from the plain panels apart from the addition of another damage phase that corresponds to the fracture of the stiffener blade for case of impact loading on the stiffener.
- The stiffeners reinforce the panel not only in the transverse direction but in the plane of the panel as well. This results in the suppression of the membrane-like behaviour of the thin panel.

8.4 RECOMMENDATIONS FOR FURTHER WORK

Up to the present time the low-velocity impact response of plain panels is being thoroughly investigated. Much has been achieved in the understanding of the mechanisms involved and many models were developed to predict the behaviour of these panels under impact loading. Although the models range in complexity from simple mass-spring systems to computationally intensive FEA simulations, their results are in general agreement with one another. What is not quite thoroughly understood is the development of damage in the material due to impact loading. Most, if not all of the models require experimentally determined parameters that need to be incorporated into the model in order to produce predictions that are in agreement with test data. Even in the FEA models of damage development, certain simplifying conditions are imposed, such as ply or element discounting, in order to account for the reduction in panel stiffness brought about by damage. This is necessitated by the inadequate knowledge of the distribution of through the thickness stresses in the material in the immediate region of the load application point. It is clear that more work needs to be done in this area to develop the analytical tools required to determine these stresses.

In the model developed in this thesis, empirical relations had to be used when the impact energy was sufficiently high to cause severe local damage in the panels. This points out the inadequacy of the present model in representing impact events that result in significant damage in the material. A more complex model needs to be devised to more thoroughly account for the degradation of the panel load-carrying capacity when it experiences severe local damage.

The work on the stiffened panels brought forth some possibilities for further investigation. The stiffened panels used in this study were blade-stiffened panels that easily fractured at the blade whenever it was loaded above a stiffener. It might be worthwhile to investigate other stiffener geometries, such as J or I sections, that could prove to be more resistant to blade fracture. It would also be of interest to investigate the effect of stiffener spacing and to determine if there is an optimum spacing to satisfy design requirements.

REFERENCES

1. **Abrate, S (1991).** *Impact on Laminated Composite Materials.* Appl. Mech. Rev. Vol 44. No 4. Apr 1991. pp. 155-190

2. **Abrate, S (1994).** *Impact on Laminated Composites: Recent Advances.* Appl. Mech. Rev. Vol 47. No 11. Nov 1994. pp. 517-544.

3. **Banerjee, R (1992).** *Numerical Simulation of Impact Damage in Composite Laminates.* Proceedings of the 7th Technical Conference of the American Society for Composites, Pennsylvania, USA, 1992, pp. 539-552.

4. **Bishop, S (1989).** *Strength and Failure of Woven Carbon Fibre-Reinforced Plastics for High Performance Applications.* Textile Structural Composites. 1989. Elsevier Applied Science.

5. **Cairns, D S and Lagace. P A (1989).** *Transient Response of Graphite/Epoxy and Kevlar/Epoxy Laminates Subjected to Impact.* AIAA Journal. Vol 27. No 11. Nov 1989. pp. 1590-1597

6. **Calcote, L R (1969).** The Analysis of Laminated Composite Structures. Van Nostrand Reinhold Co. 1969

7. **Cantwell, W. J, Curtis P.T. and Morton J (1983).** *Post-Impact fatigue performance of carbon fibre laminates with non-woven and mixed-woven layers.* Composites, Vol. 14, No. 3, July 1983, pp. 301-305.

8. **Cantwell, W. J, Curtis P.T. and Morton J (1984).** *Impact and Subsequent Fatigue Damage Growth in Carbon Fibre Laminates.* Int J Fatigue,Vol 6, No 2 April 1984. pp. 113-118.

9. **Cantwell, W J and Morton, J (1985).** *Detection of Impact Damage in CFRP Laminates.* Composite Structures. Vol 3. 1985. pp. 241-257

10. **Cantwell, W J and Morton, J (1990).** *Impact Perforation of Carbon Fibre Reinforced Plastic.* Composites Sci. and Tech. 1990. Elsevier Science Publishers. pp. 119-141

11. **Cantwell, W J and Morton, J (1991).** *The Impact resistance of Composite Materials - A Review.* Composites. Vol 22. N0 5. Sept 1991. pp. 347-361

12. **Caprino, G (1984).** *Residual Strength Prediction of Impacted Composite Laminates.* Composite Materials. Vol. 18. pp 508-518.

13. **Chang and Chang (1987).** *A Progressive Damage Model for Laminated Composites containing Stress Concentrations.* J. of Composite Materials. Vol. 26. 1987. pp 834-855

14. **Charalambides, M; Kinloch, A J; Wang, Y and Williams, J G (1992).** *On the Analysis of Mixed-Mode Failure.* Int. Journal of Fracture. Vol. 54. 1992. pp. 269-291.

15. **Chaturvedi, S K and Sierakowski, R L (1985).** *Effects of Impactor Size on Impact Damage-Growth and Residual Properties in SMC-R50 Composite.* J. of Composites Materials. Vol 19. Mar 1985. pp. 100-113.

16. **Cheung, A K H and Scott, M L (1995).** *Low Velocity Impact and Static Indentation of Thin, Stiffened, Composite Panels.* International Aerospace Congress, PICAST 2-AAC 6, March 1995, pp. 631-638.

17. **Choi, H Y; Downs, R J and Chang, F K (1991a).** *A New Approach toward Understanding Damage Mechanisms and Mechanics of Laminated Composites due to Low-Velocity Impact: Part I - Experiments.* J. of Composite Materials. Vol 25. Aug 1991. pp. 992-1011

18. **Choi, H Y; Downs, R J and Chang, F K (1991b).** *A New Approach toward Understanding Damage Mechanisms and Mechanics of Laminated Composites due to Low-Velocity Impact: Part II - Analysis.* J. of Composite Materials. Vol 25. Aug 1991. pp. 1012-1038

19. **Clark, G (1989).** *Modelling of Impact Damage in Composite Laminates.* Composites. Vol 20. No 3. May 1989. pp. 209-214

20. **Curtis, P T (1988).** *CRAG Test Methods for the Measurement of Engineering Properties of Fibre Reinforced Plastics.* RAE TR 88012. Royal Aerospace Establishment, UK. 1988

21. **Davidson, B D and Krafchak, T M (1993).** *Analysis of Instability-Related Delamination Growth Using a Crack Tip Element.* AIAA Journal. Vol. 31. No. 11. 1993. pp. 2130-2136.

22. **Davies, G A O; Zhang, X; Zhou, G and Watson, S (1994).** *Numerical Modelling of Impact Damage.* Composites. Vol 25. No 5. 1994. pp. 342-350

23. **Davies, G A O and Zhang, X (1995).** *Impact Damage Prediction in Carbon Composite Structures.* Int. J. of Impact Engng. Vol 16. No 1. 1995. pp. 149-170

24. **Davies, G A O. Hitchings, D. and Zhou, G (1996).** *Impact damage and residual strengths of woven fabric glass/polyester laminates.* Composites Part A 27A, 1996. Elsevier Science Ltd, 1996, pp. 1147-1156.

25. **Davies, G. A. O., Robinson, P., Robson J. and Eady, D (1997).** *Shear driven delamination propagation in two-dimensions. Composites Part A 28A.* Elsevier Science Limited, 1997. pp. 757-765.

26. **Delfosse, D. and Poursartip, A (1997).** *Energy-based approach to impact damage in CFRP laminates.* Composites Part A 28A (1997). Elsevier Science Limited, pp. 647-655.

27. **Dobyns, A. L (1980).** *Analysis of Simply-Supported Orthotropic Plates Subject to Static and Dynamic Loads.* AIAA Journal, Vol.19, No. 5, 1980. Pp. 642-650.

28. **Found, M S., Howard I.C. and Paran A P (1997).** *Size Effects in Thin CFRP Panels Subjected to Impact.* Composite Structures Vol. 38, No. 1-4, pp. 599-607. Elsevier Science Ltd., 1997.

29. **Found, M S, Howard I C and Paran, A P (1998a).** *Impact Perforation of Thin Stiffened CFRP Panels.* 2nd International Conference on Composite Science and Technology. 9-11 June 1998. Durban: ICCST/2.

30. **Found, M.S., Howard I C. and Paran A P (1998b).** *Impact Behaviour of Stiffened CFRP Sections.* Composite Structures, Vol 39, Nos 3-4, pp 229-235. Elsevier Science Ltd., 1998.

31. **Goldsmith, W (1960).** Impact-The Theory and Physical Behaviour of Colliding Solids. Edward Arnold (Publishers) Ltd. London. 1960.

32. **Greenhalgh, E., Bishop, S. M., Bray, D., Hughes, D., Lahiff, S., and Millson, B (1997).** *Characterisation of Impact Damage in Skin-Stringer Composite Structures.* Composite Structures, Vol. 36 1996, pp 187-207. Elsevier Applied Science Ltd. 1997

33. **Harris, C M and Crede, C E (1961).** Shock and Vibration Handbook Vol. 1. McGraw-Hill Book Co. Inc. 1961.

34. **Hong, S and Liu, D (1989).** *On the Relationship between Impact Energy and Delamination Area.* Experimental Mechanics. Vol 29. No 2. Jun 1989. pp. 115-120

35. **Jackson, K J and Scott, M L (1996).** *Hail Impact Testing of Thin-Skinned Carbon Fibre Composite Panels.* Proc. 1st Int. Conf. Composite Science and Technology. Eds. S Adali and V E Vesijenko. Durban, South Africa. 1996. pp 209-214

36. **Jones, R M (1975).** Mechanics of Composite Materials. Int. Student Edition. McGraw-Hill Kogakusha, Ltd. Tokyo. 1975

37. **Kistler, L. S. and Waas, A. M (1997).** *Impact Response of Cylindrically Curved Laminates Including a Large Deformation Scaling Study.* Int. J. Impact Engng., Vol. 21, Nos. 1-2, pp. 61-75. Elsevier Science Ltd., 1997.

38. **Kolax, M W (1992)**. *Composite Wing Results of Deutsche Airbus Technology Program*. 37th International SAMPE Symposium. 9-12 Mar 1992

39. **Lal, K M (1983 a)**. *Low Velocity Transverse Impact Behavior of 8-Ply, Graphite-Epoxy Laminates*. J. of Reinforced Plastics and Composites. Vol 2. Oct 1983. pp. 216-225

40. **Lal, K M (1983 b)**. *Residual Strength Assessment of Low Velocity Impact Damage of Graphite-Epoxy Laminates*. J. of Reinforced Plastics and Composites. Vol 2. Oct 1883. pp. 226-238

41. **Leissa, A W (1969)**. Vibration of Plates. NASA SP-160. National Aeronautics and Space Administration. 1969

42. **Liu, D (1988)**. *Impact-Induced Delamination - A view of bending Stiffness Mismatching*. J. of Composite Materials. Vol 22. 1988. pp. 674-692

43. **Madan, R. C. and Sutton, J. O (1988)**. *Design, Testing, and Damage Tolerance Study of Bonded Stiffened Composite Wing Cover Panels*. 29 Structures, Structural Dynamics and Materials Conference, Williamsburg, Va, USA, Apr. 1988, pp. 623-630.

44. **Mindlin, R. D (1951)**. *Influence of Rotatory Inertia and Shear on Flexural Motions of Isotropic, Elastic Plates*. Journal of Applied Mechanics, March 1951, pp.31-38.

45. **Morton, J (1998)**. *Scaling of Impact-Loaded Carbon Fiber Composites*. AIAA Journal, Vol. 26, No. 8, August 1998. pp. 989-994.

46. **Murphy, D (1994)**. *Non-linear analysis provides new insights into impact damage of composite structures*. Composites, Vol. 25, No. 1, 1994, pp. 65-69.

47. **Olsson, R (1992)**. *Impact Response of Orthotropic Composite Plates Predicted from a One-Parameter Differential Equation*. AIAA Journal, Vol. 30, No. 6, June 1992. pp 1587-1596.

48. **Oxley, M (1991)**. *The Effect of Low Velocity Impact Damage on the Performance of s Woven CFRP*. Ph.D. Thesis. Univ. of Sheffield. 1991

49. **Prichard, J C and Hogg, P J (1990)**. *The Role of Impact Damage in Post-Impact Compression Testing*. Composites. Vol 21. No 6. Nov 1990. pp. 503-511

50. **Qian, Y and Swanson, S (1990)**. *Experimental Measurement of Impact Response in Carbon/Epoxy Plates*. AIAA Journal. Vol 28. No 6. Jun 1990. pp 1069-1074.

51. **Qian, Y., Swanson, S.R., Nuismer, R. J., and Bucinell, R. B (1990).** *An Experimental Study of Scaling Rules for Impact Damage in Fiber Composites.* Journal of Composite Materials, Vol. 24, May 1990, pp. 559-570.

52. **Richardson, M O W. and Wisheart, M J (1996).** *Review of low-velocity impact properties of composite materials.* Composites Part A 27A. Elsevier Science Limited, 1996, pp. 1123-1131.

53. **Robinson, P and Davies, G. A (1992).** *Impactor Mass and Specimen Geometry Effects in Low Velocity Impact of Laminated Composites.* Int. J. Impact Engng. Vol. 12, No. 2. 1992. pp. 189-207.

54. **Shigley, J. E (1963).** *Mechanical Engineering Design.* 2nd Edition. McGraw-Hill Book Company.

55. **Shivakumar, K. N., Elber, W. and Illg, W (1985).** *Prediction of Impact Force and Duration Due to Low-Velocity Impact on Circular Composite Laminates.* Journal of Applied Mechanics, Vol. 52, September 1985, pp. 674-680.

56. **Sjoblom, P (1987).** *Simple Design Approach Against Low-Velocity Impact Damage.* Proceedings 32nd Int. SAMPE Symposium. 6-9 Apr 1987. pp. 529-539.

57. **Sjoblom, P; Hartness, J and Cordell, T (1988).** *On Low-Velocity Impact Testing of Composite Materials.* Journal of Compoaite Materials. Vol. 22. No. 1. pp 30-52

58. **Timoshenko, S and Woinowsky-Krieger, S (1959).** Theory of Plates and Shells. 2nd Ed. McGraw-Hill Book Co. Inc. 1959

59. **Timoshenko, S, Young, D H and Weaver, Jr, W (1974).** Vibration Problems in Engineering. 4th Ed. John Wiley and Sons. 1974

60. **Tropis, A; Thomas, M; Bounie, J L and Lafon, P (1995).** *Certification of the Composite Outer Wing of the ATR72.* Proc. Instn. of Mech. Engrs. Vol 209. No 4. 1995

61. **Tsai, S W (1985).** Composites Design-1985. United States Air Force Materials Laboratory. (AFWAL-TR-84-4183). Think Composites

62. **Tsai, S W and Hahn, H T (1980).** Introduction to Composite Materials. Technomic Publishing Co. Inc. 1980

63. **Ursenbach, D O; Vaziri, R and Delfosse, D (1995).** *An Engineering Model for Deformation CFRP Plates during Penetration.* Composite Structures 32 (1995). 8th Int. Conf. on Composite Structures. I H Marshall, Editor. Elsevier Applied Science. pp197-202

64. **Verpoest, I; Marien, J; Devos, J and Wevers, M (1987).** *Absorbed Energy, Damage and Residual Strength After Impact of Glass Fibre Epoxy Composites.*

6th Int. Conf. on Composite Materials. Vol 3. London. 1987. Elsevier Applied Science. pp. 3.485-3.493

65. **Whitney, J M, and Pagano, N J (1970).** *Shear Deformation in Heterogeneous Anisotropic Plates.* Journal of Applied Mechanics, Dec. 1970, pp.1031-1036.

66. **Wu, H T and Springer, G S (1988).** *Impact Induced Stresses, Strains and Delaminations in Composite Plates.* Journal of Composite Materials, Vol. 22, June 1988. Technomic Publishing Co., pp. 533-560.

67. **Zhou, G and Davies, G A O (1995).** *Impact Response of Thick Glass Fibre Reinforced Polyester Laminates.* Int. J. Impact Engng. Vol 16. No 3. 1995. pp. 357-374

APPENDIX A

Properties of Fibredux 914C-713-40

	Warp	Weft
Tensile strength	750 MPa	730 MPa
Tensile modulus	67 GPa	65 GPa
Compression strength	740 MPa	700 MPa
Compression modulus	64 GPa	63 GPa

In-plane shear strength	110 MPa
In-plane shear modulus	4.6 GPa
In-plain Poisson's ratio	0.05

Through-the-thickness modulus	8 GPa
Through-the-thickness shear modulus	6 GPa
Through-the-thickness Poisson's ratio	0.025

APPENDIX B

Laminate Properties

	3, 6, 9 Ply Laminates	4 Ply Laminate	5 Ply Laminate
E_1 GPa	46.245	47.631	47.125
E_2 GPa	45.821	47.034	46.637
ν_{12}	0.33495	0.314417	0.321196

Quasi-isotropic Properties

E_r	46764	MPa
E_z	8000	MPa
G_r	4600	MPa
G_{zr}	6000	MPa
ν_r	0.32904	
ν_{zr}	0.025	

APPENDIX C

Ingredients for the x-ray penetrant solution.

Water	10 ml
Zinc Iodide Powder	60 g
Propan-2-ol	10 ml
Kodak Photoflo	0.5 ml

Precautions.

Zinc Iodide is a very reactive chemical. Do not handle without gloves. Do not get on to clothing or metal surfaces. Always thoroughly rinse any article used to apply the solution (such as brushes) to the CFRP.

Instructions for mixing and storage.

Dissolve Zinc Iodide powder in water by adding the powder to the water a little at a time. Add Propan-2-ol and Kodak Photoflo. Mix well. Unused solution must be refrigerated.

APPENDIX D

Typical projected delamination damage patterns as revealed by penetrant-enhanced x-ray techniques (delamination patterns for the 3-ply plain panels are shown).

IPE – Impact Penetration Energy.

0.384 J (16.4% IPE)

0.510 J (21.8% IPE)

0.618 J (26.4% IPE)

0.873 J (37.3% IPE)

1.080 J (46.1% IPE)

1.228 J (52.4% IPE)

1.437 J (61.4% IPE)

1.747 J (74.6% IPE)

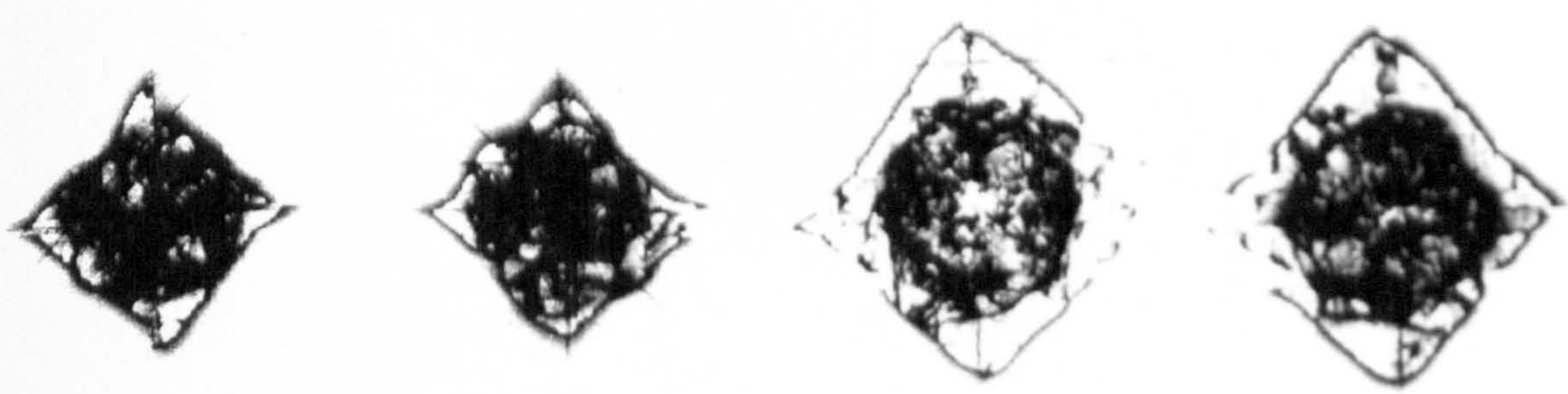

1.914 J (81.7% IPE)

2.038 J (87.0% IPE)

2.311 J (98.7% IPE)

2.378 J (101.5% IPE)